Physics of Atomic Nuclei, Vol. 65, No. 12, 2002, pp. 2101–2108. From Yadernaya Fizika, Vol. 65, No. 12, 2002, pp. 2165–2172.

NEW PHYSICS BEYOND THE STANDARD MODEL

Muon g-2 and Implications for Supersymmetry*

U. Chattopadhyay and P. Nath[1)]

Department of Theoretical Physics, Tata Institute of Fundamental Research, Mumbai, India

Received February 13, 2002

Abstract—A brief review is given of the implications of the recent Brookhaven result on the muon anomaly (a_μ) for supersymmetry. We focus mainly on the implications of the recent results for the minimal supergravity unified model. We show that the observed difference implies the existence of sparticles, most of which should become observable at the Large Hadron Collider. Further, as foreseen in works prior to the Brookhaven experiment, the sign of the difference between experimental prediction of a_μ and its Standard Model value determines the sign of the Higgs mixing parameter μ. The μ sign has important implications for the direct detection of dark matter. Implications of the Brookhaven result for other low-energy phenomena are also discussed. © *2002 MAIK "Nauka/Interperiodica".*

1. INTRODUCTION

In this paper, we briefly consider the recent developments in the analyses of the muon anomaly. First, we will discuss the recent Brookhaven National Laboratory (BNL) result on a_μ [1] ($a = (g-2)/2$, where g is the gyromagnetic ratio) and its Standard Model prediction. We then discuss the supersymmetric electroweak effects on a_μ. We will also discuss briefly the effects of extra dimensions on a_μ. Finally, we will discuss the implications of the BNL result for the direct detection of supersymmetry. The anomalous moment is a sensitive probe of new physics since

$$a_l^{\text{new physics}} \sim m_l^2/\Lambda^2. \tag{1}$$

Thus, a_μ is more sensitive to new physics relative to a_e, even though a_e is more accurately determined [2] since $a_\mu/a_e \sim 4\times 10^4$. Regarding the experimental determination of a_μ, one has first the classic CERN experiment of 1977 [3], which gave $a_\mu^{\text{exp}} = 11\,659\,230(84)\times 10^{-10}$. The error in this measurement was reduced by a factor of 2 in 1998 by the BNL experiment [4], which gave $a_\mu^{\text{exp}} = 11\,659\,205(46)\times 10^{-10}$, and the same error was further reduced by a factor of 3 by the most recent BNL result [1]:

$$a_\mu^{\text{exp}} = 11\,659\,203(15)\times 10^{-10}. \tag{2}$$

The Standard Model contribution consists of several parts [5]:

$$a_\mu^{\text{SM}} = a_\mu^{\text{qed}} + a_\mu^{\text{EW}} + a_\mu^{\text{had}}, \tag{3}$$

where the "qed" correction is computed to order α^5 [5]:

$$a_\mu^{\text{qed}} = 11\,658\,470.57(0.29)\times 10^{-10} \tag{4}$$

and a_μ^{EW} including the one-loop [6] and the two-loop [5] Standard Model electroweak correction is

$$a_\mu^{\text{EW}} = 15.2(0.4)\times 10^{-10}. \tag{5}$$

The most difficult part of the analysis relates to the hadronic contribution. It consists of several parts: the α^2 hadronic vacuum polarization contribution, the α^3 hadronic correction, and the light-by-light contribution. The α^2 hadronic vacuum polarization contribution can be related to observables. Specifically, one can write

$$a_\mu^{\text{had}}(\text{vac.pol.}) = \frac{1}{4\pi^3}\int\limits_{4m_\pi^2}^{\infty} dsK(s)\sigma_h(s), \tag{6}$$

where $\sigma_h(s) = \sigma(e^+e^-\to \text{hadrons})$ and $K(s)$ is a kinematical factor. The integral in (6) is dominated by the low-energy part, i.e., the part up to 2 GeV, which correspondingly is also very sensitive to errors in the input data. In the evaluations of (6), one uses a combination of experimental data at low energy and a theoretical (QCD) extrapolation in the high-energy tail. The analysis of a_μ^{had}(vac.pol.) is the most contentious part of the analysis. In computing the difference $a_\mu^{\text{exp}} - a_\mu^{\text{SM}}$, BNL used the result of Davier and Höcker [7]: $a_\mu^{\text{had}}(\text{vac.pol.}) = 692.4(6.2)\times 10^{-10}$. However, other estimates have appeared more recently, and we will mention these later. The α^3 hadronic correction can also be related to observables

*This article was submitted by the authors in English.

[1)]Theoretical Physics Division, CERN, Geneva, Switzerland; Permanent address: Department of Physics, Northeastern University, Boston, USA; E-mail: nath@neu.edu

but is generally small with a correspondingly small error [8]: $\Delta a_\mu^{\rm had}(\text{vac.pol.}) = -10.1(0.6) \times 10^{-10}$. The light-by-light hadronic correction is the second most contentious part of $a_\mu^{\rm SM}$. This part cannot be related to any observables and is thus a purely theoretical construct. In the free quark model, it evaluates to a positive contribution. However, more realistic analyses give a negative contribution [9]: $\Delta a_\mu^{\rm had}(\text{light-by-light}) = -8.5(2.5) \times 10^{-10}$. This result, which is though more reliable than the result from the free-quark model, still has a degree of model dependence. Overall, however, $\Delta a_\mu^{\rm had}$(light-by-light) is not the controlling factor in interpreting the BNL result unless, of course, its sign is reversed. The total result then is $a_\mu^{\rm had}(\text{total}) = a_\mu^{\rm had}(\text{vac.pol.}) + \Delta a_\mu^{\rm had}(\text{vac.pol.}) + \Delta a_\mu^{\rm had}(\text{light-by-light})$, which gives

$$a_\mu^{\rm had} = 673.9(6.7) \times 10^{-10}. \quad (7)$$

Together, one finds

$$a_\mu^{\rm SM} = 11\,659\,159.7(6.7) \times 10^{-10} \quad (8)$$

and a 2.6σ deviation of experiment from theory,

$$a_\mu^{\rm exp} - a_\mu^{\rm SM} = 43(16) \times 10^{-10}. \quad (9)$$

After the new $g-2$ result from Brookhaven became available, there have been several reanalyses of the hadronic uncertainty [10–14]. Thus, the analysis of [11] gives $\Delta = 33.3(17.1)$ and the analysis of [12] gives $\Delta = 37.7 \pm (15.0)_{\rm exp} \pm (15.6)_{\rm th}$, where $\Delta = (a_\mu^{\rm exp} - a_\mu^{\rm SM}) \times 10^{10}$. One finds that the difference $(a_\mu^{\rm exp} - a_\mu^{\rm SM})$ in these analyses is somewhat smaller and the error is somewhat larger compared to the result of (9). Similar trends are reported in the analyses of [10, 13]. An interesting assessment of the hadronic contribution and the possibilities for improvement in the future is given in [14]. For the discussion of the rest of this paper, we will assume the validity of (9).

One may ask what is the nature of new physics in view of (9). Some possibilities that present themselves are supersymmetry, compact extra dimensions, muon compositeness, technicolor, anomalous W couplings, new gauge bosons, leptoquarks, and radiative muon masses. We shall focus here mostly on supersymmetry as the possible origin of the difference observed by the BNL experiment. Supersymmetry has many attractive features. It helps to stabilize the hierarchy problem with fundamental Higgs, and it leads to the unification of the gauge coupling constants consistent with the LEP data. To extract meaningful results from SUSY models, however, one needs a mechanism of supersymmetry breaking. There are several mechanisms proposed for the breaking of supersymmetry such as gravity-mediated, gauge-mediated, and anomaly-mediated. We focus in this paper mainly on the gravity-mediated models, i.e., the supergravity (SUGRA) unified models [15]. In the minimal version of this model based on a flat Kähler potential, i.e., mSUGRA, the SUSY-breaking sector is described by the parameters m_0, $m_{1/2}$, A_0, $\tan\beta$, and $\mathrm{sgn}(\mu)$. Here, m_0 is the universal scalar mass; $m_{1/2}$ is the universal gaugino mass; A_0 is the universal trilinear coupling; $\tan\beta = \langle H_2\rangle/\langle H_1\rangle$, where H_2 gives mass to the up-quark and H_1 gives mass to the down-quark and the lepton; and μ is the Higgs mixing parameter. The use of the curved Kähler potential results in a SUGRA model with nonuniversalities consisting of the minimal set of soft SUSY parameters and additional parameters that, for example, describe deviations from universality in the Higgs sector and in the third generation sector.

Some of the interesting features of SUGRA models include the fact that the radiative-breaking constraints of the electroweak symmetry lead to the lightest neutralino being the lightest supersymmetric particle (LSP) and, thus, under the constraint of R parity, the lightest neutralino is a possible candidate for dark matter over most of the parameter space of the model. Also, analyses in SUGRA models show that the lightest Higgs must have a mass $m_h \leq 130$ GeV under the usual assumptions of naturalness, i.e., $m_0, m_{\tilde{g}} < 1$ TeV. Finally, SUGRA models bring in new sources of CP violation that in any case are needed for baryogenesis. Thus, mSUGRA has two soft CP-violating phases, while many more soft CP-violating phases arise in nonuniversal SUGRA models and in the minimal supersymmetric standard model (MSSM). Regarding some of the other alternatives of SUSY breaking, one finds that the gauge-mediated breaking (GMSB) does not produce a candidate for cold dark matter, while the anomaly-mediated supersymmetry-breaking (AMSB) scenario now appears very stringently constrained by the BNL data when combined with its specially characteristic $b \to s + \gamma$ constraint.

Our analysis in mSUGRA includes two-loop renormalization group evolutions (RGE) for the couplings as well as soft parameters with the Higgs potential at the complete one-loop level [16] minimized at the scale $Q \sim \sqrt{m_{\tilde{t}_1} m_{\tilde{t}_2}}$ for radiative electroweak symmetry breaking. We have also included the SUSY QCD corrections [17] to the top quark (with $m_t = 175$ GeV) and the bottom quark masses, and we have used the code FeynHiggsFast [18] for the mass of the light Higgs boson.

2. SUSY CONTRIBUTION TO a_μ AT ONE LOOP

It is well known that a_μ vanishes in the exact supersymmetric limit [19] and is nonvanishing only in the presence of supersymmetry breaking. Not surprisingly then, $a_\mu^{\rm SUSY}$ (where $a_\mu = a_\mu^{\rm SM} + a_\mu^{\rm SUSY}$) is sensitive to the nature of new physics [20]. Thus, the analysis of $a_\mu^{\rm SUSY}$ requires a realistic model of supersymmetry breaking. The first such analysis within the well-motivated SUGRA model was given in [21, 22]. We partially reproduce here the result of [22]

$$a_\mu^{\rm SUSY} = a_\mu^{\tilde W} + a_\mu^{\tilde Z}, \tag{10}$$

where $a_\mu^{\tilde W}$ is the chargino contribution and $a_\mu^{\tilde Z}$ is the neutralino contribution. The chargino contribution is typically the larger contribution over most of the parameter space and is

$$a_\mu^{\tilde W} = \frac{m_\mu^2}{48\pi^2}\frac{{A_R^{(a)}}^2}{m_{\tilde W_a}^2}F_1\left(\frac{m_{\tilde\nu_\mu}^2}{m_{\tilde W_a}^2}\right) + \frac{m_\mu}{8\pi^2}\frac{A_R^{(a)}A_L^{(a)}}{m_{\tilde W_a}}F_2\left(\frac{m_{\tilde\nu_\mu}^2}{m_{\tilde W_a}^2}\right). \tag{11}$$

Here, $A_L(A_R)$ are the left (right) chiral amplitudes

$$A_L^{(1)} = (-1)^\theta\frac{em_\mu\cos\gamma_2}{2M_W\sin\theta_{\rm W}\cos\beta}, \qquad A_R^{(1)} = -\frac{e}{\sqrt{2}\sin\theta_{\rm W}}\cos\gamma_1, \tag{12}$$

$$A_L^{(2)} = -\frac{em_\mu\sin\gamma_2}{2M_W\sin\theta_{\rm W}\cos\beta}, \qquad A_R^{(2)} = -\frac{e}{\sqrt{2}\sin\theta_{\rm W}}\sin\gamma_1, \tag{13}$$

where $\theta = 0$ (1) if the light chargino eigenvalue λ_1 is positive (negative), and $\gamma_{1,2}$ are mixing angles. We wish to point out that the most dominant contribution to $a_\mu^{\rm SUSY}$ comes from the chirality nondiagonal lighter chargino part of $a_\mu^{\tilde W}$. First, we note that, for the most contributing term in the chargino part, the coupling is proportional to $1/\cos\beta(\sim\tan\beta)$ and thus a_μ increases almost linearly with $\tan\beta$ [23, 24]; second, due to the same dominant term, the sign of $a_\mu^{\rm SUSY}$ is correlated strongly with the sign of μ (we use here the μ-sign convention of [25]). It is easy to exhibit this by considering the eigenvalues λ_i $(i = 1, 2)$ of the chargino mass matrix (where we define λ_1 as the eigenvalue corresponding to the lighter chargino) $\lambda_1 < 0$ for $\mu > 0$ and $\lambda_1 > 0$ for $\mu < 0$ except for $\tan\beta \sim 1$, which leads to [23, 24] $a_\mu^{\rm SUSY} > 0$, $\mu > 0$ and $a_\mu^{\rm SUSY} < 0$, $\mu < 0$.

3. IMPLICATIONS OF PRECISE BNL DATA

In the following analysis, we assume CP conservation. Under this constraint and setting $a_\mu^{\rm SUSY} = a_\mu^{\rm exp} - a_\mu^{\rm SM}$, we immediately find that the BNL data determines [26–29] $\mathrm{sgn}(\mu) = +1$. In imposing the BNL constraint, we use a 2σ corridor

$$10.6\times10^{-10} < a_\mu^{\rm SUSY} < 76.2\times10^{-10}. \tag{14}$$

We utilize (14) in determining the allowed parameter space of mSUGRA using the one-loop formula for which the chargino part is given by (11) [22]. (The leading-order correction to one loop as computed in [30] gives a fractional contribution of $-(4\alpha/\pi)\ln(M_S/m_\mu)$, where M_S is an average sparticle mass. This is typically less than 10% and is ignored in the analysis here.) In Fig. 1, we give an analysis of this constraint in the m_0–$m_{1/2}$ plane for the case of $\tan\beta = 10$. One finds that there is now an upper limit on m_0 and $m_{1/2}$. Interestingly, we find that the allowed region of the parameter space which is below the $a_\mu^{\rm SUSY} = \delta a_\mu^{\rm small} = 10.6\times10^{-10}$ line allows for a light Higgs consistent with the lower limit of about 115 GeV as given by the possible signal at LEP [31]. The white region close to the $m_{1/2}$ axis in Fig. 1 is excluded for stau turning to be the LSP. The left-side white region near the m_0 axis is excluded by the constraints from the chargino mass lower limit or radiative electroweak symmetry breaking.

Next, we discuss the case of a large $\tan\beta$, i.e., $\tan\beta = 55$. This is the largest $\tan\beta$ before one gets into a nonperturbative domain for most of the parameter space. The results of the analysis on the allowed parameter space in the m_0–$m_{1/2}$ plane are given in Fig. 2 consistent with the constraints of (14). One finds that in this case there is both a lower limit and an upper limit and the allowed parameter space is the shaded area contained between the lines. The white region near the m_0 axis for larger m_0 and smaller $m_{1/2}$ values is excluded because of the chargino mass lower limit or the radiative electroweak-symmetry-breaking constraints. The white region near the $m_{1/2}$ axis having smaller m_0 values is excluded via the tachyonic stau constraint, and the region just above this, corresponding to moderately large m_0 values, is excluded because of the CP-odd Higgs boson turning tachyonic at the tree level, which is a large $\tan\beta$ effect. Again, the Higgs signal corresponding to the LEP lower limit is indicated by the solid nearly vertical line and is seen to lie in the allowed region of the parameter space.

A full analysis was carried out also including values of $\tan\beta = 5$, 30 and 45 in [26]. We discuss the results of the full analysis from the point of view of

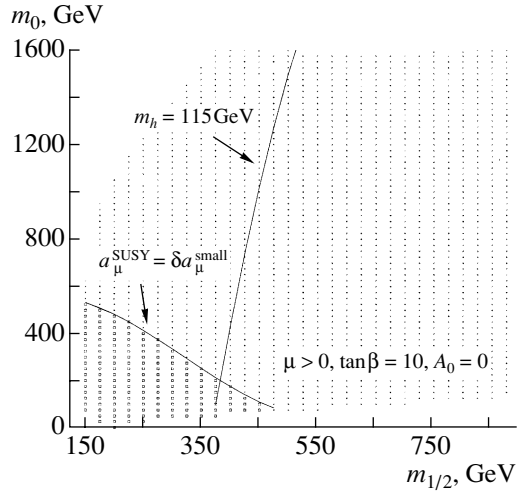

Fig. 1. Upper limit in the m_0–$m_{1/2}$ plane implied by the BNL $g-2$ constraint for $\tan\beta = 10$ indicated by the line $a_\mu^{\rm SUSY} = \delta a_\mu^{\rm small} = 10.6 \times 10^{-10}$. The allowed region in the parameter consistent with the constraint of (14) lies below this line. The 115-GeV Higgs signal [31] is also indicated (from [26]).

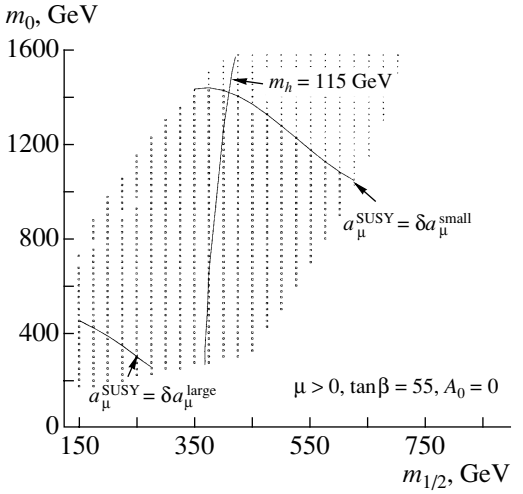

Fig. 2. Upper and lower limits in the m_0–$m_{1/2}$ plane implied by the BNL $g-2$ constraint for $\tan\beta = 55$ indicated by lines $a_\mu^{\rm SUSY} = \delta a_\mu^{\rm small} = 10.6 \times 10^{-10}$ and $a_\mu^{\rm SUSY} = \delta a_\mu^{\rm large} = 76.2 \times 10^{-10}$. The allowed region in the parameter consistent with the constraint of (14) lies between the lines. The 115-GeV Higgs signal is also indicated (from [26]).

sparticle spectra. In Fig. 3, the upper limits in the sneutrino–light chargino plane are given for $\tan\beta = 5$ and 10. A similar analysis is given for $\tan\beta = 30$, 45, and 55 in Fig. 4. From Figs. 3 and 4, one finds, as expected, that there are strong correlations between the upper limits and $\tan\beta$. Using the entire data set in Figs. 3 and 4, one finds

$$m_{\tilde\chi_1^\pm} \leq 650\ \text{GeV}, \quad m_{\tilde\nu_\mu} \leq 1.5\ \text{TeV} \quad (\tan\beta \leq 55). \tag{15}$$

The corresponding limits in the m_0–$m_{1/2}$ plane are

$$m_{1/2} \leq 800\ \text{GeV}, \quad m_0 \leq 1.5\ \text{TeV} \quad (\tan\beta \leq 55). \tag{16}$$

The upper limits that arise in mSUGRA from the analysis of [26] are consistent with the fine-tuning criteria (see, e.g., [32]) and are very encouraging from the point of view of discovery of superparticles at colliders. Thus, the LHC can discover squarks and gluinos up to 2 TeV [33, 34]. This means that essentially all of the squark and gluino mass spectrum allowed within mSUGRA by the Brookhaven $g-2$ constraint will become visible at the LHC [26, 34]. A comparison of the upper limits in the m_0–$m_{1/2}$ plane allowed by the $g-2$ constraint versus the discovery potential of the LHC is given in the work of Baer *et al.* [34], and we reproduce one of the figures from that analysis here (Fig. 5).

Many further investigations of the implications of the BNL result have been carried out over the recent months [35–39] exploring the effects of the $g-2$ constraint on a variety of low-energy phenomena such as on $b \to s+\gamma$, dark matter, lepton-flavor violation, trileptonic signal [40], and on other low-energy SUSY signals. We briefly discuss two of these: $b \to s+\gamma$ and dark matter. Regarding $b \to s+\gamma$, the Standard Model branching ratio for this process is estimated to be [41] $B(b \to s+\gamma) = (3.29 \pm 0.33) \times 10^{-4}$. A recent experiment gives [42] $B(b \to s+\gamma) = (3.15 \pm 0.35 \pm 0.32 \pm 0.26) \times 10^{-4}$, where the first error is statistical and there are two types of systematic errors. Now, it is well known that the imposition of the $b \to s+\gamma$ constraint puts severe limits on the mSUGRA parameter space when $\mu < 0$, eliminating most of the parameter space in this case [43, 44]. Thus, had the sign of μ from the BNL experiment turned out to be negative it would have eliminated most of the parameter space of the minimal model. On the other hand, for the $\mu > 0$ case, one finds that the constraint $b \to s+\gamma$ is much less severe. Thus, most of the parameter space of mSUGRA in this case, at least for small and moderately large values of $\tan\beta$, is left unconstrained. For large values of $\tan\beta$ nearing 50, the $b \to s+\gamma$ constraint does become more stringent, but a significant part of the parameter space is still allowed [37]. However, it has been emphasized in [39] that $B(b \to s+\gamma)$ is not a pure observable and requires hard cuts for its extraction experimentally. This provides a note of caution on imposing the $B(b \to s+\gamma)$ constraint too stringently.

A closely related phenomenon that is sensitive to the sign of μ is the analysis of dark matter. It

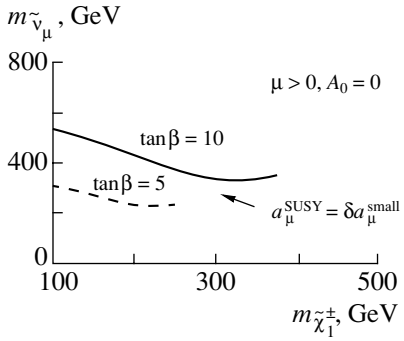

Fig. 3. Upper limits in the $m_{\tilde{\nu}_\mu}$–$m_{\tilde{\chi}_1^\pm}$ plane implied by the BNL $g-2$ constraint for $\tan\beta = 5$ and 10 are indicated by the lines $a_\mu^{\rm SUSY} = \delta a_\mu^{\rm small} = 10.6 \times 10^{-10}$. The allowed region in the parameter consistent with the constraint of (14) lies below the lines (from [26]).

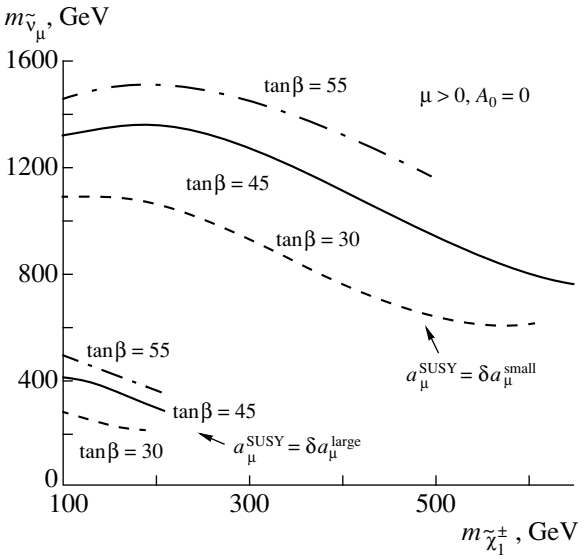

Fig. 4. Upper and lower limits in the $m_{\tilde{\nu}_\mu}$–$m_{\tilde{\chi}_1^\pm}$ plane implied by the BNL $g-2$ constraint for $\tan\beta = 30$, 45, and 55 are indicated by lines $a_\mu^{\rm SUSY} = \delta a_\mu^{\rm small} = 10.6 \times 10^{-10}$ and $a_\mu^{\rm SUSY} = \delta a_\mu^{\rm large} = 76.2 \times 10^{-10}$. The allowed region in the parameter consistent with the constraint of (14) lies between the lines (from [26]).

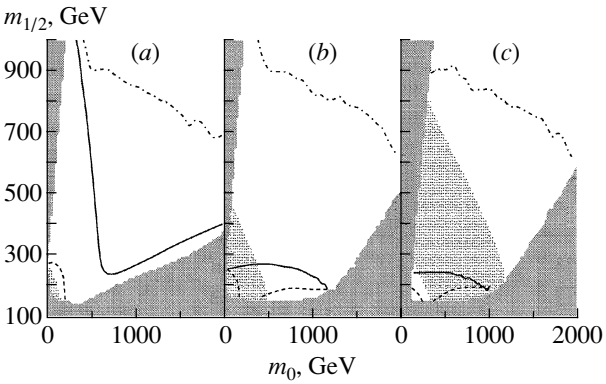

Fig. 5. A plot of the m_0 vs. $m_{1/2}$ parameter space in the mSUGRA model for $\mu > 0$ and (*a*) $A_0 = -2m_0$ and $\tan\beta = 3$, (*b*) $A_0 = 0$ and $\tan\beta = 10$, and (*c*) $A_0 = 0$ and $\tan\beta = 35$. The 2σ region favored by the E821 measurement is shaded with dots. The region below the solid contour has $m_h < 113.5$ GeV. The region below the dashed contour is accessible to Tevatron searches with 25 fb^{-1} of integrated luminosity, while the region below the dash-dotted contour is accessible via LHC sparticle searches with 10 fb^{-1} of integrated luminosity (from [34]).

was shown in the early days when the first measurement of $b \to s + \gamma$ was made that the $b \to s + \gamma$ branching ratio has a strong correlation with the neutralino–proton cross sections in the direct detection of dark matter [43] in regard to the sign of μ. This happens due to the fact that the neutralino–proton cross sections are smaller for the case of $\mu < 0$ than for the case of $\mu > 0$. Additionally, with the $b \to s + \gamma$ constraint, which eliminates most of the parameter space for $\mu < 0$, one finds that the neutralino–proton cross sections are very small for the available region of parameters for this sign of μ. Consequently, direct detection of neutralino dark matter is strongly disfavored for $\mu < 0$ as opposed to what one finds for $\mu > 0$. Thus, the fact that the BNL experiment determines the μ sign to be positive is indeed good news for the direct detection of dark matter [26, 29, 37, 38].

We now turn to a brief discussion of models other than mSUGRA. One such model is AMSB. The details of this model and procedure for its implementation can be found in [45]. The analysis for this case is given in [26], where the upper limits in the sneutrino–chargino plane corresponding to three values of $\tan\beta$, i.e., $\tan\beta = 10$, 30, and 40 (the maximum allowed), were analyzed, which produced upper limits of $m_{\tilde{\nu}_\mu} \leq 1.1$ TeV and $m_{\chi_1^\pm} \leq 300$ GeV. These limits are lower than those of (15). Further, for $\mu > 0$, one finds that the constraint from $b \to s + \gamma$ in this case excludes a significant amount of parameter space when the BNL $g-2$ constraint is imposed [28]. Further, analyses within the framework of the unconstrained supersymmetric standard model and analyses within more general scenarios and their implications for colliders are given in [36, 46].

One possibility that must be discussed along with supersymmetry is that of contributions from extra spacetime dimensions to $g-2$. In [47], a class of realistic models with extra spacetime dimensions was considered (for reviews see [48]). It was shown that, for the case of one extra dimension compactified on S^1/Z_2 with matter and Higgs fields residing on the

orbifolds and the gauge fields propagating in the bulk, the massless spectrum of the model coincides with the massless spectrum of MSSM. The Kaluza–Klein modes for W contribute to the Fermi constant, and the current good agreement between the Standard Model determination of G_F and its experimental value leaves only a small error corridor in which the contributions from extra dimensions can reside. This constraint leads to a lower limit of about 3 TeV on the inverse compactified dimension and severely constrains the contribution of extra dimensions to the muon anomalous magnetic moment. One finds that, for the case of one extra dimension, the contribution of Kaluza–Klein states is smaller than the supersymmetric contribution by more than two orders of magnitude. For the case of more than one extra dimension, the contribution to a_μ is larger than for the case of one extra dimension but still significantly smaller than the one arising from supersymmetry. Thus, we conclude that models with extra dimensions of the type considered in [47] do not create a strong background relative to the supersymmetric effects (see, however, the analysis of [49]).

4. CONCLUSIONS

In this review, we have given a brief summary of the developments on the analyses of the muon anomaly. Implications of the difference $a_\mu^{\rm exp} - a_\mu^{\rm SM}$ seen at BNL for supersymmetric models and specifically for mSUGRA were explored. An effect of the size seen at Brookhaven for $a_\mu^{\rm exp} - a_\mu^{\rm SM}$ was already predicted within the SUGRA model in 1984, where it was found that the supersymmetric correction could be as large as or larger than the Standard Model electroweak correction [22]. Furthermore, we have also explored the implications of the BNL result for the direct detection of supersymmetry at accelerators and in dark matter searches. Thus, a detailed analysis within mSUGRA of the BNL result using a 2σ error corridor on the difference $a_\mu^{\rm exp} - a_\mu^{\rm SM}$ leads to upper limits on sparticle masses that all lie below 2 TeV. Since the LHC can discover squarks and the gluino up to 2 TeV, most if not all of the sparticles should become visible at the LHC. Further, it was pointed out that the BNL data determine the sign of μ to be positive within the minimal model, which is very encouraging for direct dark matter searches. It was also pointed out that there is little chance of confusing the supersymmetric contribution to a_μ with effects from extra dimensions. This is so at least in models where the Standard Model is obtained by a direct compactification of a five dimensional model on S^1/Z_2 which gives a contribution to a_μ from Kaluza–Klein excitations significantly smaller than a typical supersymmetric contribution. The BNL data also imposes impressive constraints on CP phases. It was shown in [50] that the BNL constraint eliminates up to 60–90% of the parameter space in the θ_μ and ξ_2 (phase of $\tilde{m}_2$) plane. In the presence of phases, the relationship between the sign of $a_\mu^{\rm SUSY}$ and the phase of μ may also be modified.

There is a significant amount of data from the run of 2000 that could be analyzed in the near future, and BNL eventually hopes to measure a_μ to an accuracy of 4×10^{-10}. Analyses including data from Beijing [51] and from Novosibirsk [52], and additional τ data from CLEO [53] should delineate the hadronic error more reliably. Further, if the deviation between theory and experiment persists at the current level after the analysis of the new data currently underway is carried out, and also if the error corridor shrinks, then a signal for new physics will be undeniable. Such a signal interpreted as arising from supersymmetry then has dramatic new predictions for the direct observation of sparticles at accelerators. Further, if supersymmetry is the right explanation for such an effect, and there is a great bulk of theoretical reasoning in justification of this expectation, then the search for a fundamental Higgs boson becomes all the more urgent. Thus, the Brookhaven $g-2$ result further heightens the expectation for the observation of a light supersymmetric Higgs boson at RUN II of the Tevatron. Finally, we point out that the BNL constraint, specifically the positivity of μ for a class of models, has an important implication for Yukawa unification in grand unified models [54] and this area is likely to be explored further in the future.

ACKNOWLEDGMENTS

This research was supported in part by the NSF, grant no. PHY-9901057.

REFERENCES

1. Muon g-2 Collab. (H. N. Brown *et al.*), hep-ex/0102017.
2. R. S. van Dyck, Jr., P. B. Schwinberg, and H. G. Dehmelt, Phys. Rev. Lett. **59**, 26 (1987).
3. Particle Data Group (C. Caso *et al.*), Eur. Phys. J. C **3**, 1 (1998).
4. Muon g-2 Collab. (H. N. Brown *et al.*), Phys. Rev. D **62**, 091101 (2000).
5. A. Czarnecki and W. J. Marciano, Nucl. Phys. B (Proc. Suppl.) **76**, 245 (1999).
6. K. Fujikawa, B. W. Lee, and A. I. Sanda, Phys. Rev. D **6**, 2923 (1972); R. Jackiw and S. Weinberg, Phys. Rev. D **5**, 2473 (1972); G. Altarelli, N. Cabibbo, and L. Maiani, Phys. Lett. B **40B**, 415 (1972); I. Bars and M. Yoshimura, Phys. Rev. D **6**, 374 (1972); W. A. Bardeen, R. Gastmans, and B. E. Lautrup, Nucl. Phys. B **46**, 315 (1972).

7. M. Davier and A. Höcker, Phys. Lett. B **435**, 427 (1998).
8. B. Krause, Phys. Lett. B **390**, 392 (1997).
9. J. Bijnens, E. Pallante, and J. Prades, Nucl. Phys. B **474**, 379 (1996); M. Hayakawa and T. Kinoshita, Phys. Rev. D **57**, 465 (1998).
10. F. J. Yndurain, hep-ph/0102312; J. F. de Troconiz and F. J. Yndurain, hep-ph/0106025.
11. S. Narison, Phys. Lett. B **513**, 53 (2001).
12. K. Melnikov, hep-ph/0105267.
13. G. Cvetic, T. Lee, and I. Schmidt, hep-ph/0107069.
14. W. J. Marciano and B. L. Roberts, hep-ph/0105056; J. Prades, hep-ph/0108192.
15. A. H. Chamseddine, R. Arnowitt, and P. Nath, Phys. Rev. Lett. **49**, 970 (1982); R. Barbieri, S. Ferrara, and C. A. Savoy, Phys. Lett. B **119B**, 343 (1982); L. Hall, J. Lykken, and S. Weinberg, Phys. Rev. D **27**, 2359 (1983); P. Nath, R. Arnowitt, and A. H. Chamseddine, Nucl. Phys. B **227**, 121 (1983); For reviews, see P. Nath, R. Arnowitt, and A. H. Chamseddine, *Applied N = 1 Supergravity* (World Scientific, Singapore, 1984); H. P. Nilles, Phys. Rep. **110**, 1 (1984).
16. R. Arnowitt and P. Nath, Phys. Rev. D **46**, 3981 (1992); V. Barger, M. S. Berger, and P. Ohmann, Phys. Rev. D **49**, 4908 (1994).
17. L. J. Hall, R. Rattazzi, and U. Sarid, Phys. Rev. D **50**, 7048 (1994); R. Hempfling, Phys. Rev. D **49**, 6168 (1994); M. Carena, M. Olechowski, S. Pokorski, and C. Wagner, Nucl. Phys. B **426**, 269 (1994); D. Pierce, J. Bagger, K. Matchev, and R. Zhang, Nucl. Phys. B **491**, 3 (1997).
18. S. Heinemeyer, W. Hollik, and G. Weiglein, hep-ph/0002213.
19. S. Ferrara and E. Remiddi, Phys. Lett. B **53B**, 347 (1974).
20. P. Fayet, in *Unification of the Fundamental Particle Interactions,* Ed. by S. Ferrara, J. Ellis, and P. van Nieuwenhuizen (Plenum, New York, 1980), p. 587; J. A. Grifols and A. Mendez, Phys. Rev. D **26**, 1809 (1982); J. Ellis, J. S. Hagelin, and D. V. Nanopoulos, Phys. Lett. B **116B**, 283 (1982); R. Barbieri and L. Maiani, Phys. Lett. B **117B**, 203 (1982).
21. D. A. Kosower, L. M. Krauss, and N. Sakai, Phys. Lett. B **133B**, 305 (1983).
22. T. C. Yuan, R. Arnowitt, A. H. Chamseddine, and P. Nath, Z. Phys. C **26**, 407 (1984).
23. J. L. Lopez, D. V. Nanopoulos, and X. Wang, Phys. Rev. D **49**, 366 (1994).
24. U. Chattopadhyay and P. Nath, Phys. Rev. D **53**, 1648 (1996); T. Moroi, Phys. Rev. D **53**, 6565 (1996); M. Carena, M. Giudice, and C. E. M. Wagner, Phys. Lett. B **390**, 234 (1997); E. Gabrielli and U. Sarid, Phys. Rev. Lett. **79**, 4752 (1997); K. T. Mahanthappa and S. Oh, Phys. Rev. D **62**, 015012 (2000); T. Blazek, hep-ph/9912460.
25. SUGRA Working Group Collab. (S. Abel *et al.*), hep-ph/0003154.
26. U. Chattopadhyay and P. Nath, Phys. Rev. Lett. **86**, 5854 (2001).
27. L. L. Everett, G. L. Kane, S. Rigolin, and L. Wang, Phys. Rev. Lett. **86**, 3484 (2001).
28. J. L. Feng and K. T. Matchev, Phys. Rev. Lett. **86**, 3480 (2001).
29. E. A. Baltz and P. Gondolo, Phys. Rev. Lett. **86**, 5004 (2001).
30. G. Degrassi and G. F. Giudice, Phys. Rev. D **58**, 053007 (1998).
31. ALEPH Collab. (R. Barate *et al.*), Phys. Lett. B **495**, 1 (2000); L3 Collab. (M. Acciarri *et al.*), Phys. Lett. B **495**, 18 (2000); DELPHI Collab. (P. Abrieu *et al.*), Phys. Lett. B **499**, 23 (2001); OPAL Collab. (G. Abbiendi *et al.*), Phys. Lett. B **499**, 38 (2001).
32. K. L. Chan, U. Chattopadhyay, and P. Nath, Phys. Rev. D **58**, 096004 (1998).
33. CMS Collab., Technical Proposal, CERN-LHCC 94-38 (1994); ATLAS Collab., Technical Proposal, CERN-LHCC 94-43 (1994); H. Baer, C-H. Chen, F. Paige, and X. Tata, Phys. Rev. D **52**, 2746 (1995); **53**, 6241 (1996).
34. H. Baer, C. Balazs, J. Ferrandis, and X. Tata, Phys. Rev. D **64**, 035004 (2001).
35. There is now a considerable body of work exploring the implications of the BNL experiment for supersymmetry. A partial list consists of: A. Czarnecki and W. J. Marciano, Phys. Rev. D **64**, 013014 (2001); J. Hisano and K. Tobe, Phys. Lett. B **510**, 197 (2001); K. Choi, K. Hwang, S. K. Kang, *et al.*, Phys. Rev. D **64**, 055001 (2001); R. A. Diaz, R. Martinez, and J. A. Rodriguez, Phys. Rev. D **64**, 033004 (2001); J. E. Kim, B. Kyae, and H. M. Lee, hep-ph/0103054; S. K. Kang and K. Y. Lee, hep-ph/0103064; K. Cheung, C.-H. Chou, and O. C. W. Kong, hep-ph/0103183; S. Baek, P. Ko, and H. S. Lee, hep-ph/0103218; D. F. Carvalho, J. Ellis, M. E. Gomez, and S. Lola, hep-ph/0103256; A. Bartl *et al.*, hep-ph/0103324; Y.-L. Wu and Y.-F. Zhou, hep-ph/0104056; B. Baek, T. Goto, Y. Okada, and K. Okumura, hep-ph/0104146; C.-H. Chen and C. Q. Geng, Phys. Lett. B **511**, 77 (2001); K. Enqvist, E. Gabrielli, and K. Huitu, Phys. Lett. B **512**, 107 (2001); A. Arhrib and S. Baek, hep-ph/0104225; D.-G. Cerdeno *et al.*, hep-ph/0104242; Y. G. Kim and M. M. Nojiri, hep-ph/0104258; Z. Chacko and G. D. Kribs, hep-ph/0104317; T. Blazek and S. F. King, hep-ph/0105005; R. Arnowitt, B. Dutta, and Y. Santoso, hep-ph/0106089; G. Belanger *et al.*, hep-ph/0106275; S. P. Martin, hep-ph/0106280; A. B. Lahanas, D. V. Nanopoulos, and V. C. Spanos, hep-ph/0107151; M. Frank, Mod. Phys. Lett. A **16**, 795 (2001); R. Adhikari and G. Rajasekaran, hep-ph/0107279; R. Adhikari, E. Ma, and G. Rajasekaran, hep-ph/0108167; A. Dedes, H. K. Dreiner, and U. Nierste, hep-ph/0108037.
36. S. Komine, T. Moroi, and M. Yamaguchi, Phys. Lett. B **506**, 93 (2001); **507**, 224 (2001).

37. J. Ellis, D. V. Nanopoulos, and K. A. Olive, Phys. Lett. B **508**, 65 (2001).
38. R. Arnowitt, B. Dutta, B. Hu, and Y. Santoso, Phys. Lett. B **505**, 177 (2001).
39. S. P. Martin and J. D. Wells, Phys. Rev. D **64**, 035003 (2001).
40. P. Nath and R. Arnowitt, Mod. Phys. Lett. A **2**, 331 (1987); H. Baer and X. Tata, Phys. Rev. D **47**, 2739 (1993); V. Barger and C. Kao, Phys. Rev. D **60**, 115015 (1999).
41. A. L. Kagan and M. Neubert, Eur. Phys. J. C **7**, 5 (1999).
42. CLEO Collab. (S. Ahmed *et al.*), hep-ex/9908022.
43. P. Nath and R. Arnowitt, Phys. Lett. B **336**, 395 (1994); Phys. Rev. Lett. **74**, 4592 (1995); F. Borzumati, M. Drees, and M. Nojiri, Phys. Rev. D **51**, 341 (1995); H. Baer, M. Brhlik, D. Castano, and X. Tata, Phys. Rev. D **58**, 015007 (1998).
44. M. Carena, D. Garcia, U. Nierste, and C. E. M. Wagner, Phys. Lett. B **499**, 141 (2001); G. Degrassi, P. Gambino, and G. F. Giudice, JHEP **0012**, 009 (2000), and references therein; W. de Boer, M. Huber, A. V. Gladyshev, and D. I. Kazakov, Eur. Phys. J. C **20**, 689 (2001).
45. U. Chattopadhyay, D. K. Ghosh, and S. Roy, Phys. Rev. D **62**, 115001 (2000).
46. M. Byrne, C. Kolda, and J. E. Lennon, hep-ph/0108122.
47. P. Nath and M. Yamaguchi, Phys. Rev. D **60**, 116004 (1999); **60**, 116006 (1999).
48. P. Nath, hep-ph/0011177; hep-ph/0105077.
49. K. Agashe, N. G. Deshpande, and G. H. Wu, Phys. Lett. B **511**, 85 (2001).
50. T. Ibrahim, U. Chattopadhyay, and P. Nath, Phys. Rev. D **64**, 016010 (2001); T. Ibrahim and P. Nath, hep-ph/0105025; T. Ibrahim and P. Nath, Phys. Rev. D **61**, 095008 (2000); **62**, 015004 (2000).
51. BES Collab. (J. Z. Bai *et al.*), Phys. Rev. Lett. **84**, 594 (2000); Zheng-guo Zhao, Reported at XXX ICHEP, Osaka.
52. R. R. Akhmetshin *et al.*, Phys. Lett. B **475**, 190 (2000); hep-ex/9904027; Nucl. Phys. A **675**, 424 (2000), and references therein.
53. CLEO Collab. (S. Anderson *et al.*), Phys. Rev. D **61**, 112002 (2000).
54. W. de Boer, M. Huber, C. Sander, and D. I. Kazakov, hep-ph/0106311; H. Baer and J. Ferrandis, hep-ph/0106352; T. Blazek, R. Dermisek, and S. Raby, hep-ph/0107097.

Physics of Atomic Nuclei, Vol. 65, No. 12, 2002, pp. 2109–2115. From Yadernaya Fizika, Vol. 65, No. 12, 2002, pp. 2173–2178.

NEW PHYSICS BEYOND THE STANDARD MODEL

Electric Dipole Moments in the Generic Supersymmetric Standard Model*

O. C. W. Kong**

Institute of Physics, Academia Sinica, Nankang, Taipei, Taiwan

Received February 13, 2002

Abstract—The generic supersymmetric standard model is a model built from a supersymmetrized standard model field spectrum and the gauge symmetries only. The popular minimal supersymmetric standard model differs from the generic version in having R parity imposed by hand. We review an efficient formulation of the model and some of the recently obtained interesting phenomenological features, focusing on one-loop contributions to fermion electric dipole moments. © *2002 MAIK "Nauka/Interperiodica".*

1. INTRODUCTION

Fermion electric dipole moments (EDMs) are known to be extremely useful constraints on (the CP-violating part of) models depicting interesting scenarios beyond Standard Model (SM) physics. In particular, the experimental bounds on neutron EDM (d_n) and electron EDM (d_e) are very stringent. The current numbers are given by $d_n < 6.3 \times 10^{-26} e$ cm and $d_e < 4.3 \times 10^{-27} e$ cm. The SM contributions are known to be very small ($d_n \sim 10^{-32} e$ cm and $d_e \sim 8 \times 10^{-41} e$ cm), given that the only source of CP violation has to come from the phase in (charged current) quark flavor mixings.

Extensions of the SM normally are expected to have potentially large EDM contributions. For instance, for the Minimal Supersymmetric Standard Model (MSSM), there are a few sources of such new contributions. For example, they can come in through LR sfermion mixings. The latter have two parts, an A-term contribution as well as a F-term contribution. The F term is a result of the complex phase in the so-called μ term. The resulting constraints on MSSM have been studied extensively. We are interested here in the modified version with R parity not imposed. We will illustrate that there are extra contributions at the same level and will discuss the class of important constraints resulting from them [1–6].

2. THE GENERIC SUPERSYMMETRIC STANDARD MODEL

A theory built with the minimal superfield spectrum incorporating the SM particles and the admissible renormalizable interactions dictated by the SM (gauge) symmetries together with the idea that supersymmetry (SUSY) is softly broken is what should be called the generic supersymmetric standard model (GSSM). The popular MSSM differs from the generic version in having a discrete symmetry, called R parity, imposed by hand to enforce baryon and lepton number conservation. With the strong experimental hints at the existence of lepton-number-violating neutrino masses, such a theory of SUSY without R parity deserves ever more attention. The GSSM contains all kinds of (so-called) R-parity-violating (RPV) parameters. These include the more popular trilinear (λ_{ijk}, λ'_{ijk}, and λ''_{ijk}) and bilinear (μ_i) couplings in the superpotential, as well as soft SUSY breaking parameters of the trilinear, bilinear, and soft mass (mixing) types. In order not to miss any plausible RPV phenomenological features, it is important that all of the RPV parameters be taken into consideration without a priori bias. We do, however, expect some sort of symmetry principle to guard against the very dangerous proton decay problem. The emphasis is hence put on the lepton-number-violating phenomenology. The renormalizable superpotential for the GSSM can be written as

$$W = \varepsilon_{ab}\Big[\mu_\alpha \hat{H}_u^a \hat{L}_\alpha^b + h_{ik}^u \hat{Q}_i^a \hat{H}_u^b \hat{U}_k^c + \lambda'_{\alpha jk}\hat{L}_\alpha^a \hat{Q}_j^b \hat{D}_k^c + \frac{1}{2}\lambda_{\alpha\beta k}\hat{L}_\alpha^a \hat{L}_\beta^b \hat{E}_k^c\Big] + \frac{1}{2}\lambda''_{ijk}\hat{U}_i^c \hat{D}_j^c \hat{D}_k^c, \quad (1)$$

where (a, b) are $SU(2)$ indices, (i, j, k) are the usual family (flavor) indices, and (α, β) are extended flavor indices going from 0 to 3. At the limit where $\lambda_{ijk}, \lambda'_{ijk}, \lambda''_{ijk}$, and μ_i all vanish, one recovers the expression for the R-parity preserving MSSM, with $\hat{L}_0$ identified as $\hat{H}_d$. Without R parity imposed, the

*This article was submitted by the author in English.

**e-mail: kongcw@phys.sinica.edu.tw

1063-7788/02/6512-2109$22.00

latter is not a priori distinguishable from $\hat{L}_i$. Note that λ is antisymmetric in the first two indices, as required by the $SU(2)$ product rules, as shown explicitly here with $\varepsilon_{12} = -\varepsilon_{21} = 1$. Similarly, λ'' is antisymmetric in the last two indices, from $SU(3)_c$.

R parity is exactly an ad hoc symmetry put in to make $\hat{L}_0$ stand out from the other $\hat{L}_i$ as the candidate for $\hat{H}_d$. It is defined in terms of baryon number, lepton number, and spin as, explicitly, $\mathcal{R} = (-1)^{3B+L+2S}$. The consequence is that the random symmetries of baryon number and lepton number in the SM are preserved, at the expense of making particles and superparticles having a categorically different quantum number, R parity. The latter is actually not the most effective discrete symmetry to control superparticle-mediated proton decay [7], but is most restrictive in terms of what is admitted in the Lagrangian or the superpotential alone. On the other hand, R parity also forbids neutrino masses in the supersymmetric SM. The strong experimental hints for the existence of (Majorana) neutrino masses [8] is an indication of lepton-number violation, hence suggestive of R-parity violation.

The soft SUSY-breaking part of the Lagrangian is more interesting, if only for the fact that many of its interesting details have been overlooked in the literature. However, we will postpone the discussion until after we address the parametrization issue.

3. PARAMETRIZATION

Doing phenomenological studies without specifying a choice of flavor bases is ambiguous. It is like doing SM quark physics with 18 complex Yukawa couplings, instead of the 10 real physical parameters. As far as the SM itself is concerned, the extra 26 real parameters are simply redundant, and attempts to relate the full 36 parameters to experimental data will be futile. In the GSSM, the choice of an optimal parametrization mainly concerns the $4\hat{L}_\alpha$ flavors. We use here the single-VEV parametrization [9, 10] (SVP), in which flavor bases are chosen such that: (1) among the $\hat{L}_\alpha$, only $\hat{L}_0$ bears a VEV, i.e., $\langle \hat{L}_i \rangle \equiv 0$; (2) $h^e_{jk} (\equiv \lambda_{0jk}) = (\sqrt{2}/v_0)\mathrm{diag}\{m_1, m_2, m_3\}$; (3) $h^d_{jk} (\equiv \lambda'_{0jk} = -\lambda_{j0k}) = (\sqrt{2}/v_0)\mathrm{diag}\{m_d, m_s, m_b\}$; (4) $h^u_{ik} = (\sqrt{2}/v_u) V^T_{\mathrm{CKM}} \mathrm{diag}\{m_u, m_c, m_t\}$, where $v_0 \equiv \sqrt{2}\langle \hat{L}_0 \rangle$ and $v_u \equiv \sqrt{2}\langle \hat{H}_u \rangle$. The big advantage of the SVP is that it gives the complete tree-level mass matrices of all the states (scalars and fermions) the simplest structure [1, 10].

4. LEPTONS IN GSSM

The SVP gives quark mass matrices exactly in the SM form. For the masses of the color-singlet fermions, all the RPV effects are parametrized by μ_i only. For example, for the five charged fermions (gaugino + Higgsino + three charged leptons), we have

$$\mathcal{M}_c = \begin{pmatrix} M_2 & \frac{g_2 v_0}{\sqrt{2}} & 0 & 0 & 0 \\ \frac{g_2 v_u}{\sqrt{2}} & \mu_0 & \mu_1 & \mu_2 & \mu_3 \\ 0 & 0 & m_1 & 0 & 0 \\ 0 & 0 & 0 & m_2 & 0 \\ 0 & 0 & 0 & 0 & m_3 \end{pmatrix}. \qquad (2)$$

Moreover, each μ_i parameter here directly characterizes the RPV effect on the corresponding charged lepton ($l_i = e$, μ, and τ). This, as well as the corresponding neutrino–neutralino masses and mixings, has been exploited to implement a detailed study of the tree-level RPV phenomenology from the gauge interactions, with interesting results [9].

Neutrino masses and oscillations are no doubt one of the most important aspects of the model. Here, it is particularly important that the various RPV contributions to neutrino masses, up to the one-loop level, be studied in a framework that makes no assumption on the other parameters. Our formulation provides such a framework. Interested readers are referred to [1, 11–14].

5. SOFT SUSY-BREAKING TERMS AND THE SCALAR MASSES

Obtaining the squark and slepton masses is straightforward once all the admissible soft SUSY-breaking terms are explicitly written [1]. The soft SUSY-breaking part of the Lagrangian can be written as

$$\begin{aligned} V_{\mathrm{soft}} &= \epsilon_{ab} B_\alpha H_u^a \tilde{L}_\alpha^b + \epsilon_{ab}[A^U_{ij} \tilde{Q}_i^a H_u^b \tilde{U}_j^c \\ &+ A^D_{ij} H_d^a \tilde{Q}_i^b \tilde{D}_j^c + A^E_{ij} H_d^a \tilde{L}_i^b \tilde{E}_j^c] + \mathrm{h.c.} \\ &+ \epsilon_{ab}\left[A^{\lambda'}_{ijk} \tilde{L}_i^a \tilde{Q}_j^b \tilde{D}_k^c + \frac{1}{2} A^{\lambda}_{ijk} \tilde{L}_i^a \tilde{L}_j^b \tilde{E}_k^c\right] \\ &+ \frac{1}{2} A^{\lambda''}_{ijk} \tilde{U}_i^c \tilde{D}_j^c \tilde{D}_k^c + \mathrm{h.c.} + \tilde{Q}^\dagger \tilde{m}_Q^2 \tilde{Q} + \tilde{U}^\dagger \tilde{m}_U^2 \tilde{U} \\ &+ \tilde{D}^\dagger \tilde{m}_D^2 \tilde{D} + \tilde{L}^\dagger \tilde{m}_L^2 \tilde{L} + \tilde{E}^\dagger \tilde{m}_E^2 \tilde{E} + \tilde{m}_{H_u}^2 |H_u|^2 \\ &+ \frac{M_1}{2} \tilde{B}\tilde{B} + \frac{M_2}{2} \tilde{W}\tilde{W} + \frac{M_3}{2} \tilde{g}\tilde{g} + \mathrm{h.c.}, \end{aligned} \qquad (3)$$

where we have separated the R-parity-conserving A terms from the RPV ones (recall $\hat{H}_d \equiv \hat{L}_0$). Note that $\tilde{L}^\dagger \tilde{m}_L^2 \tilde{L}$, unlike the other soft mass terms, is given

by a 4×4 matrix. Explicitly, $\tilde{m}^2_{L_{00}}$ corresponds to $\tilde{m}^2_{H_d}$ of the MSSM case, while $\tilde{m}^2_{L_{0k}}$ give RPV mass mixings.

The only RPV contribution to the squark masses is given by a $-(\mu^*_i\lambda'_{ijk})v_u/\sqrt{2}$ term in the LR mixing part. Note that the term contains flavor-changing ($j\neq k$) parts which, unlike the A-terms ones, cannot be suppressed through a flavor-blind SUSY-breaking spectrum. Hence, it has very interesting implications to quark EDMs and related processes such as $b\to s\gamma$ [2, 3, 15, 16].

The mass matrices are a bit more complicated in the scalar sectors [1, 17]. The $1+4+3$ charged scalar masses are given in terms of the blocks

$$\widetilde{\mathcal{M}}^2_{H_u}=\tilde{m}^2_{H_u}+\mu^*_\alpha\mu_\alpha+M_Z^2\cos 2\beta\left[\frac{1}{2}-\sin^2\theta_{\rm W}\right]+M_Z^2\sin^2\beta[1-\sin^2\theta_{\rm W}], \quad (4)$$

$$\widetilde{\mathcal{M}}^2_{LL}=\tilde{m}^2_L+m^\dagger_L m_L+M_Z^2\cos 2\beta\left[-\frac{1}{2}+\sin^2\theta_{\rm W}\right]+\begin{pmatrix} M_Z^2\cos^2\beta[1-\sin^2\theta_W] & 0_{1\times 3}\\ 0_{3\times 1} & 0_{3\times 3}\end{pmatrix}+(\mu^*_\alpha\mu_\beta),$$

$$\widetilde{\mathcal{M}}^2_{RR}=\tilde{m}^2_E+m_E m^\dagger_E+M_Z^2\cos 2\beta\left[1-\sin^2\theta_{\rm W}\right];$$

$$\widetilde{\mathcal{M}}^2_{LH}=(B^*_\alpha)+\begin{pmatrix}\frac{1}{2}M_Z^2\sin 2\beta[1-\sin^2\theta_{\rm W}]\\ 0_{3\times 1}\end{pmatrix}, \quad (5)$$

$$\widetilde{\mathcal{M}}^2_{RH}=-(\mu^*_i\lambda_{i0k})\frac{v_0}{\sqrt{2}}, \quad (6)$$

$$(\widetilde{\mathcal{M}}^2_{RL})^T=\begin{pmatrix}0\\ A^E\end{pmatrix}\frac{v_0}{\sqrt{2}}-(\mu^*_\alpha\lambda_{\alpha\beta k})\frac{v_u}{\sqrt{2}}. \quad (7)$$

For the neutral scalars, we have explicitly

$$\mathcal{M}^2_S=\begin{pmatrix}\mathcal{M}^2_{SS} & \mathcal{M}^2_{SP}\\ (\mathcal{M}^2_{SP})^T & \mathcal{M}^2_{PP}\end{pmatrix}, \quad (8)$$

where the scalar, pseudoscalar, and mixing parts are given by

$$\mathcal{M}^2_{SS}=\mathrm{Re}(\mathcal{M}^2_{\phi\phi^\dagger})+\mathcal{M}^2_{\phi\phi},$$
$$\mathcal{M}^2_{PP}=\mathrm{Re}(\mathcal{M}^2_{\phi\phi^\dagger})-\mathcal{M}^2_{\phi\phi}, \quad (9)$$
$$\mathcal{M}^2_{SP}=-\mathrm{Im}(\mathcal{M}^2_{\phi\phi^\dagger}),$$

respectively,[1)] with

$$\mathcal{M}^2_{\phi\phi}=\frac{1}{2}M_Z^2\times\begin{pmatrix}\sin^2\beta & -\cos\beta\sin\beta & 0_{1\times 3}\\ -\cos\beta\sin\beta & \cos^2\beta & 0_{1\times 3}\\ 0_{3\times 1} & 0_{3\times 1} & 0_{3\times 3}\end{pmatrix} \quad (10)$$

and

$$\mathcal{M}^2_{\phi\phi^\dagger}=\mathcal{M}^2_{\phi\phi}+\begin{pmatrix}\tilde{m}^2_{H_u}+\mu^*_\alpha\mu_\alpha-\frac{1}{2}M_Z^2\cos 2\beta & -(B_\alpha)\\ -(B^*_\alpha) & \tilde{m}^2_L+(\mu^*_\alpha\mu_\beta)+\frac{1}{2}M_Z^2\cos 2\beta\end{pmatrix}. \quad (11)$$

Note that $\tilde{m}^2_L$ here is a 4×4 matrix of soft masses for L_α, and B_α are the corresponding bilinear soft terms of μ_α. A^E is just the 3×3 R-parity-conserving leptonic A term. There is no contribution from the admissible RPV A terms under the SVP. Also, we have used $m_L\equiv\mathrm{diag}\{0,m_E\}\equiv\mathrm{diag}\{0,m_1,m_2,m_3\}$.

6. NEUTRON ELECTRIC DIPOLE MOMENT

Let us take a look first at the quark dipole operator through one-loop diagrams with LR squark mixing. A simple direct example is given by the gluino diagram. In comparison with the MSSM case, the extra (RPV) to the d-squark LR mixing in GSSM obvious modified the story. If one naively imposes the constraint for this RPV contribution itself not to exceed the experimental bound on neutron EDM, one gets roughly $\mathrm{Im}(\mu^*_i\lambda'_{i11})\lesssim 10^{-6}$ GeV, a constraint that is interesting even in comparison to the bounds on the corresponding parameters obtainable from asking no neutrino masses to exceed the Super-Kamiokande atmospheric oscillation scale [2].

In fact, there are important contributions beyond the gluino diagram and without LR squark mixings involved. For the MSSM, it is well known that there is such a contribution from the chargino diagram, which is likely to be more important than the gluino one when a unification-type gaugino mass relationship is imposed. The question then is whether the GSSM has a similar RPV analog. An RPV version of the chargino diagram is given in Fig. 1. The diagram,

[1)] Note that the original expression given in [1] has a typo in the $\mathcal{M}^2_{SP}$ expression.

Numerical one-loop neutron EDM results from SUSY without R parity for four illustrative cases (all EDM numbers are in e cm)

Choice of parameters						
$\tilde{m}_Q = 300$ GeV, $\tilde{m}_u = \tilde{m}_d = 200$ GeV, $A = M_2 = 300$ GeV, $\mu_0 = -300$ GeV						
$\tan\beta$			3	3	3	50
μ_3 [GeV]			1×10^{-3}	1	1	5×10^{-3}
λ'_{311}			0.05	0.05	0.05	0.05
Parameters (complex phases)			$\lambda'_{311}(\pi/4)$	$\lambda'_{311}(\pi/4)$	$\mu_0(0.5°)$, $A(10°)$	$\mu_0(0.02°)$, $\mu_3(-\pi/4)$
EDM Results						
Couplings	Fig.	LR mixing	Case A	Case B	Case C	Case D
d-quark EDM						
gluino loop:						
α_s	1	RPV	8.8×10^{-28}	8.8×10^{-25}	-3.9×10^{-26}	-6.7×10^{-29}
neutralino-like loop:						
g^2	1	RPV	-1.9×10^{-29}	-1.9×10^{-26}	8.3×10^{-28}	2.7×10^{-30}
gy_d	2	No	~ 0	~ 0	-1.6×10^{-27}	-1.2×10^{-27}
$g\lambda'_{i11}$	3	No	-1.0×10^{-28}	-1.0×10^{-25}	1.1×10^{-27}	1.1×10^{-27}
y_d^2	4	RPV	9.7×10^{-37}	9.7×10^{-34}	-3.9×10^{-35}	-2.6×10^{-33}
$y_d\lambda'_{ijk}$	4	Yes	-1.7×10^{-36}	-1.7×10^{-33}	8.5×10^{-35}	2.5×10^{-33}
two λ'_{ijk}	4	Yes	-2.1×10^{-39}	-3.4×10^{-34}	9.0×10^{-35}	-8.6×10^{-37}
chargino-like loop:						
gy_d	5	No	~ 0	0	2.5×10^{-26}	1.7×10^{-26}
$g\lambda'_{i11}$	6	No	2.1×10^{-27}	2.1×10^{-24}	-1.3×10^{-26}	-1.7×10^{-26}
$y_u y_d$	7	Yes	~ 0	0	-2.7×10^{-34}	-8.0×10^{-36}
$y_u\lambda'_{ijk}$	7	Yes	-2.1×10^{-37}	-2.1×10^{-33}	3.8×10^{-34}	8.3×10^{-36}
u-quark EDM						
gluino loop:						
α_s	1	Yes	0	0	4.5×10^{-26}	-1.8×10^{-30}
neutralino-like loop:						
g^2	1	Yes	~ 0	0	2.6×10^{-27}	-1.4×10^{-31}
gy_u	2	No	~ 0	0	2.1×10^{-28}	5.3×10^{-31}
y_u^2	4	Yes	~ 0	0	1.3×10^{-37}	4.0×10^{-41}
chargino-like loop:						
gy_u	5	No	~ 0	~ 0	-1.3×10^{-27}	-3.2×10^{-30}
$y_u y_d$	7	RPV	-7.6×10^{-36}	-7.6×10^{-33}	3.2×10^{-34}	6.4×10^{-34}
$y_u\lambda'_{ijk}$	7	RPV	9.7×10^{-36}	9.7×10^{-33}	-5.1×10^{-34}	-6.4×10^{-34}
Neutron EDM						
from gluino loop			1.8×10^{-27}	1.8×10^{-24}	-1.0×10^{-25}	-1.4×10^{-28}
from chargino-like loop			4.3×10^{-27}	4.3×10^{-24}	2.5×10^{-26}	2.4×10^{-28}
from neutralino-like loop			-2.9×10^{-28}	-2.9×10^{-25}	-8.6×10^{-28}	-2.0×10^{-29}
total			5.8×10^{-27}	5.8×10^{-24}	-7.8×10^{-26}	8.0×10^{-29}

Note: The quark EDM numbers are direct output from the numerical program applying our quark dipole formulas, while the neutron EDM numbers are from the valence quark model formula. R-parity-violating parameters not given are taken as essentially zero. All parameters are taken to be real except those with complex phases explicitly listed in each case, where the real number(s) listed then give the magnitude(s). Parameter A here means a common A_u and A_d. Only M_2 is shown for the gaugino masses; the others are fixed by the unification relationship. Explicitly, we use $M_1 = 0.5M_2$ and $M_3 = 3.5M_2$. The first column under "EDM Results" gives the couplings of the loop vertices involved. A g indicates either one of the electroweak gauge couplings, while a λ' coupling means one with the appropriate admissible flavor indices. In the explicit results of the four cases, the latter is always λ'_{311}. The second column gives the reference Feynman diagram figures, when available. The third column indicates whether the particular contribution involves a LR squark mixing. In the case that mixing is involved and an R-parity-violating one is involved in generating an RPV EDM contribution, it is marked with "RPV".

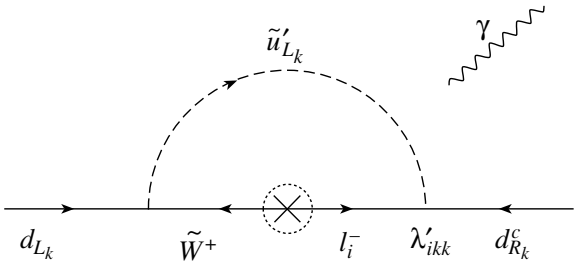

Fig. 1. The new chargino-like diagram.

however, looks ambiguous. Looking at the diagram in terms of the electroweak states involved under our formulation, it seems like a $l_k^- - \tilde{W}^+$ mass insertion is required, which is, however, vanishing. However, an extra mass insertion, with a μ_i flipping the l_k^- into a $\tilde{h}_u^+$, first seems to give a nonzero result. The structure obviously indicates a GIM-like cancellation at work, and we have to check its violation due to the lack of mass degeneracy.

We have performed an extensive analytical and numerical study, including the complete chargino-like contributions, as well as the neutralino-like contributions, to the neutron EDM [3]. The chargino-like part is given by the following formula:

$$\left(\frac{d_f}{e}\right)_{\chi^-} = \frac{\alpha_{\rm em}}{4\pi\sin^2\theta_W}\sum_{\tilde{f}'\mp}\sum_{n=1}^{5}{\rm Im}(\mathcal{C}_{fn\mp}) \qquad (12)$$

$$\times\frac{M_{\chi_n^-}}{M^2_{\tilde{f}'\mp}}\left[\mathcal{Q}_{\tilde{f}'}B\left(\frac{M^2_{\chi_n^-}}{M^2_{\tilde{f}'\mp}}\right)+(\mathcal{Q}_f-\mathcal{Q}_{\tilde{f}'})A\left(\frac{M^2_{\chi_n^-}}{M^2_{\tilde{f}'\mp}}\right)\right],$$

for f being $u\,(d)$ quark and f' being $d\,(u)$, where

$$\mathcal{C}_{un-} = \frac{y_u}{g_2}V^*_{2n}\mathcal{D}_{d11}\left(-U_{1n}\mathcal{D}^*_{d11}+\frac{y_d}{g_2}U_{2n}\mathcal{D}^*_{d21}\right. \qquad (13)$$
$$\left.+\,\frac{\lambda'_{k11}}{g_2}U_{(k+2)n}\mathcal{D}^*_{d21}\right),$$

$$\mathcal{C}_{un+} = \frac{y_u}{g_2}V^*_{2n}\mathcal{D}_{d12}\left(-U_{1n}\mathcal{D}^*_{d12}+\frac{y_d}{g_2}U_{2n}\mathcal{D}^*_{d22}\right.$$
$$\left.+\,\frac{\lambda'_{k11}}{g_2}U_{(k+2)n}\mathcal{D}^*_{d22}\right),$$

$$\mathcal{C}_{dn-} = \left(\frac{y_d}{g_2}U_{2n}+\frac{\lambda'_{k11}}{g_2}U_{(k+2)n}\right)\mathcal{D}_{u11}$$
$$\times\left(-V^*_{1n}\mathcal{D}^*_{u11}+\frac{y_u}{g_2}V^*_{2n}\mathcal{D}^*_{u21}\right),$$

$$\mathcal{C}_{dn+} = \left(\frac{y_d}{g_2}U_{2n}+\frac{\lambda'_{k11}}{g_2}U_{(k+2)n}\right)\mathcal{D}_{u12}$$
$$\times\left(-V^*_{1n}\mathcal{D}^*_{u12}+\frac{y_u}{g_2}V^*_{2n}\mathcal{D}^*_{u22}\right)$$

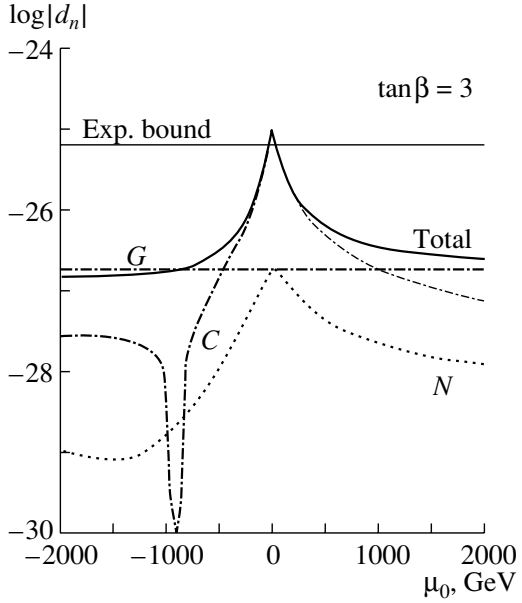

Fig. 2. Logarithmic plot of (the magnitude of) the RPV neutron EDM result for μ_0 value between ± 2000 GeV, with the other parameters set at the same values as case A in the table. The lines marked by G, C, N, and "Total" give the complete gluino, chargino-like, neutralino-like, and total (i.e., sum of the three) contributions, respectively. Note that the values of the N contributions and those of the C line for $\mu_0 < -900$ GeV are negative.

(only repeated index i is to be summed). $V^\dagger\mathcal{M}_c U = {\rm diag}\{M_{\chi_n^-}\} \equiv {\rm diag}\{M_{c1}, M_{c2}, \ m_e, m_\mu, m_\tau\}$, while $\mathcal{D}_u$ and $\mathcal{D}_d$ diagonalize the $\tilde{u}$ and $\tilde{d}$ squark mass-squared matrices, respectively; and

$$A(x) = \frac{1}{2(1-x)^2}\left(3-x+\frac{2\ln x}{1-x}\right), \qquad (14)$$
$$B(x) = \frac{1}{2(x-1)^2}\left[1+x+\frac{2x\ln x}{(1-x)}\right].$$

To extract the contribution from the diagram of Fig. 1, we have to look at the pieces in $\mathcal{C}_{dn\mp}$ with a V^*_{1n} and a $U_{(k+2)n}$. It is easy to see that the $n=1$ and 2 mass eigenstates, namely, the chargino states, do give the dominating contribution. With the small μ_i mixings strongly favored by the sub-eV neutrino masses, we have

$$U_{(k+2)1} = \frac{\mu_k^*}{M_{c1}}R_{R_{21}}, \quad U_{(k+2)2} = \frac{\mu_k^*}{M_{c2}}R_{R_{22}}, \quad (15)$$

where the R_R denotes the right-handed rotation that would diagonalize the first 2×2 block of $\mathcal{M}_c$. The latter rotation matrix is expected to have elements of order 1. Hence, we have the dominating result proportional to $\sum_{n=1,2}R^*_{R_{12}}R_{R_{2n}}\mu_k^*\lambda'_{k11}F_{BA}(M^2_{c_n})$, where F_{BA} denotes the mass-eigenvalue-dependent part.

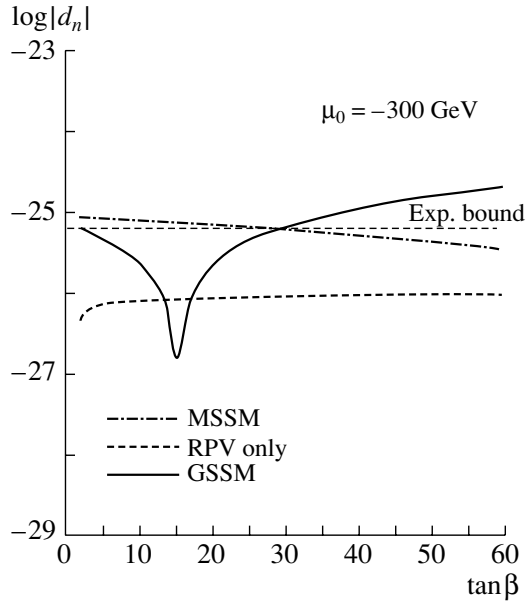

Fig. 3. Logarithmic plot of (the magnitude of) the neutron EDM result vs. $\tan\beta$. We show here the MSSM result, our general result with RPV phase only, and the generic result with complex phases of both kinds. In particular, the A and μ_0 phases are chosen as 7° and 0.1°, respectively, for the MSSM line. They are zero for the RPV-only line, with which we have a phase of $\pi/4$ for λ'_{311}. All the given nonzero values are used for the three phases for the generic result (from our complete formulas) marked by GSSM. Again, the other unspecified input parameters are the same as for case A of the table.

The result agrees with what we have said above. It vanishes for $M_{c1} = M_{c2}$, showing a GIM-like mechanism. However, with unequal chargino masses, our numerical results indicate that the cancellation is generically badly violated. More interestingly, it can be seen from the above analysis that a complex phase in $\mu^*_k\lambda'_{k11}$ is actually not necessary for this potentially dominating chargino contribution to be there, as long as complex CP-violating phases exist in the R_R matrix, i.e., in the R-parity-conserving parameters such as μ_0.

Some illustrative sets of our numerical results are presented in the table. In Fig. 2, we illustrate a comparison of the gluino, chargino-like, and neutralino-like contributions for a range of μ_0 values. Figure 3 gives the variation against the $\tan\beta$ value, while comparing the overall GSSM result with the MSSM result. On the whole, the magnitude of the parameter combination $\mu^*_i\lambda'_{i11}$ is shown to be responsible for the RPV one-loop contribution to neutron EDM and is hence well constrained. This applies not only to the complex phase, or imaginary part of, the combination.

7. EDMs OF THE ELECTRON AND OTHER FERMIONS

The above quark EDM formula obviously applies with some trivial modifications to the cases of the other quarks. For leptons, while the exact formulas would be different, there are major basic features that are more or less the same. For instance, for the charged lepton, the λ couplings play the role of the λ' couplings. The $\mu^*_i\lambda_{i11}$ combination contributes to electron EDM, while the $\mu^*_i\lambda_{i22}$ combination contributes to that of the muon. As we have no explicit numerical results to show at the moment, we refrain from showing any details here.

There is in fact a second class of one-loop diagrams contributing to the quark EDMs. These are diagrams with quarks and scalars in the loop, and hence superpartners of the chargino-like and neutralino-like diagrams discussed above. The basic formulas are also given in [3]. The R-parity-conserving analog of the class of diagrams has no significance due to the unavoidable small Yukawa couplings involved. With the latter replaced by flavor-changing λ' couplings, we can have a t-quark loop contributing to neutron EDM, for example. For the case of charged leptons, the two classes of superpartner diagrams merge into one. But then, all scalars have to be included. The assumption hidden in our quark EDM formula above that only the (two) superpartner sfermions have a significant role to play, does not stand anymore. We have finished a $\mu \to e\gamma$ study, from which the charged lepton EDM formula could be extracted without too much effort [17]. Interested readers may check the reference to get an idea or just tune in for our future publications [18].

REFERENCES

1. O. C. W. Kong, JHEP **0009**, 037 (2000).
2. Y.-Y. Keum and O. C. W. Kong, Phys. Rev. Lett. **86**, 393 (2001).
3. Y.-Y. Keum and O. C. W. Kong, Phys. Rev. D **63**, 113012 (2001).
4. O. C. W. Kong, in *Proceedings of the 30th International Conference on High Energy Physics (ICHEP2000),* Ed. by C. S. Lim and T. Yamanaka (World Sci., Singapore, 2001), Vol. II, p. 1048.
5. O. C. W. Kong, Nucl. Phys. B (Proc. Suppl.) **101**, 421 (2001).
6. O. C. W. Kong, hep-ph/0104276.
7. L. E. Ibáñez and G. G. Ross, Nucl. Phys. B **368**, 3 (1992).
8. See, for example, M. Maltoni, Yad. Fiz. **65**, 2188 (2002) [Phys. At. Nucl. **65**, 2125 (2002)].
9. M. Bisset, O. C. W. Kong, C. Macesanu, and L. H. Orr, Phys. Lett. B **430**, 274 (1998); Phys. Rev. D **62**, 035001 (2000).
10. O. C. W. Kong, IPAS-HEP-k008 (in preparation).

11. O. C. W. Kong, Mod. Phys. Lett. A **14**, 903 (1999).
12. K. Cheung and O. C. W. Kong, Phys. Rev. D **61**, 113012 (2000).
13. S. K. Kang and O. C. W. Kong, IPAS-HEP-k009 (in preparation).
14. See also, A. Abada and M. Losada, hep-ph/9908352; S. Davidson and M. Losada, JHEP **0005**, 021 (2000); hep-ph/0010325.
15. O. C. W. Kong *et al.*, work in progress.
16. K. Choi, E. J. Chun, and K. Hwang, Phys. Rev. D **63**, 013002 (2001).
17. K. Cheung and O. C. W. Kong, Phys. Rev. D **64**, 095007 (2001).
18. K. Cheung, Y.-Y. Keum, and O. C. W. Kong, IPAS-HEP-k011 (in preparation).

Physics of Atomic Nuclei, Vol. 65, No. 12, 2002, pp. 2116–2124. From Yadernaya Fizika, Vol. 65, No. 12, 2002, pp. 2179–2187.

NEW PHYSICS BEYOND THE STANDARD MODEL

Complete LEP Data: Status of Higgs Boson Searches*

A. Sopczak**

Lancaster University, UK

Received February 13, 2002

Abstract—The LEP experiments completed data taking in November 2000. New preliminary combined results of the four LEP experiments ALEPH, DELPHI, L3, and OPAL are presented for various Higgs boson searches. © *2002 MAIK "Nauka/Interperiodica"*.

1. INTRODUCTION

After 11 years of operation, the LEP experiments have completed data taking. In 2000, the center-of-mass energy was pushed to 209 GeV with most data taken around 206 GeV. In the last three years of operation, a luminosity of about 687 pb^{-1} was delivered to each experiment, which exceeded expectations. Despite hints for a Higgs boson discovery around 116 GeV, data-taking was not continued in 2001.

2. STANDARD MODEL HIGGS BOSON

In September 2000, ALEPH presented a data excess consistent with the reaction $e^+e^- \to HZ \to b\bar{b}q\bar{q}$ for a Higgs boson mass of about 115 GeV [1], which was not confirmed by the other LEP experiments. In November 2000, L3 provided support for a signal observation with a $HZ \to b\bar{b}\nu\bar{\nu}$ candidate event at the same mass. For the summer conferences in 2001, all experiments updated their analyses, and the probability of the data being consistent with the Standard Model (SM) background is increased, as detailed in Table 1 [2]. The confidence levels CL_b for a signal observation and CL_s for setting mass limits are shown in Fig. 1. The resulting SM Higgs boson mass limit is 114.1 GeV at 95% C.L. The reconstructed mass distribution and a list of candidate events are shown in Fig. 2. In extensions of the SM, the HZZ coupling might be weaker and thus the production cross section is reduced. Figure 3 shows limits on the reduction factor at 95% C.L. Even if the SM cross section is reduced by a factor of 3, a Higgs boson mass up to 110 GeV is excluded.

3. MSSM BENCHMARK RESULTS

The minimal supersymmetric extension of the Standard Model (MSSM) is the most attractive alternative to the SM. The $e^+e^- \to hA$ and $e^+e^- \to hZ$ production cross sections are complementary. The LEP experiments have searched for the reactions $e^+e^- \to hA \to b\bar{b}b\bar{b}$ and $b\bar{b}\tau^+\tau^-$. Confidence levels CL_b and CL_s are given in Fig. 4 for the so-called benchmark results in the MSSM for large mixing in the scalar-top sector (m_h-max) [5].

4. A GENERAL MSSM PARAMETER SCAN

Important reductions of the mass limits compared to benchmark results were reported for LEP1 and first LEP2 data [6, 7]. With increasing statistics, the reduction was only a few GeV by including the 189-GeV data of one LEP experiment (DELPHI) [8], and similar for OPAL [9]. Figure 5 shows new results from a MSSM parameter scan for complete DELPHI data up to 209 GeV, leading to mass limits of 89 GeV on both scalar and pseudoscalar neutral Higgs bosons [10]. These are almost identical to the DELPHI benchmark limits [11]. Figure 5 (lower right) shows the importance of searches for invisible Higgs bosons [12] which could decay into neutralinos for some parameter combinations of the scan (outside of the benchmark).

Limits on the $e^+e^- \to hA \to b\bar{b}b\bar{b}$ and $b\bar{b}\tau^+\tau^-$ production rates are given in Fig. 6 [5] for the example of $m_h \approx m_A$. As noted previously for 202-GeV data, taken in 1999, and first 2000 data, h and A mass limits were 2 GeV below expectation [13] and this tendency is enhanced by including 209-GeV data, in which case they are 3.1 to 3.6 GeV below the expectations of about 95 GeV. A possible explanation is given that the HZ excess at about 115 GeV is due to the heavier scalar and that, in addition, the production of hA with masses between 90 and 100 GeV occurs [13]. Figure 6 shows a data excess above 2σ for $m_h +$

*This article was submitted by the author in English.

**e-mail: andre.sopczak@cern.ch

Table 1. Background probabilities $1 - CL_b$ at a Higgs boson test mass of $m_H = 115$ GeV, for the individual experiments and for the LEP data combined

	ALEPH	DELPHI	L3	OPAL	LEP	Significance (σ)
Sep. 5, 2000	1.6×10^{-4}	0.67	0.84	0.47	2.5×10^{-2}	2.2
Nov. 3, 2000	6.5×10^{-4}	0.68	6.8×10^{-2}	0.19	4.2×10^{-3}	2.9
Summer 2001	2.6×10^{-3}	0.77	0.32	0.20	3.4×10^{-2}	2.1

Note: The results presented at the LEPC of September 5 were revised for the LEPC of November 3. The revised values are listed.

Table 2. Left: Observed and expected Higgs boson mass limits from complete LEP data in various models. Right: Benchmark (b) and scan (s) mass limits in the MSSM (all limits are in GeV at 95% C.L.)

Model	Obs.	Exp.	$\sqrt{s}$ (GeV)	Data	m_h^b	m_A^b	m_h^s	m_A^s
SM	114.1	115.6	91 [21, 6]	L3	41.0	none	25	none
MSSM (m_h)	91.0	94.6	172 [22, 7]	DELPHI	59.5	51.0	30	none
MSSM (m_A)	91.9	95.0	183 [23, 24]	DELPHI	74.4	75.2	67	75
H^+H^-	78.6	78.8	189 25, 8]	DELPHI	82.6	84.1	75	78
Invisible	114.3	113.6	189 [9]	OPAL	74.8	76.5	72	76
Flavor-independent	112.9	113.0	202 [26]	DELPHI	85.9	86.5	85	86
Fermiophobic	108.2	109.0	202 [27, 4]	LEP	88.3	88.4	86	87
			209 [11, 10]	DELPHI	89.6	90.7	89	89

$m_A = 187$ GeV in the $b\bar{b}b\bar{b}$ channel. The same data excess is also expressed in the CL_b and CL_s distributions as shown in Fig. 7. The hypothesis of the production of three MSSM Higgs bosons is supported by the data excess seen in Fig. 2 at 100 GeV, which could result from hZ production in addition to HZ production. For the reported MSSM parameters [13], $\cos^2(\beta - \alpha) \approx 0.9$; therefore, $\sin^2(\beta - \alpha) = \xi^2 \approx 0.1$. The ξ^2 limit in the 100-GeV mass region shows a deviation of about 2σ between expected and observed limit, as seen in Fig. 3 (left). Figure 3 (right) shows that this new support is only observed in the complete LEP data.

5. CHARGED HIGGS BOSONS

The search for charged Higgs bosons is performed in the framework of the general extension of the SM with two Higgs boson doublets. The combined CL_b distributions from the four LEP experiments for the reactions $e^+e^- \to H^+H^- \to c\bar{s}\bar{c}s$ and $\tau^+\nu\tau^-\bar{\nu}$ are presented in Fig. 8 [14]. The resulting mass limit, which also includes the $cs\tau\nu$ channel, is 78.6 GeV at 95% C.L., and it is valid for any branching ratio BR($H^+ \to \tau^+\nu$) as shown in Fig. 9. The cross-section limit for the $c\bar{s}\bar{c}s$ channel shows that the barrier from irreducible WW background events is almost passed. Optimization of the analyses of each individual experiment for higher masses could increase the decay-mode-independent reach by more

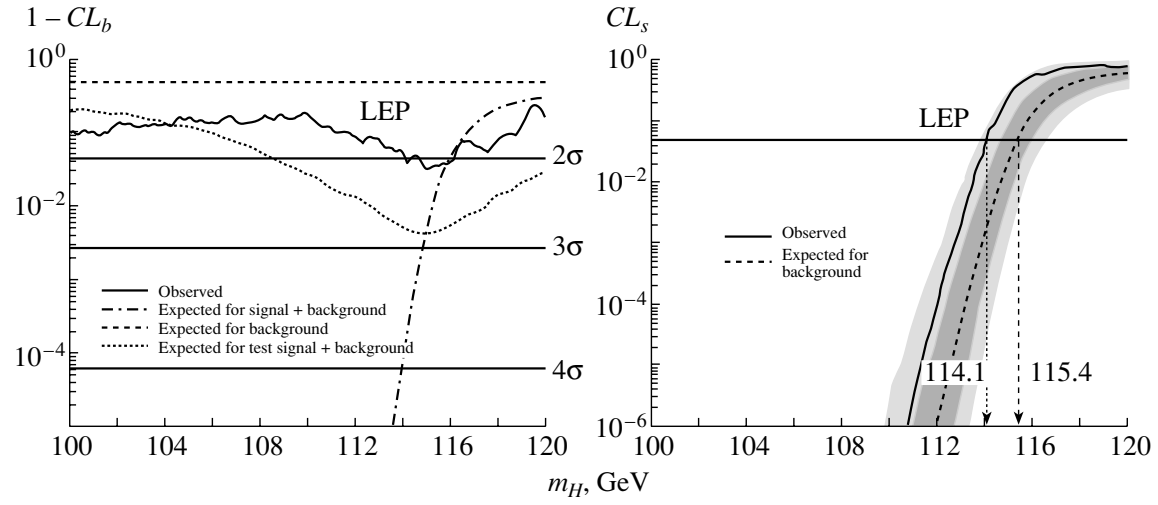

Fig. 1. Confidence levels $1 - CL_b$ and CL_s from combining the data collected by the four LEP experiments at energies from 189 to 209 GeV. The solid curve is the observed result. The shaded areas represent the symmetric 1σ and 2σ probability bands. The horizontal line at $CL_s = 0.05$ gives the mass limits at 95% C.L.

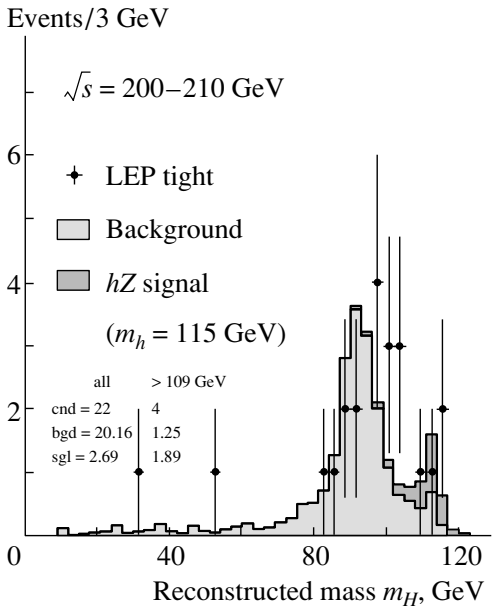

Experiment	Channel	m_H^{rec}, GeV	ln(1 + *s*/*b*)
ALEPH	4-jet	114.3	1.73
ALEPH	4-jet	112.9	1.21
ALEPH	4-jet	110.0	0.64
L3	*E*-miss	115.0	0.53
OPAL	4-jet	110.7	0.53
DELPHI	4-jet	114.3	0.49
ALEPH	Lept	118.1	0.47
ALEPH	Tau	115.4	0.41
ALEPH	4-jet	114.5	0.40
OPAL	4-jet	112.6	0.40
DELPHI	4-jet	97.2	0.36
L3	4-jet	108.3	0.31
ALEPH	4-jet	114.4	0.27
ALEPH	4-jet	103.0	0.26
OPAL	*E*-miss	104.0	0.25
ALEPH	4-jet	110.2	0.22
L3	*E*-miss	110.1	0.21
OPAL	*E*-miss	112.1	0.20
DELPHI	4-jet	110.1	0.20
L3	*E*-miss	110.1	0.18

Fig. 2. (Left) Distribution of the reconstructed SM Higgs boson mass in searches conducted at energies between 200 and 210 GeV. The figure displays the data (dots with error bars), the predicted SM background, and the prediction for a Higgs boson of 115-GeV mass. The number of data events selected with mass larger than 109 GeV is 4, while 1.25 are expected from SM background processes and 1.89 from a 115-GeV signal. (Right) Properties of the candidates with the highest signal-over-background ratio $\ln(1 + s/b)$ at 115 GeV. The corresponding expected signal and background rates are 8.8 and 16.5 events, respectively.

than 5 GeV. Already a pre-LEP2 study [17] based on a luminosity of 500 pb^{-1} pointed out that "the kinematic region above m_W will be a challenge for the decay-mode-independent sensitivity; it might even be unfeasible."

6. INVISIBLE HIGGS BOSON DECAYS

In some models, the Higgs boson can decay into invisible particles, such as neutralinos or majorons. The search for these Higgs bosons is performed in the Higgs bremsstrahlung process in association with a Z boson. All hadronic and charged leptonic Z decays are investigated [18]. The CL_s distribution and the

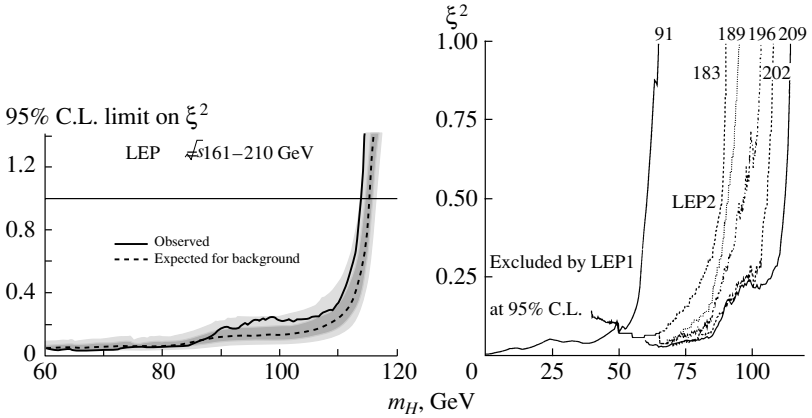

Fig. 3. (Left) The 95% C.L. upper bound on ξ^2 as a function of m_H, where $\xi = g_{HZZ}/g^{\mathrm{SM}}_{HZZ}$ is the HZZ coupling relative to the SM coupling. About 2σ deviations from the expectation are observed at $m_H = 98$ GeV and $m_H = 115$ GeV. (Right) The excluded (ξ^2, m_H) region including 209-GeV data is compared with the results from combined LEP1 data [3], taken around 91-GeV center-of-mass energy, and previous LEP2 limits [4] up to 183, 189, 196, and 202 GeV. The ξ^2 limit below 100 GeV does not become significantly stronger when the 209-GeV data, taken in 2000, is included.

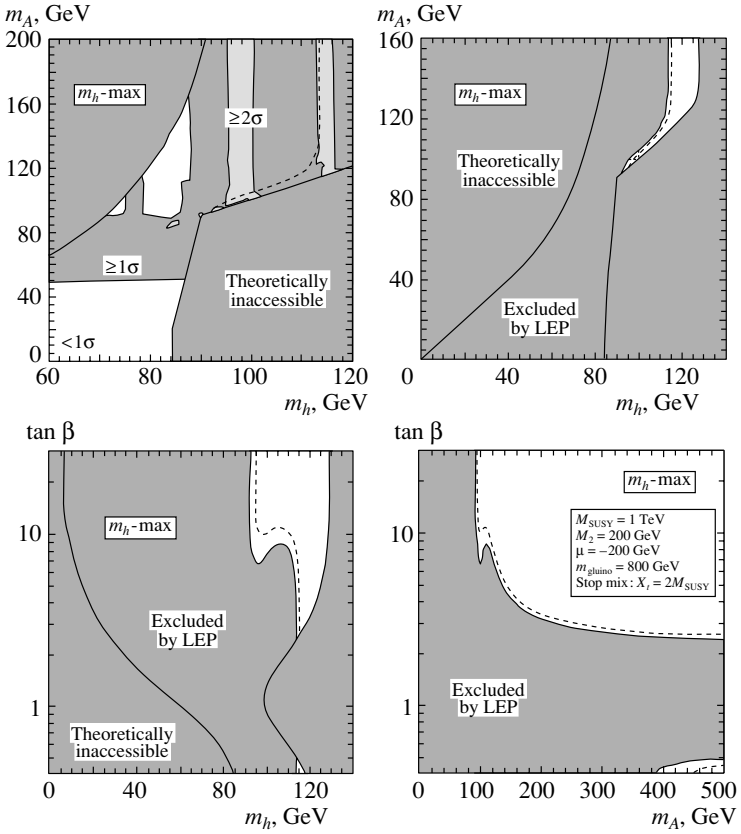

Fig. 4. (Upper left) Distribution of the discovery confidence level $1 - CL_b$ for the m_h-max benchmark, projected onto the (m_h, m_A) plane by combining the data of the four LEP experiments at energies from 88 to 209 GeV. In the white domain, the observation either shows a deficit or is less than 1σ above the background prediction; in the domains labeled $\geq 1\sigma$ and $\geq 2\sigma$, the observation is between 1σ and 2σ and larger than 2σ above the prediction, respectively. The other plots show the 95% C.L. bounds on m_h, m_A, and $\tan\beta$ for the m_h-max benchmark. The solid curves represent the actual observation and the dashed lines the limits expected on the basis of "background-only" Monte Carlo experiments. (Upper right) Projection (m_h, m_A); (lower left) projection $(m_h, \tan\beta)$; (lower right) projection $(m_A, \tan\beta)$.

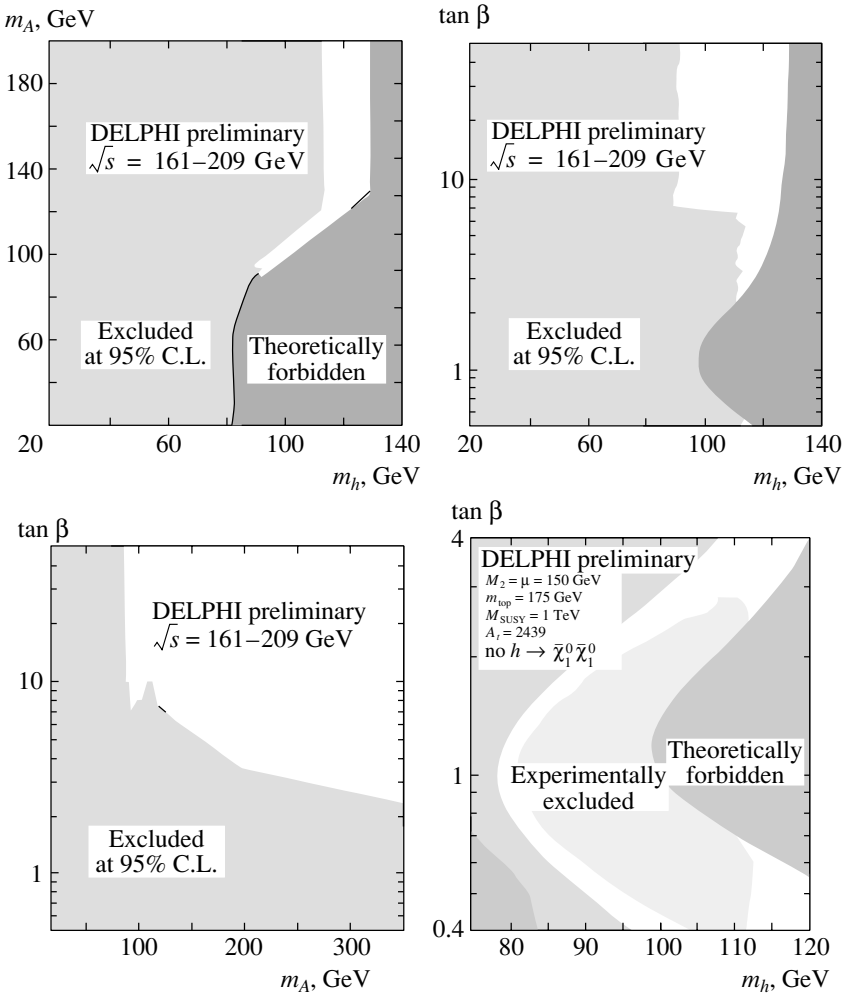

Fig. 5. MSSM parameter scan results for DELPHI data at energies from 161 to 209 GeV. (Upper left) Projection (m_h, m_A); (upper right) projection $(m_h, \tan\beta)$; (lower left) projection $(m_A, \tan\beta)$. (Lower right) Excluded parameter combinations from searches for invisibly decaying Higgs bosons from 189- to 209-GeV data.

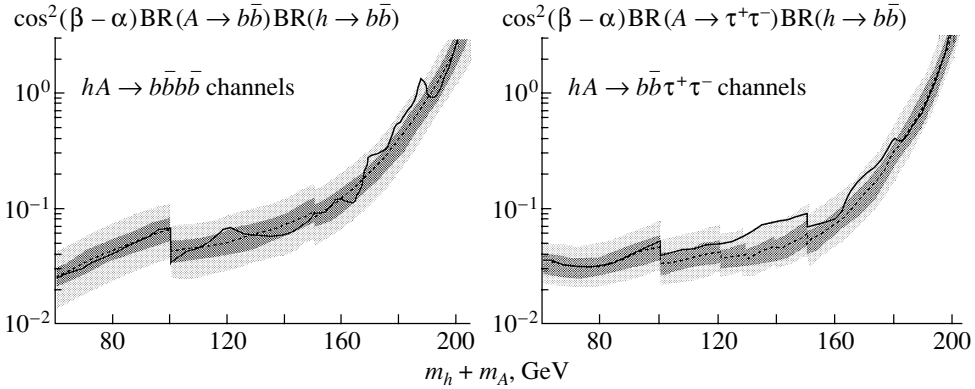

Fig. 6. Limits on the hA cross section as a function of $m_h + m_A$ at 95% C.L. ($m_h \approx m_A$) for the MSSM processes $e^+e^- \to hA \to b\bar{b}b\bar{b}$ and $b\bar{b}\tau^+\tau^-$. This corresponds to limits of $\cos^2(\beta-\alpha)$ in the general extension of the SM with two Higgs boson doublets. The data of the four LEP experiments collected at energies from 88 to 209 GeV are combined. The solid curve is the observed result and the dashed curve shows the expected median. Shaded areas indicate the 1σ and 2σ probability bands.

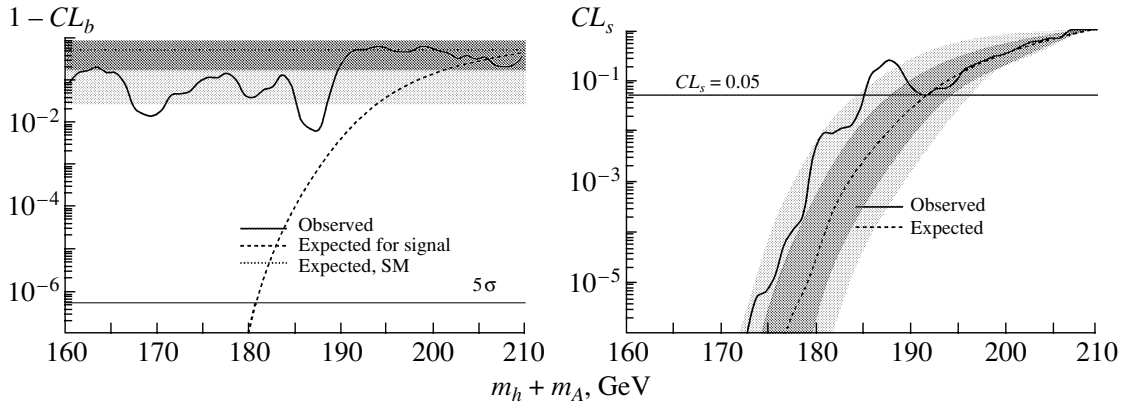

Fig. 7. The confidence levels $1 - CL_b$ and CL_s as a function of $m_h + m_A$ for the case $m_h \approx m_A$ (where only the $e^+e^- \to hA$ process contributes since $\sin^2(\beta - \alpha) \approx 0$). The straight line at 0.5 and the shaded 1σ and 2σ probability bands represent the expected background-only result. The solid curve is the observed result and the dashed curve shows the expected median for a signal. The horizontal line at $1 - CL_b = 5.7 \times 10^{-7}$ indicates the level for a 5σ discovery, and the intersections of the curves with the horizontal line at $CL_s = 0.05$ give the limit on $m_h + m_A$ at 95% C.L. The data of the four LEP experiments collected at energies from 88 to 209 GeV are combined.

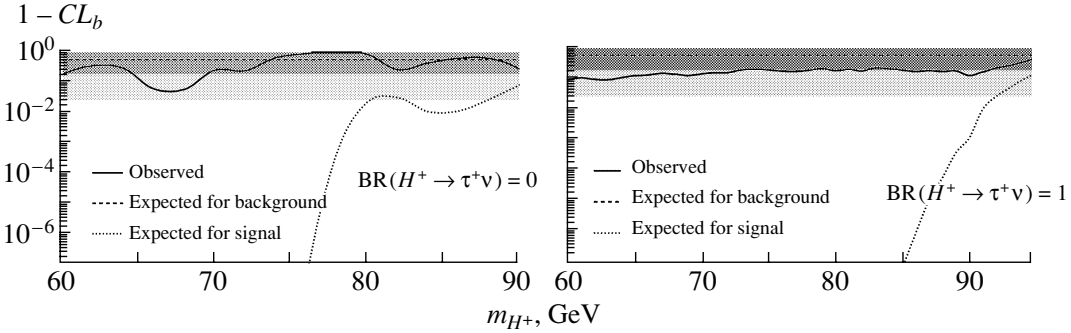

Fig. 8. The $1 - CL_b$ distributions for the $c\bar{s}\bar{c}s$ and $\tau^+\nu\tau^-\bar{\nu}$ channels, combining the data collected by the four LEP experiments at energies from 189 to 209 GeV. The shaded areas represent the 1σ and 2σ probability bands. Owing to the large irreducible $WW \to c\bar{s}\bar{c}s$ background, less sensitivity is obtained near the W mass for the case BR($H^+ \to \tau^+\nu$) = 0, as can be seen from the expected signal probability curve.

cross-section limit are given in Fig. 10. The mass limit is 114.4 GeV.

7. FLAVOR-INDEPENDENT HIGGS BOSON DECAYS

While in the SM the Higgs boson decays predominantly into b quarks, in many extensions such as the general two Higgs doublet model, the b-quark coupling could be suppressed. Therefore, the search for Higgs boson bremsstrahlung in the four-jet, two-jet and two-lepton, and two-jet and missing-energy channels is generalized for flavor-independent hadronic Higgs boson decays [19]. Stringent limits are given in Fig. 11. The expected limit is only 2.6 GeV below the SM limit, which is remarkable since b tagging is a very important search tool.

8. PHOTONIC HIGGS BOSON DECAYS

It is possible that the Higgs boson does not decay into fermions. In this case the decays into $\gamma\gamma$, WW, and ZZ are dominant. As a fermiophobic benchmark model, the production and decays of the SM Higgs boson are assumed and all couplings to fermions are set to zero [20]. Figure 12 shows the expected Higgs boson branching fractions and the mass limits from the search by all LEP experiments in the $h \to \gamma\gamma$ channel.

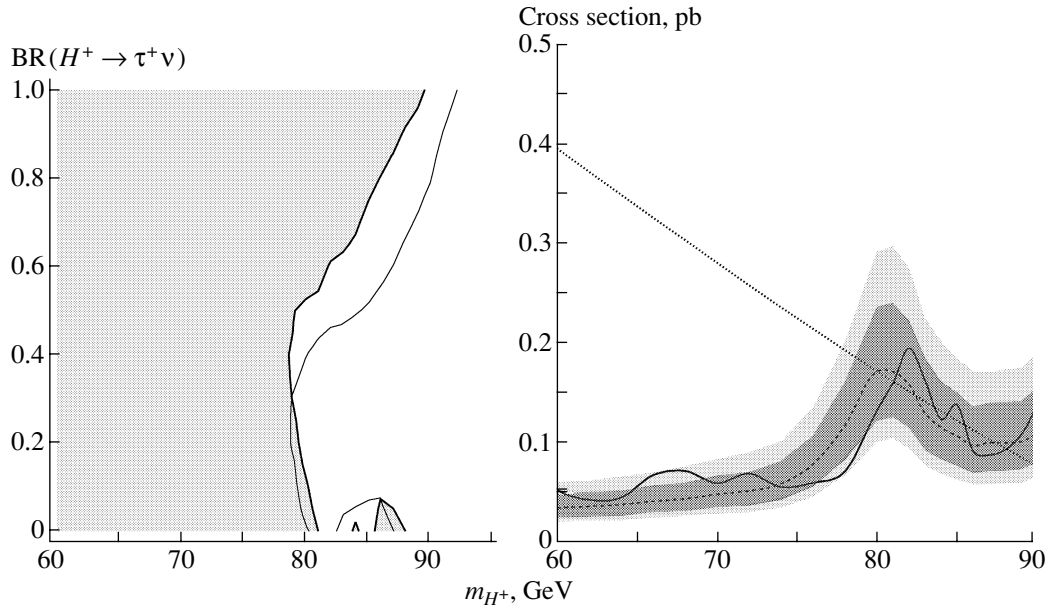

Fig. 9. (Left) The 95% C.L. bounds on m_{H^+} as a function of the branching ratio BR($H^+ \to \tau^+\nu$), combining the data collected by the four LEP experiments at energies from 189 to 209 GeV. The expected median limits are indicated by the thin curve and the observed limits by the thick curve. (Right) The 95% C.L. bounds on the production cross section for BR($H^+ \to \tau^+\nu$) = 0. The observed limit is given by the solid curve, and the expected limits are indicated by the dashed curve and the shaded bands (1σ and 2σ). The dotted curve gives the expected cross section at 206-GeV center-of-mass energy. Radiative corrections vary the cross section by typically $\pm 10\%$ depending on the model parameters [15, 16].

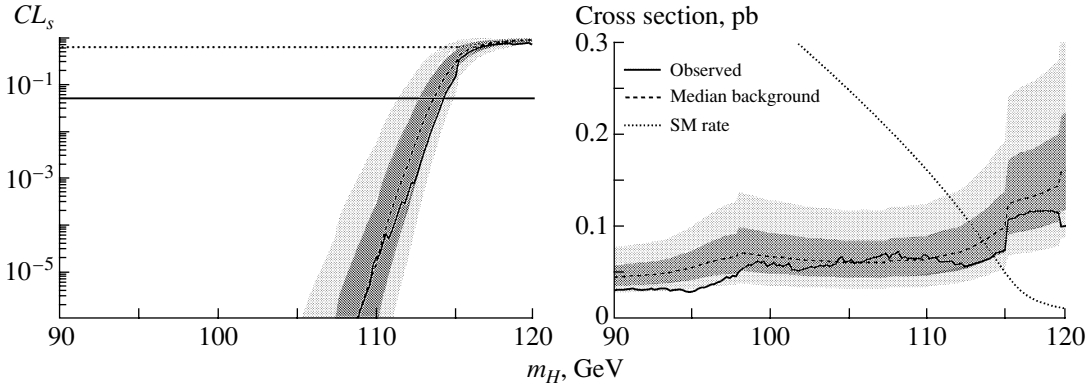

Fig. 10. (Left) The CL_s distribution for all hadronic and charged leptonic channels for invisible Higgs boson decays, combining the data collected by the four LEP experiments at energies from 200 to 209 GeV. The observed limit is given by the solid curve, and the expected limits are indicated by the dashed curve and the shaded bands (1σ and 2σ). The horizontal line at $CL_s = 0.05$ gives the limit at 95% C.L. (Right) The 95% C.L. bounds on the production cross section for BR($H' \to$ invisible) = 1. The observed limit is given by the solid curve, and the expected limits are indicated by the dashed curve and the shaded bands (1σ and 2σ). The dotted curve gives the expected cross section at 206 GeV for Higgs bosons decaying 100% invisibly.

9. CONCLUSIONS

The combination of the complete data from the four LEP experiments resulted in a large increase for the sensitivity of Higgs bosons. The data shows a preference for a SM Higgs boson of 115.6 GeV. Further small data excesses for Higgs boson pair production and bremsstrahlung between 90 and 100 GeV allow the hypothesis that h, A, and H of the MSSM all have masses between 90 and 116 GeV. Previously reported MSSM parameter combinations from a general scan are supported by the complete data set. The data is also consistent with the background-only hypothesis which results in stringent mass limits for the SM Higgs boson, the neutral Higgs bosons of the MSSM, charged Higgs bosons, invisible Higgs boson decays, flavor-independent hadronic Higgs bo-

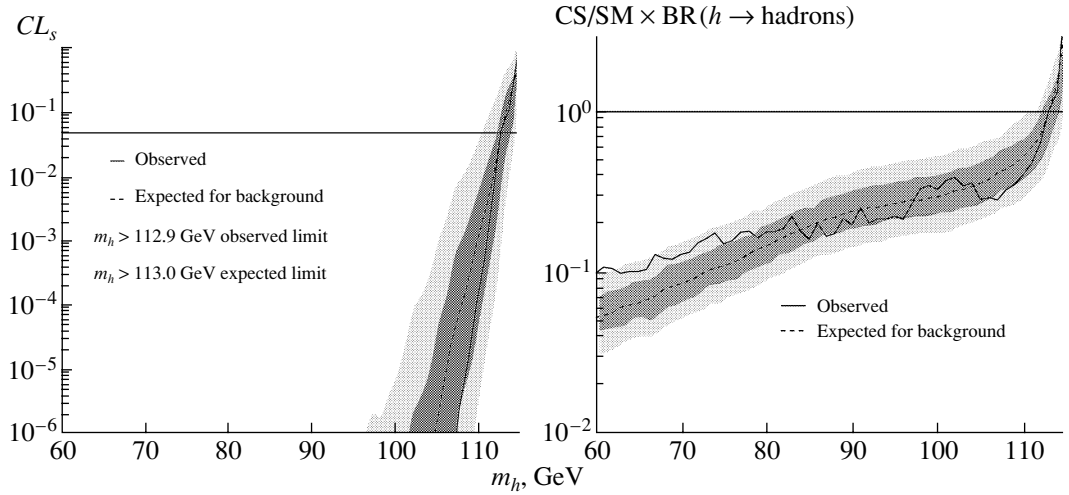

Fig. 11. (Left) The CL_s distribution for all hadronic and charged leptonic channels for flavor-independent hadronic Higgs boson decays, combining the data collected by the four LEP experiments at energies up to 209 GeV. The production cross section of the SM and BR($h \to q\bar{q}$) = 1 is assumed. The observed limit is given by the solid curve, and the expected limits are indicated by the dashed curve and the shaded bands (1σ and 2σ). The horizontal line at $CL_s = 0.05$ gives the limit at 95% C.L. (Right) The 95% C.L. bounds on the production cross section normalized to the SM cross section. The observed limit is given by the solid curve, and the expected limits are indicated by the dashed curve and the shaded bands (1σ and 2σ).

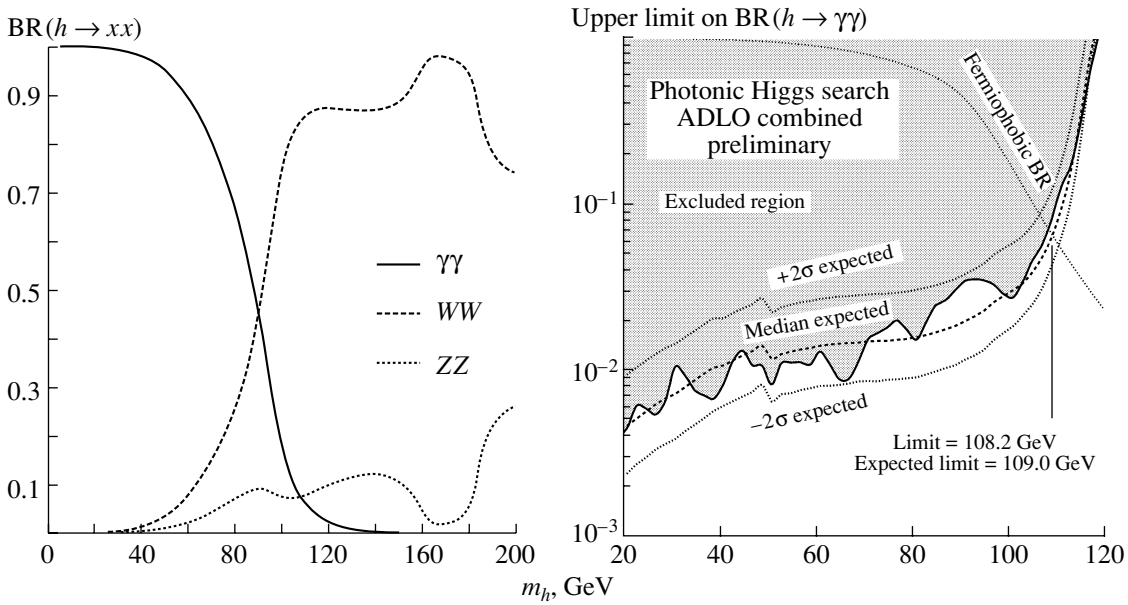

Fig. 12. (Left) Branching fraction of the fermiophobic benchmark model, where only the bosonic Higgs decay modes are allowed. (Right) Limits at 95% C.L. on the branching fraction $h \to \gamma\gamma$ assuming SM production cross sections. The observed limit is given by the solid curve, and the expected limits are indicated by the dashed curve and the 2σ bands. The dotted curve gives the expected branching fraction in the fermiophobic benchmark model.

son decays, and fermiophobic Higgs boson decays. Table 2 summarizes these limits and, in addition, compares benchmark and scan limits in the MSSM.

ACKNOWLEDGMENTS

I would like to thank the organizers of the conference for their kind hospitality, and Pierre Lutz, Bill Murray, and Alex Read for comments on the manuscript.

REFERENCES

1. ALEPH Collab. (D. Schlatter *et al.*), *LEP Committee Open Session, 2000.*

2. ALEPH, DELPHI, L3, and OPAL Collabs. and the LEP Working Group for Higgs Boson Searches, CERN-EP/2001-55.
3. A. Sopczak, DESY 97-129; Indian J. Phys. A **72**, 495 (1998).
4. A. Sopczak, in *Proceedings of the 7th International Symposium on Particles, Strings, and Cosmology, PASCOS-99, Granlibakken, USA, 1999* (World Sci., Singapore, 2000), p. 511; hep-ph/0004015.
5. ALEPH, DELPHI, L3, and OPAL Collabs. and the LEP Working Group for Higgs Boson Searches, LHWG Note/2001-04.
6. J. Rosiek and A. Sopczak, Phys. Lett. B **341**, 419 (1995).
7. A. Sopczak, Eur. Phys. J. C **9**, 107 (1999).
8. DELPHI Collab. (P. Abreu *et al.*), Eur. Phys. J. C **17**, 549 (2000).
9. OPAL Collab. (G. Abbiendi *et al.*), Eur. Phys. J. C **12**, 567 (2000).
10. DELPHI Collab., DELPHI 2001-081 CONF 509, contributed paper for EPS HEP 2001 (Budapest) and LP01 (Rome).
11. DELPHI Collab., DELPHI 2001-078 CONF 506, contributed paper for EPS HEP 2001 (Budapest) and LP01 (Rome).
12. DELPHI Collab., DELPHI 2001-079 CONF 507, contributed paper for EPS HEP 2001 (Budapest) and LP01 (Rome).
13. A. Sopczak, hep-ph/0011285; in *Proceedings of DPF-2000, Columbus, Ohio, 2000,* http://www.dpf2000.org/BSM1.htm#ses4.
14. ALEPH, DELPHI, L3 and OPAL Collabs. and the LEP Working Group for Higgs Boson Searches, LHWG Note/2001-05.
15. A. Arhrib and G. Moultaka, Nucl. Phys. B **558**, 3 (1999).
16. J. Guasch, W. Hollik, and A. Kraft, Nucl. Phys. B **596**, 66 (2001).
17. A. Sopczak, Int. J. Mod. Phys. A **9**, 1747 (1994).
18. ALEPH, DELPHI, L3, and OPAL Collabs. and the LEP Working Group for Higgs Boson Searches, LHWG Note/2001-06.
19. ALEPH, DELPHI, L3 and OPAL Collabs. and the LEP Working Group for Higgs Boson Searches, LHWG Note/2001-07.
20. ALEPH, DELPHI, L3, and OPAL Collabs. and the LEP Working Group for Higgs Boson Searches, LHWG Note/2001-08.
21. A. Sopczak, PhD Thesis (Univ. of California, San Diego, 1992); L3 Collab. (O. Adriani *et al.*), Phys. Lett. B **294**, 457 (1992); Z. Phys. C **57**, 355 (1993).
22. DELPHI Collab. (P. Abreu *et al.*), Eur. Phys. J. C **2**, 1 (1998).
23. DELPHI Collab., DELPHI 98-95 CONF-163, contributed paper for ICHEP 1998 (Vancouver).
24. DELPHI Collab., DELPHI 98-124 CONF-185, contributed paper for ICHEP 1998 (Vancouver).
25. DELPHI Collab. (P. Abreu *et al.*), Eur. Phys. J. C **17**, 187 (2000).
26. DELPHI Collab. (P. Abreu *et al.*), submitted to Eur. Phys. J. C; CERN-EP/2001-87.
27. ALEPH, DELPHI, L3, and OPAL Collabs. and the LEP Working Group for Higgs Boson Searches, ALEPH 2000-074 CONF 2000-051, DELPHI 2000-148 CONF 447, L3 Note 2600, OPAL TN 661.

Physics of Atomic Nuclei, Vol. 65, No. 12, 2002, pp. 2125–2134. From Yadernaya Fizika, Vol. 65, No. 12, 2002, pp. 2188–2197.

NEUTRINO PHYSICS AND ASTROPHYSICS

Global Analysis of Solar and Atmospheric Neutrino Data*

M. Maltoni**

Instituto de Física Corpuscular—CSIC/UVEG,
Edificio Institutos de Paterna, Apt. 22 085, E-46071 Valencia, Spain

Received February 13, 2002

Abstract—A global analysis of solar (including the recent SNO result), atmospheric, and reactor neutrino data is presented in terms of three- and four-neutrino oscillations. We first present the allowed regions of solar and atmospheric oscillation parameters assuming three-neutrino families, showing that in this framework it is possible to reconcile the two anomalies and providing an unified fit of all the observables at a time. Then, we consider scenarios where a sterile neutrino is added to the three standard ones and the mass spectra present two separate doublets. We evaluate the allowed active-sterile admixture in both solar and atmospheric oscillations, showing that, although the Super-Kamiokande data disfavor both the pure $\nu_\mu \to \nu_s$ atmospheric channel and, in combination with SNO, the pure $\nu_e \to \nu_s$ solar channel, the result from the combined analysis still favors close-to-pure active and sterile oscillations and disfavors oscillations into a near-maximal active-sterile admixture. © *2002 MAIK "Nauka/Interperiodica".*

1. INTRODUCTION

Super-Kamiokande high statistics data [1, 2] indicate that the observed deficit in μ-like atmospheric events is due to the neutrinos arriving at the detector at large zenith angles, strongly suggestive of the ν_μ oscillation hypothesis. Similarly, their data on the zenith-angle dependence and recoil-energy spectrum of solar neutrinos [3, 4] in combination with the results from Homestake [5], SAGE [6], and GALLEX + GNO [7, 8] and the recent SNO results [9] have put on a firm observational basis the long-standing problem of solar neutrinos, strongly indicating the need for ν_e conversions. In addition to this, there is also an indication for neutrino oscillations in the $\bar{\nu}_\mu \to \bar{\nu}_e$ channel provided by the LSND experiment [10].

Altogether, the solar and atmospheric neutrino anomalies constitute the only solid present-day evidence for physics beyond the Standard Model. It is clear that the minimum joint description of both anomalies requires neutrino conversions amongst all the three known neutrinos, since at least two mass-squared differences are needed to account simultaneously for the two phenomena. Furthermore, to accommodate also the result of the LSND experiment, another mass-squared difference is required, and the simplest case in which this condition is satisfied requires the existence of a fourth light neutrino, which must be sterile in order not to affect the invisible Z decay width precisely measured at LEP.

The purpose of this paper is to present a global and combined analysis of solar, atmospheric, and reactor neutrino data in the framework of both three- and four-neutrino oscillation schemes. We include in our analysis the most recent solar neutrino rates of Homestake [5], SAGE [6], and GALLEX and GNO [7, 8], as well as the latest 1258-d Super-Kamiokande data sample [4] and the recent results from the CC event rates at SNO [9]. Concerning atmospheric neutrinos, we consider all the contained events from Fréjus [11], IMB [12], Nusex [13], Kamiokande [14], Soudan-2 [15], and the latest 79.5-kt yr Super-Kamiokande data set [2], as well as the upward-going neutrino-induced muon fluxes from both Super-Kamiokande and the MACRO detector [16]. The constraints arising from the relevant reactor (mainly CHOOZ [17] and Bugey [18]) and accelerator (CDHSW [19] and CCFR [20]) experiments are also imposed.

The outline of the paper is the following. In Section 2, we fix our notation and summarize the most relevant properties of the neutrino oscillation probabilities that we use in the analysis of solar and atmospheric neutrino data. In Section 3, we describe our results for the case of three-family oscillations, while in Section 4 we present our analysis of the four-neutrino case. Finally, in Section 5, we summarize the work and present our conclusions.

2. DATA SAMPLES AND NEUTRINO OSCILLATION PROBABILITIES

In order to determine the values of neutrino masses and mixing for the oscillation solution of the solar

*This article was submitted by the author in English.

** e-mail: maltoni@hal.ific.uv.es

neutrino problem, we have used the data on the total event rates of the Chlorine [5] and Gallium [6–8] experiments, as well as the recent SNO result on the CC event rate [9]. For the Gallium experiments, we have used the weighted average of the results from GALLEX + GNO and SAGE detectors. We have also included the Super-Kamiokande recoil-electron energy spectrum measured separately during the day and night periods (corresponding to the 1258-d data sample), which will be referred to in the following as the day–night spectral data and contain 19 + 19 data bins. Thus, we have a total of 41 independent inputs. The analysis includes the latest standard solar model fluxes, the BP00 model [21], with updated distributions for neutrino production points and solar matter density; details of the statistical analysis applied to the different observables can be found in [22–24].

Concerning atmospheric neutrinos, for the four-neutrino case, we have used all the samples of Super-Kamiokande [2] data: e-like and μ-like samples of sub- and multi-GeV contained events data, each given as a five-bin zenith-angle distribution, and upgoing-muon data including the stopping (five bins in zenith angle) and through-going (ten angular bins) muon fluxes. We have also included the latest MACRO [16] upgoing muon samples, with ten angular bins, which is also sensitive to the active-sterile admixture. In addition to this, for the three-neutrino case, we have included in our analysis the results of the two water-Cerenkov experiments IMB [12] and Kamiokande [14] and of the three iron-calorimeter detectors Fréjus [11], Nusex [13], and Soudan-2 [15], as well as the result of the CHOOZ reactor experiment [17]. Thus, we have a total of 45 independent inputs for the 4-ν case and 65 for the 3-ν case (66 when CHOOZ is also included). For details on the statistical analysis applied to the different observables, we refer to [25, 26].

In general, the determination of the oscillation probabilities requires the solution of the Schrödinger evolution equation of the neutrino system in the Sun- and/or Earth-matter background:

$$i\frac{d\boldsymbol{\nu}}{dt} = H\boldsymbol{\nu}, \qquad H = UH_0^dU^\dagger + V, \tag{1}$$

where U is the unitary matrix connecting the flavor basis and the mass basis in vacuum, H_0^d is the vacuum Hamiltonian, and V describes forward interactions in matter. For a CP-conserving three-flavor scenario, we have

$$H_0^d = \frac{1}{2E_\nu}\mathrm{diag}(-\Delta m^2_{21}, 0, \Delta m^2_{32}), \tag{2}$$
$$U = U_{23}(\theta_{23})U_{13}(\theta_{13})U_{12}(\theta_{12}),$$
$$V = \pm\sqrt{2}G_\mathrm{F}\mathrm{diag}(N_e, 0, 0),$$
$$\boldsymbol{\nu} = (\nu_e, \nu_\mu, \nu_\tau).$$

In general, the three-neutrino transition probabilities depend on five parameters, namely, the two mass-squared differences Δm^2_{21}, Δm^2_{32} and the three mixing angles θ_{12}, θ_{13}, θ_{23}; however, in order to accommodate both solar and atmospheric neutrino data in a unified framework, an hierarchy between Δm^2_{21} and Δm^2_{32} is required:

$$(\Delta m^2_\odot = \Delta m^2_{21}) \ll (\Delta m^2_\mathrm{atm} = \Delta m^2_{32}). \tag{3}$$

Both for the solar and the atmospheric neutrino data analysis, we can take advantage of this hierarchy to reduce the number of parameters. In particular, for what concerns the solar case, we can set $\Delta m^2_{32} \to \infty$ and also disregard the atmospheric angle θ_{23}, since it never appears in the relevant transition probabilities. Conversely, for the atmospheric case, we can set $\Delta m^2_{21} \approx 0$ and in this limit the solar angle θ_{12} cancels out from the equations. So, in both cases, we are left with only three parameters, among which only the reactor angle θ_{13} is common to both problems.

Concerning the four-neutrino case, again we assume CP conservation and (2) is replaced by

$$H_0^d = \frac{1}{2E_\nu}\mathrm{diag}(-\Delta m^2_{21}, 0, \Delta m^2_{32}, \Delta m^2_{32} + \Delta m^2_{43}), \tag{4}$$
$$U = U_{24}(\theta_{24})U_{23}(\theta_{23})U_{14}(\theta_{14})U_{13}(\theta_{13})$$
$$\times U_{34}(\theta_{34})U_{12}(\theta_{12}),$$
$$V = \pm\sqrt{2}G_\mathrm{F}\mathrm{diag}\left(N_e, \frac{1}{2}N_n, 0, 0\right),$$
$$\boldsymbol{\nu} = (\nu_e, \nu_s, \nu_\mu, \nu_\tau).$$

There are six possible four-neutrino schemes that can accommodate the results from solar and atmospheric neutrino experiments as well as the LSND evidence. They can be divided in two classes: (3 + 1) and (2 + 2). In the (3 + 1) schemes, there is a group of three neutrino masses separated from an isolated one by a gap on the order of 1 eV^2, which is responsible for the short-baseline oscillations observed in the LSND experiment. In (2 + 2) schemes, there are two pairs of close masses separated by the LSND gap. Although still marginally allowed [27], the (3 + 1) schemes are now disfavored by the experimental data with respect to the (2 + 2) schemes [28, 29]; therefore, in the present work, we concentrate on the latter.

In general, the four-neutrino transition probabilities depend on nine parameters, but, as for the three-neutrino case, a mass hierarchy is required to reconcile the solar and atmospheric neutrino data with the LSND result:

$$(\Delta m^2_\odot = \Delta m^2_{21}) \ll (\Delta m^2_\mathrm{atm} = \Delta m^2_{43}) \tag{5}$$

$$\ll (\Delta m^2_{\rm LSND} = \Delta m^2_{32}).$$

Moreover, the negative results from the reactor experiments, and, in particular, the Bugey one [18], provide an upper bound on the projection of the ν_e over the 3–4 states, so that we can make the simplifying assumption $\theta_{13} = \theta_{14} = 0$. In addition to this, for what concerns the solar analysis, the atmospheric angle θ_{34} does not appear in the relevant probabilities, and we can safely set $\Delta m^2_{32} \approx \Delta m^2_{43} \to \infty$, so that the only mass scale involved in the problem is Δm^2_{21}. Moreover, the two angles θ_{23} and θ_{24} only contribute in the combination $c^2_{23}c^2_{24} = |U_{s1}|^2 + |U_{s2}|^2$, which gives the size of the projection of the sterile neutrino onto the state in which the solar ν_e oscillates [30], so in the end we are left with only three parameters.

Concerning the atmospheric analysis, we can set $\Delta m^2_{32} \to \infty$ and $\Delta m^2_{21} \approx 0$, in which case the solar angle θ_{12} also cancels out; the two angles θ_{23} and θ_{24} now contribute independently, so that we are left with four parameters. However, the quantity $s^2_{23} = |U_{\mu 1}|^2 + |U_{\mu 2}|^2$, which determines the size of the projection of the ν_μ over the "atmospheric" neutrino oscillating states, is bounded by the negative results of the ν_μ-disappearance experiments CDHSW [19] and CCFR [20] to be smaller than 0.2, and in order to determine the impact of such small but possible deviations from zero, we also study the "restricted" case $\theta_{23} = 0$, widely discussed in [31].

Note that, both in the three- and in the four-neutrino case, we can assume without loss of generality that all the mass-squared differences are positive and all the angles lie in the interval $[0, \pi/2]$, except for the θ_{34} angle [30] in the four-neutrino case, which spans the whole range $[-\pi/2, \pi/2]$.

3. RESULTS OF THE THREE-NEUTRINO ANALYSIS

Let us start our discussion from the analysis of the CHOOZ experiment. This experiment performed a search for disappearance of the $\bar{\nu}_e$ produced in a nuclear reactor, and since no evidence of such a disappearance was found, the net result is a bound on the mixing of ν_e with all the other neutrino species. Under the assumption $\Delta m^2_{21} \approx 0$, the only relevant parameters are θ_{13} and $\Delta m^2_{31} \approx \Delta m^2_{32}$, and in Fig. 1 we show the exclusion plot in this plane. From this figure, we see that the CHOOZ data strongly disfavor the region $0.044 \lesssim \tan^2\theta_{13} \lesssim 23$ if $\Delta m^2_{32} \gtrsim 10^{-3}$ eV^2; however, for smaller values of Δm^2_{32}, the corresponding bound on θ_{13} is much weaker. Therefore, an independent lower bound on Δm^2_{32} is required for the CHOOZ constraint on θ_{13} to be applicable.

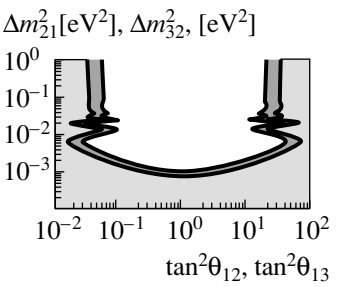

Fig. 1. Allowed region (90, 95, 99, 99.73% C.L. with 2 d.o.f.) in the $(\theta, \Delta m^2)$ plane from the nonobservation of $\bar{\nu}_e$ oscillations in the CHOOZ experiment. The same bound can be applied both to the solar parameters $(\theta_{12}, \Delta m^2_{21})$ and to the atmospheric parameters $(\theta_{13}, \Delta m^2_{32} \approx \Delta m^2_{31})$.

Such a lower bound is presently provided by the atmospheric data. In order to understand the relevance that different data sets have on the determination of the neutrino oscillation parameters, in Fig. 2 we display the 90, 95, 99, and 99.73% C.L. three-dimensional allowed regions for the combination of CHOOZ with the following atmospheric data sets:

CONT-BIN (40 points), including all the e-like and μ-like event rates from Fréjus, IMB, Nusex, Kamiokande sub-GeV, and Soudan-2 together with the e-like and μ-like angular spectrum (5 bins) of Kamiokande multi-GeV and Super-Kamiokande sub- and multi-GeV;

UP-μ (25 points), including upgoing-muon fluxes for stopping (five angular bins) and through-going (ten bins) muons at Super-Kamiokande and MACRO;

ALL-ATM (65 points), combining the two previous data sets and thus corresponding to the full sample of all atmospheric neutrino data.

Concerning contained events (CONT-BIN), we immediately see that the lower bound on Δm^2_{32} is rather weak, and values smaller than 10^{-3} eV^2 are still allowed. As a consequence, although the region $\Delta m^2_{32} > 10^{-3}$ eV^2 is ruled out as soon as θ_{13} deviates from zero, there is still a part of the parameter space which survives up to $\tan^2\theta_{13} \approx 0.52$ at 99% C.L. Therefore, the bound on θ_{13} for this data sample is not very strong.

This situation is completely reversed when considering upgoing-muon events (UP-μ). This combination is complementary to CONT-BIN, in the sense that the corresponding data sets are completely disjoint. Since the energy range covered by this sample is much higher than the CONT-BIN one and the neutrino transition probabilities only depend on the $\Delta m^2/E$ ratio, the UP-μ sample is more sensitive than CONT-BIN to large values of Δm^2_{23}, while it

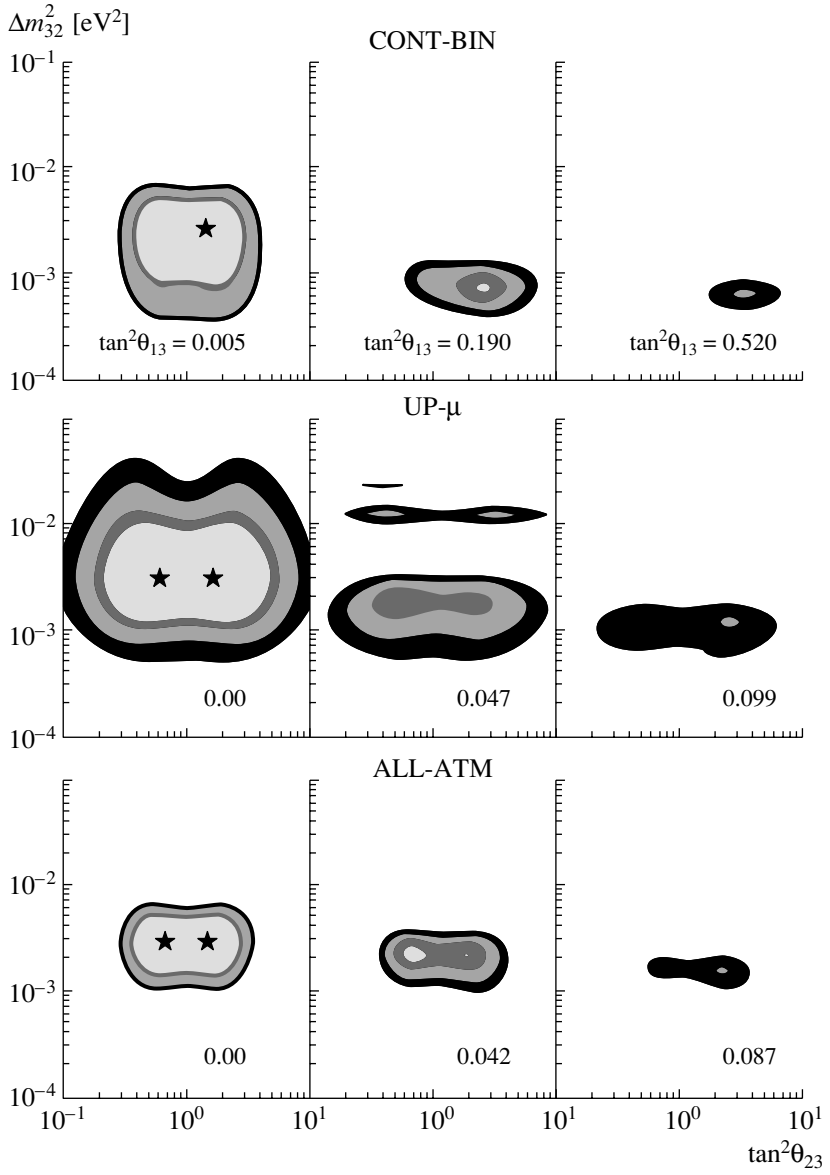

Fig. 2. Allowed regions (90, 95, 99, 99.73% C.L. with 3 d.o.f.) in the $(\theta_{23}, \Delta m^2_{32})$ plane for different values of θ_{13} and different combinations of atmospheric data. The CHOOZ experiment is also included in the analysis. The best fit point is represented by a star.

is less sensitive to small values. As a consequence, the mass region $\Delta m^2_{32} < 10^{-3}$ eV^2 is now disfavored and the allowed region lies in the mass range where the CHOOZ experiment should have observed oscillations for sizable θ_{13} values. This clearly implies a very strong bound on θ_{13}.

Due to the complementarity between the properties of the CONT-BIN and UP-μ combinations, merging them into a single data set (ALL-ATM) leads to much stronger constraints on the parameter space. Thanks to the large statistics provided by the Super-Kamiokande experiment, the parameter Δm^2_{32} is strongly bounded both from above and from below; moreover, no region of parameter space is allowed, even at 99% C.L., for values of $\tan^2\theta_{13}$ larger than $\sim$0.09, which can therefore be regarded as the strongest bound on θ_{13} from the combined analysis of atmospheric and reactor data. Note that the value $\theta_{13} = 0$ corresponds to pure $\nu_\mu \to \nu_\tau$ vacuum oscillations, so that the preference of the experimental data for small values of θ_{13} is a clear indication that electron neutrinos and matter effects do not play a relevant role in the atmospheric neutrino conversion mechanism.

The CHOOZ experiment also plays a very important role in the context of the solar data analysis.

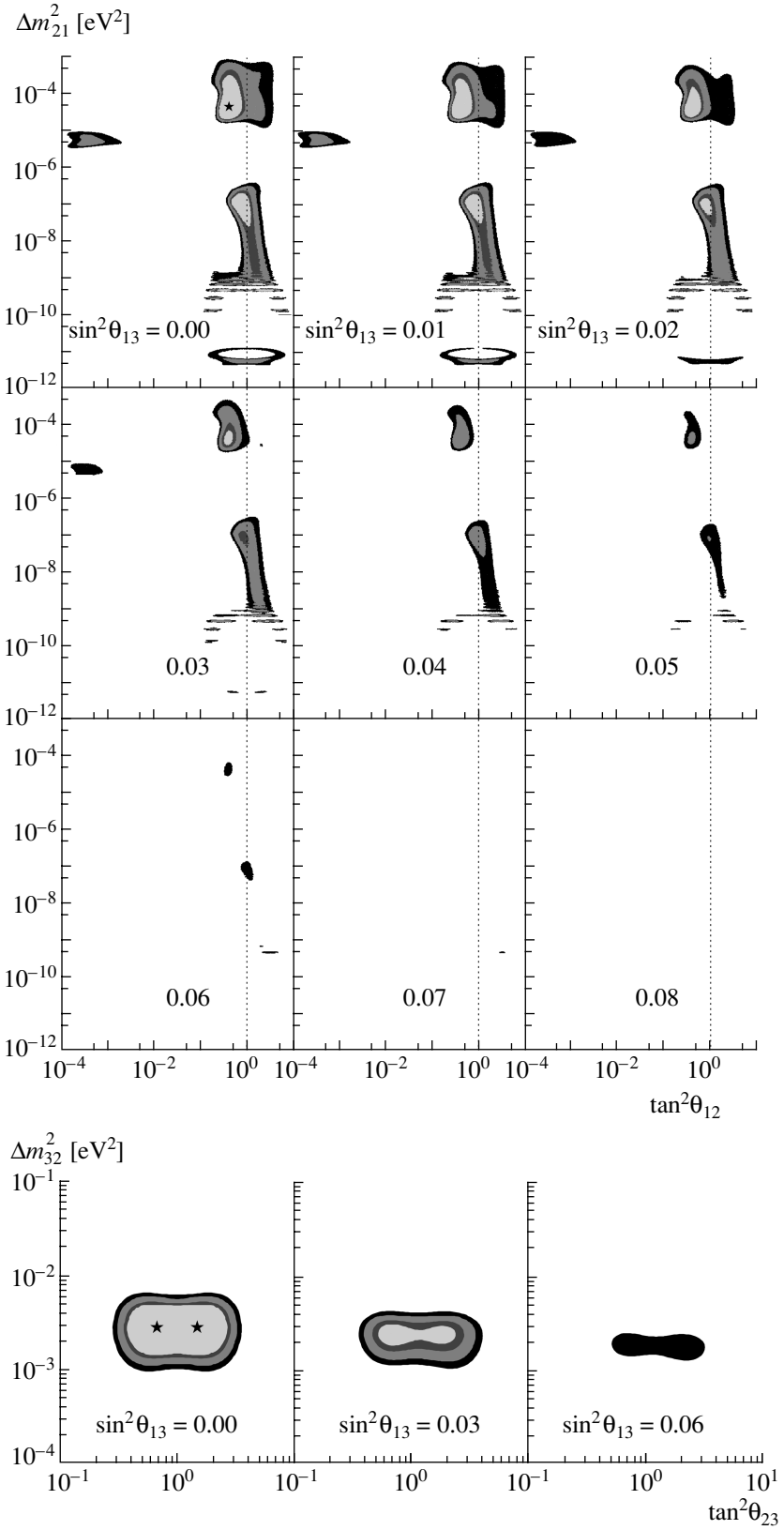

Fig. 3. Allowed regions (90, 95, 99, 99.73% C.L.) for the unified analysis of solar, atmospheric, and reactor data for different values of θ_{13}. Both the solar ($\theta_{12}, \Delta m^2_{21}$) and the atmospheric ($\theta_{23}, \Delta m^2_{32}$) planes are shown.

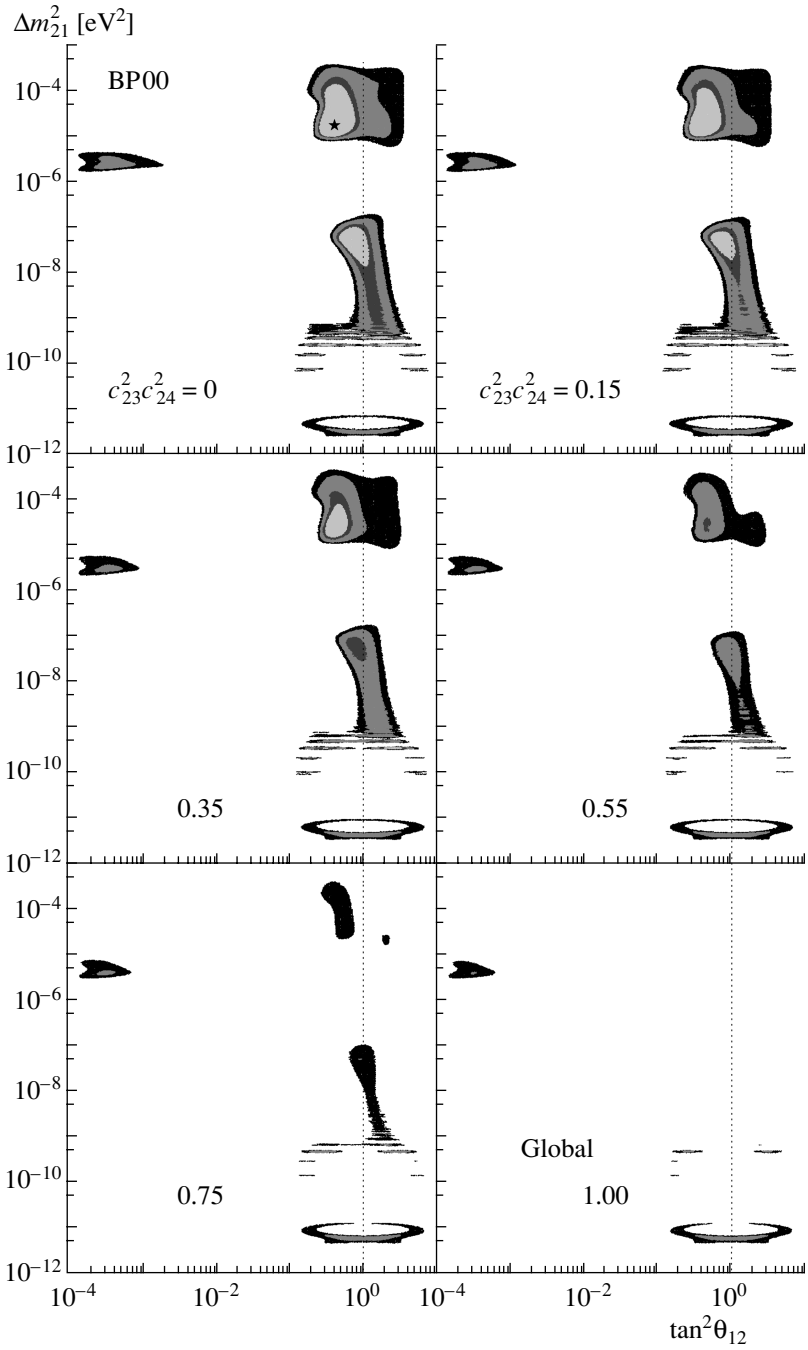

Fig. 4. Allowed regions (90, 95, 99, 99.73% C.L. with 3 d.o.f.) in the solar $(\theta_{12}, \Delta m^2_{21})$ plane for different values of the active-sterile admixture $|U_{s1}|^2 + |U_{s2}|^2 = c^2_{23}c^2_{24}$.

As we stated in the previous section, all our calculations are performed under the simplifying assumption $\Delta m^2_{21} \ll \Delta m^2_{32}$. However, the upper bound on Δm^2_{21} from the analysis of the solar data alone is rather poor in the LMA region, and values as large as 10^{-3} eV^2 are still allowed at 99% C.L. On the other hand, the solar LMA solution also requires an almost maximal mixing angle, namely, $\theta_{12} \approx 45^\circ$, and from Fig. 1—now interpreted in terms of the solar, rather than atmospheric, parameters—we see that the corresponding mass splitting Δm^2_{21} must be small. In this sense, the CHOOZ experiment prevents the solar and atmospheric mass splittings from being too close to each other, thus imposing a hierarchy and justifying a posteriori the simplifying assumption that we made in Section 2.

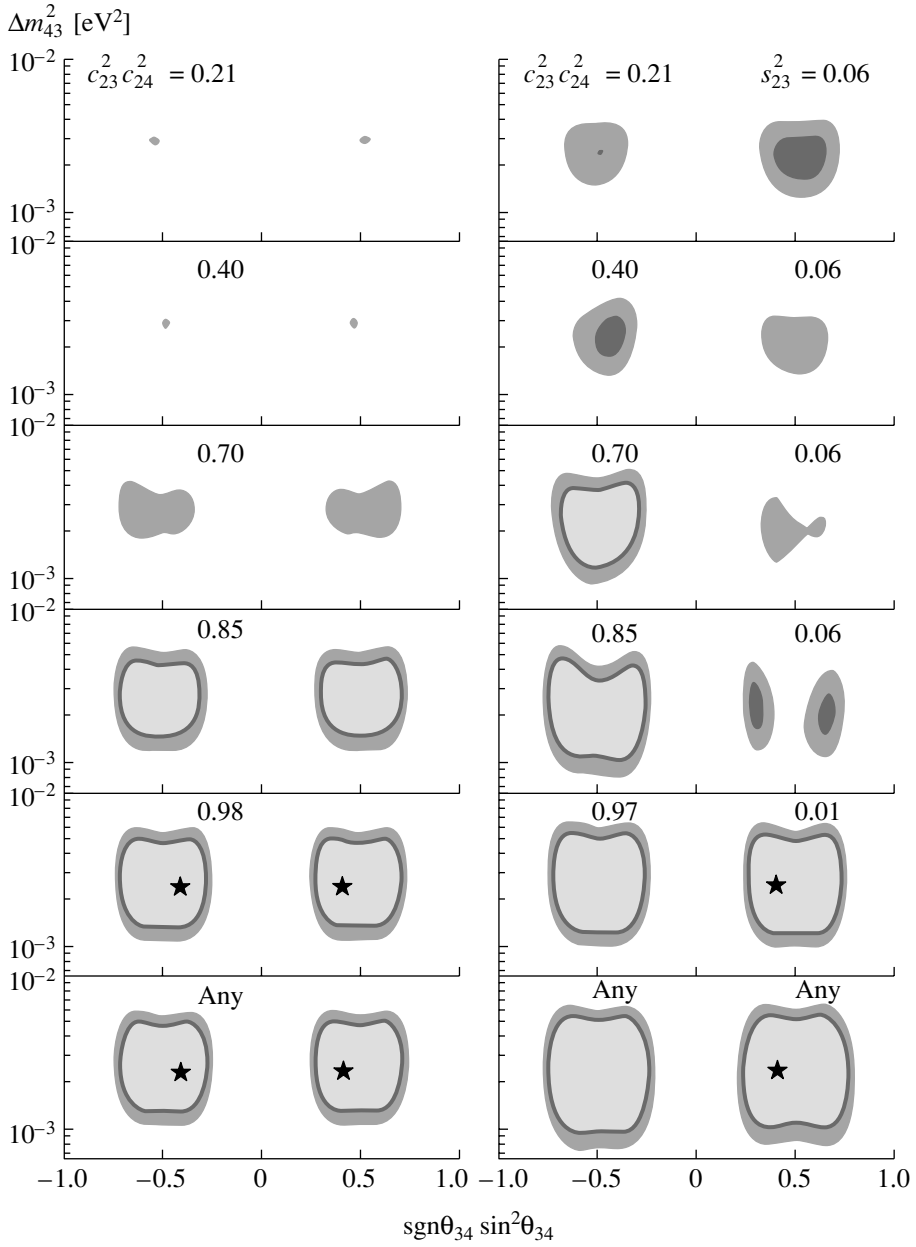

Fig. 5. Allowed regions (90, 95, 99% C.L. with 3 (left) and 4 (right) d.o.f.) in the atmospheric $(\theta_{34}, \Delta m^2_{43})$ plane for different values of the active-sterile admixture $|U_{s1}|^2 + |U_{s2}|^2 = c^2_{23}c^2_{24}$. The left panels correspond to the "restricted" case $|U_{\mu 1}|^2 + |U_{\mu 2}|^2 = s^2_{23} = 0$.

In Fig. 3, we present the allowed region from the unified analysis of solar, atmospheric, and reactor data. The upper bound on Δm^2_{21} follows from the inclusion of the CHOOZ result, as we just explained. The combination of the atmospheric and CHOOZ data is also responsible for the strong bound on θ_{13}, which is now slightly strengthened by the inclusion of solar data which also prefers small values of this angle; as a consequence, we have now $\sin^2\theta_{13} \lesssim 0.06$ at 99% C.L. In the solar plane, the best-fit point lies in the LMA region, although the LOW solution is also rather good. On the other hand, the recent result from the SNO experiment strongly disfavors the SMA solution, which is now excluded at more that 95% C.L.

4. RESULTS OF THE FOUR-NEUTRINO ANALYSIS

Let us now present our results for the four-neutrino case. Concerning the solar neutrino data, the parameter space for the global combination of

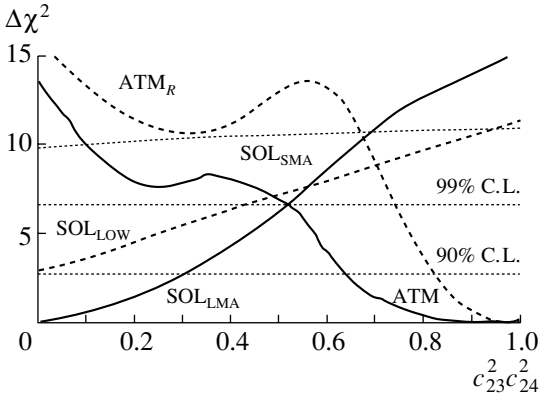

Fig. 6. $\Delta\chi^2$ as a function of the active-sterile admixture $|U_{s1}|^2 + |U_{s2}|^2 = c_{23}^2 c_{24}^2$ for the three solar solutions (LMA, SMA, and LOW) as well as the "unrestricted" and "restricted" atmospheric case (ATM and ATM$_R$).

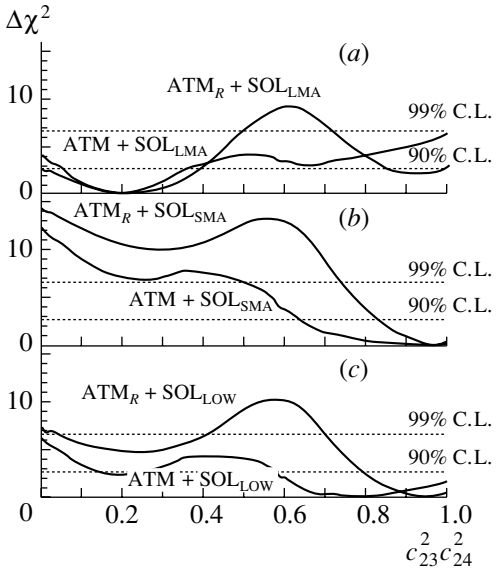

Fig. 7. $\Delta\chi^2$ as a function of the active-sterile admixture $|U_{s1}|^2 + |U_{s2}|^2 = c_{23}^2 c_{24}^2$ for the six different combinations of the solar (LMA, SMA, and LOW) solutions with the atmospheric (ATM and ATM$_R$) cases.

solar observables is three-dimensional, and in Fig. 4 we plot the sections of such a volume in the plane $(\theta_{12}, \Delta m_{21}^2)$ for different values of the active-sterile admixture $|U_{s1}|^2 + |U_{s2}|^2 = c_{23}^2 c_{24}^2$. The global minimum used in the construction of the regions lies in the LMA region and corresponds to pure ν_e-active oscillations. Note that, as discussed in the previous section, we have used the CHOOZ reactor bound [17] to cut off the allowed solutions for mass values above $(7{-}8) \times 10^{-4}$ eV^2. The SMA region appears to be strongly disfavored; however, it is still a valid solution for any value of $c_{23}^2 c_{24}^2$ at 99% C.L. On the other hand, the quality of the fit in the LMA and LOW region is pretty good; however, both these solutions only exist for small values of the active-sterile admixture and rapidly disappear when larger values are considered.

Concerning atmospheric neutrinos, the parameter space for the global combination of atmospheric observables is four-dimensional, and in Fig. 5 we plot the sections of such a volume in the plane $(\theta_{34}, \Delta m_{43}^2)$ for different values of the mixings θ_{23} and θ_{24}, which we parametrize by values of the projections $|U_{\mu 1}|^2 + |U_{\mu 2}|^2$ and $|U_{s1}|^2 + |U_{s2}|^2$. In order to determine the impact of the small but possible deviation from zero of s_{23}^2, we study both the "unrestricted" four-dimensional case (right panel) and "restricted" three-dimensional case of [31] (left panel) in which we impose $s_{23}^2 = |U_{\mu 1}|^2 + |U_{\mu 2}|^2 = 0$. In both cases, the parameter space is composed of two separated regions, each of them around maximal mixing $\theta_{34} = \pm\pi/4$, and the global minimum lies almost in the pure atmospheric $\nu_\mu \to \nu_\tau$ oscillations. The allowed regions become considerably smaller both for increasing values of the mixing angle θ_{23}, which determines the size of the projection of the ν_μ over the "atmospheric" neutrino oscillating states, and for increasing values of the mixing angle θ_{24}, which determines the active-sterile admixture in which the "almost-ν_μ" oscillates. Therefore, from the analysis of the atmospheric neutrino data, we obtain an upper bound on both mixings, which, in particular, implies a lower bound on the combination $c_{23}^2 c_{24}^2 = |U_{s1}|^2 + |U_{s2}|^2$ limited from above by the solar neutrino data.

From what we have seen so far, it is clear that both solar and atmospheric neutrino data strongly prefer oscillations into an active neutrino and disfavor oscillations into a sterile state. However, in the context of $(2+2)$ models, it is not possible to have pure active oscillations in both channels, so that a large component of sterile neutrinos should participate either in the solar or in the atmospheric neutrino conversion. There is therefore an incompatibility between the two data sets, and to better understand the nature of the problem, we show in Fig. 6 the $\Delta\chi^2$ quantity as a function of the active-sterile admixture $|U_{s1}|^2 + |U_{s2}|^2 = c_{23}^2 c_{24}^2$. It is straightforward to see that, from the analysis of solar data alone, we get the upper bound $c_{23}^2 c_{24}^2 \lesssim 0.52$ at 99% C.L., while the analysis of atmospheric data alone forces a lower limit to $c_{23}^2 c_{24}^2 \gtrsim 0.52$ at 99% C.L. These two bounds are clearly contradictory, so that there seems to be no way to reconcile solar and atmospheric data in the context of $(2+2)$ models. However, to decide whether such a scheme is now really ruled out or not, a joint analysis of the two data sets is needed.

The results of such an analysis are reported in Fig. 7 and in the table. Combining the three solar solutions with the two different atmospheric cases, we obtain six different combinations, and in the table we list the values of the $\chi^2_{\rm min}$ and its associated GOF for the best-fit point in the six-dimensional (five-dimensional for the "restricted" case) space for each of these cases, together with the best-fit value of the mixings $|U_{\mu 1}|^2 + |U_{\mu 2}|^2 = s^2_{23}$ and $|U_{s1}|^2 + |U_{s2}|^2 = c^2_{23}c^2_{24}$. In Fig. 7, we plot the shift in χ^2 from the corresponding global minimum in each of the scenarios as the mixing $|U_{s1}|^2 + |U_{s2}|^2 = c^2_{23}c^2_{24}$ varies. From the table and the figure, we find the following behaviors:

There are two favorite configurations, which we will denote as near-pure-sterile solar neutrino oscillations plus near-pure-active atmospheric neutrino oscillations (NPSS + NPAA), and close-to-active solar neutrino oscillations plus close-to-sterile atmospheric neutrino oscillations (CAS + CSA), respectively. NPSS + NPAA oscillations are characterized by the minima $|U_{s1}|^2 + |U_{s2}|^2 \sim 0.91$–$0.97$, where the exact position of the minimum depends on the allowed admixture $|U_{\mu 1}|^2 + |U_{\mu 2}|^2$. CAS + CSA oscillations are characterized by the minima $|U_{s1}|^2 + |U_{s2}|^2 \sim 0.18$–$0.2$. In both cases, and, in particular, for the CAS + CSA, the χ^2 function is rather flat around the minima.

In none of the cases is the maximal active-sterile (MAS) admixture $|U_{s1}|^2 + |U_{s2}|^2 = c^2_{23}c^2_{24} = 0.5$ favored.

The scenarios with the solar solution within the LMA region (Fig. 7*a*) prefer the CAS + CSA scenario, although the dependence of $\chi^2_{\rm atm+sol}$ with the active-sterile admixture is not very strong and it presents a secondary minimum near the complementary situation of close-to-sterile solar plus close-to-active atmospheric (CSS + CAA) scenario, which is acceptable at 90% C.L. They give the best fit to the combined analysis, with a GOF of 67% for the unrestricted case. The restricted case gives a worse fit but still with an acceptable GOF of 59%. In these scenarios, the MAS admixture is ruled out at 99% C.L. for the restricted case and it is acceptable at about 95% C.L. for the unrestricted one. This behavior arises from the fact that in these scenarios increasing the sterile admixture is strongly disfavored both in the solar and in the atmospheric case. It is precisely in this case that one would expect the combined solution to lie near MAS admixture. However, the results show that it is the solar dependence (which dominates in the combination) that leads to the slightly better description for the CAS + CSA scenario with a secondary minimum at the complementary CSS + CAA scenario.

$\chi^2_{\rm min}$ of the best-fit point and its associated GOF in the six-dimensional (five-dimensional for the "restricted" case) space in each of the cases discussed in the text, together with the best fit value of the mixings $s^2_{23} = |U_{\mu 1}|^2 + |U_{\mu 2}|^2$ and $c^2_{23}c^2_{24} = |U_{s1}|^2 + |U_{s2}|^2$

Scenario	d.o.f.	s^2_{23}	$c^2_{23}c^2_{24}$	$\chi^2_{\rm min}$	GOF, %
ATM + $\rm SOL_{LMA}$	86–6	0.065	0.21	73.8	67
$\rm ATM_R$+ $\rm SOL_{LMA}$	86–5	0	0.22	77.4	59
ATM + $\rm SOL_{SMA}$	86–6	0.030	0.91	75.4	62
$\rm ATM_R$+ $\rm SOL_{SMA}$	86–5	0	0.98	75.5	65
ATM + $\rm SOL_{LOW}$	86–6	0.030	0.78	74.5	65
$\rm ATM_R$+ $\rm SOL_{LOW}$	86–5	0	0.95	75.6	65

On the other hand, scenarios with the solar solution within the SMA region (Fig. 7*b*) prefer the NPSS + NPAA scenario. They give a worse fit to the combined analysis for the unrestricted case, with a GOF of 62% improving to 65% for the restricted case. In these scenarios, the dependence of χ^2 with the active-sterile admixture is more pronounced and it is dominated by the dependence of the atmospheric neutrino analysis, although there is a secondary minimum at the CAS + CSA configuration which for the unrestricted case is acceptable at 99% C.L. In all these scenarios, the MAS admixture is ruled out at more than 99% C.L. Qualitatively this behavior arises from the fact that, in these scenarios, increasing the sterile admixture in the atmospheric pair is strongly disfavored while it is still acceptable for the solar pair since the SMA solution is valid for pure $\nu_e \to \nu_s$ solar oscillations.

5. SUMMARY AND CONCLUSIONS

In this article, we have presented a global analysis of solar, atmospheric, and reactor neutrino data in terms of both three- and four-flavor oscillations.

Concerning the three-neutrino case, our results show that the most favorable scenario is the simplest two-neutrino mixing case $\nu_e \to \nu_a$ for solar neutrinos and the pure $\nu_\mu \to \nu_\tau$ vacuum oscillation hypothesis for the atmospheric case. However, from the analysis of solar and atmospheric data alone, it is not possible to derive a strong bound on θ_{13}, while the inclusion of the CHOOZ data drastically improves this limit. The Standard Model is now completely ruled out by the experimental data, while there is full agreement between solar, atmospheric, and reactor results in the context of three-neutrino oscillations.

Conversely, for the four-neutrino case in the framework of (2 + 2) schemes, there is a clear disagreement between solar and atmospheric data, since

both of them strongly disfavor oscillations into a sterile neutrino. However, a combined analysis show that the global fit is characterized by a GOF of 67%, a perfectly good value. The best-fit point lies in the LMA region and has $|U_{s1}|^2 + |U_{s2}|^2 \approx 0.2$, although there is another possible configuration, favored by the SMA solution, with $|U_{s1}|^2 + |U_{s2}|^2 \approx 1$. Finally, oscillations into a nearly maximal active-sterile admixture is always disfavored.

ACKNOWLEDGMENTS

I wish to thank my collaborators M.C. Gonzalez-Garcia, C. Peña-Garay, and J.W.F. Valle.

This work is supported by Spanish DGICYT under grant no. PB98-0693, by the European Commission RTN network HPRN-CT-2000-00148, by the European Science Foundation network grant no. 86, and by the European Union Marie Curie contract no. HPMF-CT-2000-01008.

REFERENCES

1. Y. Fukuda *et al.*, Phys. Lett. B **433**, 9 (1998); **436**, 33 (1998); **467**, 185 (1999); Phys. Rev. Lett. **82**, 2644 (1999).
2. T. Toshito, talk at *Moriond 2001, XXXVI Rencontres de Moriond on Electroweak Interactions and Unified Theories, Les Arcs, France, 2001*.
3. Super-Kamiokande Collab. (Y. Fukuda *et al.*), Phys. Rev. Lett. **81**, 1158 (1998); **81**, 4279 (1998); **82**, 1810 (1999); **82**, 2430 (1999); Y. Suzuki, Nucl. Phys. B (Proc. Suppl.) **77**, 35 (1999).
4. Super-Kamiokande Collab. (S. Fukuda *et al.*), hep-ex/0103032.
5. B. T. Cleveland *et al.*, Astrophys. J. **496**, 505 (1998); R. Davis, Prog. Part. Nucl. Phys. **32**, 13 (1994); K. Lande, in *Proceedings of ν-2000 XIX International Conference on Neutrino Physics and Astrophysics,* http://nu2000.sno.laurentian.ca.
6. SAGE Collab. (J. N. Abdurashitov *et al.*), Phys. Rev. C **60**, 055801 (1999); V. Gavrin, in *Proceedings of ν-2000 XIX International Conference on Neutrino Physics and Astrophysics,* http://nu2000.sno.laurentian.ca.
7. GALLEX Collab. (W. Hampel *et al.*), Phys. Lett. B **447**, 127 (1999).
8. E. Belotti, in *Proceedings of ν-2000 XIX International Conference on Neutrino Physics and Astrophysics,* http://nu2000.sno.laurentian.ca.
9. SNO Collab. (Q. R. Ahmad *et al.*), nucl-ex/0106015.
10. C. Athanassopoulos, Phys. Rev. Lett. **75**, 2650 (1995); **77**, 3082 (1996); **81**, 1774 (1998).
11. K. Daum *et al.*, Z. Phys. C **66**, 417 (1995).
12. R. Becker-Szendy *et al.*, Phys. Rev. D **46**, 3720 (1992).
13. M. Aglietta *et al.*, Europhys. Lett. **8**, 611 (1989).
14. H. S. Hirata *et al.*, Phys. Lett. B **280**, 146 (1992); Y. Fukuda *et al.*, Phys. Lett. B **335**, 237 (1994).
15. W. W. M. Allison *et al.*, Phys. Lett. B **449**, 137 (1999); A. Mann, in *Proceedings of ν-2000 XIX International Conference on Neutrino Physics and Astrophysics,* http://nu2000.sno.laurentian.ca.
16. MACRO Collab. (B. Barish *et al.*), in *Proceedings of ν-2000 XIX International Conference on Neutrino Physics and Astrophysics,* http://nu2000.sno.laurentian.ca.
17. CHOOZ Collab. (M. Apollonio *et al.*), Phys. Lett. B **466**, 415 (1999).
18. B. Achkar *et al.*, Nucl. Phys. B **434**, 503 (1995).
19. F. Dydak *et al.*, Phys. Lett. B **134B**, 281 (1984).
20. I. E. Stockdale *et al.*, Phys. Rev. Lett. **52**, 1384 (1984).
21. J. N. Bahcall, S. Basu, and M. H. Pinsonneault, astro-ph/0010346.
22. M. C. Gonzalez-Garcia, P. C. de Holanda, C. Peña-Garay, and J. W. F. Valle, Nucl. Phys. B **573**, 3 (2000).
23. M. C. Gonzalez-Garcia and C. Peña-Garay, Nucl. Phys. B (Proc. Suppl.) **91**, 80 (2000).
24. J. N. Bahcall, M. C. Gonzalez-Garcia, and C. Peña-Garay, hep-ph/0106258.
25. N. Fornengo, M. C. Gonzalez-Garcia, and J. W. F. Valle, Nucl. Phys. B **580**, 58 (2000); M. C. Gonzalez-Garcia, H. Nunokawa, O. L. Peres, and J. W. F. Valle, Nucl. Phys. B **543**, 3 (1999).
26. M. C. Gonzalez-Garcia, M. Maltoni, C. Peña-Garay, and J. W. F. Valle, Phys. Rev. D **63**, 033005 (2001); hep-ph/0009350, and references therein.
27. M. Maltoni, T. Schwetz, and J. W. F. Valle, Phys. Lett. B **518**, 252 (2001); hep-ph/0107150, and references therein.
28. S. M. Bilenky, C. Giunti, W. Grimus, and T. Schwetz, Phys. Rev. D **60**, 073007 (1999).
29. V. Barger, S. Pakvasa, T. J. Weiler, and K. Whisnant, Phys. Rev. D **58**, 093016 (1998).
30. M. C. Gonzalez-Garcia, M. Maltoni, and C. Peña-Garay, Phys. Rev. D **64**, 093001 (2001); hep-ph/0105269; hep-ph/0108073, and references therein.
31. G. L. Fogli, E. Lisi, and A. Marrone, Phys. Rev. D **63**, 053008 (2001); hep-ph/0105139.

Physics of Atomic Nuclei, Vol. 65, No. 12, 2002, pp. 2135–2146. From Yadernaya Fizika, Vol. 65, No. 12, 2002, pp. 2198–2209.

NEUTRINO PHYSICS AND ASTROPHYSICS

Neutrinoless Double-Beta Decay—Status of Evidence and Future*

H. V. Klapdor-Kleingrothaus[1)]

Max-Planck-Institut für Kernphysik, Heidelberg, Germany

Received February 13, 2002

Abstract—Double-beta decay is indispensable to solve the question of the neutrino mass matrix together with ν oscillation experiments. Recent analysis of the most sensitive experiment in the last eight years—the Heidelberg–Moscow experiment in Gran Sasso—yields evidence for the neutrinoless decay mode at a 97% C.L. This result is the first indication for lepton number violation and for the neutrino to be a Majorana particle. We give the present status of the analysis in these proceedings. It excludes several of the neutrino mass scenarios allowed from present neutrino oscillation experiments—essentially only degenerate and partially degenerate mass scenarios survive. To improve the present result, considerably enlarged experiments are required, such as GENIUS. A GENIUS Test Facility has just been funded and will come into operation by the end of 2002. © *2002 MAIK "Nauka/Interperiodica".*

1. INTRODUCTION

Recently atmospheric and solar neutrino oscillation experiments have shown that neutrinos are massive. This was the first indication of beyond Standard Model physics. The absolute neutrino mass scale was, however, still unknown, and only neutrino oscillations and neutrinoless double-beta decay together can solve this problem (see, e.g. [1–3]). Another question of fundamental importance is whether the neutrino is a Dirac or Majorana particle. Only double-beta decay can solve this problem. Finally double-beta decay has a unique sensitivity to probe lepton number conservation.

In this paper, we will discuss the status of double-beta-decay search. We shall, in Section 2, discuss the expectations for the observable of neutrinoless double-beta decay, the effective neutrino mass $\langle m_\nu \rangle$, from the most recent ν oscillation experiments. In Section 3, we shall discuss the recent evidence for the neutrinoless decay mode and discuss the consequences for the neutrino mass scenarios that could be realized in nature. In Section 4, we discuss the possible future potential of $0\nu\beta\beta$ experiments, which could improve the present accuracy.

2. ALLOWED RANGES OF $\langle m \rangle$ BY ν OSCILLATION EXPERIMENTS

The observable of double-beta decay

$$\langle m \rangle = \left| \sum U_{ei}^2 m_i \right|$$

$$= |m_{ee}^{(1)}| + e^{i\phi_2}|m_{ee}^{(2)}| + e^{i\phi_3}|m_{ee}^{(3)}|,$$

with U_{ei} denoting elements of the neutrino mixing matrix, m_i-neutrino mass eigenstates, and ϕ_i-relative Majorana CP phases, can be written in terms of oscillation parameters [1]

$$|m_{ee}^{(1)}| = |U_{e1}|^2 m_1, \quad (1)$$

$$|m_{ee}^{(2)}| = |U_{e2}|^2 \sqrt{\Delta m_{21}^2 + m_1^2}, \quad (2)$$

$$|m_{ee}^{(3)}| = |U_{e3}|^2 \sqrt{\Delta m_{32}^2 + \Delta m_{21}^2 + m_1^2}. \quad (3)$$

The effective mass $\langle m \rangle$ is related to the half-life for $0\nu\beta\beta$ decay via $(T_{1/2}^{0\nu})^{-1} \sim \langle m_\nu \rangle^2$.

Neutrino oscillation experiments fix or restrict some of the parameters in (1)–(3), e.g., in the case of normal hierarchy, solar neutrino experiments yield Δm_{21}^2, $|U_{e1}|^2 = \cos^2\theta_\odot$ and $|U_{e2}|^2 = \sin^2\theta_\odot$. Atmospheric neutrinos fix Δm_{32}^2, and experiments like Chooz, looking for ν_e disappearance, restrict $|U_{e3}|^2$. The phases ϕ_i and the mass of the lightest neutrino, m_1, are free parameters. Double-beta decay can fix the parameter m_1 and thus the absolute mass scale. The expectations for $\langle m \rangle$ from oscillation experiments in different neutrino mass scenarios have been carefully analyzed in [1, 2]. In Subsections 2.1 to 2.3, we give some examples.

2.1. Hierarchical Spectrum ($m_1 \ll m_2 \ll m_3$)

In hierarchical spectra (Fig. 1), motivated by analogies with the quark sector and the simplest seesaw models, the main contribution comes from m_2 or m_3. For the large mixing angle (LMA) MSW solution which is favored at present for the solar

*This article was submitted by the author in English.

[1)]Spokesman of Heidelberg–Moscow and GENIUS collaborations; E-mail: klapdor@mickey.mpi-hd.mpg.de; home page: http://www.mpi-hd.mpg.de.non_acc/

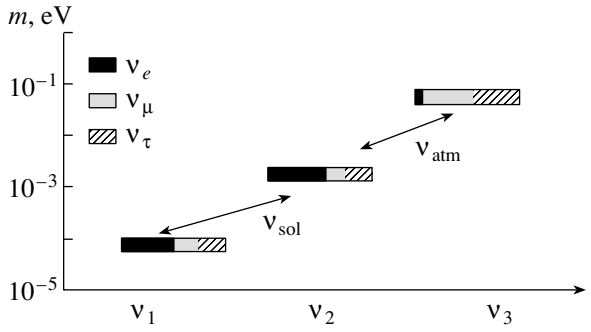

Fig. 1. Neutrino masses and mixings in the scheme with mass hierarchy. Bars correspond to flavor admixtures in the mass eigenstates ν_1, ν_2, ν_3. The quantity $\langle m \rangle$ is determined by the dark bars denoting the admixture of the electron neutrino U_{ei}.

neutrino problem (see [4]), the contribution of m_2 becomes dominant in the expression for $\langle m \rangle$, and

$$\langle m \rangle \simeq m_{ee}^{(2)} = \frac{\tan^2\theta}{1+\tan^2\theta}\sqrt{\Delta m^2_{\odot}}. \qquad (4)$$

In the region allowed at 90% C.L. by Super-Kamiokande according to [5], the prediction for $\langle m \rangle$ becomes

$$\langle m \rangle = (1\text{–}3) \times 10^{-3} \text{ eV}. \qquad (5)$$

The prediction extends to $\langle m \rangle = 10^{-2}$ eV in the 99% C.L. range (Fig. 2).

2.2. Inverse Hierarchy $(m_3 \approx m_2 \gg m_1)$

In inverse hierarchy scenarios (Fig. 3), the heaviest state with mass m_3 is mainly the electron neutrino, its mass being determined by atmospheric neutrinos, $m_3 \simeq \sqrt{\Delta m^2_{\text{atm}}}$. For the LMA MSW solution, one finds [1]

$$\langle m \rangle = (1\text{–}7) \times 10^{-2} \text{ eV}. \qquad (6)$$

2.3. Degenerate Spectrum $(m_1 \simeq m_2 \simeq m_3 \gtrsim 0.1\ eV)$

In degenerate scenarios (Fig. 3), the contribution of m_3 is strongly restricted by Chooz. The main contributions come from m_1 and m_2, depending on their admixture to the electron flavors, which is determined by the solar neutrino solution. We find [1]

$$m_{\min} < \langle m \rangle < m_1 \quad \text{with} \qquad (7)$$
$$\langle m_{\min} \rangle = (\cos^2\theta_{\odot} - \sin^2\theta_{\odot}) m_1.$$

This leads for the LMA solution to $\langle m \rangle = (0.25\text{–}1)m_1$, the allowed range including the uncertainty from the unknown Majorana CP phases.

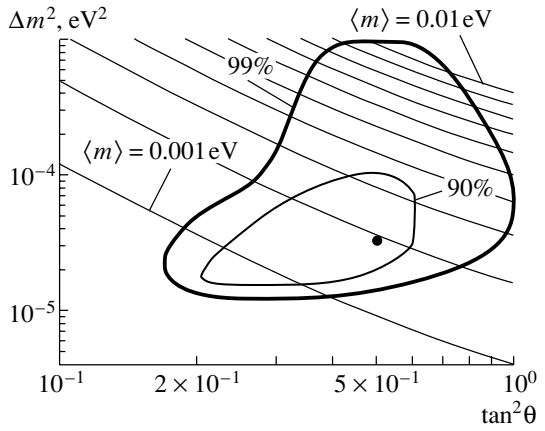

Fig. 2. Double-beta decay observable $\langle m \rangle$ and oscillation parameters in the case of the LMA MSW solution of the solar neutrino deficit, where the dominant contribution to $\langle m \rangle$ comes from the second state. Shown are lines of constant $\langle m \rangle$, the lowest line corresponding to $\langle m_\nu \rangle = 0.001$ eV, the upper line to 0.01 eV. The inner and outer closed lines show the regions allowed by present solar neutrino experiments with 90% C.L. and 99% C.L., respectively. Double-beta decay with sufficient sensitivity could check the LMA MSW solution. Complementary information could be obtained from the search for a day–night effect and spectral distortions in future solar neutrino experiments as well as a disappearance signal in KamLAND (from [1]).

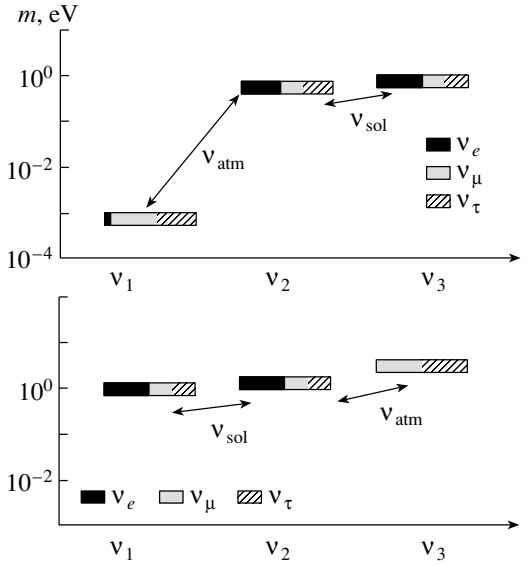

Fig. 3. Top: Neutrino masses and mixings in the inverse hierarchy scenario. Bottom: Neutrino masses and mixings in the degenerate scheme.

After these examples, we give a summary of our analysis [1, 2] of the $\langle m \rangle$ allowed by ν oscillation experiments for neutrino mass models in the presently favored scenarios in Fig. 4. The size of the bars in-

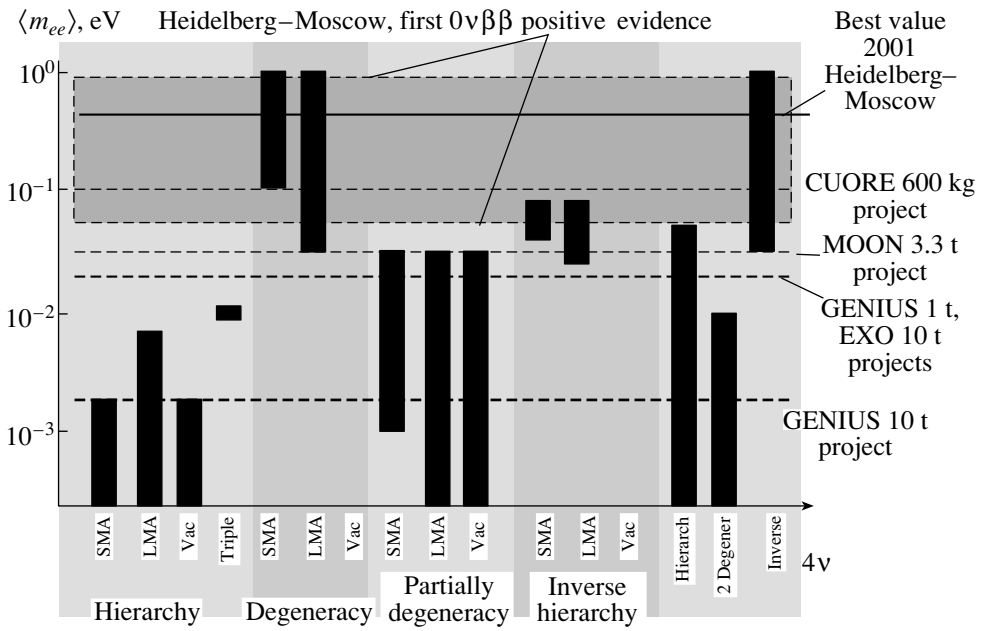

Fig. 4. The impact of the evidence obtained for neutrinoless double-beta decay [6] (best value of the effective neutrino mass $\langle m \rangle = 0.39$ eV, 95% C.L. range 0.05–0.84 eV—allowing already for an uncertainty of the nuclear matrix element of a factor of ±50%) on possible neutrino mass schemes. The bars denote allowed ranges of $\langle m \rangle$ in different neutrino mass scenarios, still allowed by neutrino oscillation experiments (see [1, 2]). Hierarchical models are excluded by the new $0\nu\beta\beta$ decay result. Also shown are the expected sensitivities for the future potential double-beta experiments CUORE, MOON, EXO, and the 1- and 10-t project of GENIUS [3, 7].

clude the uncertainty in mixing angles and the unknown Majorana CP phases.

3. EVIDENCE FOR THE NEUTRINOLESS DECAY MODE

The status of present double-beta experiments is shown in Fig. 5 and is extensively discussed in [3]. The Heidelberg–Moscow experiment [8] using the largest source strength of 11 kg of enriched ^{76}Ge in form of five HPGe detectors has been running since August 1990 in the Gran Sasso underground laboratory [3, 6, 9–11], and for a long time (eight years), it has been the most sensitive one. The prominent features of this experiment are as follows:

(i) Since the sensitivity for the $0\nu\beta\beta$ half-life is $T^{0\nu}_{1/2} \sim a\sqrt{Mt/\Delta EB}$, with a denoting the degree of enrichment, M the detector (source) mass, ΔE the energy resolution, B the background, and t the measuring time, the sensitivity of our 11-kg enriched ^{76}Ge experiment corresponds to that of an at least 1.2-t natural Ge experiment. After enrichment, energy resolution, background, source strength, and efficiency are the most important features of a $\beta\beta$ experiment.

(ii) The high-energy resolution of the Ge detectors of 0.2% assures that there is no background for a $0\nu\beta\beta$ line from the two-neutrino double-beta decay in this experiment, in contrast to most other present experimental approaches, where limited energy resolution is a severe drawback.

(iii) The efficiency of the Ge detectors for detection of $0\nu\beta\beta$ events is close to 100%.

(iv) The source strength in this experiment of 11 kg is the largest source strength ever operated in a double-beta-decay experiment.

(v) The background reached in this experiment is, with 0.17 event/(kg yr keV) in the $0\nu\beta\beta$ decay region (2000–2080 keV), the lowest limit ever obtained in such type of experiment.

(vi) The statistics collected in this experiment during 10 years of stable running is the largest ever collected in a double-beta-decay experiment.

We communicate here the status of the analysis of November 2001.

3.1. Data from the Heidelberg–Moscow Experiment

The data taken in the period of August 1990–May 2000 (54.9813 kg yr, or 723.44 mol yr) are shown in Fig. 6. Also shown in Fig. 6 are the data of single site events (SSE) taken in the period of November 1995–May 2000 with our methods of pulse shape analysis (PSA) [15–17]. We have analyzed [6] those data with various statistical methods, in particular,

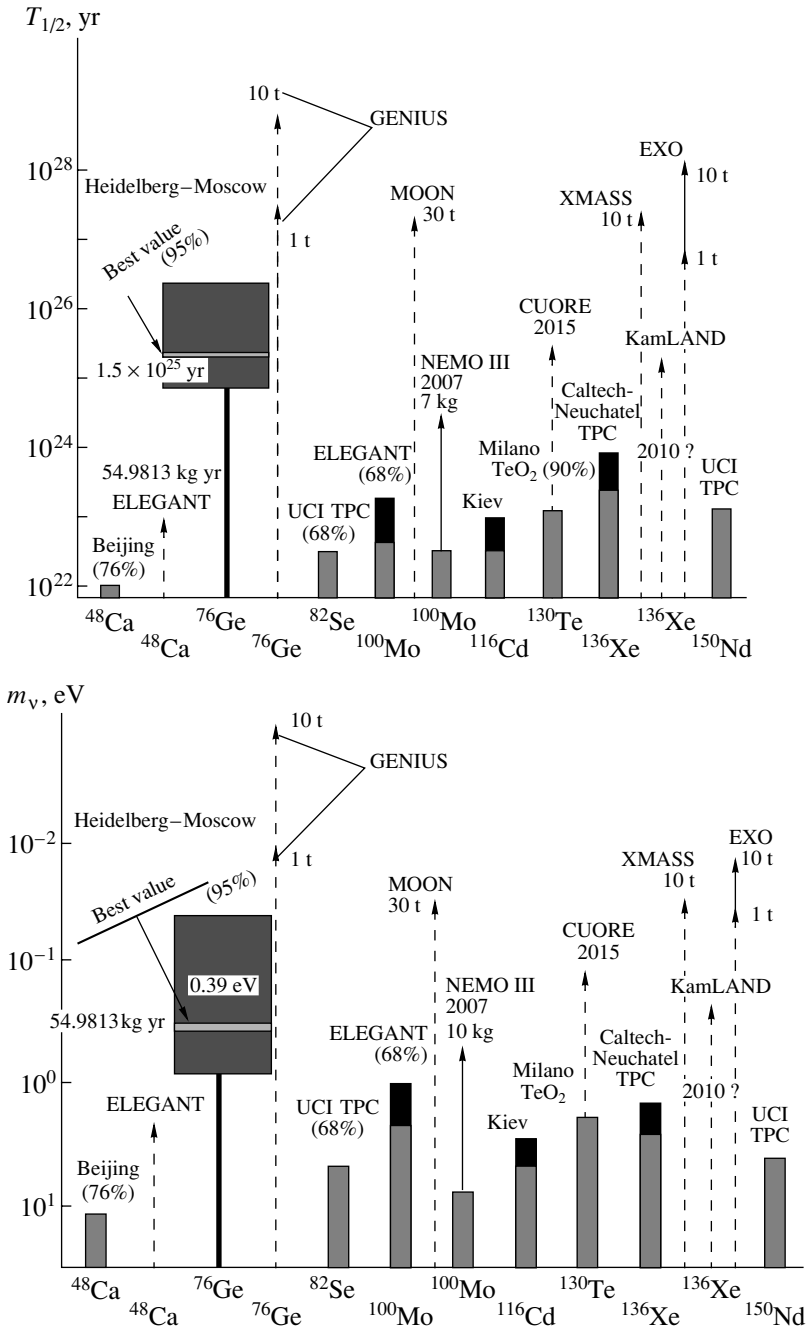

Fig. 5. Present sensitivity, and expectation for the future, of the most sensitive $\beta\beta$ experiments. Given are limits for the $0\nu\beta\beta$ half-life (upper) and $\langle m \rangle$ (lower), except for the Heidelberg–Moscow experiment, where the recently observed value [6] is given (95% C.L. range), and the best value. Light (dark) shaded bars correspond to present status (expectations) for running experiments; solid and dashed lines correspond to experiments under construction and proposed, respectively. For references see [3, 6, 12, 13].

also with the Bayesian method [18]. This method is particularly suited for low counting rates, where the data follow a Poisson distribution, that cannot be approximated by a Gaussian.

We have probably for the first time applied the Bayesian method to the analysis of double-beta decay. We have shown [19] that the method is clearly superior to other methods usually used, like maximum likelihood or χ^2 analysis, in the case of extremely low counting rates. We have proved this in thousands of computer-generated spectra, and, in particular, we can prove that we can indeed find a line with a content of five counts on a Poisson-distributed background level as we have in our experiment, with the given

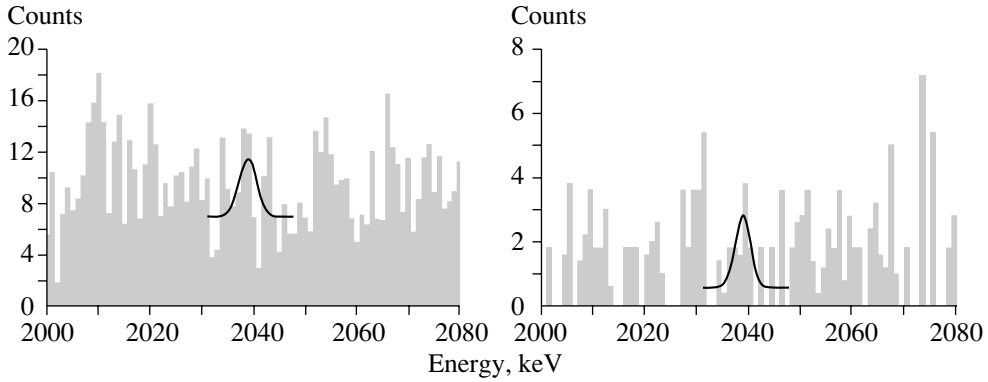

Fig. 6. Heidelberg–Moscow experiment. Left: Energy spectrum in the range between 2000 and 2080 keV, after 54.9813 kg yr. $Q_{\beta\beta} = 2039.006(50)$ keV according to [14]. Right: Spectrum of SSE after 28.053 kg yr. The accepted events have been identified as SSE events by all our three methods of pulse shape analysis [15, 16]. Shown are also the lines identified by the Bayesian method (see text).

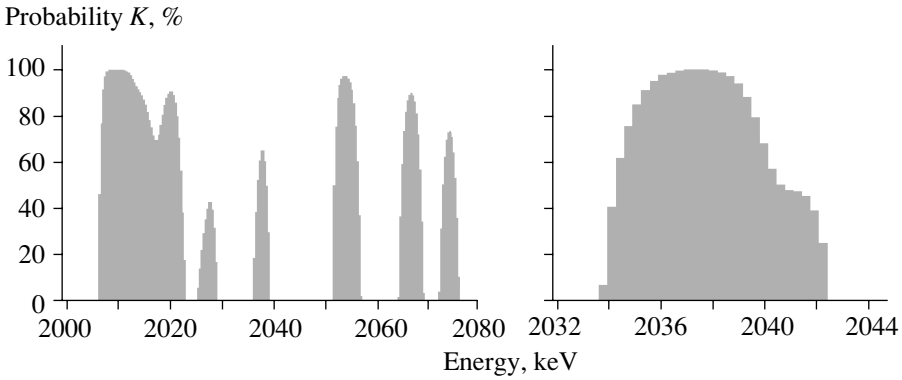

Fig. 7. Left: Probability K that a line exists at a given energy in the range of 2000–2080 keV derived via Bayesian inference from the spectrum shown in Fig. 6 (left part). Right: Result of a Bayesian scan for lines as in the left part of this figure, but in an energy range of $\pm 5\sigma$ around $Q_{\beta\beta}$.

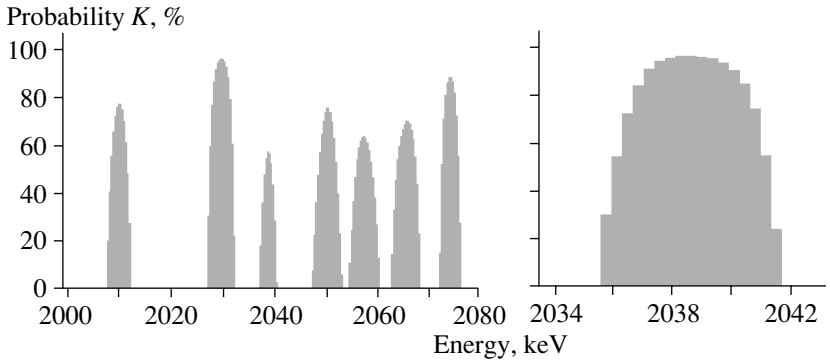

Fig. 8. Scan for lines in the SSE spectrum taken from 1995–2000 with detectors 2, 3, 5 (Fig. 6, right part), with the Bayesian method. Left: Energy range 2000–2080 keV. Right: Energy range of interest for double-beta decay.

confidence level. This is the case because we know the position of the line from the very precisely determined Q value of ^{76}Ge decay and because we know the shape of the line from background lines that we have at other energies in the spectrum.

Figures 7 and 8 show the results of the analysis of the data with the Bayesian method. Shown is the probability K of finding a (Gaussian) line with known standard deviation of $\sigma = 1.70$ (1.59) keV corresponding to 4.00 (3.74), for 3.74-keV FWHM, as a

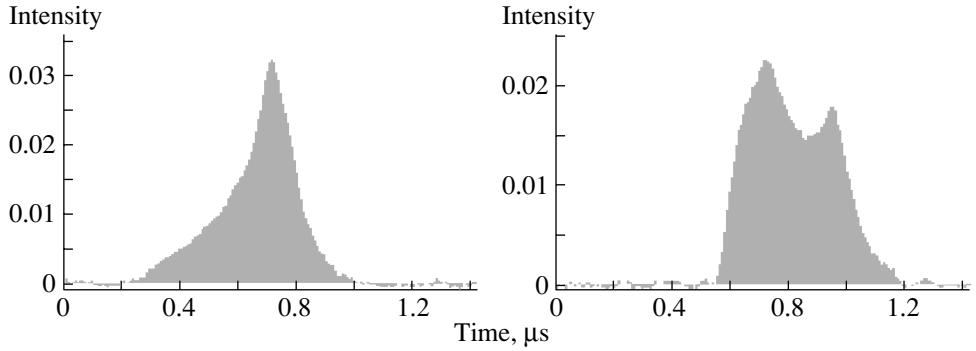

Fig. 9. Left: Shape of one candidate for $0\nu\beta\beta$ decay (energy 2038.61 keV) classified as SSE by all three methods of pulse shape discrimination. Right: Shape of one candidate (energy 2038.97 keV) classified as MSE by all three methods.

function of energy. This information was obtained by two-parametric Bayesian inference. We have asked for the intensity I of a line at a given energy E and for the background level. The background was assumed to be constant over the spectral range of 2000–2080 keV. For details of the procedure see [6]. The probability K is the ordinate in Figs. 7 and 8.

This procedure reproduces γ lines at the position of known weak lines from the decay of ^{214}Bi at 2010.7, 2016.7, 2021.8, and 2052.9 keV [20]. In addition, a line centered at 2039 keV shows up. This is compatible with the Q value [14, 21] of the double-beta-decay process. We emphasize that, at this energy, no γ line is expected according to Monte Carlo simulations of the experimental setup and to the compilations in [20]. The background on the left-hand side identified by the Bayesian method is too high, because the procedure averages the background over all the spectrum (including lines), except the line that it is trying to single out.

The right side of Fig. 7 shows the same as the left side, but in the spectral range of interest for double-beta decay. Here, the background is determined from a $\pm 5\sigma$ energy interval, around $Q_{\beta\beta}$, where no lines are expected. The Bayesian analysis of this energy range yields a confidence level (i.e., the probability K) for a line to exist at 2039.0 keV of 96.5% C.L. (2.1σ). We repeated the analysis for the same data, but without detector 4, which had no muon shield and a slightly worse energy resolution (46.502 kg yr). The result is similar to that given in Fig. 7; the probability that we find for a line at 2039.0 keV is 97.4% (2.2σ) [6]. We also applied the method recommended by the Particle Data Group [22]. This method (which does not use the information that the line is Gaussian) finds a line at 2039 keV at a confidence level of 3.1σ (99.8% C.L.).

The spectrum of single site events selects events confined to a few-millimeter region in the detector corresponding to the track length of the emitted electrons—such as double-beta events—and rejects multiple site events (MSE)—such as multiple Compton scattering events [15–17]. The expectation for a $0\nu\beta\beta$ signal would be a line of single site events on some background of multiple site events but also single site events, the latter coming, e.g., from the continuum of the 2614-keV γ line from ^{208}Tl (see, e.g., the simulation in [15]).

Installation of PSA was performed in 1995 for the four large detectors. Detector 5 has been running since February 1995, and detectors 2, 3, and 4 since November 1995 with PSA. The measuring time with PSA from November 1995 until May 2000 is 36.532 kg yr; for detectors 2, 3, and 5, it is 28.053 kg yr.

Figure 6 shows the SSE spectrum obtained under the restriction that the signal simultaneously fulfills the criteria of all three methods for a single site event. Figure 9 shows typical SSE and MSE from our spectrum.

Analysis with the Bayesian method of the range 2000–2080 keV again shows evidence for a line at the energy of 2039.0 keV (Fig. 8). In total, we find nine SSE in the region of 2034.1–2044.9 keV ($\pm 3\sigma$ around $Q_{\beta\beta}$). The analysis of the line before correction for the efficiency yields 4.6 events (best value) or 0.3–8.0 events within 95% C.L. Corrected for the efficiency to identify an SSE signal by successive application of all three PSA methods, which is 0.55 ± 0.10, we obtain a $0\nu\beta\beta$ signal with 92.4% C.L. The signal is 3.6–12.5 events with 68.3% C.L. (best value 8.3 events). The PDG method gives a signal at 2039.0 keV of 2.8σ (99.4% C.L.).

3.2. Half-Life and Effective Neutrino Mass

Under the assumption that the signal at $Q_{\beta\beta}$ is not produced by a background line of at present unknown origin, we can translate the observed number of events into half-lifes for neutrinoless double-beta decay. In Table 1, we give conservatively the

Table 1. Half-life for the neutrinoless decay mode and deduced effective neutrino mass from the Heidelberg–Moscow experiment [6]

Significance, kg yr	Detectors	$T^{0\nu}_{1/2}$, 10^{25} yr	$\langle m \rangle$, eV	C.L., %
54.9813	1, 2, 3, 4, 5	0.80–35.07	0.08–0.54	95
		1.04–3.46	0.26–0.47	68
		1.61	0.38	Best Value
46.502	1, 2, 3, 5	0.75–18.33	0.11–0.56	95
		0.98–3.05	0.28–0.49	68
		1.50	0.39	Best Value
28.053	2, 3, 5 SSE	0.88–22.38	0.10–0.51	90
		1.07–3.69	0.25–0.47	68
		1.61	0.38	Best Value

values obtained with the Bayesian method. Also given are the effective neutrino masses $\langle m_\nu \rangle$ deduced using matrix elements from [23]. We derive from the data taken with 46.502 kg yr the half-life $T^{0\nu}_{1/2} = (0.8–18.3) \times 10^{25}$ yr (95% C.L.). The analysis of the other data sets shown in Table 1, in particular, of the SSE data, confirms this result.

The result obtained is consistent with the limits given earlier by the Heidelberg–Moscow experiment [11]. It is also consistent with all other double-beta experiments which still reach less sensitivity. A second Ge experiment [24], which stopped operation in 1999 after reaching a significance of 9 kg yr, yields (if one believes their method of "visual inspection" in their data analysis) in a conservative analysis a limit of $T^{0\nu}_{1/2} > 0.55 \times 10^{25}$ yr (90% C.L.). The ^{128}Te geochemical experiment [25] yields $\langle m_\nu \rangle < 1.1$ eV (68% C.L.), the ^{130}Te cryogenic experiment [26] yields $\langle m_\nu \rangle < 1.8$ eV, and the $CdWO_4$ experiment [27] yields $\langle m_\nu \rangle < 2.6$ eV, all derived with the matrix elements of [23] to make the results comparable to the present value.

Concluding, we have obtained, with about 95% probability, the first evidence for the neutrinoless double-beta decay mode. As a consequence, with 95% C.L., lepton number is not conserved. Further, the neutrino is a Majorana particle. The effective mass $\langle m \rangle$ is deduced to be $\langle m \rangle = 0.11–0.56$ eV (95% C.L.), with the best value of 0.39 eV. Allowing conservatively for an uncertainty of the nuclear matrix elements of $\pm 50\%$ (for detailed discussions of the status of nuclear matrix elements, we refer to [3, 28, 29] and references therein), this range may widen to $\langle m \rangle = 0.05–0.84$ eV (95% C.L.). In this conclusion, it is assumed that contributions to $0\nu\beta\beta$ decay from processes other than the exchange of a Majorana neutrino (see, e.g., [3] and references therein) are negligible.

With the limit deduced for the effective neutrino mass, the Heidelberg–Moscow experiment excludes several of the neutrino mass scenarios allowed from present neutrino oscillation experiments (Fig. 4)—allowing mainly only for degenerate mass scenarios and an inverse hierarchy scenario. In particular, hierarchical mass schemes are already excluded at the present level of accuracy.

Assuming the degenerate scenarios to be realized in nature, we fix according to [1] the common mass eigenvalue of the degenerate neutrinos to $m = 0.05–3.4$ eV. Part of the upper range is already excluded by tritium experiments, which give a limit of $m < 2.2$ eV (95% C.L.) [30]. The full range can only partly (down to ~ 0.5 eV) be checked by future tritium decay experiments, but could be checked by some future $\beta\beta$ experiments (see, e.g., next section). The deduced 95% interval for the sum of the degenerate neutrino masses is consistent with the range for Ω_ν deduced from recent cosmic microwave background measurements and large-scale structure (redshift) surveys, which still allow for $\sum_i m_i \leq 4.4$ eV ($\Omega_\nu h^2 \leq 0.05$) [31, 32]. The range of $\langle m \rangle$ fixed in this work is, already now, in the range to be explored by the satellite experiments MAP and PLANCK [33, 34] (Fig. 10). The deduced best value for the mass lies in a range of interest for Z-burst models recently discussed as an explanation for superhigh-energy cosmic ray events beyond the GKZ cutoff [35].

The neutrino mass deduced may allow neutrinos to still play an important role as hot dark matter in the Universe.

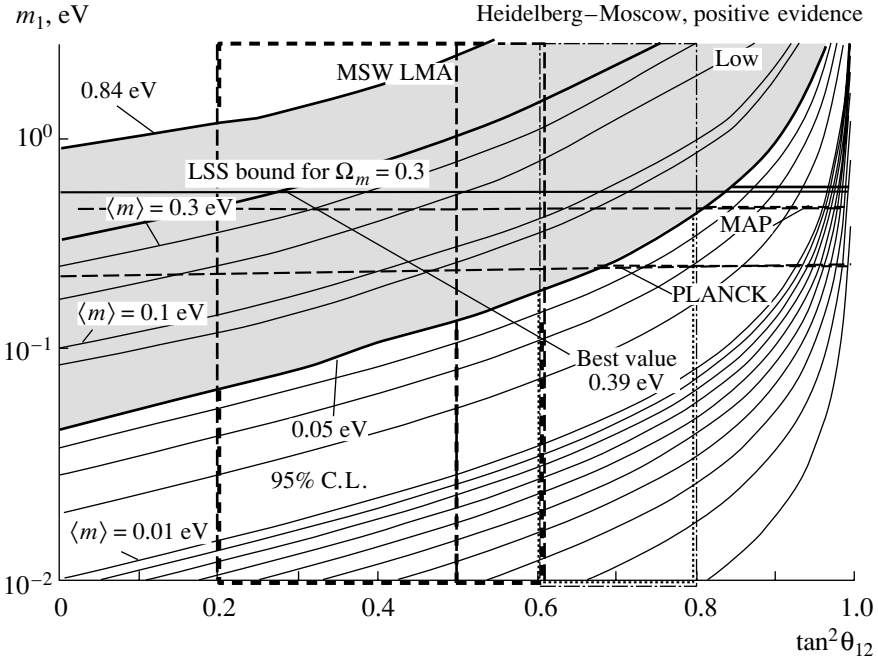

Fig. 10. Double-beta decay observable $\langle m \rangle$ and oscillation parameters: The case for degenerate neutrinos. Plotted on the axes are the overall scale of neutrino masses m_1 and mixing $\tan^2\theta_{12}$. Also shown is a cosmological bound deduced from a fit of CMB and large-scale structure [33] and the expected sensitivity of the satellite experiments MAP and PLANCK. The present limit from tritium β decay of 2.2 eV [30] would lie near the top of the figure. The range of $\langle m \rangle$ fixed by the Heidelberg–Moscow experiment [6] is already in the range to be explored by MAP and PLANCK [33].

4. FUTURE OF $\beta\beta$ EXPERIMENTS

To improve the present sensitivity for the effective neutrino mass considerably, as well as to fix this quantity more accurately, requires new experimental approaches, as discussed extensively in [3, 13, 36–39]. Some of them are indicated in Figs. 4 and 5. It has been discussed earlier [3, 13, 36, 38, 39] that, of present-generation experiments, probably none has a potential to probe $\langle m \rangle$ below (and probably even down to) the present Heidelberg–Moscow level (see Fig. 5).

The Milano cryogenic experiment using TeO_2 bolometers improved their values for the $\langle m \rangle$ from $\beta\beta$ decay of ^{130}Te from 5.3 eV in 1994 to 1.8 eV in 2000 [26]. NEMO III, originally aiming at a sensitivity of 0.1 eV, reduced their goals recently to 0.3–0.7 eV [40] (which is more consistent with estimates given by [41]), to be reached in 6 years from the start of running, foreseen for the year 2002. The problems there are the low efficiency of the detector of only 14%, which reduces their 7-kg ^{100}Mo experiment to a 1-kg experiment, and the weak energy resolution, which forces them to search for the $0\nu\beta\beta$ signal (with ^{100}Mo) in the wide energy range 2880–3200 keV [42].

4.1. GENIUS and Other Proposed Future Double-Beta Experiments

With the era of the Heidelberg–Moscow experiment, the time of the small smart experiments is over. To reach significantly larger sensitivity, $\beta\beta$ experiments have to become large. On the other hand, source strengths of up to 10 t of enriched material touch the world production limits. This means that the background has to be reduced by the order of a factor of 1000 or more compared to that of the Heidelberg–Moscow experiment.

Table 2 lists some key numbers for GENIUS [36, 37, 39], which was the first proposal for a third-generation double-beta experiment, and of some other proposals made after the GENIUS proposal. The potential of some of them is shown also in Fig. 4, and it is seen that not all of them may lead to large improvements in sensitivity. This is, in particular, the case for those which do not (cannot) fully eliminate materials near the detector, such as CUORE [49] and MAJORANA [58]. The first cannot do without copper around the bolometers for cooling purposes and thus has, with the complexity of cryogenic techniques, still to overcome serious problems of background entering interesting regions of $\langle m_\nu \rangle$. Also MAJORANA still has material close to the crystals. It is known, on the other hand, from the

Table 2. Some key numbers of future double-beta-decay experiments and of the Heidelberg–Moscow experiment

$\beta\beta$–Isotope	Name of experiment	Status	Mass, t	Assumed background, ∗—events/(kg yr keV), ∗∗—events/(kg yr FWHM), ∗∗∗—events/(yr FWHM)	Running time, t yr	Results limit for $0\nu\beta\beta$ half-life, yr	$\langle m_\nu \rangle$, eV
^{76}Ge	**Heidelberg–Moscow [6, 11, 48]**	**Running since 1990**	0.011 (enrich.)	0.06∗ 0.24∗∗ 2∗∗∗	**54.98 kg yr**	**$(0.8–18.3)\times10^{25}$ yr 95% C.L. NOW!!**	**(0.05–0.84)[a] 95% C.L. NOW!!**
^{100}Mo	NEMO III [40]	*Under constr. end 2001?*	∼0.01 (enrich.)	**0.0005**∗ 0.2∗∗ 2∗∗∗	50 kg yr	10^{24}	0.3–0.7
^{130}Te	CUORE[b] [49]	*Idea since 1998*	0.75 (nat.)	0.5∗ 4.5∗∗ 1000∗∗∗	5	9×10^{24}	0.2–0.5
^{130}Te	CUORE [49, 50]	*Idea since 1998*	0.75 (nat.)	0.005∗ 0.045∗∗ 45∗∗∗	5	9×10^{25}	0.07–0.2
^{100}Mo	MOON [51, 52]	*Idea since 1999*	10 (enrich.) 100 (nat.)	?	30 300	?	 0.03
^{116}Cd	CAMEOII CAMEOIII [53]	*Idea since 2000*	0.65 1 (enr.)	3.0∗∗∗ ?	5–8 5–8	10^{26} 10^{27}	0.06 0.02
^{136}Xe	EXO [54, 55]	Proposal since 1999	1 10	0.4∗∗∗ 0.6∗∗∗	5 10	8.3×10^{26} 1.3×10^{28}	0.05–0.14 0.01–0.04
^{76}Ge	**GENIUS-TF [56, 57]**	*Under constr. end 2001?*	11 kg (enrich.)	**6×10^{-3}** ∗	3	**1.6×10^{26}**	**0.15**
^{76}Ge	**GENIUS [36, 37]**	Proposal since 1997	1 (enrich.) 1	**0.04×10^{-3}**∗ **0.15×10^{-3}** ∗∗ ∗ **0.15** ∗∗∗ ∗ **1.5**	1 10	**5.8×10^{27}** **2×10^{28}**	**0.02–0.05** **0.01–0.028**
^{76}Ge	**GENIUS [36, 37]**	Proposal since 1997	10 (enrich.)	**0.15×10^{-3}** ∗∗ **0**[c]	10 10	**6×10^{28}** **5.7×10^{29}**	**0.006–0.016** **0.002–0.0056**

[a] With matrix element from [23, 43–46] (see Table II in [44]).

[b] Assuming the background of the present pilot project.

[c] This case shown to demonstrate the ultimate limit of such experiments. For details see [3].

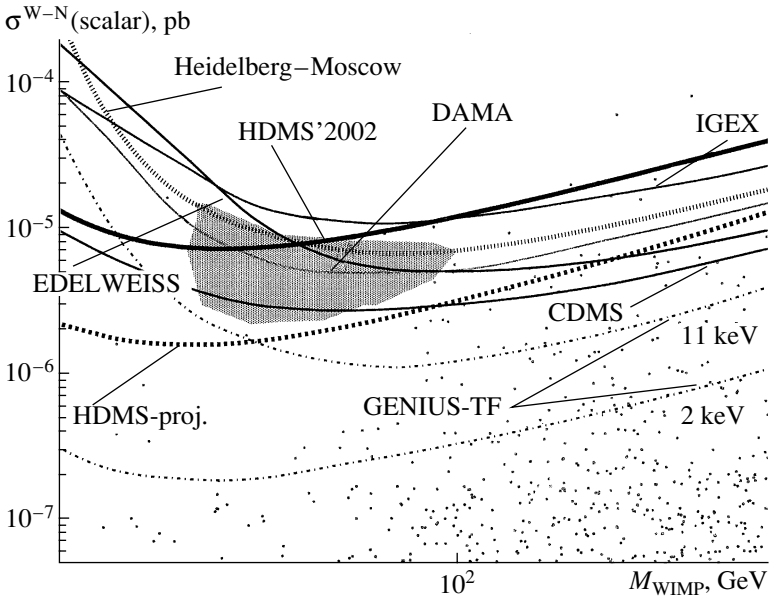

Fig. 11. The potential of GENIUS-TF for dark matter search. WIMP–nucleon cross-section limits as a function of the WIMP mass for spin-independent interactions. Shown are the current limits of the Heidelberg–Moscow experiment, the HDMS, the DAMA, and the CDMS experiments. Further, the expectation for HDMS and for GENIUS-TF with an energy threshold of 11 and 2 keV (no tritium contamination), respectively, and a background index of 2 events/(kg yr keV) below 50 keV. The filled contour represents the evidence region of the DAMA experiment.

Heidelberg–Moscow experiment, that the remaining background in this experiment is mainly coming from the materials around the detector. So, the MAJORANA project may not really have a striking new strategy for background reduction, particularly also after it was found that the projected segmentation of detectors may not work.

For recent information on the XMASS, EXO, and MOON experiments, we refer to the contributions of Y. Suzuki, G. Gratta, and H. Ejiri in [52]. The CAMEO project [53] in its now propagated variant GEM seems to be nothing more than a variant of GENIUS (see below) put into the BOREXINO tank at some later time. EXO [54] still needs extensive research and development to probe the applicability of the proposed detection method. In particular, if it were confirmed that tracks will be too short to be identified, it would act essentially only as a highly complicated calorimeter. In the GENIUS project, a reduction by a factor of more than 1000 down to a background level of 0.1 event/(t yr keV) in the range of $0\nu\beta\beta$ decay is planned to be reached by removing all material close to the detectors and by using naked Ge detectors in a large tank of liquid nitrogen. It has been shown that the detectors show excellent performance under such conditions [37, 59]. For technical questions and extensive Monte Carlo simulations of the GENIUS project for its application in double-beta decay, dark matter search, and solar neutrino search, we refer to [7, 12, 37, 39, 59, 60].

Table 3. Some of the new projects under discussion for future double-beta-decay experiments (see [3])

Name of experiment	Background reduction	Mass increase	Potential for dark matter	Potential for solar ν's
GENIUS	+	+	+	+*
CUORE	(+)	+	–	–
MOON	(+)	+	–	+
EXO	+	+	–	–
MAJORANA	–	+	–	–

* Real-time measurement of *pp* neutrinos with threshold of 20 keV (!!).

4.2. GENIUS and Other Physics beyond the Standard Model

GENIUS will allow, besides the large increase in sensitivity for double-beta decay described above, access to a broad range of other physics topics beyond SM in the multi-TeV range [3, 48, 61]. Even now, $\beta\beta$ decay probes the TeV scale on which new physics should manifest itself (see, e.g., [3, 36, 48, 61]). Based to a large extent on the theoretical work of the Heidelberg group in the last six years,

the Heidelberg–Moscow experiment has yielded results for SUSY models (R-parity breaking, neutrino mass), leptoquarks (leptoquark–Higgs coupling), compositeness, right-handed W mass, nonconservation of Lorentz invariance and equivalence principle, and mass of a heavy left- or right-handed neutrino, competitive to corresponding results from high-energy accelerators like TEVATRON and HERA.

4.3. GENIUS Test Facility

Construction of a test facility for GENIUS (GENIUS-TF) consisting of ~40 kg of HPGe detectors suspended in a liquid nitrogen box has been started. Up to summer of 2001, six detectors each of ~2.5 kg and with a threshold of as low as ~500 eV have been produced. Besides a test of various parameters of the GENIUS project, the test facility would allow [60], with the projected background of 2–4 events/(kg yr keV) in the low-energy range, probing the DAMA evidence for dark matter by the seasonal modulation signature (see Fig. 11 and [56, 57]).

5. CONCLUSION

The status of present double-beta-decay search has been discussed, and recent evidence for a nonvanishing Majorana neutrino mass obtained by the Heidelberg–Moscow experiment has been presented. Future projects to improve the present accuracy of the effective neutrino mass have been briefly discussed. The most sensitive of them (and perhaps at the same time the most realistic one) is the GENIUS project. GENIUS is the only one of the new projects (see also Table 3) that simultaneously has a huge potential for cold dark matter search and for real-time detection of low-energy neutrinos [13, 36, 39, 48, 52, 60, 62].

REFERENCES

1. H. V. Klapdor-Kleingrothaus, H. Päs, and A. Yu. Smirnov, Phys. Rev. D **63**, 073005 (2001); hep-ph/0003219; in *Proceedings of Third International Conference on Dark Matter in Astro- and Particle Physics "DARK'2000",* Ed. by H. V. Klapdor-Kleingrothaus (Springer-Verlag, Heidelberg, 2001), p. 420.
2. H. V. Klapdor-Kleingrothaus and U. Sarkar, Mod. Phys. Lett. A **16**, 2469 (2001); http://www.mpi-hd.mpg.de/non_acc/
3. H. V. Klapdor-Kleingrothaus, *60 Years of Double Beta Decay—From Nuclear Physics to Beyond the Standard Model* (World Sci., Singapore, 2001).
4. Y. Suzuki, Nucl. Phys. B (Proc. Suppl.) **91**, 29 (2001).
5. M. C. Gonzalez-Garcia *et al.*, hep-ph/0009350; Phys. Rev. D **63**, 033005 (2001).
6. H. V. Klapdor-Kleingrothaus, A. Dietz, H. L. Harney, and I. V. Krivosheina, Mod. Phys. Lett. A **16**, 2409 (2001); http://www.mpi-hd.mpg.de/non_acc/
7. H. V. Klapdor-Kleingrothaus, in *Proceedings of International Workshop on Neutrino Oscillations and Their Origin, NOON'2000, Tokyo, 2000* (World Sci., Singapore, 2001); hep-ph/0103074.
8. H. V. Klapdor, *Vorschlag eines Experiments,* Internal Report MPI-H-V17-1987, p. 18.
9. H. V. Klapdor-Kleingrothaus, in *Proceedings of the International Symposium on Advances in Nuclear Physics* (World Sci., Singapore, 2000), p. 123.
10. Heidelberg–Moscow Collab. (M. Günther *et al.*), Phys. Rev. D **55**, 54 (1997).
11. Heidelberg–Moscow Collab. (H. V. Klapdor-Kleingrothaus *et al.*), Eur. Phys. J. A **12**, 147 (2001); hep-ph/0103062; in *Proceedings of Third International Conference on Dark Matter in Astro- and Particle Physics "DARK'2000,"* Ed. by H. V. Klapdor-Kleingrothaus (Springer-Verlag, Heidelberg, 2001), p. 520.
12. H. V. Klapdor-Kleingrothaus, in *Proceedings of International Workshop on Low Energy Solar Neutrinos* (World Sci., Singapore, 2001); hep-ph/0104028.
13. H. V. Klapdor-Kleingrothaus, Part. Nucl. Lett., No. 1 [**104**], 20 (2001); hep-ph/0102319.
14. G. Douysset *et al.*, Phys. Rev. Lett. **86**, 4259 (2001).
15. J. Hellmig and H. V. Klapdor-Kleingrothaus, Nucl. Instrum. Methods Phys. Res. A **455**, 638 (2000).
16. B. Majorovits and H. V. Klapdor-Kleingrothaus, Eur. Phys. J. A **6**, 463 (1999).
17. J. Hellmig, F. Petry, and H. V. Klapdor-Kleingrothaus, Patent DE19721323A.
18. G. D'Agostini, hep-ex/0002055; W. von der Linden and V. Dose, Phys. Rev. E **59**, 6527 (1999); F. H. Fröhner, JEFF Report 18 NEA OECD (2000); Nucl. Sci. Eng. **126**, 1 (1997); K. Weise and W. Wöger, *Messungsicherheit und Messdatenauswertung* (Wiley-VCH, Weinheim, 1999); P. M. Lee, *Bayesian Statistics: An Introduction* (Arnold, London, 1997, 2nd ed.); A. O'Hagan, *Kendall's Advanced Theory of Statistics,* Vol. 2B: *Bayesian Inference* (Arnold, London, 1997).
19. H. V. Klapdor-Kleingrothaus and A. Dietz, in press.
20. R. B. Firestone and V. S. Shirley, *Table of Isotopes* (Wiley, New York, 1998, 8th ed.).
21. J. G. Hykawy *et al.*, Phys. Rev. Lett. **67**, 1708 (1991).
22. Particle Data Group (D. E. Groom *et al.*), Eur. Phys. J. C **15**, 1 (2000).
23. A. Staudt, K. Muto, and H. V. Klapdor-Kleingrothaus, Europhys. Lett. **13**, 31 (1990).
24. IGEX Collab. (C. E. Aalseth *et al.*), Yad. Fiz. **63**, 1299 (2000) [Phys. At. Nucl. **63**, 1225 (2000)].
25. T. Bernatowicz *et al.*, Phys. Rev. Lett. **69**, 2341 (1992); Phys. Rev. C **47**, 806 (1993).
26. A. Alessandrello *et al.*, Phys. Lett. B **486**, 13 (2000); S. Pirro *et al.*, Nucl. Instrum. Methods Phys. Res. A **444**, 71 (2000).
27. F. A. Danevich *et al.*, Phys. Rev. C **62**, 045501 (2000).

28. F. Simkovic *et al.*, Phys. Rev. C **64**, 035501 (2001).
29. S. Stoica and H. V. Klapdor-Kleingrothaus, Eur. Phys. J. A **9**, 345 (2000); Nucl. Phys. A **694**, 269 (2001); Phys. Rev. C **63**, 064304 (2001).
30. J. Bonn *et al.*, Nucl. Phys. B (Proc. Suppl.) **91**, 273 (2000).
31. M. Tegmark *et al.*, hep-ph/0008145.
32. X. Wang, M. Tegmark, and M. Zaldarriaga, astro-ph/0105091.
33. R. E. Lopez, astro-ph/9909414; J. R. Primack and M. A. K. Gross, astro-ph/0007165; J. R. Primack, astro-ph/0007187; J. Einasto, in *Proceedings of Third International Conference on Dark Matter in Astro- and Particle Physics "DARK'2000",* Ed. by H. V. Klapdor-Kleingrothaus (Springer-Verlag, Heidelberg, 2001).
34. H. V. Klapdor-Kleingrothaus, Prog. Part. Nucl. Phys. **48** (1) (2002).
35. T. J. Weiler, in *Proceedings of Beyond the Desert, 1999* (Institute of Physics, Bristol, 2000), p. 1085; H. Päs and T. J. Weiler, Phys. Rev. D **63**, 113015 (2001).
36. H. V. Klapdor-Kleingrothaus, in *Proceedings of First International Conference on Particle Physics Beyond the Standard Model, BEYOND'97, Castle Ringberg, Germany, 1997,* Ed. by H. V. Klapdor-Kleingrothaus and H. Päs (Institute of Physics, Bristol, 1998), p. 485.
37. H. V. Klapdor-Kleingrothaus *et al.*, MPI Report MPI-H-V26-1999; hep-ph/9910205; in *Proceedings of the 2nd International Conference on Particle Physics Beyond the Standard Model, BEYOND'99, Castle Ringberg, Germany, 1999,* Ed. by H. V. Klapdor-Kleingrothaus and I. V. Krivosheina (Institute of Physics, Bristol, 2000), p. 915.
38. H. V. Klapdor-Kleingrothaus, Nucl. Phys. B (Proc. Suppl.) **77**, 357 (1999).
39. H. V. Klapdor-Kleingrothaus, Nucl. Phys. B (Proc. Suppl.) **100**, 309 (2001).
40. NEMO Collab. (C. J. M. Longuemare *et al.*), Part. Nucl. Lett., No. 3 [**106**], 62 (2001); *Contributed Paper for XIX International Conference NEUTRINO 2000,* LAL 00-31 (2000), p. 1.
41. V. I. Tretyak and Yu. G. Zdesenko, At. Data Nucl. Data Tables **61**, 43 (1995).
42. NEMO Collab. (X. Sarazin *et al.*), *Talk given on ApPEC, Astroparticle Physics European Coordination, Paris, France, 2002.*
43. T. Tomoda, Rep. Prog. Phys. **54**, 53 (1991).
44. W. C. Haxton and G. J. Stephenson, Prog. Part. Nucl. Phys. **12**, 409 (1984).
45. X. R. Wu *et al.*, Phys. Lett. B **272**, 169 (1991).
46. X. R. Wu, A. Staudt, T. T. S. Kuo, and H. V. Klapdor-Kleingrothaus, Phys. Lett. B **276**, 274 (1992).
47. Heidelberg–Moscow Collab. (L. Baudis *et al.*), Phys. Rev. Lett. **83**, 41 (1999).
48. H. V. Klapdor-Kleingrothaus, Springer Tracts Mod. Phys. **163**, 69 (2000).
49. CUORE Collab. (A. Giuliani *et al.*), in *Proceedings of "Lepton–Baryon'98"* (Institute of Physics, Bristol, 1999), p. 302.
50. E. Fiorini, in *Proceedings of International Conference NEUTRINO 2000,* Nucl. Phys. B (Proc. Suppl.) **91**, 262 (2001).
51. H. Ejiri *et al.*, Phys. Rev. Lett. **85**, 2917 (2000); nucl-ex/9911008.
52. *Proceedings of International Workshop on Low Energy Solar Neutrinos* (World Sci., Singapore, 2001).
53. G. Bellini *et al.*, Phys. Lett. B **493**, 216 (2000).
54. M. Danilov *et al.*, Phys. Lett. B **480**, 12 (2000).
55. G. Gratta, in *Proceedings of International Workshop on Low Energy Solar Neutrinos* (World Sci., Singapore, 2001).
56. H. V. Klapdor-Kleingrothaus *et al.*, Internal Report MPI-H-V32-2000.
57. H. V. Klapdor-Kleingrothaus *et al.*, hep-ph/0103082.
58. L. De Braekeleer, *Talk at Workshop on the Next Generation US Underground Science Facility, WIPP, Carlsbad, N.M., USA, 2000.*
59. H. V. Klapdor-Kleingrothaus, J. Hellmig, and M. Hirsch, J. Phys. G **24**, 483 (1998).
60. I. V. Krivosheina, Yad. Fiz. **65** (12), 2228 (2002) [Phys. At. Nucl. **65**, 2165 (2002)].
61. H. V. Klapdor-Kleingrothaus, in *Proceedings of International Symposium on Lepton and Baryon Number Violation* (Institute of Physics, Bristol, 1999), p. 251; hep-ex/9901021.
62. V. A. Bednyakov and H. V. Klapdor-Kleingrothaus, Phys. Rev. D **63**, 095005 (2001).

Physics of Atomic Nuclei, Vol. 65, No. 12, 2002, pp. 2147–2155. From Yadernaya Fizika, Vol. 65, No. 12, 2002, pp. 2210–2218.

NEUTRINO PHYSICS AND ASTROPHYSICS

Measurement of the Rate of $\nu_e + d \to p + p + e^-$ Interactions Produced by ^{8}B Solar Neutrinos at the Sudbury Neutrino Observatory*

J. Farine**
(for the SNO Collaboration)
Carleton University, Ottawa, Canada
Received April 17, 2002

Abstract—Solar neutrinos from the decay of ^{8}B have been detected at the Sudbury Neutrino Observatory (SNO) via the charged current (CC) reaction on deuterium and by the elastic scattering (ES) of electrons. The CC reaction is sensitive exclusively to ν_e, while the ES reaction also has a small sensitivity to ν_μ and ν_τ. The flux of ν_e from ^{8}B decay measured by the CC reaction rate is $\phi^{\mathrm{CC}}(\nu_e) = [1.75 \pm 0.07\ (\mathrm{stat.})^{+0.12}_{-0.11}\ (\mathrm{syst.}) \pm 0.05\ (\mathrm{theor.})] \times 10^6\ \mathrm{cm}^{-2}\ \mathrm{s}^{-1}$. Assuming no flavor transformation, the flux inferred from the ES reaction rate is $\phi^{\mathrm{ES}}(\nu_x) = [2.39 \pm 0.34\ (\mathrm{stat.})^{+0.16}_{-0.14}\ (\mathrm{syst.})] \times 10^6\ \mathrm{cm}^{-2}\ \mathrm{s}^{-1}$. Comparison of $\phi^{\mathrm{CC}}(\nu_e)$ to the Super-Kamiokande collaboration's precision value of $\phi^{\mathrm{ES}}(\nu_x)$ yields a 3.3σ difference, assuming the systematic uncertainties are normally distributed, providing evidence that there is a nonelectron flavor active neutrino component in the solar flux. The total flux of active ^{8}B neutrinos is thus determined to be $(5.44 \pm 0.99) \times 10^6\ \mathrm{cm}^{-2}\ \mathrm{s}^{-1}$, in close agreement with the predictions of solar models.

Solar-neutrino experiments over the past 30 years [1–6] have measured fewer neutrinos than are predicted by models of the Sun [7, 8]. One explanation for the deficit is the transformation of the Sun's electron-type neutrinos into other active flavors. The Sudbury Neutrino Observatory (SNO) measures the ^{8}B solar neutrinos through the reactions

$$\nu_e + d \to p + p + e^- \,(\mathrm{CC}),$$
$$\nu_x + d \to p + n + \nu_x \,(\mathrm{NC}),$$
$$\nu_x + e^- \to \nu_x + e^- \,(\mathrm{ES}).$$

The charged current reaction (CC) is sensitive exclusively to electron-type neutrinos, while the neutral current (NC) is sensitive to all active neutrino flavors ($x = e, \mu, \tau$). The elastic scattering (ES) reaction is sensitive to all flavors as well, but with reduced sensitivity to ν_μ and ν_τ. By itself, the ES reaction cannot provide a measure of the total ^{8}B flux or its flavor content. Comparison of the ^{8}B flux deduced from the ES reaction assuming no neutrino oscillations ($\phi^{\mathrm{ES}}(\nu_x)$) to that measured by the CC reaction ($\phi^{\mathrm{CC}}(\nu_e)$) can provide clear evidence of flavor transformation without reference to solar model flux calculations. If neutrinos from the Sun change into other active flavors, then $\phi^{\mathrm{CC}}(\nu_e) < \phi^{\mathrm{ES}}(\nu_x)$.

The first results from SNO on the ES and CC reactions are presented. SNO's measurement of $\phi^{\mathrm{ES}}(\nu_x)$ is consistent with previous measurements described in [5]. The measurement of $\phi^{\mathrm{CC}}(\nu_e)$, however, is significantly smaller and is therefore inconsistent with the null hypothesis that all observed solar neutrinos are ν_e. A measurement using the NC reaction, which has equal sensitivity to all neutrino flavors, will be reported in a future publication.

SNO [9] is an imaging water Cerenkov detector located at a depth of 6010 mwe in the INCO, Ltd. Creighton mine near Sudbury, Ontario. It features 1000 metric tons of ultrapure D_2O contained in a 12-m-diameter spherical acrylic vessel. This sphere is surrounded by a shield of ultrapure H_2O contained in a 34-m-high barrel-shaped cavity of maximum diameter equal to 22 m. A stainless steel structure 17.8 m in diameter supports 9456 20-cm photomultiplier tubes (PMTs) with light concentrators. Approximately 55% of the light produced within 7 m of the center of the detector will strike a PMT.

The data reported here were recorded between November 2, 1999, and January 15, 2001, and correspond to a live time of 240.95 d. Events are defined by a multiplicity trigger of 18 or more PMTs exceeding a threshold of ~ 0.25 photoelectrons within a time window of 93 ns. The trigger reaches 100% efficiency at 23 PMTs. The total instantaneous trigger rate is 15–18 Hz, of which 6–8 Hz is the data trigger. For

*This article was submitted by the author in English.
**e-mail: farine@surf.sno.laurentian.ca

Table 1. Calibration devices for the SNO detector and their principal uses

Calibration	Device
Electronics: Time slope (ns/count); Time pedestal; Charge slope (pC/count); Charge pedestal	Electronic pulsers
Optics: Common time reference; D_2O attenuation and scattering; Acrylic attenuation and scattering; H_2O attenuation and scattering; Reflection and scattering from structures; Single photoelectron (pe) response; Relative single pe efficiency; Multiple pe response; Walk (time vs. pulse amplitude)	Laser ball: Pulsed laser ~2 ns (337, 365, 386, 420, 500, and 620 nm)
Energy: Gamma energy response; Electron energy response; Neutron-capture efficiency; Angular response	Radioactive sources: ^{16}N; ^{3}H(p,γ)^{3}He accelerator source; ^{252}Cf; ^{8}Li; Th; U
Low-energy backgrounds:	Encapsulated Th and U sources

every event trigger, the time and charge responses of each participating PMT are recorded.

The data were partitioned into two sets, with approximately 70% used to establish the data analysis procedures and 30% reserved for a blind test of statistical bias in the analysis. The analysis procedures were frozen before the blind data set was analyzed, and no statistically significant differences in the data sets were found. We present here the analysis of the combined data sets.

The sources deployed for the calibration of the SNO detector are listed in Table 1. A manipulator device allows movement of these sources in a large fraction of the AV volume. The laser ball is a diffuser mounted at the end of a fiber-optic cable from a nitrogen or dye laser. The laser provides light pulses of 600 ps at a rate up to 45 Hz. Used directly or as a pump to other dye lasers, it covers the wavelength range 337–620 nm. The light pulse at the diffuser is about 2 ns FWHM.

Table 2. Data reduction steps

Analysis step	Number of events
Total event triggers	355 320 964
Neutrino data triggers	143 756 178
$N_{\mathrm{hit}} \geq 30$	6 372 899
Instrumental background cuts	1 842 491
Muon followers	1 809 979
High level cuts*	923 717
Fiducial volume cut	17 884
Threshold cut	1169
Total events	1169

* Reconstruction figures of merit, prompt light, and $\langle\theta_{ij}\rangle$.

The ^{16}N source provides essentially monoenergetic electrons. ^{16}N is a β-delayed γ emitter with a branching ratio of 66% and a predominant γ energy of 6.131 MeV. The β particle is tagged by a scintillator. The source can provide an event rate of 50 Hz. The 7.13-s half-life ^{16}N is produced by exposing gaseous CO_2 to a d–t neutron generator located 50 m from the cavity. The gas is quickly transferred in a capillary tube to a decay chamber attached to the manipulator in the heavy water.

Calibration of the PMT time and charge pedestals, slopes, offsets, charge vs. time dependences, and second-order rate dependences are performed using electronic pulsers and pulsed light sources.

Figure 1 illustrates data obtained from calibration sources. For every source, the data is plotted using symbols and the corresponding Monte Carlo predictions using a histogram, except for the CC reaction Monte Carlo prediction, which is represented by stars. The normalized distributions are plotted as a function of the number of hit PMTs. The absolute energy scale and uncertainties are established with the triggered ^{16}N source (circles) deployed over two planar grids within the D_2O and a linear grid in the

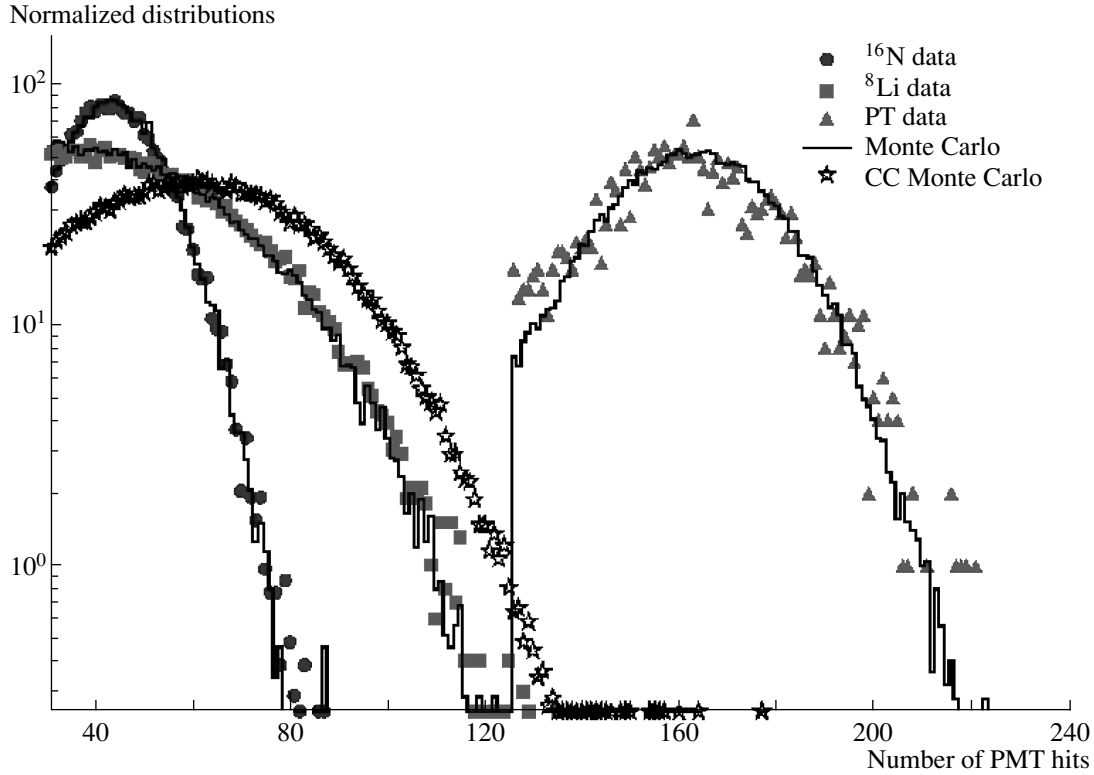

Fig. 1. Energy calibration of the SNO detector. The absolute energy scale and uncertainties are established with the triggered ^{16}N source (circles). The resulting Monte Carlo predictions of detector response (histograms) are tested using a ^{3}H$(p,\gamma)^4$He source providing 19.8-MeV γ rays (triangles). The shape of the CC reaction Monte Carlo prediction is represented by stars.

H_2O. The resulting Monte Carlo predictions of detector response are tested using a ^{3}H$(p,\gamma)^4$He [10] source, which provides 19.8-MeV γ rays (triangles), and a ^{252}Cf neutron source (Fig. 2), which provides an extended distribution of 6.25-MeV γ rays from neutron capture. The volume-weighted mean response is approximately nine PMT hits per 1 MeV of electron energy.

Table 2 details the steps in data reduction. The first is the elimination of instrumental backgrounds. Electrical pickup may produce false PMT hits, while electrical discharges in the PMTs or insulating detector materials produce light. These backgrounds have characteristics very different from Cerenkov light and are eliminated using cuts based only on the PMT positions, the PMT time and charge data, event-to-event time correlations, and veto PMTs. This step in the data reduction is verified by comparing results from two independent background rejection analyses.

For events passing the first stage, the calibrated times and positions of the hit PMTs are used to reconstruct the vertex position and the direction of the particle. The reconstruction accuracy and resolution are measured using Compton electrons from the ^{16}N source, and the energy and source variation of reconstruction are checked with a ^{8}Li β source. Angular resolution is measured using Compton electrons produced more than 150 cm from the ^{16}N source. At these energies, the vertex resolution is 16 cm and the angular resolution is 26.7°.

An effective kinetic energy, T_{eff}, is assigned to each event passing the reconstruction stage. T_{eff} is calculated using prompt (unscattered) Cerenkov photons and the position and direction of the event. The derived energy response of the detector can be characterized by a Gaussian:

$$R(E_{\text{eff}}, E_e) = \frac{1}{\sqrt{2\pi}\sigma_E(E_e)} \exp\left\{-\frac{1}{2}\left(\frac{E_{\text{eff}} - E_e}{\sigma_E(E_e)}\right)^2\right\},$$

where E_e is the total electron energy, $E_{\text{eff}} = T_{\text{eff}} + m_e$, and $\sigma_E(E_e) = (-0.4620 + 0.5470\sqrt{E_e} + 0.008722E_e)$ MeV is the energy resolution. The uncertainty on the energy scale is found to be $\pm 1.4\%$, which results in a flux uncertainty nearly 4 times larger. For validation, a second energy estimator counts all PMTs hit in each event, N_{hit}, without position and direction corrections.

Further instrumental background rejection is obtained using reconstruction figures of merit, PMT time residuals, and the average angle between hit PMTs, $\langle\theta_{ij}\rangle$, measured from the reconstructed vertex.

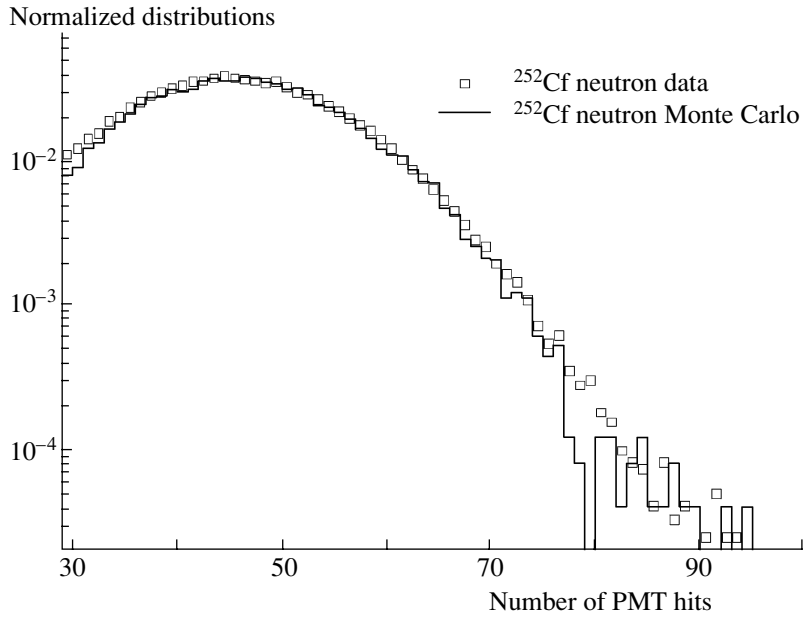

Fig. 2. Another test of the Monte Carlo prediction (histogram) of detector response to a ^{252}Cf neutron source, which provides an extended distribution of 6.25-MeV γ rays from neutron capture (squares).

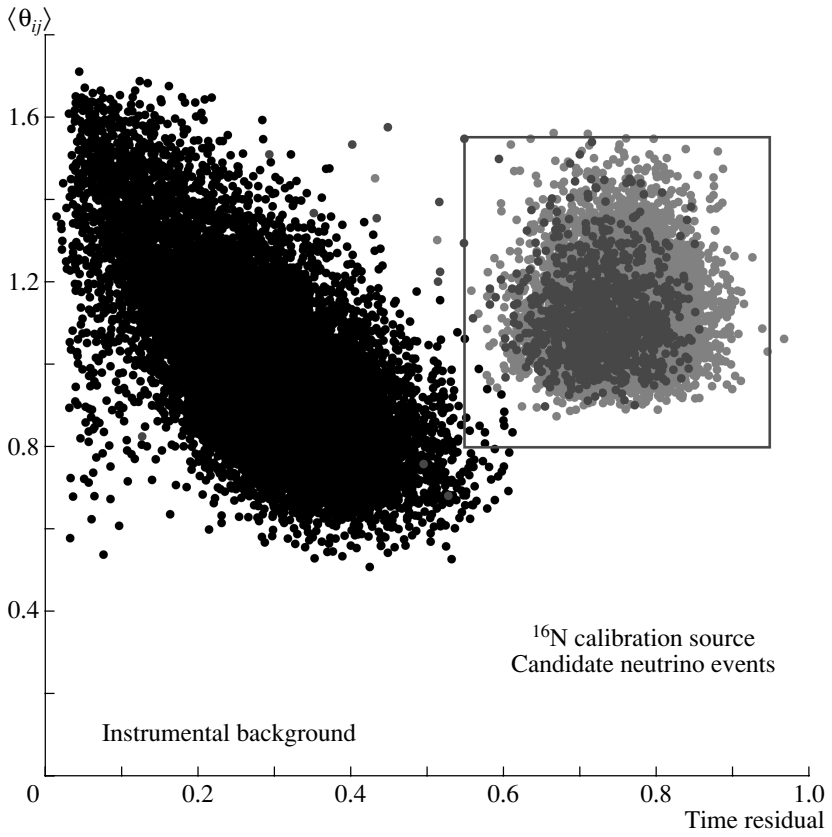

Fig. 3. Performance of high-level parameters. The average angle between hit PMTs, $\langle\theta_{ij}\rangle$, measured from the reconstructed vertex, is plotted against the PMT time residual on an event-by-event basis. Data from instrumental backgrounds distributes on the low-time residual sector, whereas data from the radioactive source ^{16}N and from the set of candidate neutrino events overlay each other in a region of high-time residual, distinct from the instrumental backgrounds. The box represents the cut applied to retain neutrino candidates.

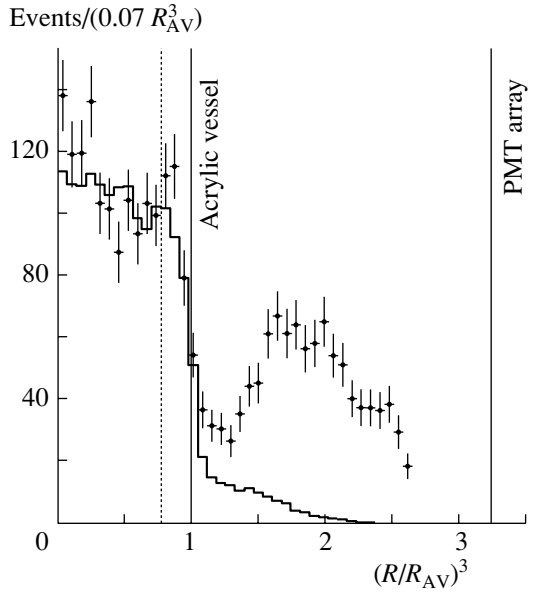

Fig. 4. Distribution of event candidates with $T_{\rm eff} \geq 6.75$ MeV as a function of the volume-weighted radial variable $(R/R_{\rm AV})^3$. The Monte Carlo simulation of the signals, weighted by the results from the signal extraction, is shown as a histogram. The dotted vertical line indicates the fiducial volume cut used in this analysis.

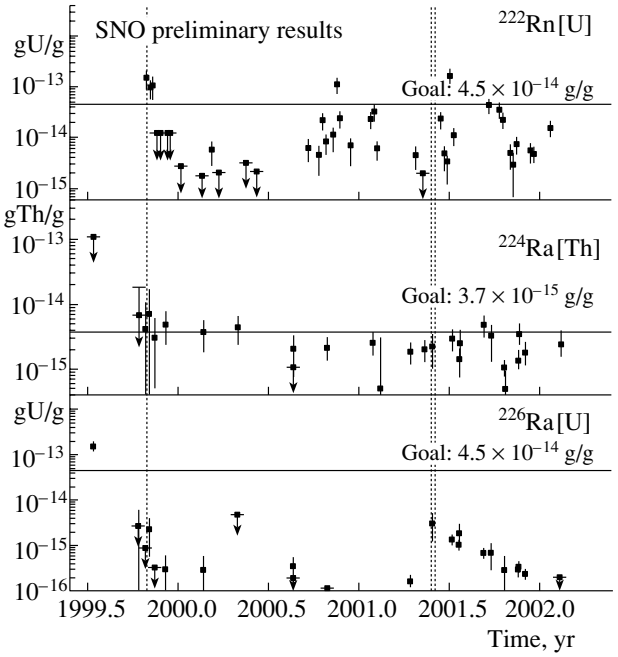

Fig. 5. Time evolution of the concentration of ^{222}Rn (top), ^{224}Ra (middle), and ^{226}Ra (bottom) in the D_2O as measured by low-level radioassays. Target levels correspond to a neutron production rate by deuteron photodisintegration of about 5% of the predicted neutron production rate from the NC reaction using the Solar Standard Model flux. The vertical dotted lines indicate the pure D_2O data-taking period.

These cuts test the hypothesis that each event has the characteristics of single-electron Cerenkov light, as shown in Fig. 3.

The effects of these and the rest of the instrumental background removal cuts on neutrino signals are quantified using the ^{8}Li and ^{16}N sources deployed throughout the detector. The volume-weighted neutrino signal loss is measured to be $1.4^{+0.7}_{-0.6}\%$, and the residual instrumental contamination for the data set within the D_2O is $<0.2\%$. Lastly, cosmic-ray-induced neutrons and spallation products are removed using a 20-s coincidence window with the parent muon.

Figure 1 shows the radial distribution of all remaining events above a threshold of $T_{\rm eff} \geq 6.75$ MeV. The distribution is expressed as a function of the volume-weighted radial variable $(R/R_{\rm AV})^3$, where $R_{\rm AV} = 6.00$ m is the radius of the acrylic vessel. Above this energy threshold, there are contributions from CC events in the D_2O, ES events in the D_2O and H_2O, a residual tail of neutron capture events, and high-energy γ rays from radioactivity in the outer detector. The data show a clear signal within the D_2O volume. For $(R/R_{\rm AV})^3 > 1.0$, the distribution rises into the H_2O region until it is cut off by the acceptance of the PMT light collectors at $R \sim 7.0$ m. A fiducial volume cut is applied at $R = 5.50$ m to reduce backgrounds from regions exterior to the D_2O and to minimize systematic uncertainties associated with optics and reconstruction near the acrylic vessel.

Possible backgrounds from radioactivity in the D_2O and H_2O are measured by regular low-level radioassays of U and Th decay chain products in these regions, as shown in Figs. 5 and 6. Four complementary techniques have been developed by SNO to measure the purity of the detector water. Three methods illustrated by Fig. 7 are based on discharging water to an external extraction system where a chemical separation of Ra, Th, or Rn is performed; the other method uses the Cherenkov light signals from the photomultipliers to directly infer the concentrations of ^{214}Bi and ^{208}Tl. In the MnO_x assay method, water is passed through columns that contain beads coated with a manganese oxide compound. The coating extracts Ra from the flowing water and, to a lesser extent, other dissolved species, such as Th and Pb. After a large volume of water has passed through the columns, they are removed and dried. The Rn produced from Ra decay is swept from the columns into an electrostatic chamber, where it decays. The charged Po ions from the decay of Rn are carried by the electric field onto an alpha counter, where the decays of the Po are detected. In the second assay method, water

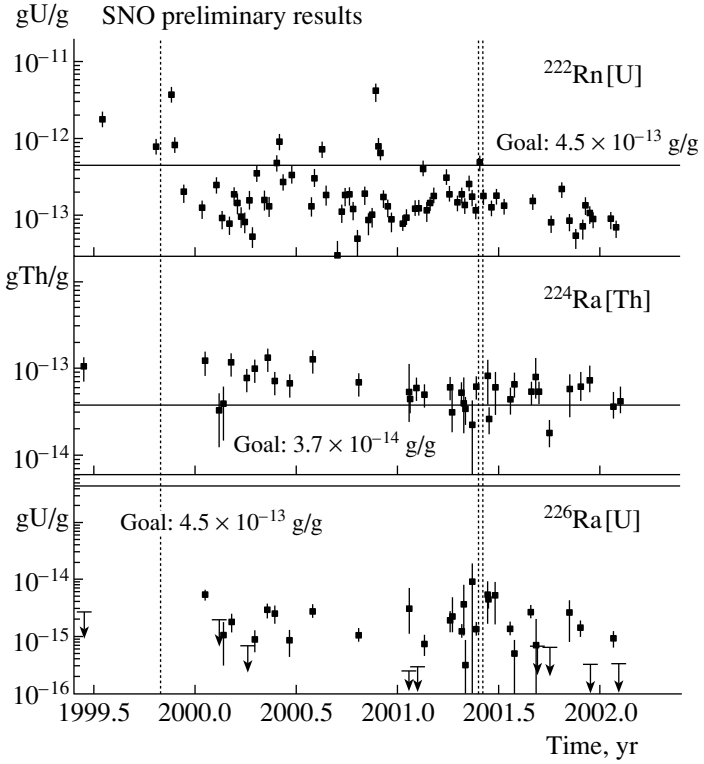

Fig. 6. Time evolution of the concentration of ^{222}Rn (top), ^{224}Ra (middle), and ^{226}Ra (bottom) in the H_2O as measured by low-level radioassays. Here, the target levels are set to reduce the fraction of β–γ events reconstructed inside 6 m. The vertical dotted lines indicate the period of taking pure H_2O data.

from the detector is discharged through a degasser to liberate Rn. The Rn is purified and collected, and its alpha decays are counted in a Lucas cell scintillator chamber on a photomultiplier. Since there is a delay of at least an hour between collection and counting, all ^{220}Rn will have decayed, so this method is sensitive only to the U chain contamination from ^{222}Rn. In the third chemical assay method, the water is discharged over a filter coated with an adsorber of hydrous titanium oxide (HTiO). After water discharge, the filter is eluted with acid to remove the extracted Ra, Th, and Pb. These elements are then concentrated and mixed with liquid scintillator, and the β–α coincidences of ^{212}Bi and ^{214}Bi are detected with a photomultiplier. The potential sensitivity of the HTiO technique for the assay of ^{212}Pb is currently being investigated. The radioassay techniques and the direct counting method will be described elsewhere. As illustrated by Figs. 5 and 6, the backgrounds are very low. The low-energy radioactivity backgrounds are removed by the high threshold imposed, as are most neutron-capture events.

Monte Carlo calculations predict that the H_2O shield effectively reduces contributions of low-energy (<4 MeV) γ rays from the PMT array, and these predictions are verified by deploying an encapsulated Th source in the vicinity of the PMT support sphere. High-energy γ rays from the cavity are also attenuated by the H_2O shield. A limit on their leakage into the fiducial volume is estimated by deploying the ^{16}N source near the edge of the detector's active volume. The total contribution from all radioactivity in the detector is found to be $<0.2\%$ for low-energy backgrounds and $<0.8\%$ for high-energy backgrounds.

The final data set contains 1169 events after the fiducial volume and kinetic energy threshold cuts. Figure 8*a* displays the distribution of $\cos\theta_\odot$, the angle between the reconstructed direction of the event and the instantaneous direction from the Sun to the Earth. The forward peak in this distribution arises from the kinematics of the ES reaction, while CC electrons are expected to have a distribution that is $(1 - 0.340\cos\theta_\odot)$ [11] before accounting for detector response.

The data are resolved into contributions from CC, ES, and neutron events above threshold using probability density functions (pdfs) in T_{eff}, $\cos\theta_\odot$, and $(R/R_{\text{AV}})^3$, generated from Monte Carlo simulations assuming no flavor transformation and the shape of the standard ^{8}B spectrum [12] (*hep* neutrinos are not included in the fit). The extended maximum likelihood method used in the signal extraction yields

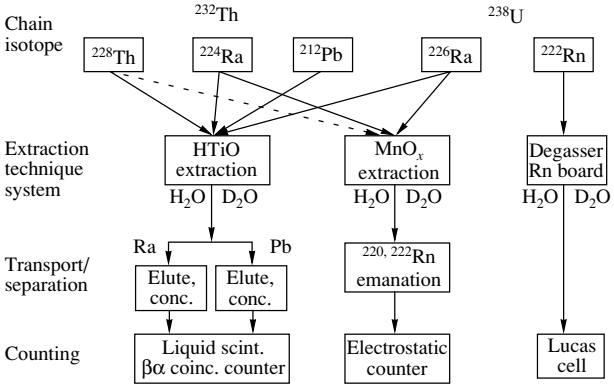

Fig. 7. Radioassay monitoring techniques developed at SNO. Water is discharged to an external extraction system where separation of Ra, Th, or Rn is performed on the basis of their physical or chemical properties. The two concurrent Ra monitoring techniques are based on entirely distinct extraction, separation, and counting methods. See text for details.

975.4 ± 39.7 CC events, 106.1 ± 15.2 ES events, and 87.5 ± 24.7 neutron events for the fiducial volume and the threshold chosen, where the uncertainties given are statistical only. The dominant sources of systematic uncertainty in this signal extraction are the energy scale uncertainty and reconstruction accuracy, as shown in Table 3. The CC and ES signal decomposition gives consistent results when used with the $N_{\rm hit}$ energy estimator, as well as with different choices of the analysis threshold and the fiducial volume up to 6.20 m with backgrounds characterized by pdfs.

The CC spectrum can be extracted from the data by removing the constraint on the shape of the CC pdf and repeating the signal extraction.

Figure 8*b* shows the kinetic energy spectrum with statistical error bars, with the ^{8}B spectrum of Ortiz *et al.* [12] scaled to the data. The ratio of the data to the prediction [7] is shown in Fig. 8*c*. The bands represent the 1σ uncertainties derived from the most significant energy-dependent systematic errors. There is no evidence for a deviation of the spectral shape from the predicted shape under the nonoscillation hypothesis.

Normalized to the integrated rates above the kinetic energy threshold of $T_{\rm eff} = 6.75$ MeV, the measured ^{8}B neutrino fluxes assuming the standard spectrum shape [12] are

$$\phi^{\rm CC}_{\rm SNO}(\nu_e) = [1.75 \pm 0.07\ ({\rm stat.})^{+0.12}_{-0.11}\ ({\rm syst.}) \pm 0.05\ ({\rm theor.})] \times 10^6\ {\rm cm}^{-2}\ {\rm s}^{-1},$$

$$\phi^{\rm ES}_{\rm SNO}(\nu_x) = [2.39 \pm 0.34\ ({\rm stat.})^{+0.16}_{-0.14}\ ({\rm syst.})] \times 10^6\ {\rm cm}^{-2}\ {\rm s}^{-1},$$

where the theoretical uncertainty is the CC cross-section uncertainty [13]. Radiative corrections have not been applied to the CC cross section, but they are expected to decrease the measured $\phi^{\rm CC}(\nu_e)$ flux [14] by up to a few percent. The difference between the ^{8}B flux deduced from the ES rate and that deduced from the CC rate in SNO is $(0.64 \pm 0.40) \times 10^6$ cm^{-2} s^{-1}, or 1.6σ. SNO's ES rate measurement is consistent with the precision measurement by the Super-Kamiokande collaboration of the ^{8}B flux using the same ES reaction [5]:

$$\phi^{\rm ES}_{\rm SK}(\nu_x) = [2.32 \pm 0.03\ ({\rm stat.})^{+0.08}_{-0.07}\ ({\rm syst.})] \times 10^6\ {\rm cm}^{-2}\ {\rm s}^{-1}.$$

The difference between the flux $\phi^{\rm ES}(\nu_x)$ measured by Super-Kamiokande via the ES reaction and the $\phi^{\rm CC}(\nu_e)$ flux measured by SNO via the CC reaction is

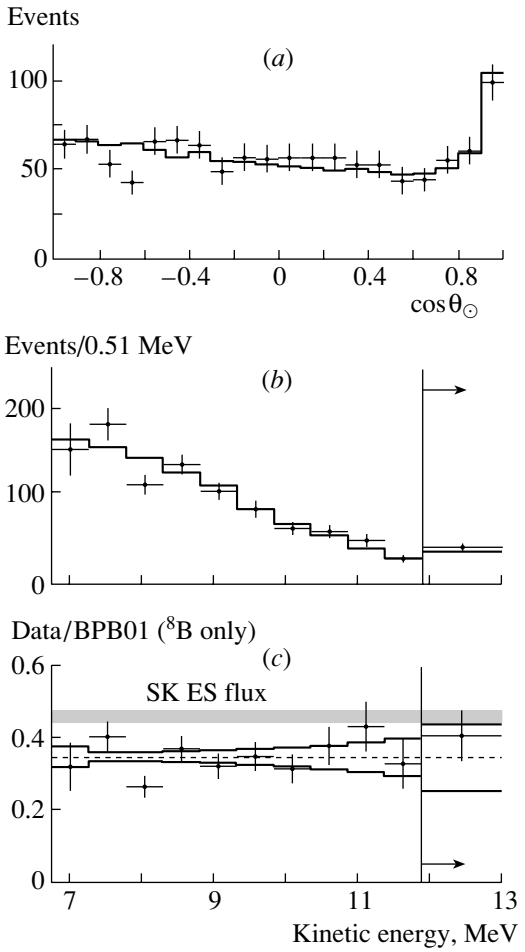

Fig. 8. Distributions of (*a*) $\cos\theta_\odot$ and (*b*) extracted kinetic energy spectrum for CC events with $R \le 5.50$ m and $T_{\rm eff} \ge 6.75$ MeV. The Monte Carlo simulations for an undistorted ^{8}B spectrum are shown as histograms. The ratio of the data to the expected kinetic energy distribution with correlated systematic errors is shown in (*c*). The uncertainties in the ^{8}B spectrum [12] have not been included.

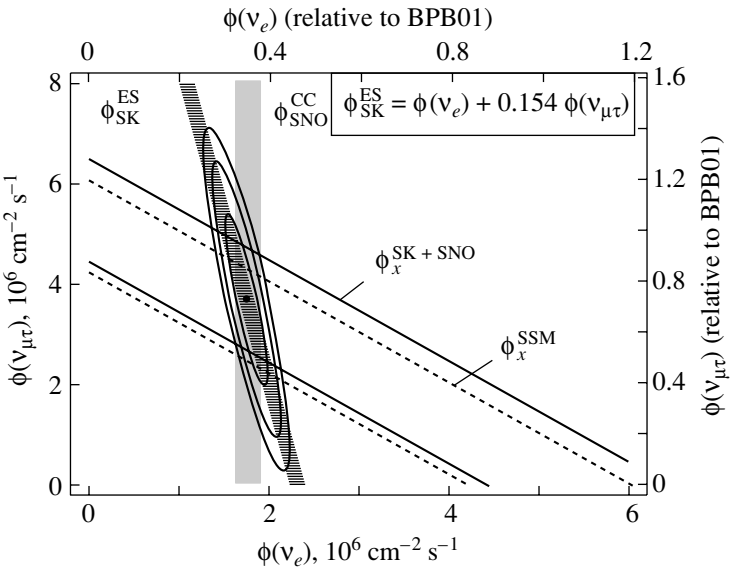

Fig. 9. Flux of ^{8}B solar neutrinos that are μ or τ flavor vs. the flux of electron neutrinos as deduced from the SNO and Super-Kamiokande data. The diagonal bands show the total ^{8}B flux $\phi(\nu_x)$ as predicted by BPB01 [7] (dashed lines) and that derived from the SNO and Super-Kamiokande measurements [5] (solid lines). The intercepts of these bands with the axes represent the $\pm 1\sigma$ errors.

$(0.57 \pm 0.17) \times 10^6$ cm^{-2} s^{-1}, or 3.3σ [15], assuming that the systematic errors are normally distributed. The probability that a downward fluctuation of the Super-Kamiokande result would produce a SNO result $\geq 3.3\sigma$ is 0.04%. For reference, the ratio of the SNO CC ^{8}B flux to that of the BPB01 Solar Model [7] is 0.347 ± 0.029, where all uncertainties are added in quadrature.

Table 3. Systematic error on fluxes

Error source	CC error, %	ES error, %
Energy scale	−5.2, +6.1	−3.5, +5.4
Energy resolution	±0.5	±0.3
Energy scale nonlinearity	±0.5	±0.4
Vertex accuracy	±3.1	±3.3
Vertex resolution	±0.7	±0.4
Angular resolution	±0.5	±2.2
High-energy gammas	−0.8, +0.0	−1.9, +0.0
Low-energy background	−0.2, +0.0	−0.2, +0.0
Instrumental background	−0.2, +0.0	−0.6, +0.0
Trigger efficiency	0.0	0.0
Live time	±0.1	±0.1
Cut acceptance	−0.6, +0.7	−0.6, +0.7
Earth orbit eccentricity	±0.1	±0.1
^{17}O, ^{18}O	0.0	0.0
Experimental uncertainty	−6.2, +7.0	−5.7, +6.8
Cross section	3.0	0.5
Solar Model	−16, +20	−16, +20

These data are evidence of a nonelectron active flavor component in the solar-neutrino flux. These data are also inconsistent with the "Just-So^2" parameters for neutrino oscillation [16].

Figure 9 displays the inferred flux of nonelectron flavor active neutrinos ($\phi(\nu_{\mu\tau})$) against the flux of electron neutrinos. The two data bands represent the one standard deviation measurements of the SNO CC rate and the Super-Kamiokande ES rate. The error ellipses represent the 68, 95, and 99% joint probability contours for $\phi(\nu_e)$ and $\phi(\nu_{\mu\tau})$. The best fit to $\phi(\nu_{\mu\tau})$ is

$$\phi(\nu_{\mu\tau}) = (3.69 \pm 1.13) \times 10^6 \text{ cm}^{-2} \text{ s}^{-1}.$$

The total flux of active ^{8}B neutrinos is determined to be

$$\phi(\nu_x) = (5.44 \pm 0.99) \times 10^6 \text{ cm}^{-2} \text{ s}^{-1}.$$

This result is displayed as a diagonal band in Fig. 9 and is in excellent agreement with predictions of standard solar models [7, 8].

Assuming that the oscillation of massive neutrinos explains both the evidence for electron-neutrino flavor change presented here and the atmospheric neutrino data of the Super-Kamiokande collaboration [17], two separate splittings of the squares of the neutrino mass eigenvalues are indicated: $<10^{-3}$ eV^2 for the solar sector [16, 18] and $\simeq 3.5 \times 10^{-3}$ eV^2 for atmospheric neutrinos. These results, together

with the β spectrum of tritium [19], limit the sum of mass eigenvalues of active neutrinos to be between 0.05 and 8.4 eV, corresponding to a constraint of $0.001 < \Omega_\nu < 0.18$ for the contribution to the critical density of the Universe [20, 21].

In summary, the results presented here are the first direct indication of a nonelectron flavor component in the solar-neutrino flux and enable the first determination of the total flux of ^{8}B neutrinos generated by the Sun.

ACKNOWLEDGMENTS

This research was supported by the Natural Sciences and Engineering Research Council of Canada, Industry Canada, National Research Council of Canada, Northern Ontario Heritage Fund Corporation and the Province of Ontario, the United States Department of Energy, and in the United Kingdom by the Science and Engineering Research Council and the Particle Physics and Astronomy Research Council. Further support was provided by INCO, Ltd.; Atomic Energy of Canada Limited (AECL); Agra-Monenco; Canatom; Canadian Microelectronics Corporation; AT&T Microelectronics; Northern Telecom; and British Nuclear Fuels, Ltd. The heavy water was loaned by AECL with the cooperation of Ontario Power Generation. For a full list of the SNO collaboration members see [22].

REFERENCES

1. B. T. Cleveland *et al.*, Astrophys. J. **496**, 505 (1998).
2. K. S. Hirata *et al.*, Phys. Rev. Lett. **65**, 1297 (1990); Phys. Rev. D **44**, 2241 (1991); **45**, 2170 (1992); Y. Fukuda *et al.*, Phys. Rev. Lett. **77**, 1683 (1996).
3. J. N. Abdurashitov *et al.*, Phys. Rev. C **60**, 055801 (1999).
4. W. Hampel *et al.*, Phys. Lett. B **447**, 127 (1999).
5. S. Fukuda *et al.*, Phys. Rev. Lett. **86**, 5651 (2001).
6. M. Altmann *et al.*, Phys. Lett. B **490**, 16 (2000).
7. J. N. Bahcall, M. H. Pinsonneault, and S. Basu, astro-ph/0010346.
8. A. S. Brun, S. Turck-Chièze, and J. P. Zahn, Astrophys. J. **525**, 1032 (1999); S. Turck-Chièze *et al.*, Astrophys. J. Lett. **555**, L69 (2001).
9. The SNO Collab., Nucl. Instrum. Methods Phys. Res. A **449**, 172 (2000).
10. A. W. P. Poon *et al.*, Nucl. Instrum. Methods Phys. Res. A **452**, 115 (2000).
11. J. F. Beacom and P. Vogel, hep-ph/9903554; Phys. Rev. Lett. **83**, 5222 (1999).
12. C. E. Ortiz *et al.*, Phys. Rev. Lett. **85**, 2909 (2000).
13. S. Nakamura, T. Sato, V. Gudkov, and K. Kubodera, Phys. Rev. C **63**, 034617 (2001); M. Butler, J.-W. Chen, and X. Kong, Phys. Rev. C **63**, 035501 (2001); G.'t Hooft, Phys. Lett. B **37B**, 195 (1971).
14. I. S. Towner, J. Beacom, and S. Parke, private communication; I. S. Towner, Phys. Rev. C **58**, 1288 (1998); J. Beacom and S. Parke, hep-ph/0106128; J. N. Bahcall, M. Kamionkowski, and A. Sirlin, Phys. Rev. D **51**, 6146 (1995).
15. Given the limit set for the *hep* flux by Ref. [5], the effects of the *hep* contribution may increase this difference by a few percent.
16. J. N. Bahcall, P. I. Krastev, and A. Yu. Smirnov, JHEP **05**, 015 (2001).
17. T. Toshito *et al.*, hep-ex/0105023.
18. M. Apollonio *et al.*, Phys. Lett. B **466**, 415 (1999).
19. J. Bonn *et al.*, Nucl. Phys. B (Proc. Suppl.) **91**, 273 (2001).
20. *Allen's Astrophysical Quantities,* Ed. by A. Cox (Springer-Verlag, New York, 2000, 4th ed.); Particle Data Group (D. E. Groom *et al.*), Eur. Phys. J. C **15**, 1 (2000).
21. H. Pas and T. J. Weiler, Phys. Rev. D **63**, 113015 (2001).
22. Q. R. Ahmad *et al.*, Phys. Rev. Lett. **87**, 071301 (2001).

Physics of Atomic Nuclei, Vol. 65, No. 12, 2002, pp. 2156–2160. From Yadernaya Fizika, Vol. 65, No. 12, 2002, pp. 2219–2223.

Solar Neutrino Results and Present Status*

V. V. Gorbachev, J. N. Abdurashitov, T. J. Bowles[1)], M. L. Cherry[2)], B. T. Cleveland[3)], R. Davis, Jr.[4)], S. R. Elliott[3)], V. N. Gavrin, S. V. Girin, P. P. Gurkina, T. V. Ibragimova, A. V. Kalikhov, N. G. Khairnasov, T. V. Knodel, K. Lande[4)], I. N. Mirmov, J. S. Nico[5)], A. A. Shikhin, W. A. Teasdale[1)], E. P. Veretenkin, V. M. Vermul, D. L. Wark[6)], P. S. Wildenhain[4)], J. F. Wilkerson[3)], V. E. Yants, and G. T. Zatsepin**

The SAGE Collaboration

Institute for Nuclear Research, Russian Academy of Sciences, pr. Shestidesyatiletiya Oktyabrya 7a, Moscow, 117312 Russia

Received April 17, 2002

Abstract—The solar neutrino capture rate measured by the Russian–American Gallium Experiment on a metallic gallium target SAGE during the time from January 1990 through December 2000 is $77.0^{+6.2}_{-6.2}\ ^{+3.5}_{-3.0}$ SNU, where the uncertainties are statistical and systematic, respectively. The experimental procedures and data analysis are presented. © *2002 MAIK "Nauka/Interperiodica".*

1. INTRODUCTION

Models describing the processes of nuclear fusion in the Sun have been very successful in explaining numerous solar features. Although these models have had great success, the deficit in the solar neutrino flux relative to the predictions of the Standard Solar Model (SSM) still remains one of the outstanding problems. For 30 years, the Homestake chlorine experiment [1] has consistently observed a flux 33% of that predicted by SSM. In the mid-1980s, the water Cherenkov detector (Kamiokande) began its measurement of the solar neutrino flux that is 54% of the SSM, and the results from Super-Kamiokande are in agreement with its predecessor [2]. In the middle of 2001, results of measurements of a high-energy ^{8}B neutrino flux from the Sudbury Neutrino Observatory (SNO)—a new high-rate real-time detector—were presented [3]. The elastic scattering results of Super-Kamiokande and the charge current results from SNO indicate that, in addition to electron neutrinos, active neutrinos of other flavors originate from the Sun. Since the Sun produces only electron neutrinos, these results are interpreted as strong evidence for neutrino oscillation in the solar sector. But despite this progress with the new generation of large water Cherenkov detectors, there has been no new information on the region of the solar neutrino spectrum below 6 MeV that contains the proton–proton (*pp*) and CNO spectra as well as the ^{7}Be and *pep* lines.

In the early 1990s, the Russian–American Gallium Experiment (SAGE) [4] and the Gallium Experiment (GALLEX) [5] began measuring the low-energy neutrinos from the *pp* fusion reaction on the Sun using Ga as a target material [6]. Because of the low threshold of 233 keV, the reaction $^{71}\mathrm{Ga}(\nu_e, e^-)^{71}\mathrm{Ge}$ provides the only feasible means at present to measure the predominant *pp* neutrinos that are directly related to the solar luminosity and are insensitive to alterations in the solar models. SSM calculations [7] show that the dominant contribution to the total expected capture rate in ^{71}Ga 129^{+8}_{-6} SNU arises from the *pp* neutrinos and is 69.6 SNU, where 1 SNU = 1 interaction/s in a target that contains 10^{36} atoms of the neutrino-absorbing isotope. Contributions by ^{7}Be and ^{8}B neutrinos are 34.4 and 12.4 SNU, respectively. The uncertainty to variation in the SSM for Ga is seen in the independently calculated result of 127.2 SNU [8] for the total capture rate.

2. THE SAGE EXPERIMENT

The SAGE detector is situated in a specially built underground laboratory at the Baksan Neutrino Ob-

*This article was submitted by the authors in English.

[1)]Los Alamos National Laboratory, Los Alamos, NM, USA.
[2)]Louisiana State University, Baton Rouge, LA 70803, USA.
[3)]University of Washington, Seattle, WA 98195, USA.
[4)]University of Pennsylvania, Philadelphia, PA 19104, USA.
[5)]National Institute of Standards and Technology, Gaithersburg, MD, USA.
[6)]Department of Particle and Nuclear Physics, Oxford University, Oxford, UK.
**e-mail: gavrin@dionis.iasnet.ru

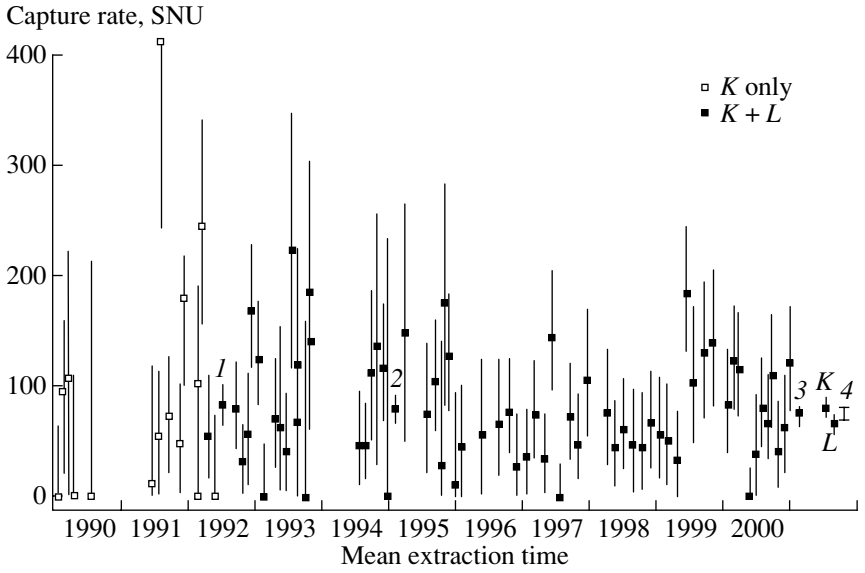

Fig. 1. Capture rate for each extraction as a function of time. All uncertainties are statistical. The symbols *1, 2,* and *3* show the combined result for SAGE I, II, and III, respectively. The symbol *4* shows the total combined result.

servatory in the Northern Caucasus Mountains. It is located 3.5 km from the entrance of a horizontal adit excavated into the side of Mount Andyrchi and has an overhead shielding of 4700 mwe. Today, about 50 t of Ga are contained in seven chemical reactors with approximately the same amount of Ga in each of them. The data span a 10-yr period during which many improvements to the experiment were made. As a result, the data naturally divide into three periods differentiated by experimental conditions. SAGE I refers to extractions on approximately 30 t of Ga beginning in 1989 with backgrounds becoming low enough to begin solar neutrino extractions in 1990. In the summer of 1991, the extraction mass was increased to nearly 60 t. The majority of those data were taken without digitized waveforms, and thus electronic noise levels were such that the L peak was inaccessible. After SAGE I was completed, the experiment was greatly improved with respect to electronic noise, and the analysis of the L-peak region became tractable. The period of data taking from September 1992 through December 1994 is referred to as SAGE II. The majority of SAGE II data had waveform recording capability. Only extractions for which we have waveform data are analyzed in the L-peak region. Beginning in December of 1994, an experiment using a ^{51}Cr source was undertaken; we refer to all data taken after January 1995 as SAGE III.

3. EXPERIMENTAL PROCEDURES

Each measurement of the solar neutrino flux begins by adding to the gallium approximately 350 μg of stable Ge carrier (distributed equally among all of the reactors) as a Ga–Ge alloy with known Ge content. The reactor contents are stirred thoroughly to disperse the carrier throughout the Ga metal. After exposure time of about one month, the Ge carrier with ^{71}Ge atoms produced in solar neutrino interactions are extracted from the Ga using procedures described elsewhere [4]. The final step of the chemical extraction procedure is the synthesis of germane (GeH_4), which is used as a proportional counter (PC) gas with an admixture of Xe. The total efficiency of extraction, now typically 90%, is determined by measuring the germane volume.

The PC with extracted germanium is placed in a passive shield of the eight-channel counting system, where it is counted for about five months. ^{71}Ge decays via electron capture with a half-life of 11.43 d with Auger electron emission [9]. The pulse spectrum of ^{71}Ge decays in the PC contains three peaks of 10.4, 1.2, and 0.1 keV (K, L, and M peaks). The energy region of our counting system (from 0.3 to 16 keV) allows us to detect K and L events. To minimize noises and backgrounds, we analyze the waveform of each pulse written by the digital oscilloscope. Short tracks of Auger electrons in the countig gas make a low rise time of the waveform in contrast to long trecks of background particles. The active shield on the basis of the NaI crystal detects γ radiation accompanying the PC pulses. Thus, the criteria we use to select ^{71}Ge events are as follows: (i) the amplitude of the pulse falls inside the K- or L-energy region; (ii) the rise time is less than 18.4 ns for the K-peak event and 10 ns for the L-peak event; (iii) there is no γ radiation accompanying the pulse.

A summary of systematic effects and their uncertainties in SNU (The values for extraction and counting efficiencies are based on the rate of 77 SNU)

Extraction efficiency	Ge carrier mass	± 1.6
	Extracted Ge mass	± 1.9
	Residual carrier Ge	± 0.6
	Ga mass	± 0.2
Counting efficiency	Counter effects	± 1.9
	Gain shifts	$+2.4$
	Resolution	$-0.4, +0.5$
	Rise time limits	± 0.7
	Lead and exposure times	± 0.6
Background	Neutrons, U, Th, muons	< -0.07
	Other Ge isotopes	< -0.07
	External radon	0.0
Internal radon		< -0.2
	Total	$-3.5, +4.1$

4. STATISTICAL ANALYSIS

The sets of selected events gathered after the end of counting are analyzed by the likelihood method on the assumption that the events were detected from exponentially decaying ^{71}Ge and that there is some constant for the measurement background process [10]. The maximum of the likelihood function built by multiplication of the likelihood function for each data set indicates the production rate of ^{71}Ge, and the width of the function gives us the statistical uncertainty of our result.

The results of individual run analyses with 68% statistical uncertainty are plotted in Fig. 1. Combining the total data set over the three periods of SAGE, the statistical result of the 136 separate counting sets is $77.0^{+6.2}_{-6.2}$ SNU. If one considers the K-peak and L-peak data independently, the results are $82.8^{+7.9}_{-7.6}$ and $66.5^{+10.2}_{-9.8}$ SNU, respectively. The agreement between the two peaks serves as a strong check on the robustness of the event selection criteria.

5. SYSTEMATIC EFFECTS

The table summarizes the systematic effects that may affect the measured solar neutrino production rate. We have three main categories of systematics: extraction efficiencies, counting efficiencies, and backgrounds. Certain of them are discussed below.

Extensive measurements were performed on all the PCs used in SAGE counting to establish their efficiencies and the associated uncertainties. A series of three separate measurements using PCs filled with ^{37}Ar, ^{71}Ge, and ^{69}Ge was employed to establish the counter efficiencies. The uncertainties in the efficiencies are composed of the volume efficiency, end effects, and gas efficiency. Adding the uncertainties from each of these effects in quadrature gives a $\pm 2.8\%$ uncertainty due to the counters.

Some contribution to the ^{71}Ge signal is made by background processes. Limits on the creation of Ge isotopes through the (n, p) reaction on Ga and by cosmic ray muons come from measurements of both the fast neutron [11] and muon fluxes [12] in the Ga chamber. The production of the germanium isotopes in (α, p) reactions depends on the concentrations of U and Th in the target. The concentrations of U and Th in the Ga were measured independently by low-background counting in a Ge detector and by glow discharge mass spectrometry. No observable level of U or Th was found, and upper limits are given in the table.

The radon background is a problem for any low-background experiment. Decays of radon and its daughters make false ^{71}Ge pulses in the PC. To determine the influence of radon in the counting gas of the counters, we carried out measurements with a counter with a large amount of radon inside. On the basis of the measurements, we calculated pulse spectra from decays of each radon chain element in the counter. The initial α from the chain makes a pulse overflow the energy range of the counting system. To minimize the radon influence on the SAGE data, we use a time cut of 15 min before and of 3 h after each overflow event. The probability of a false ^{71}Ge event from one radon decay in the counter after the ^{71}Ge pulse selection criteria is about 4×10^{-4} for the L peak and 8×10^{-4} for the K peak. Since the mean value of the overflow pulses per run assigned to ^{222}Rn is 7.7 and the mean value of ^{71}Ge events per run is 2.3 for the L peak and 2.8 for the K peak, the relative systematic error due to radon is found to be 0.1% for the L peak and 0.2% for the K peak. It corresponds to 0.2 SNU [13]. The contribution to the ^{71}Ge signal from other germanium isotopes ^{68}Ge and ^{69}Ge was estimated using calculations on the basis of measurements with muon beams and α and neutron sources [4, 14, 15].

A large time of measurements allows us to make a direct search for some kinds of systematic uncertainties in the solar neutrino data. We carried out a search for ^{68}Ge and ^{69}Ge events in our data. Our counting system allows us to detect ^{68}Ge and ^{69}Ge decays with about 3% and 5% efficiency, respectively [16].

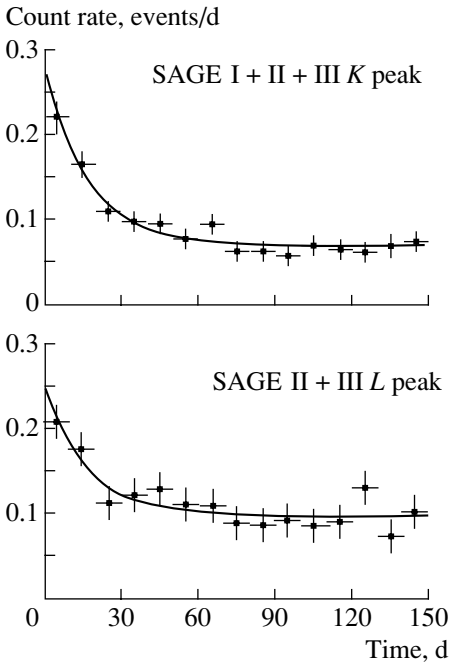

Fig. 2. Count rate for all runs in L and K peaks. The solid curve is a fit to the data points with the 11.4-d half-life of ^{71}Ge plus a constant background. The vertical error bar at each point is proportional to the square root of the number of counts and is shown only to give the scale of the error. The horizontal error bar is ±5 d, equal to the 10-d bin size.

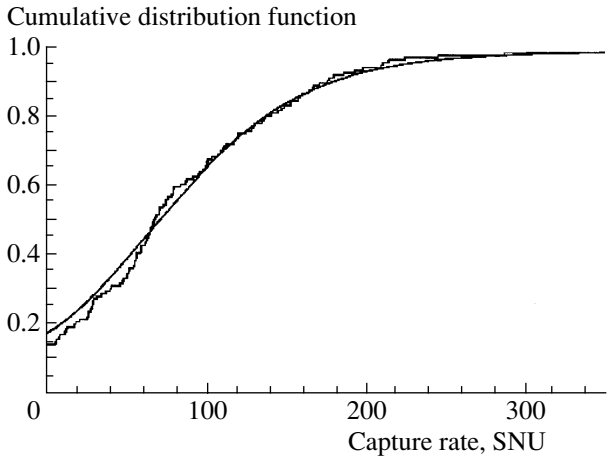

Fig. 3. Measured capture rate for all SAGE data sets (jagged curve) and the expected distribution derived by 1000 Monte Carlo simulations of each set (smooth curve). The capture rate in the simulations was assumed to be 77 SNU.

The number of recognized ^{68}Ge events (4.5 events in 32 runs) gives the production rate of the isotope about 6.5 times higher than expected, but with a 100% statistical error. Since the production rate of ^{69}Ge does not exceed the expected value, one can explain the discrepancy for ^{68}Ge by possible underestimation of the cosmic ray muon background. But we want to carry out measurements with a part of our gallium target (maybe 7 t) in the Baksan Underground Scintillation Telescope, where the cosmic ray muon flux is about 1000 times higher than in the Ga chamber.

6. RESULTS

The global best fit capture rate for the 136 separate counting sets of SAGE I, SAGE II, and SAGE III is $77.0^{+6.2}_{-6.2}$ SNU, where the uncertainty is statistical only, or $77.0^{+7.1}_{-6.9}$ SNU, where statistical and systematic uncertainties are combined in quadrature. There are 360.7 counts assigned to ^{71}Ge among 1594 selected events. The total counting lifetime is 27.1 yr. The probability of the global fit that corresponds to von Mises statistics of $N\omega^2 = 0.049$ is 79%.

Consistency of the data with the analysis hypotheses is shown by the best fit of the ^{71}Ge half-life of $10.2^{+1.6}_{-1.4}$ d, which is close to its tabular value of 11.43 d. Figure 2 shows the count rate of events selected in L and K peaks in comparison with the ^{71}Ge decay curve against the constant background.

Another important hypothesis that we use in the analysis is constancy of the production rate of ^{71}Ge in time. The cumulative distribution of the ^{71}Ge production rate in the Ga target for each data set is shown in Fig. 3. The consistency of the data with the constant ^{71}Ge production rate of 77 SNU has the probability of 12%.

The results of the calibration experiment with a 517-kCi ^{51}Cr neutrino source performed in 1995 coincided with the one expected in [14].

7. CONCLUSION

Ten years of measurement of the solar neutrino flux give the capture rate of $77.0^{+6.2}_{-6.2}$ SNU, where the uncertainty is statistical only. The systematic effects give the total systematic uncertainty of +3.5/−3.0 SNU, considerably smaller than the statistical one. We have examined the counting data and have shown that there is good evidence that ^{71}Ge is being counted, that the counting data fit the analysis hypotheses, and that the counting data are self-consistent.

The SAGE result of 77 SNU represents 60% [7, 8] of SSM predictions. Given the extensive systematic checks and auxiliary measurements that have been performed, especially the ^{51}Cr neutrino source experiment [17], this 6σ reduction in the solar neutrino flux compared to SSM predictions is very strong evidence

that the solar neutrino spectrum below 2 MeV is significantly depleted, as was previously shown for the ^{8}B flux by the Cl and Super-Kamiokande and SNO experiments. Now, gallium detectors remain the only technique able to monitor low-energy solar neutrinos.

ACKNOWLEDGMENTS

We thank J.N. Bahcall, M. Baldo-Ceolin, P. Barnes, S. Brice, L. Callis, A. Dar, G.T. Garvey, W. Haxton, V.N. Kornoukhov, V.A. Kuzmin, V.A. Matveev, L.B. Okun, V.A. Rubakov, R.G.H. Robertson, N. Sapporo, A.Yu. Smirnov, A.A. Smolnikov, A.N. Tavkhelidze, and many members of GALLEX and GNO for their continued interest and for fruitful and stimulating discussions. We acknowledge the support of the Russian Academy of Sciences; the Institute for Nuclear Research of the Russian Academy of Sciences; the Russian Ministry of Industry, Science, and Technology; the Division of Nuclear Physics of the US Department of Energy; and the US National Science Foundation.

This research was made possible in part by the Russian Foundation for Basic Research (project nos. 96-02-18399, 99-02-16110, 00-1596632 (this grant is supported by the Council for Grants of the President of Russian Federation)), in part by the International Science Foundation (grant no. M7F000) and the International Science Foundation and the Russian Government (grant no. M7F300), and in part by the US Civilian Research and Development Foundation (award nos. RP2-159, RP2-2253).

REFERENCES

1. B. T. Cleveland *et al.*, Astrophys. J. **496**, 505 (1998).
2. Y. Fukuda *et al.*, Phys. Rev. Lett. **81**, 1158 (1998).
3. Q. R. Ahmad *et al.*, Phys. Rev. Lett. **87**, 071301 (2001).
4. J. N. Abdurashitov *et al.*, Phys. Lett. B **328**, 234 (1994); Phys. Rev. C **60**, 055801 (1999).
5. W. Hampel *et al.*, Phys. Lett. B **447**, 127 (1999).
6. V. A. Kuzmin, Zh. Éksp. Teor. Fiz. **49**, 1532 (1965) [Sov. Phys. JETP **22**, 1051 (1966)].
7. J. N. Bahcall, S. Basu, and M. H. Pinsonneault, Phys. Lett. B **433**, 1 (1998).
8. A. S. Brun, S. Turck-Chièze, and P. Morel, Astrophys. J. **506**, 913 (1998).
9. W. Hampel and L. Remsberg, Phys. Rev. C **31**, 666 (1985).
10. B. T. Cleveland, Nucl. Instrum. Methods Phys. Res. **214**, 451 (1983).
11. I. R. Barabanov, V. N. Gavrin, P. P. Prokopeva, and V. Yants, Report No. P-0559, INR AS USSR (Moscow, 1987).
12. Yu. I. Zakharov, Candidate's Dissertation in Physics and Mathematics (Inst. Yad. Issled. Akad. Nauk SSSR, Moscow, 1987).
13. V. N. Gavrin, V. V. Gorbachev, and I. N. Mirmov, Yad. Fiz. (in press) [Phys. At. Nucl. (in press)].
14. M. Cribier, B. Pichard, and J. Rich, Astropart. Phys. **6**, 1351 (1997).
15. J. N. Bahcall, B. T. Cleveland, R. Davis, Jr., *et al.*, Phys. Rev. Lett. **40**, 1351 (1978).
16. B. T. Cleveland, V. N. Gavrin, V. V. Gorbachev, and T. V. Ibragimova, Yad. Fiz. **65**, 1309 (2002) [Phys. At. Nucl. **65**, 1276 (2002)].
17. J. N. Abdurashitov *et al.*, Phys. Rev. Lett. **77**, 4708 (1996); Phys. Rev. C **59**, 2246 (1999).

Physics of Atomic Nuclei, Vol. 65, No. 12, 2002, pp. 2161–2164. From Yadernaya Fizika, Vol. 65, No. 12, 2002, pp. 2224–2227.

NEUTRINO PHYSICS AND ASTROPHYSICS

Detector Lens as a New Tool for Solar Neutrino Spectroscopy*

V. N. Kornoukhov **
(for the LENS Collaboration)

Institute of Theoretical and Experimental Physics,
Bol'shaya Cheremushkinskaya ul. 25, Moscow, 117259 Russia

Received April 17, 2002

Abstract—The LENS detector is a ν_e-flavor real-time detector for measurement of low-energy solar neutrino flux and spectral shape, specifying the *pp* and ^{7}Be neutrinos individually. It will complement future low-energy neutrino experiments (BOREXINO, HELLAZ, GENIUS), all of which are scattering experiments. The main goal of the LENS collaboration is to develop final formulation of Yb- and In-loaded liquid scintillators and to build a prototype of suitable volume to study the backgrounds and detector performance. © *2002 MAIK "Nauka/Interperiodica"*.

1. INTRODUCTION

The solar neutrino experiments Chlorine [1], Super-Kamiokande [2], GALLEX [3], and SAGE [4] have observed neutrino fluxes with substantially lower intensity than the Standard Solar Model (SSM) has predicted. This discrepancy constitutes the so-called solar neutrino problem. Most physicists consider the solution of this problem to lie in new physics, namely, physics of flavor oscillation of massive neutrinos. The flavor oscillation models are based on either vacuum oscillation ("just-so" mechanism) or matter conversion (MSW effect) with distinct sets of neutrino parameters. These scenarios have very different predictions on the solar neutrino spectral distortion. The excellent Sudbury Neutrino Observatory (SNO) measurement [5] of the CC rate for solar neutrino absorption by deuterium provided dramatic and convincing evidence for neutrino oscillations and has strengthened the case for active oscillations with large mixing angles. Nevertheless, even this measurement has not qualitatively changed the globally allowed solution space for solar neutrinos [6].

Thus, the scenarios for flavor conversion will likely be discriminated through measurement of the solar neutrino flux, including temporal variations, at all energies and for all neutrino species. The robust predictions of the SSM are for the *pp*, *pep*, and ^{7}Be fluxes, the *pp* flux being most strongly constrained by the solar luminosity. In this context, it is no surprise that real-time detection of the complete ν_e spectrum from the Sun and source-specific fluxes is of crucial importance for solving the solar neutrino problem. Only the integral signal rate above a threshold from the low-threshold Ga detectors has been available until now, but not the fluxes from specific solar neutrino sources. So far, there exist several proposals to measure the *pp* flux in real time: HERON [7], GENIUS [8], HELLAZ [9], MOON [10], and LENS [11, 12]. The first three experiments are based on neutrino–electron scattering, which is caused by both the neutral and the charged weak currents; thus, the signal is determined by the flavor composition of the incident neutrino. The scientific aim of MOON and LENS is direct observation of the specific ν_e fluxes from *pp*, ^{7}Be, and CNO reactions. In this paper, we discuss the LENS (low-energy solar spectroscopy) project.

2. THE DETECTION PRINCIPLE: ^{176}Yb AND ^{115}In CASES

The detector LENS is based on charged current (inverse β^-) transitions on a target of ytterbium/indium to excited levels in lutetium/tin (Figs. 1 and 2).

Neutrino capture by the ^{176}Yb nucleus results in a 194.5-keV excited isomer and 339-keV excited states in ^{176}Lu, which decay to the 123-keV long-lived isomer state in ^{176}Lu with a time delay of 50 ns (so-called "tagged" event). These neutrino events have a highly specific signature of two events produced at the same point in the detector with an average delay time: a prompt electron with energy $E_\nu - Q$ and a 72-keV γ ray. Such a signature gives the possibility of discriminating the neutrino signal against the background by a factor of 10^6.

Neutrino capture in ^{115}In leads to the 613-keV isomeric state in ^{115}Sn with the emission of a prompt

*This article was submitted by the author in English.

** e-mail: kornoukhov@mail.ru

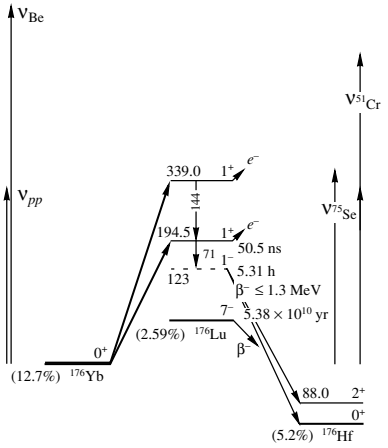

Fig. 1. The structure of ^{176}Yb–^{176}Lu–^{176}Hf levels and tag (energy in keV): (left) the neutrino lines from the Sun and (right) ^{51}Cr and ^{75}Se neutrino sources.

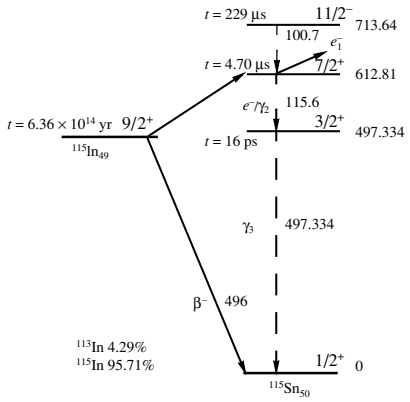

Fig. 2. The ^{115}In–^{115}Sn levels and tags (energy values in keV).

electron e_1. The transition can be tagged by the delayed coincidence with the cascade $[(e/\gamma)_2 + \gamma_3]$ with energy of (115 + 495) keV and a tag time of 4.76 μs. This reaction can also be identified in detail by additional spatiotemporal coincidences [12]. Notice that energies of the $e_1 - (e/\gamma)_2$ event are deposited in spatial coincidence in a primary "microcell" (μ cell) and an energy γ_3 event is deposited in a "macrocell" surrounding the primary μ cell. The neutrino thresholds $Q = 301$ keV (^{176}Yb) and 118 keV (^{115}In) imply sensitivity to the complete spectrum of low-energy solar neutrinos identifying the *pp* and ^{7}Be fluxes.

Charge exchange (p, n) and (^{3}He, t) measurements on ^{176}Yb and ^{115}In gave the values of a matrix element BG(GT) equal to 0.20 and 0.11 for the 195- and 339-keV exited states of ^{176}Lu respectively [13, 14]. Charge exchange (p, n) measurements on ^{115}In indicate a ν_e capture matrix element B(GT) of 0.17 [12]. The results are attractive because of the reasonable rates per ton of Yb and even a 10 times larger one for In (due to 95.7% isotopic abundance of ^{115}In). A 20-t ytterbium target could detect about 180 *pp* events and 140 ^{7}Be events per year, and a 4-t indium target could detect 377 events of *pp* and 102 events of ^{7}Be neutrinos.

As envisaged from the beginning, the basic method for implementation of the LENS detector is the scintillator technique. The main technology for the Yb/In-loaded scintillator now under study is a liquid scintillator (LS) doped (up to 10% by mass) with natural Yb/In.

The detector consists of modules (segmentation design). The main parameters for a good detection of the signal with the LS are as follows:

The light output of the loaded scintillator should be no less than 50% of that of the unloaded scintillator, as one needs to detect an energy release of 50–100 keV.

The light transmission length is several meters.

Fast pulse timing, in order to identify pulses separated by tens of ns.

Long-term stability over periods of several years.

3. THE BACKGROUND: ^{176}Yb AND ^{115}In CASES

The neutrino signature in LENS is a delayed coincidence between at least two pulses occurring at the same point in the detector.

3.1. ^{176}Yb Case

The background can be classified in three different categories:

Self-correlation (SC) of single pulses. These SC events mimic the low energy of the tag (72 keV) in the short tag time of about 50 ns. The main defense against SC is a minimum delay cut (MDC) in the ν_e tag at the cost of signal efficiency (see below).

Accidental background. Random coincidence between two uncorrelated single pulses is responsible for this type of background. The rate will depend upon the contamination of the detector in α, β, and γ emitters plus the fraction of radiation from the environment (γ rays, neutrons) able to reach the detector, and the coincidence rate will be inversely proportional to the spatial granularity of the detector ($\eta \sim 10^4$). For the time gate $\tau \sim 100$ ns, the tolerant level of U/Th concentration is 0.1 ppb and $^{\mathrm{nat}}$K/$^{\mathrm{nat}}$Lu is 0.1 ppm.

Correlated background. Two sources of correlated background in the LENS detector are coincident cascades from two specific impurities, ^{235}U and ^{176}Lu, in the Yb material.

Lutetium contains 2.6% long-lived ^{176}Lu that emits the $(\beta\gamma)$ cascade with an energy and a time

profile similar to the neutrino tag. The ^{176}Lu decay is relevant despite the short lifetime of 2 ns because its specific activity is high. At 0.1 ppm of Lu in Yb, the Lu false events reduce to ~ 4/yr if MDC = 40 ns, entailing a signal loss of $\sim 55\%$. There is a possibility of producing Yb with displacement ion exchange complexing chromatography with a purity of ~ 1 ppb of ^{nat}Lu. A laboratory test was done [15]; proper equipment and industrial-scale technology exist in Russia. The ^{235}U isotope (natural abundance 0.72%) emits a delayed ($\beta\gamma$) cascade $^{235}\mathrm{U} \rightarrow {}^{231}\mathrm{Pa}$ that closely mimics the *pp* signal tag. A purity as high as 10^{-17} g ^{235}U/g is required to keep this background at a sufficiently low level. A purity at the level 10^{-12} g ^{nat}U/g can be achieved in Yb because the rare-earth industry uses extractants which are several orders of magnitude more efficient for actinides than rare earths. Then the isotope dilution technique with U carrier depleted in ^{235}U should be applied [16]. To purify 20 t of Yb, the Institute of Theoretical and Experimental Physics (Moscow) has 6 g of ^{238}U depleted in ^{235}U at a level of 0.2 ppm.

3.2. ^{115}In Case

The sources of background arise from the following:

Intense beta decay of ^{115}In ($T_{1/2} = 5 \times 10^{14}$ yr). The practical signal rate in In (taking into account a tag efficiency and time window) is about 10^{-7} s^{-1}. The specific activity of In is 0.25 Bq/t; thus, the single rate is 10^6 s^{-1} in 4 t. As a result, the basic design feature needed is detector granularity $\eta = (1\text{–}5) \times 10^4$.

Bremsstrahlung (BS) of In beta-decay electrons. The β particles radiate BS which can mimic the neutrino tag ($(e/\gamma)_2 + \gamma_3$) because these β particles can deposit 50 keV or more of its kinetic energy in a μ cell and radiate the rest into the macrocell, inseparable from the neutrino tag. The BS problem is thus more difficult than the beta decay. The only defense is discrimination of the ν_e tag energy of 613 keV from the 495-keV BS endpoint. This is why the LS energy resolution is so important for this detector.

Radioimpurities. ($\beta\gamma$) Cascades from radioimpurities in the In LS can also mimic ($(e/\gamma)_2 + \gamma_3$) in a similar way as BS. Even single gammas could mimic the ($(e/\gamma)_2 + \gamma_3$) tag with a high probability, e.g., gammas from ^{40}K, ^{208}Tl, and ^{214}Bi which are present as an impurity in LS or in the surrounding environment. To reject these events, one needs to check candidate events in an expanded macrocell. The tolerant level of the U/Th concentration is 1 ppt and ^{nat}K is 1 ppb, which are feasible at the industrial scale of In production.

4. CALIBRATION WITH NEUTRINO SOURCE(S)

Interpretation of such experiments has one major problem: the neutrino cross section for the transition to ^{176}Yb/^{115}In to the excited states of ^{176}Lu/^{115}Sn is deduced from the cross sections of (p, n) or (^{3}He, ^{3}H) scattering reactions with an accuracy of about 20% [13, 14]. Thus, we plan to measure with a high accuracy the specific neutrino cross sections to the two states in the Yb–Lu system using two MCi-scale sources based on ^{51}Cr and ^{75}Se. For the excited state in the In–Sn system, only one source based on ^{51}Cr can be used. The nuclear reactors and the technology for producing the source(s) are available in Russia [17–19]. The LENS collaboration plans to reuse the ^{50}Cr material of GALLEX to make the ^{51}Cr source and produce a new isotopically enriched target of ^{74}Se for ^{75}Se source. The kg-scale ^{82}Se for the study of $\beta\beta$ decay has been produced in Russia with gaseous centrifugation of volatile SeF_6 [20]. The technical developments for neutrino source production are being coordinated at two suitable reactors L-2 [17,18] and SM-3 [19] by a French–German–Russian team from LENS.

5. LIQUID SCINTILLATOR TECHNOLOGY

The main problem in the preparation of the Yb/In-loaded scintillator is to find the Yb complex organic compound, highly soluble in an aromatic solvent. Generally, preparation of the Yb/In-loaded scintillator is grounded on a liquid–liquid extraction process (LLE). The LLE is a well-established technological process that proved its large application for preparation of highly concentrated and stable rare-earth complexes soluble in organic solvents. Many types of rare-earth compounds and organic extractants have already been investigated [11, 21, 22]. It was found that of greatest interest as extractants are neutral phosphorus organics (P=O): phosphates, phosphonates, and phosphine oxides, and carboxylic acids (C=O). Recently, the LENS collaboration has focused on improving the light output parameter S by introducing a certain combination of (P=O) and (C=O) extractants to reduce the acidic component that may limit the value of S. At the same time, this job aims to search for less expensive (P=O) additives that reduce the cost of the Yb/In LS. The best parameters of LS reached by the LENS collaboration for various recipes:

Yb/In content is 150 g of Yb/L and 105 g of In/L.

Light output S is up to 60% of BC505 (BPO is used as an activator).

Light transmission length L is 4–5 m at $\lambda =$ 430 nm.

The main decay component has the decay time $\tau = 2.3$ ns (89% of the signal) for Yb LS and $\tau = 2.9$ ns (95% of the signal) for In LS. Light output of LS increases by 20% if 1MN (1-methylnaphtalene) is used as an aromatic solvent instead of PC (pseudocumene). But adding of 1MN decreases the LS light transmission. It is important to note that the preparation of Yb/In-loaded LS is also compatible with the industrial scale of production and purification technology of rare earths that is based on the LLE process with the same (P=O) extractants.

6. CENTRAL LABORATORY FOR LENS (CELL)

The Central Laboratory for LENS (CELL) has been created to transfer and implement LS technologies in local laboratories and to produce test programs of interest to the prototype program using the facilities of Laboratori Nazionalle del Gran Sasso (LNGS) such as the well-instrumented chemical laboratory and underground γ-ray counting detectors [23].

The main setup of CELL is the Low Background Facility (LLBF). The aim of the LLBF is to provide sufficient shielding against cosmic ray muons, γ flux and neutrons from the rock, and radon from the air in order to measure the intrinsic background of a single LENS module filled with loaded and nonloaded LS.

The inner dimensions of the LLBF are $70 \times 70 \times 400$ cm. The central module can be operated in (anti)coincidence with the surrounding modules that thus simulate the neighboring part of the LENS detector. This basic module is thus a prototype of LENS.

The shield consists of (from inside to outside) electrolytic copper (15 cm), steel (23 cm), and polyethylene (20 cm) and has a total mass of about 75 t. The copper shielding is gas tight and serves as a radon shield. This shield is located in a clean room equipped with a ventilation system (to control humidity and temperature and to limit dust particles). We expect to begin counting operations and prototype studies with this facility in 2002.

7. CONCLUSION

The LENS detector is a ν_e-flavor real-time detector for measurement of low-energy solar neutrino flux and spectral shape, specifying the *pp* and ^{7}Be neutrinos individually. It will complement future low-energy neutrino experiments (BOREXINO, HELLAZ, GENIUS), all of which are scattering experiments. The main goal of the LENS collaboration now is to develop final formulation of Yb- and In-loaded LS and to build a prototype of suitable volume to study the backgrounds and detector performance. And the next step will be to select between Yb and In as the target element for LENS tests in the LLBF in 2002. After this selection, we hope to converge towards a proposal of the LENS project.

REFERENCES

1. B. T. Cleveland *et al.*, Astrophys. J. **496**, 505 (1998).
2. Super-Kamiokande Collab. (Y. Fukuda *et al.*), Phys. Rev. Lett. **86**, 5651 (2002).
3. GALLEX Collab. (W. Hampel *et al.*), Phys. Lett. B **477**, 127 (1999).
4. SAGE Collab. (J. N. Abdurashitov *et al.*), Phys. Rev. C **60**, 055801 (1999).
5. SNO Collab. (Q. R. Ahmad *et al.*), Phys. Rev. Lett. **87**, 071301 (2001).
6. J. N. Bahcall *et al.*, CERN-TH/2001-165.
7. R. S. Lanou *et al.*, Phys. Rev. Lett. **58**, 2498 (1987); S. R. Bandler *et al.*, Phys. Rev. Lett. **74**, 3169 (1995).
8. L. Baudis and H. V. Klapdor-Kleingrothaus, hep-ex/9906044.
9. F. Arzarello *et al.*, LPC/94-28 (CERN-LAA/94-19); J. Seguinot *et al.*, LPC/95-08 (CERN-LAA/95-11); LPC/96-31 (CERN-LAA/96-05).
10. H. Ejiri *et al.*, nucl-ex/9911008.
11. R. S. Raghavan, Phys. Rev. Lett. **78**, 3618 (1997).
12. R. S. Raghavan, Phys. Rev. Lett. **37**, 259 (1976); hep-ex/0106054.
13. M. Fujiwara *et al.*, Phys. Rev. Lett. **85**, 4442 (2000).
14. M. Bhattacharya *et al.*, Phys. Rev. Lett. **85**, 4446 (2000).
15. I. R. Barabanov *et al.*, Preprint No. 1042, INR RAS (Moscow, Institute for Nuclear Research, 2000).
16. R. Raghavan, Bell Labs Report No. 11172-990818-32T (1999).
17. V. N. Kornoukhov, Yad. Fiz. **63**, 2301 (2000) [Phys. At. Nucl. **63**, 2205 (2000)].
18. B. P. Kochurov *et al.*, Preprint No. 37-98, ITEP (Moscow, Institute of Theoretical and Experimental Physics, 1998).
19. S. N. Danshin, in *Proceedings of the Fourth International Solar Neutrino Conference, Heidelberg, Germany, 1997,* Ed. by W. Hampel (Max-Planck-Institut für Kernphysik, Heidelberg, 1997), p. 414.
20. NEMO Collab. (R. Arnold *et al.*), Nucl. Phys. A **636**, 209 (1998).
21. I. R. Barabanov *et al.*, Preprint INR RAS (March, 2000).
22. G. V. Korpusov, in *Proceedings of ISEC'88, Moscow, 1988* (Nauka, Moscow, 1988), Vol. I, p. 120.
23. R. Raghavan, Status Report on LENS, submitted to the Scientific Committee, LNGS (September 12, 2001).

Physics of Atomic Nuclei, Vol. 65, No. 12, 2002, pp. 2165–2170. From Yadernaya Fizika, Vol. 65, No. 12, 2002, pp. 2228–2233.

NEUTRINO PHYSICS AND ASTROPHYSICS

Search for Cold Dark Matter and Solar Neutrinos with GENIUS and GENIUS-TF*

I. V. Krivosheina[1)]

Radiophysical Research Institute, Nizhni Novgorod State University, ul. Lyadova 25/14, Nizhni Novgorod, 603600 Russia

Received February 13, 2002

Abstract—The new project GENIUS will cover a wide range of the parameter space of predictions of supersymmetry for neutralinos as cold dark matter. Further, it has the potential to be a real-time detector for low-energy (*pp* and ^{7}Be) solar neutrinos. The GENIUS Test Facility has just been funded and will come into operation by the end of 2001. © *2002 MAIK "Nauka/Interperiodica".*

1. INTRODUCTION

Concerning neutrino physics, without double beta decay there is no solution to the problem of the neutrino nature (Dirac or Majorana particle) and the neutrino mass matrix structure. Only investigation of neutrino oscillations and double beta decay together can lead to an absolute mass scale [1–7].

Concerning solar neutrino physics, present information on possible ν oscillations relies on 0.2% of the solar neutrino flux. The total *pp* neutrino flux has not been measured, and no real-time information is available for the latter either. Concerning the search for cold dark matter, direct detection of the latter by underground detectors remains indispensable.

The GENIUS project proposed in 1997 [7–12] as the first third-generation $\beta\beta$ detector could attack all of these problems with an unprecedented sensitivity. The main goals of GENIUS are dark matter search and double beta decay. In this paper, we concentrate on neutrino physics with emphasis on solar neutrinos and on some dark matter aspects. GENIUS will allow real-time detection of low-energy solar neutrinos with a threshold of 19 keV. For the further potential of GENIUS for other physics beyond the Standard Model, such as double beta decay and neutrino mass, supersymmetry (SUSY), compositeness, leptoquarks, and violation of Lorentz invariance and the equivalence principle, we refer to [5, 13, 14].

2. GENIUS AND LOW-ENERGY SOLAR NEUTRINOS

To solve the solar neutrino problem, measurement of the solar low-energy spectrum in real time is required. The prediction of the *pp* neutrino flux is almost solar-model independent and is strongly constrained by the solar luminosity and helioseismological measurements. The spectral distortion by oscillations allows one to distinguish between different oscillation solutions. To this end, a threshold below 300 keV is preferable [15]; i.e., the threshold should be lower than those achieved by the experiments GALLEX and SAGE and also lower than those of some future experiments. GALLEX and SAGE measure $pp + {}^7\mathrm{Be} + {}^8\mathrm{B}$ neutrinos (60% + 30% + 10%) down to 0.24 MeV, and the Chlorine experiment measured ^{7}Be + ^{8}B neutrinos (80% ^{8}B) above $E_\nu = 0.817$ MeV, all without spectral, time, and directional information. No experiment has separately measured *pp* and ^{7}Be neutrinos, and no experiment has measured the full *pp* ν flux. BOREXINO plans to measure ^{7}Be neutrinos in real time, the access to *pp* neutrinos being limited by ^{14}C contamination (the usual problem of organic scintillators). GENIUS, which was proposed for solar neutrino detection in 1999 [16, 17], could be the first detector measuring the full *pp* (and ^{7}Be) neutrino flux in real time (Fig. 1).

The main idea of GENIUS, originally proposed for double beta and dark matter search [7–12], is to achieve an extremely low radioactive background (factor of 1000 or smaller than in the Heidelberg–Moscow experiment) by using "naked" detectors in liquid nitrogen (Fig. 2). While for cold dark matter search 100 kg of natural Ge detectors are sufficient, GENIUS as a solar neutrino detector would contain 1–10 t of enriched ^{70}Ge or ^{73}Ge.

*This article was submitted by the author in English.

[1)]Max-Planck-Institut für Kernphysik, Heidelberg, Germany; e-mail: irina@mickey.mpi-hd.mpg.de

1063-7788/02/6512-2165$22.00

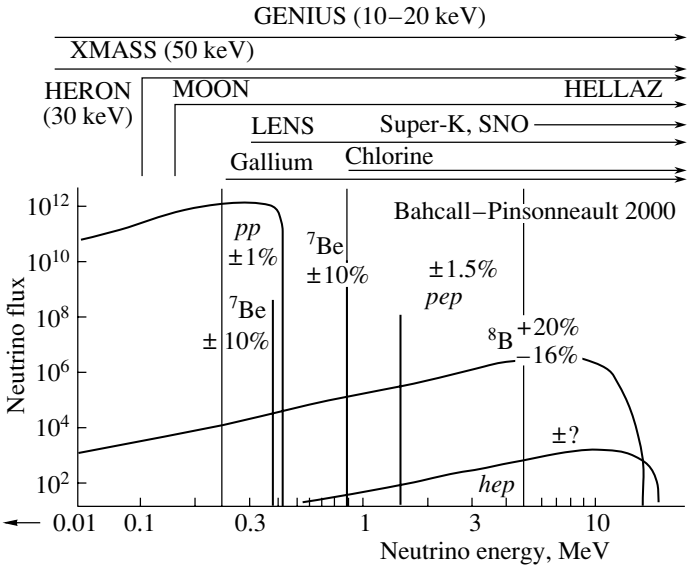

Fig. 1. The sensitivity (thresholds) of different running and projected solar neutrino detectors (see [16] and Heidelberg Nonaccelerator Particle Physics Group, http://www.mpi-hd.mpg.de/non_acc/).

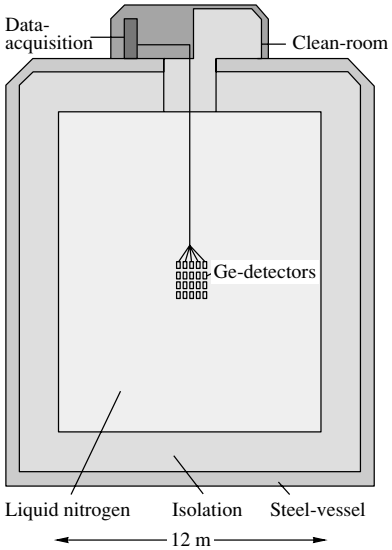

Fig. 2. Schematic view of the GENIUS project. An array of 100 kg of natural HPGe detectors for the weakly interacting massive particle (WIMP) dark matter search (first step) or between 0.1 and 1 t of enriched ^{76}Ge for the double-beta-decay search (final setup) is hanging on a support structure in the middle of the tank immersed in liquid nitrogen. For solar neutrino search, the detector would consist of one ton or more of enriched ^{73}Ge or ^{70}Ge. The size of the nitrogen shield would be 13 m in diameter at least. On top of the tank, a special low-level clean room and the room for the electronics and data acquisition will be placed.

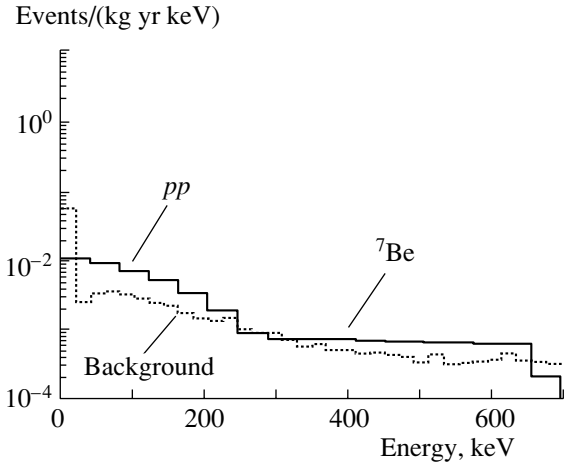

Fig. 3. Simulated spectrum of low-energy solar neutrinos (according to SSM) for the GENIUS detector (1 t of natural or enriched Ge) [16, 17] and estimated background.

The excellent operation of the Ge detectors in liquid nitrogen has been demonstrated in the Heidelberg low-level laboratory [18, 19], and the overall feasibility of the project has been shown in [9]. The potential of GENIUS to measure the spectrum of low-energy solar neutrinos in real time has been studied in [16, 17]. The detection reaction is elastic νe scattering $\nu + e^- \to \nu + e^-$. In νe scattering experiments, higher statistics are achieved than in absorption experiments, but no conicidence information is available, as in some of the future absorption experiments.

The maximum electron recoil energy is 261 keV for *pp* neutrinos and 665 keV for ^{7}Be neutrinos. The recoil electrons can be detected through their ionization in a HPGe detector with an energy resolu-

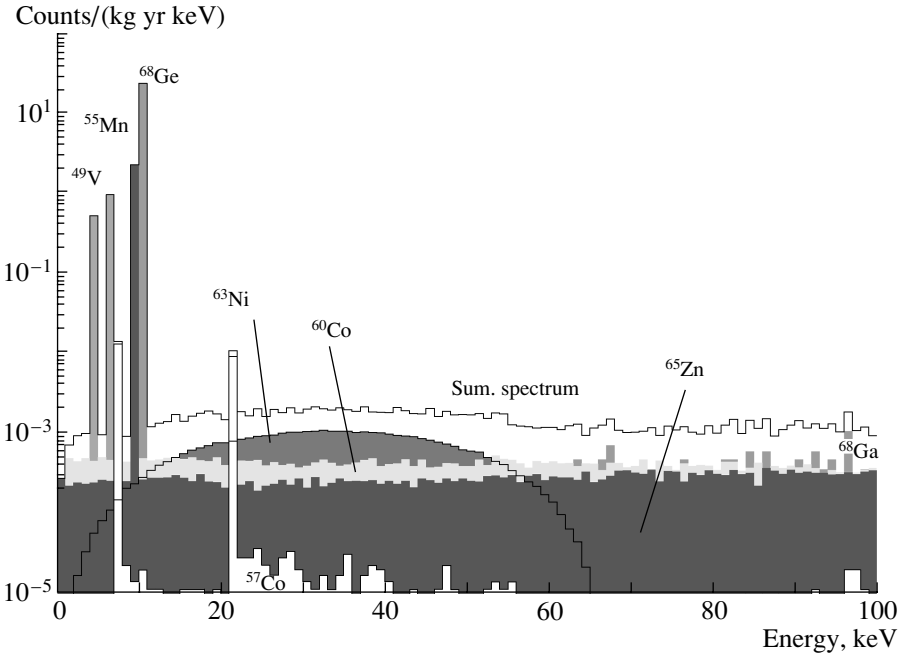

Fig. 4. Simulated cosmogenic background during detector production. Assumptions: 30-d exposure of the material before processing, 1-d activation after zone refining, and 3-yr deactivation underground (neglecting tritium production) (see [12, 14, 16, 22]).

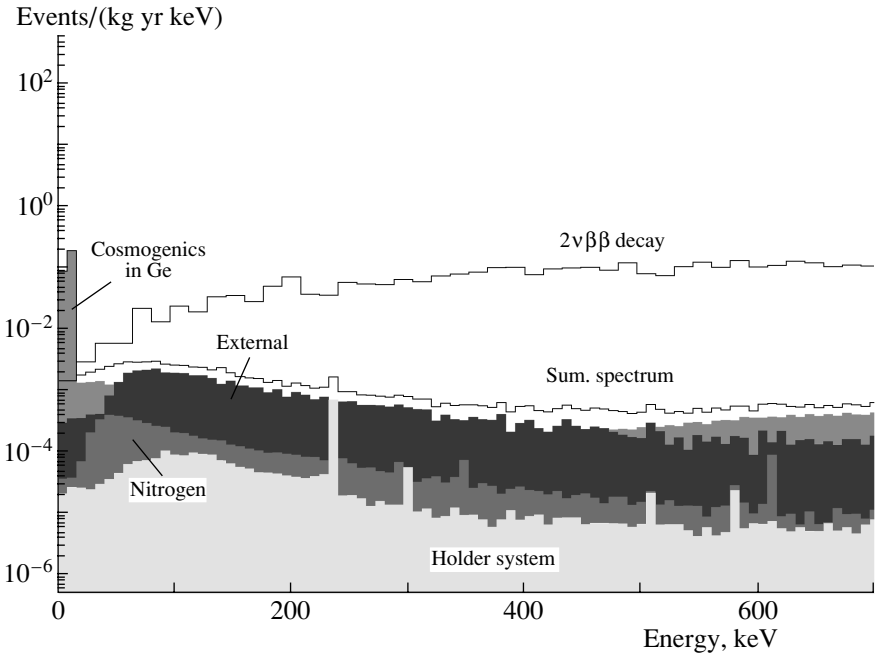

Fig. 5. Total background in a 13-m liquid-nitrogen tank for detectors produced as described in Fig. 4, but with 5-yr deactivation (tritium neglected) (see [7, 12, 14, 16, 22]).

tion of 0.3 %. Like BOREXINO (and some others experiments) GENIUS can measure only the energy distribution of recoiling electrons (but with much better energy resolution) and cannot directly determine the energy of the incoming neutrinos. The dominant part of the signal in GENIUS is produced by *pp* neutrinos (66%) and ^{7}Be neutrinos (33%). The detection rates for the *pp* and ^{7}Be fluxes are, according to the standard solar model [20], $R_{pp} = 35$ SNU =

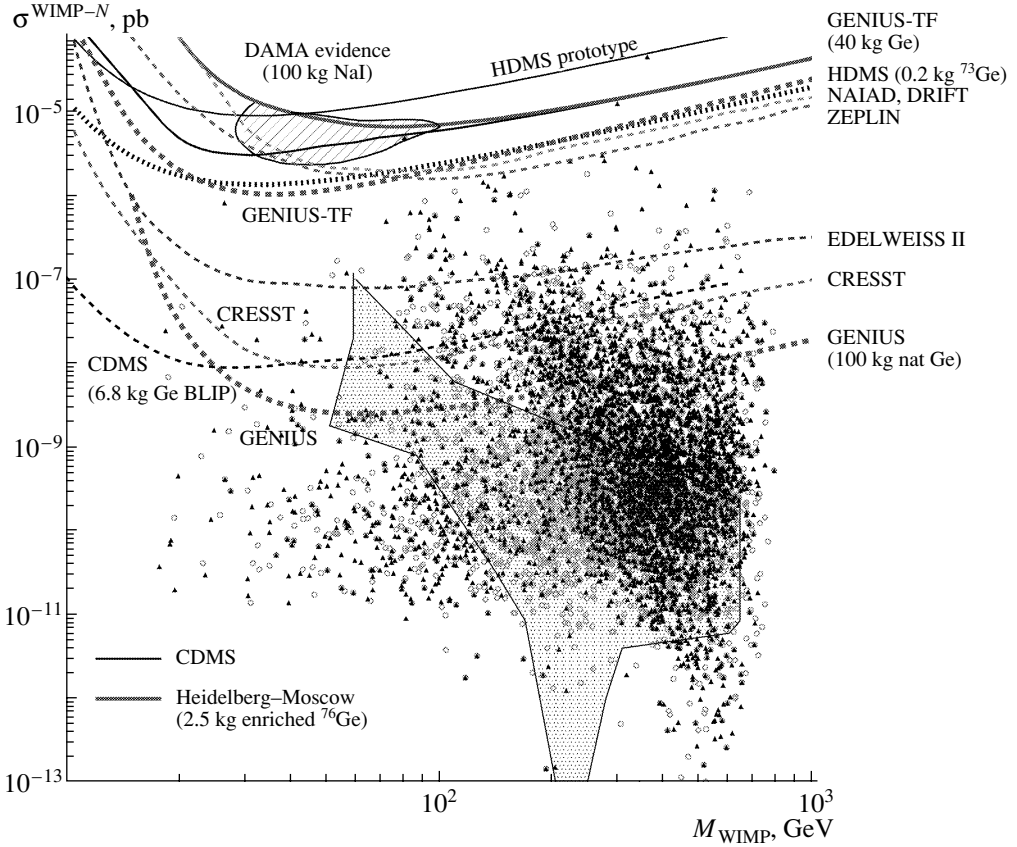

Fig. 6. WIMP-nucleon cross section limits for scalar interactions as a function of the WIMP mass. Shown are contour lines of the present experimental limits (solid curves) and of the projected experiments (dashed curves). Also shown is the region of evidence published by DAMA. The theoretical expectations are shown by two scatter plots for the nonaccelerating and accelerating Universe (from [28, 29] the MSSM) and by the gray region (from [30] SUGRA). Only GENIUS will be able to probe the shown range by the signature from seasonal modulations.

1.8 events/d/t (18 events/d in 10 t) and $R_{^7\mathrm{Be}} = 13$ SNU $= 0.6$ event/d/t (6 event/d in 10 t). The expected spectrum of the low-energy signal in the SSM is shown in Fig. 3.

After Super-Kamiokande disfavored the SMA solution of the solar neutrino problem, it is now important to distinguish the LMA and the LOW MSW solutions of the solar neutrino problem. GENIUS, due to its relatively high counting rate, will be able to test, in particular, the LOW MSW solution by the expected day/night variation of the flux [16, 17, 21].

To measure the low-energy solar neutrino flux with a signal-to-background ratio of 3 : 1, the required background rate is about 1×10^{-3} event/(kg yr keV) in this energy range. It is about a factor of 10 smaller than what is required for the application of GENIUS for cold dark matter search. This can be achieved if the liquid nitrogen shielding is increased to at least 13 m in diameter and production of the Ge detectors is performed underground [16, 17].

Most attention has to be given to the cosmogenic activation (Fig. 4) of the Ge crystals at the Earth's surface [16]. Figure 5 shows the total background in a 13-m liquid-nitrogen tank for the produced detectors assuming 30 d of exposure to cosmic rays before detector production, one day of activation after zone refining, and a deactivation time of five years.

Another source of background is the $2\nu\beta\beta$ decay of ^{76}Ge, which has 7.8% abundance in natural Ge. The expected rate for a detector of natural Ge is also shown in Fig. 5. Using enriched ^{70}Ge or ^{73}Ge ($>85\%$) as a detector material, one can reduce the abundance of the $\beta\beta$ emitter by a factor of 1500. In this case the *pp* signal will not be disturbed by the $2\nu\beta\beta$ decay.

3. GENIUS AND COLD DARK MATTER SEARCH

GENIUS is the only one of the new projects under discussion (see Table 3 from [23]) that simultaneously with its potential for real-time detection of low-energy neutrinos and for double-beta decay has a huge potential for cold dark matter search. Right now,

the Heidelberg–Moscow experiment is the most sensitive dark matter experiment worldwide concerning the raw data [24–27]. GENIUS, already at the first step with 100 kg of natural Ge detectors would cover a significant part of the MSSM parameter space for prediction of neutralinos as cold dark matter (Fig. 6) (see, e.g. [28–30]. For this purpose, the background in the energy range <100 keV has to be reduced to 10^{-2} event/(kg yr keV), which is possible if the detectors are produced and handled on the Earth's surface under heavy shielding [16, 27]. Figure 5 shows that at this level solar neutrinos as a source of background are still negligible. Figure 6 shows, together with the expected sensitivity of GENIUS, predictions for neutralinos as dark matter by two models, one based on supergravity [30] and the other based on the MSSM with relaxed unification conditions [28, 29].

The sensitivity of GENIUS for dark matter corresponds to that obtainable with a 1 km^3 AMANDA detector for indirect detection (neutrinos from annihilation of neutralinos captured at the Sun) (see [31]. Interestingly, both experiments would probe different neutralino compositions. GENIUS will mainly probe gaugino-dominated neutralinos, and AMANDA will mainly probe neutralinos with comparable gaugino and Higgsino components (see Fig. 38 in [31]. It should be stressed that GENIUS, together with DAMA, will be the only future dark matter experiment that would be able to positively identify a dark matter signal by the seasonal modulation signature. This cannot be achieved, for example, by the CDMS experiment.

4. GENIUS-TF

As the first step of GENIUS, a small test facility (GENIUS-TF) is at present under installation in the Gran Sasso Underground Laboratory [32]. With about 40 kg of natural Ge detectors operated in liquid nitrogen, GENIUS-TF could test the DAMA seasonal modulation signature for dark matter. No other experiment running, like CDMS and IGEX, or projected at present will have this potential [33]. By summer 2001, six 2.5-kg Ge detectors with an extremely low level threshold of 500 eV were produced.

5. CONCLUSION

GENIUS, proposed as the first third-generation $\beta\beta$ detector, has been shown to have a huge potential for cold dark matter search. It can further be used to investigate the full solar *pp* neutrino spectrum in real time, with a threshold of 20 keV. The GENIUS Test Facility is at present under installation in the Gran Sasso Underground Laboratory.

REFERENCES

1. Heidelberg-Moscow Collab. (H. V. Klapdor-Kleingrothaus *et al.*), Eur. Phys. J. A **12**, 147 (2001); hep-ph/0103062; in *Proceedings of the Third International Conference on Dark Matter in Astro- and Particle Physics DARK'2000,* Ed. by H. V. Klapdor-Kleingrothaus (Springer-Verlag, Heidelberg, 2001), pp. 520–533.
2. H. V. Klapdor-Kleingrothaus, A. Dietz, H. L. Harney, and I. V. Krivosheina, Mod. Phys. Lett. A **16**, 2409 (2001).
3. H. V. Klapdor-Kleingrothaus, H. Päs, and A. Yu. Smirnov, Phys. Rev. D **63**, 073005 (2001); in *Proceedings of the Third International Conference on Dark Matter in Astro- and Particle Physics DARK'2000,* Ed. by H. V. Klapdor-Kleingrothaus (Springer-Verlag, Heidelberg, 2001), pp. 420–434; hep-ph/0103076.
4. H. V. Klapdor-Kleingrothaus and U. Sarkar, Mod. Phys. Lett. A **16**, 2469 (2001).
5. H. V. Klapdor-Kleingrothaus, *60 Years of Double Beta Decay—From Nuclear Physics to Beyond the Standard Model* (World Sci., Singapore, 2001).
6. H. V. Klapdor-Kleingrothaus and H. Päs, physics/0006024.
7. H. V. Klapdor-Kleingrothaus, in *Proceedings of International Workshop on Neutrino Oscillations and Their Origin, NOON'2000, Tokyo, 2000* (World Sci., Singapore, 2001); hep-ph/0103074.
8. H. V. Klapdor-Kleingrothaus, in *Proceedings of the First International Conference on Particle Physics Beyond the Standard Model, BEYOND'97, Castle Ringberg, Germany, 1997,* Ed. by H. V. Klapdor-Kleingrothaus and H. Päs (Institute of Physics, Bristol, 1998), pp. 485–531.
9. H. V. Klapdor-Kleingrothaus *et al.*, MPI-Report MPI-H-V26-1999; hep-ph/9910205; in *Proceedings of the 2nd International Conference on Particle Physics Beyond the Standard Model, BEYOND'99, Castle Ringberg, Germany, 1999,* Ed. by H. V. Klapdor-Kleingrothaus and I. V. Krivosheina (Institute of Physics, Bristol, 2000), pp. 915–1014.
10. H. V. Klapdor-Kleingrothaus, in *Proceedings of the 18th International Conference on Neutrino Physics and Astrophysics, NEUTRINO 98, Takayama, Japan, 1998,* Ed. by Y. Suzuki *et al.*; Nucl. Phys. B (Proc. Suppl.) **77**, 357 (1999).
11. H. V. Klapdor-Kleingrothaus, in *Proceedings of the Fifth International WEIN Conference on Physics Beyond the Standard Model, WEIN'98,* Ed. by P. Herczeg, C. M. Hoffman, and H. V. Klapdor-Kleingrothaus (World Sci., Singapore, 1999), pp. 275–311.
12. H. V. Klapdor-Kleingrothaus, in *Proceedings of International Conference "Origins of Neutrino Oscillations", NOW2000, 2000*; Nucl. Phys. B (Proc. Suppl.) **100**, 309 (2001); **100**, 350 (2001); hep-ph/0102277; hep-ph/0102276.

13. H. V. Klapdor-Kleingrothaus, in *Proceedings of the "Neutrinos in Astro-, Particle and Nuclear Physics International School in Nuclear Physics (23rd course)," Erice, 2001*; Prog. Part. Nucl. Phys. **48** (2002) (in press).
14. H. V. Klapdor-Kleingrothaus, Part. Nucl. Lett., No. 1 [**104**], 20 (2001); hep-ph/0102319.
15. J. N. Bahcall and P. I. Krastev, Phys. Rev. C **56**, 2839 (1997).
16. H. V. Klapdor-Kleingrothaus, in *Proceedings of International Workshop on Low-Energy Solar Neutrinos "LowNu2," Tokyo, Japan, 2000,* Ed. by Y. Suzuki (World Sci., Singapore, 2001); hep-ph/0104028.
17. L. Baudis and H. V. Klapdor-Kleingrothaus, Eur. Phys. J. A **5**, 441 (1999); in *Proceedings of the 2nd International Conference on Particle Physics Beyond the Standard Model "BEYOND'99", Castle Ringberg, Germany, 1999,* Ed. by H. V. Klapdor-Kleingrothaus and I. V. Krivosheina (Institute of Physics, Bristol, 2000), pp. 1023–1036.
18. J. Hellmig and H. V. Klapdor-Kleingrothaus, Z. Phys. A **359**, 351 (1997).
19. L. Baudis, Heusser, B. Majorovits, *et al.*, hep-ex/9811040; Nucl. Instrum. Methods Phys. Res. A **426**, 425 (1999).
20. J. N. Bahcall, S. Basu, and M. Pinsonneault, Phys. Lett. B **433**, 1 (1998).
21. H. V. Klapdor-Kleingrothaus, Springer Tracts Mod. Phys. **163**, 69 (2000);
22. H. V. Klapdor-Kleingrothaus *et al.*, http://www.mpi-hd.mpg.de/non_acc
23. H. V. Klapdor-Kleingrothaus, Yad. Fiz. **65** (12), 2198 (2002) [Phys. At. Nucl. **65**, 2135 (2002)].
24. HEIDELBERG-MOSCOW Collab. (L. Baudis *et al.*), Phys. Rev. D **59**, 022001 (1999).
25. L. Baudis, A. Dietz, B. Majorovits, *et al.*, Phys. Rev. D **63**, 022001 (2000); astro-ph/0008339.
26. CRESST Collab. (Y. Ramachers *et al.*), in *Proceedings of the XI Rencontres de Blois, Frontiers of the Matter, France, 1999.*
27. H. V. Klapdor-Kleingrothaus *et al.*, in *Proceedings of the Third International Conference on Dark Matter in Astro- and Particle Physics, DARK'2000, Heidelberg, Germany, 2000,* Ed. by H. V. Klapdor-Kleingrothaus (Springer-Verlag, Heidelberg, 2001), pp. 553-568; hep-ph/0103082.
28. V. A. Bednyakov and H. V. Klapdor-Kleingrothaus, Phys. Rev. D **62**, 043524 (2000); hep-ph/9908427.
29. V. A. Bednyakov and H. V. Klapdor-Kleingrothaus, Phys. Rev. D **63**, 095005 (2001); hep-ph/0011233.
30. J. Ellis, A. Ferstl, and K. A. Olive, Phys. Lett. B **481**, 304 (2000); hep-ph/0007113.
31. J. Edsjö, *"Neutralinos as Dark Matter — Can We See Them?": Seminar given in the Theory Group, Department of Physics, Stockholm University, 1999,* http://www.physto.se/edsjo
32. H. V. Klapdor-Kleingrothaus, L. Baudis, A. Dietz, *et al.*, hep-ex/0012022.
33. H. V. Klapdor-Kleingrothaus, in *Proceedings of the XX Lepton Photon Symposium, Rome, Italy, 2001* (World Sci., Singapore, 2002).

Physics of Atomic Nuclei, Vol. 65, No. 12, 2002, pp. 2171–2175. From Yadernaya Fizika, Vol. 65, No. 12, 2002, pp. 2234–2238.

NEUTRINO PHYSICS AND ASTROPHYSICS

Results from the Mainz Neutrino Mass Experiment*

J. Bonn, B. Bornschein[1)], L. Bornschein, L. Fickinger, B. Flatt, A. Kovalik[2)], Ch. Kraus, E. W. Otten[**], J. P. Schall, Th. Thümmler, H. Ulrich, and Ch. Weinheimer

Institute of Physics, Joh. Gutenberg University, Mainz, Germany

Received February 13, 2002

Abstract—The presently lowest limit for the mass of the electron neutrino is $m_\nu < 2.2$ eV/c^2 (95% C.L.) derived from measurements at Mainz up to 1999. The data taken in 2000 are not fully analyzed yet, but limits of possible distortions as reported by the Troitsk group can be given. © *2002 MAIK "Nauka/Interperiodica".*

1. INTRODUCTION

Nonzero neutrino masses, strongly favored by the recent atmospheric [1] and solar neutrino [2] experiments, have strong consequences for particle physics as well as for astrophysics and cosmology. The investigation of the tritium β spectrum near its endpoint measures the mean square of the mass of the electron neutrino

$$m_{\nu_e}^2 = \sum_j |U_{ej}|^2 \, m_j^2 \qquad (1)$$

with neutrino mixing matrix U and neutrino mass eigenstates m_j; it is the most sensitive of the so-called direct methods and provides information complementary to the searches for neutrinoless double β decay. The latter experiments measure the square of a so-called effective neutrino mass

$$m_{ee}^2 = \left| \sum_j U_{ej}^2 m_j \right|^2 \qquad (2)$$

which depends on phases of the U_{ej}. This might lead to cancellations. Anyway, both results together would be cornerstones in setting up the neutrino mixing matrix [3]. Tritium β decay is also an ideal method to distinguish between hierarchical and degenerate neutrino mass models. Furthermore, neutrino masses up to about 1 eV/c^2 are especially interesting for cosmology because of their contribution to the missing hot dark matter in the universe. A mass of about 1 eV/c^2 is favorably fitting models of structure formation [4].

Tritium β-decay experiments are currently running at Mainz and Troitsk [5, 6]. Their high sensitivity is due to a new type of spectrometer, the so-called MAC-E filter (magnetic adiabatic collimation followed by an electrostatic filter) [7]. The Mainz Neutrino Mass Experiment uses as a tritium source a film of molecular tritium quench-condensed onto a highly oriented graphite substrate. The film has a diameter of 17 mm and a typical thickness of 40 nm, which is measured by laser ellipsometry.

The Mainz experiment has been recently upgraded [5, 8, 9] to improve the sensitivity to m_ν down to a limit of 2 eV/c^2 and to check the anomalous excess in the spectrum close to the endpoint reported by the Troitsk group [6, 10].

2. DATA TAKING IN 1998 AND 1999

With the improved setup, six runs (labeled Q3–Q8) of seven-month measurement time in total were taken in 1998 and 1999. Additional studies on quench-condensed T_2 films clarified their energy loss function [11], their self-charging [8, 9], and their dewetting as a function of temperature [12, 13]. In particular, the suppression of the latter effect has removed the trend towards negative values of m_ν^2 in excess of -100 eV$^2/c^4$ for wide data intervals from which our 1991 and 1994 data suffered. Still, the first two data sets of 1998 (Q3, Q4) do not fulfill the requirement of being stable with respect to the variation of the lower limit of the fit range and being compatible with the physical allowed range of $m_\nu^2 \geq 0$. But deviations were limited to -10 eV$^2/c^4$, corresponding to a 2σ level. The origin of this small residual spectral distortion has not yet been completely clarified, but is certainly connected to a minute instrumental effect depending on running conditions (see below). This statement is corroborated by the fact that the later

*This article was submitted by the authors in English.

[1)]Present address: TLK, Forschungszentrum Karlsruhe, Germany.

[2)]Joint Institute for Nuclear Research, Dubna, Moscow oblast, 141980 Russia.

[**]e-mail: Ernst.Otten@uni-mainz.de

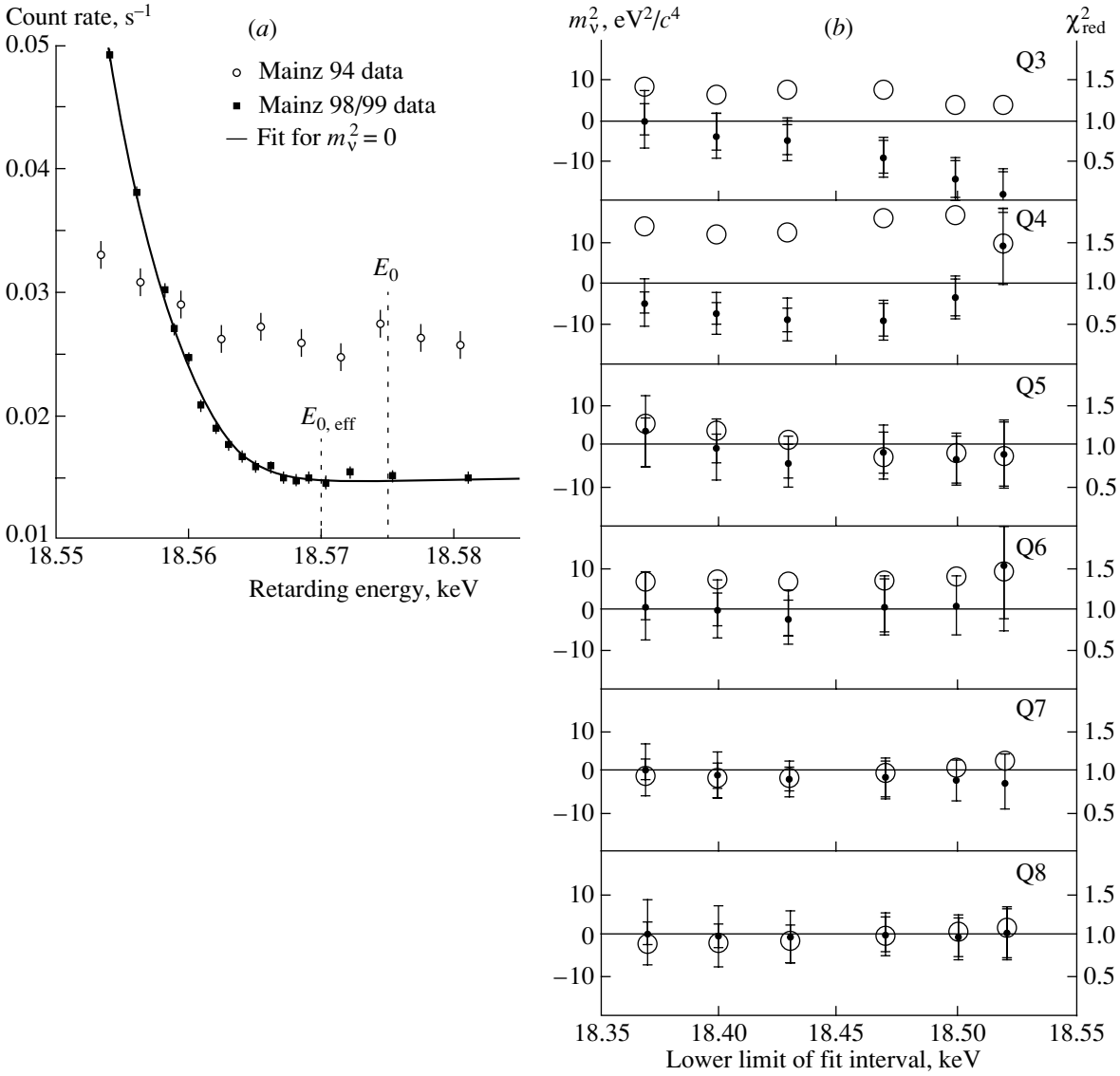

Fig. 1. (*a*) Averaged count rate of the combined 1998 and 1999 data Q3–Q8 (points) with fit (line) in comparison with previous Mainz data from 1994 as function of the retarding energy near the endpoint E_0 and effective endpoint $E_{0,\mathrm{eff}}$. The position of the latter takes into account the width of the response function of the setup and the mean rotation-vibration excitation energy of the electronic ground state of the $(\mathrm{T}^3He)^+$ daughter molecule. (*b*) Fit results on m_ν^2 (left scale, filled circles) for the different runs Q3–Q8 with statistical (inner bars) and total uncertainties (outer bars) as a function of the lower limit of the fit interval. The upper limit is always 18.66 keV, well above the endpoint $E_0 = 18.57$ keV. The corresponding values of $\chi^2_{\mathrm{red}} = \chi^2/\mathrm{d.o.f.}$ of the fits (open circles) can be read from the right scale.

runs Q5 to Q8 showed absolutely "clean" spectra (Fig. 1). This improvement was probably due to a lowering and a stabilization of the background rate achieved by applying RF pulses to one of the electrodes of the electrostatic filter in the measuring pauses during which the filter potential was changed. This way, some trapped charges were swept out of the spectrometer, apparently. Trapped particles cause background events through secondary reactions with the residual gas.

Figure 1*a* shows the integral β spectrum as function of the filter potential for the last 15 eV below the endpoint $E_0 = 18\,575$ eV plus the background region above E_0. Plotted is the count rate averaged over the runs Q3 to Q8; data obtained in 1994 [14] are shown for comparison. Three comments are to be made:

(i) The improved spectrometer yields a signal-to-background ratio 10 times better than before and meanwhile much better statistics have been obtained.

(ii) The signal separates clearly from the constant background a few eV below the effective endpoint $E_{0,\mathrm{eff}}$. The latter is shifted about 5 eV below E_0 due to

the finite width of the filter of 4.8 eV and a mean rovibrational excitation energy of 1.7 eV of the daughter molecule $(T\ ^3He)^+$. This indicates already a "prima vista" upper mass limit of a few eV.

(iii) A fit with m_ν^2 fixed to zero perfectly fits the new data set. This limits any persistent spectral anomaly in this range to an amplitude well below 10^{-3} s^{-1} (as against a total flux of 10^8 s^{-1} entering the spectrometer). The fluctuating Troitsk anomaly, on the other hand, reaches amplitudes up to 10^{-2} s^{-1} (Fig. 2) [6].

3. CHECK OF THE TROITSK ANOMALY

The Troitsk group has described its anomaly as a sharp step of the count rate close to E_0 [10]. Since their spectrometer is integrating like the Mainz one, this step corresponds to a line in the primary spectrum, its relative intensity being about 10^{-10} of the total decay rate. In 1998, the Troitsk group reported that the position of this line oscillates with a frequency of 0.5 yr between 5 and 15 eV below E_0 [6].

We tested our Mainz data from 1998 and 1999, whether they support the existence of a Troitsk anomaly or not, by adding a monoenergetic line to the β spectrum in the fits with free amplitude but with a position corresponding to the positions predicted by the Troitsk 0.5-yr oscillation hypothesis according to [6].

Figure 2 shows the fitted line amplitude with m_ν^2 fixed to zero[3)] in comparison with Troitsk results from [6] as function of the month. Whereas the fitted amplitudes for data sets Q3 and Q5–Q8 fluctuate around zero, data set Q4 is different: It shows a significantly large amplitude of 6 mHz, which is in the range of the values reported by Troitsk. No other significant Troitsk anomaly has been found in the whole data set Q3 to Q8, also not outside the predicted positions [15].

From October to the end of the year 2000, we again took data, divided up into two runs, Q9 and Q10, taking a fresh T_2 film in the break in between. Again no significant steplike anomaly was found, in particular, in those two subsets of data which were obtained in parallel to data taking at Troitsk (Dec. 6–13 and Dec. 22–28). In both periods, Troitsk observed significant steps [16], but with a drastic change in position and amplitude in between which does not fit into the previous pattern of a half-year period of the effect.

Although, we did not find steplike signatures in the latest runs Q9 and Q10, most (not all) of the data

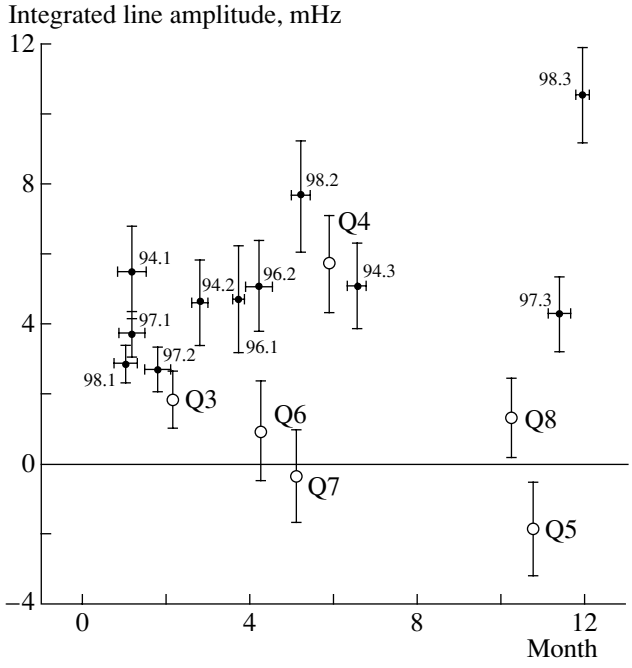

Fig. 2. Amplitude of the Troitsk anomaly from Troitsk data (points, from [6]) and from Mainz data (open circles). In the Mainz analysis, the line position was taken from the prediction of a half-year sinusoidal curve from [6]. Mainz data were fitted over the last 70 eV of the β spectrum with m_ν^2 fixed to zero. The error bars of the Mainz data contain both statistical and systematic uncertainties.

subsets suffered again from small residual perturbations which resulted in negative m_{nu}^2 fit results in the range of -10 eV$^2/c^4$. In this context, we mention that any residual disturbance count rate appearing in an interval about 5 eV around E_0 cannot be decorrelated from m_ν^2 by a χ^2 fit at the given statistics but will inevitably lead to a negative m_ν^2 fit result. Part of the data also showed a slight hysteresis between up- and down-scanning of the spectrum. If charge trapping depends on the scanning position, which is conceivable, then the resulting background events may well show a hysteresis. We ascribe the reappearance of slight spectral irregularities in our data to a somewhat less favorable status of the spectrometer. Contrary to earlier runs, we have not baked it beforehand this time. Hence, vacuum and surface conditions probably have changed a bit to the worse, which cannot be controlled with precision at a UHV level of about 10^{-10} mbar residual gas pressure. We know, on the other hand, that above 10^{-9} mbar a kind of Penning plasma develops in the spectrometer with time constants of minutes to hours, manifesting itself by a corresponding increase in background.

All these observations leave little doubt that the residual spectral anomalies discussed here are of in-

[3)] Letting m_{nu}^2 be free in the fits changes the results only marginally.

strumental origin and connected to the particular electrodynamics of MAC-E filters and, moreover, that they can be overcome by paying utmost attention to UHV and surface conditions as well as to the electromagnetic design.

4. EVALUATION OF MASS LIMITS

We present two different types of analysis (all limits are calculated by using the unified approach) [17]:

(i) The data sets of all runs within one year were taken under nearly the same conditions. Therefore, the combined data set of all runs from 1998, Q3–Q5, and all from 1999, Q6–Q8, can be used. For this analysis, these data were fitted over the last 15 eV of the β spectrum only. Due to the high thresholds for excitation of the electron shell of T_2 or the daughter $(T\,^3He)^+$, respectively, uncertainties from energy loss, final states, etc., could not affect these last 15 eV of the β spectrum. However, to decorrelate m_ν^2 from the endpoint position E_0 and amplitude A, the two data points at 18.470 keV (18.460 keV) and at 18.500 keV have been added to this fit, bringing back some influence of systematic uncertainties. Another advantage of this method is that a Troitsk-like anomaly appearing more than 10 eV below E_0 as in Q4, after having been convoluted with the response function of the experiment, does not influence the result of this fit anymore. The fit results of (Q3–Q5) $m_\nu^2 = +0.1 \pm 3.9 \pm 2.1$ eV$^2/c^4$ and (Q6–Q8) $m_\nu^2 = +1.5 \pm 3.2 \pm 3.4$ eV$^2/c^4$ can be combined to $m_\nu^2 = +0.6 \pm 2.8 \pm 2.5$ eV$^2/c^4$, which corresponds to an upper limit of $m_\nu \leq 2.8$ eV$/c^2$ (95% C.L.).

(ii) The second analysis contains data down to 70 eV below E_0. For this interval, the combined statistical and systematic uncertainty attains a minimum. Since we still insist on this extended interval to be free of any residual anomaly, we confine the analysis to the "clean" runs Q5 to Q8 (compare Fig. 1*b*). The result is $m_\nu^2 = -1.6 \pm 2.5 \pm 2.1$ eV$^2/c^4$, which corresponds to an upper limit of $m_\nu \leq 2.2$ eV$/c^2$ (95% C.L.). Looking at the m_ν^2 results first, we see that both analyses yield values fully compatible with zero and that the gain in intensity by extending the data interval from 15 to 70 eV is rather modest. It improves the resulting upper limit on m_ν^2 by only 0.2 eV$/c^2$. The additional 0.4 eV$/c^2$ improvement in the second analysis is kind of mathematical artifact introduced by the prescription of the unified model of how to transform a m_ν^2 result into an upper limit of m_ν; it favors slightly negative mass values.

5. OUTLOOK

With the present results, the Mainz neutrino mass experiment has almost exhausted its sensitivity limit. In final measurements, we attempt to regain an optimum status of the apparatus and clean spectra. Further studies will explore possibilities of how to improve background conditions substantially in view of a second generation experiment.

To clarify the possibility of a cosmologically relevant amount of neutrino dark matter, a further improvement of the sensitivity on m_ν down to less than 1 eV$/c^2$ is needed. The same holds for improving our knowledge of the neutrino mixing matrix.

In a previous paper [18], we investigated the possibility of a spectrometer based on the same MAC-E filter principle but scaled up by about two orders in magnitude in the product of luminosity and resolution. By an additional time-of-flight analysis, the spectrometer transforms from an integrating high-pass filter into a narrowband filter (MAC-E-TOF mode). In a first proof-of-principle experiment, this new method was successfully tested with the present Mainz spectrometer [18]. Recently, the feasibility and the physical prospects of a large tritium β spectrometer with a 7-m diameter aiming for a 0.3-eV$/c^2$ sensitivity to the electron neutrino mass was discussed at an international workshop at Bad Liebenzell [19]. The experiment is proposed by the KATRIN collaboration (KATRIN: KArlsruhe TRItium Neutrino experiment) presently consisting of groups from Fachhochschule Fulda, Forschungszentrum Karlsruhe (FZK), University of Karlsruhe, University of Mainz, Czech Academy of Sciences at Prague, University of Washington at Seattle, and Institute of Nuclear Research at Troitsk. It is planned to build and run the experiment at FZK to benefit from its outstanding infrastructure.

ACKNOWLEDGMENTS

This work was supported by the Deutsche Forschungsgemeinschaft under contract no. Ot33/13 and by the German Bundesministerium für Bildung und Forschung under contract no. 06MZ866I/5. A. K. is indebted to the Deutsche Forschungsgemeinschaft for funding his stays at Mainz.

REFERENCES

1. Y. Fukuda *et al.*, Phys. Rev. Lett. **85**, 3999 (2000).
2. Q. R. Ahmad *et al.*, nucl-ex/0106015.
3. Y. Farzan *et al.*, hep-ph/0105105.
4. M. Tegmark *et al.*, Phys. Rev. D **63**, 043007 (2001).
5. Ch. Weinheimer *et al.*, Phys. Lett. B **460**, 219 (1999).
6. V. M. Lobashev *et al.*, Phys. Lett. B **460**, 227 (1999).

7. A. Picard *et al.*, Nucl. Instrum. Methods Phys. Res. B **63**, 345 (1992).
8. H. Barth *et al.*, Prog. Part. Nucl. Phys. **40**, 353 (1998).
9. B. Bornschein, PhD Thesis (Mainz University, 2000).
10. A. I. Belesev *et al.*, Phys. Lett. B **350**, 263 (1995).
11. V. N. Aseev *et al.*, Eur. Phys. J. D **10**, 39 (2000).
12. L. Fleischmann *et al.*, J. Low Temp. Phys. **119**, 615 (2000).
13. L. Fleischmann *et al.*, Eur. Phys. J. B **16**, 521 (2000).
14. H. Backe *et al.*, in *Proceedings of Neutrino 96, Helsinki, 1996* (World Sci., Singapore, 1997).
15. Ch. Kraus, Diploma Thesis (Mainz University, 2000).
16. V. M. Lobashev, *Talk given at NANP01, Dubna, June 2001*.
17. J. Bonn *et al.*, Nucl. Phys. B (Proc. Suppl.) **91**, 273 (2001).
18. J. Bonn *et al.*, Nucl. Instrum. Methods Phys. Res. A **421**, 256 (1999).
19. *Proceedings of the International Workshop on the "Neutrino Masses in the sub-eV Range," Bad Liebenzell, Germany, 2001,* http://www.ik1.fzk.de/tritium/liebenzell/

Physics of Atomic Nuclei, Vol. 65, No. 12, 2002, pp. 2176–2183. From Yadernaya Fizika, Vol. 65, No. 12, 2002, pp. 2239–2246.

Weak-Interaction Observables from Nuclear-Structure Calculations of $0\nu\beta\beta$ Decay Transitions*

J. Suhonen**

Department of Physics, University of Jyväskylä, Finland

Received February 13, 2002

Abstract—The present status of the calculation of the nuclear matrix elements associated with neutrinoless double-beta decay is discussed. The currently available approaches, as well as the historical perspective, are presented in this review. The discussion is restricted to nuclear matrix elements relevant in the context of the light Majorana-neutrino-mediated decays to the ground state and excited states of the final nucleus. Special emphasis is laid on the quantitative description of the $0\nu\beta\beta$ decay transitions to the excited 0^+ states, a subject of very recent interest in the double-beta community. © *2002 MAIK "Nauka/Interperiodica".*

1. INTRODUCTION

The early attempts to calculate nuclear matrix elements associated with the two-neutrino ($2\nu\beta\beta$) and neutrinoless ($0\nu\beta\beta$) modes of double-beta decay mostly concentrate on using the nuclear shell model (SM) as the starting point [1–3]. Due to the fact that the double-beta-decaying nuclei are mostly medium-heavy or heavy nuclei, either the weak-coupling limit of the shell model or heavy truncations in the configuration space had to be used in carrying out the numerical computation. Later, more suitable truncation schemes for treating heavy open-shell nuclei were developed. These methods were based on the quasiparticle random-phase approximation, and they still continue to be popular models in discussing various aspects of double-beta decay.

The two-neutrino decay mode has been traditionally used for testing the available nuclear models to be used, in the end, for calculations of the nuclear matrix elements associated with the neutrinoless decay mode. The $2\nu\beta\beta$ decay is an ideal laboratory for nuclear-structure studies since decay half-lives for many decay transitions have been measured in the underground experiments. In addition, the $2\nu\beta\beta$ decay is simpler to study than the $0\nu\beta\beta$ decay from the nuclear-structure point of view because only the 1^+ intermediate excitations contribute to the transition amplitude, whereas in the $0\nu\beta\beta$ decay all the intermediate multipolarities are active in the decay amplitude. Furthermore, the $2\nu\beta\beta$ decay rates are strongly retarded, indicating a strong suppression in the associated nuclear matrix elements as compared to the predictions of the simple shell model. This makes the $2\nu\beta\beta$ decay sensitive to adopted truncation schemes (nuclear models). Finally, it seems that the $2\nu\beta\beta$ decay rates to excited 0^+ and 2^+ final states are not suppressed and behave in a different way than the decays to the final 0^+ ground state. As a matter of fact, in [4] it was systematically shown that the decay transitions to the excited two-phonon type of 0^+ states were very stable against the variations in the strength of the proton–neutron particle–particle interaction, and not suppressed like the ground-state transition with the increase in this strength. Experimentally, several studies of these transitions were recently performed [5], the most notable ones being the measurement of the half-life of the decay transition of ^{100}Mo to the first excited 0^+ state in ^{100}Ru [6–8] with the recommended [9] half-life value of $(6.8 \pm 1.2) \times 10^{20}$ yr. This can now be contrasted against the behavior of similar transitions in the $0\nu\beta\beta$-decay mode, discussed later in this article.

For the neutrinoless double-beta ($0\nu\beta\beta$) decay, only lower limits for the half-lives of the decay transitions to the ground and excited states are known [5, 10]. As in the case of the $2\nu\beta\beta$ decay, also for the $0\nu\beta\beta$ decay, the study of the excited-state transitions opens up a new possibility of studying the associated physical observables of interest. For the $0\nu\beta\beta$ decay, these observables are the weak-interaction parameters of theories predicting Majorana neutrinos, right-handed currents, sparticles (supersymmetry), leptoquarks, etc. (see, e.g., [11–13]). In the decays to the excited states, one loses in the lepton phase space but gains in the signal-to-background ratio due to the possibility of using coincidense techniques

*This article was submitted by the author in English.

**e-mail: suhonen@phys.jyu.fi

for the γ rays that deexcite the $0\nu\beta\beta$ final state. An efficient use of these techniques requires, however, a massive enough source, so that only experiments with huge active-mass detectors can serve for this purpose. Many such experiments are currently being planned (e.g. CAMEO, EXO, GENIUS, MOON).

As mentioned above, there is one argument favoring and one argument disfavoring the detection of $0\nu\beta\beta$ decay to excited states. The third decisive component in the game is the magnitude of the associated nuclear matrix elements. This component was first studied for the decays to the first excited 2^+ states in [14, 15]. In these works, it was found that the nuclear matrix elements disfavored these decay transitions with respect to the ground-state transitions, and thus the probability of observing this decay mode would be very small. This is along the lines of the corresponding decays for the $2\nu\beta\beta$ mode, where it was found [4, 16] that the matrix elements corresponding to the $2\nu\beta\beta$ decays to the first 2^+ state were very much suppressed relative to the ones corresponding to the ground-state transitions.

As above, using the $2\nu\beta\beta$ decay as a guideline [4, 17], one could predict that the $0\nu\beta\beta$ decay to the excited 0^+ states would be much more favorable than the decay to the 2^+ state. In this article, this problem is being addressed by performing a systematical study of the $0\nu\beta^-\beta^-$ decays to excited 0^+ states by using the quasiparticle random-phase approximation (QRPA) framework with realistic nucleon–nucleon two-body interactions derived from the Bonn one-boson-exchange potential with the G-matrix techniques. These transitions have already been discussed in the same framework in [18] for the $0\nu\beta\beta$ decay to two-phonon 0^+ states in ^{76}Se and ^{82}Kr, in [19] for the $0\nu\beta\beta$ decay to two-phonon and monopole-vibrational 0^+ states in ^{96}Zr and ^{116}Cd, and in [20] for both types of decay transitions to ^{100}Ru. The structure of the involved states is given in Section 3.

2. NUCLEAR-STRUCTURE MODELS AND THEIR EVOLUTION

During the last 20 years, the evolution and time span of the nuclear models used to describe the double-beta-decay transitions has been a very interesting one. This progress on the nuclear theory side is represented by the horizontal histograms in Fig. 1. These histograms present the time spans of the models during which active calculations took place and results of these calculations were published. The black histograms are generally accepted formulations of theory, whereas the gray histograms represent model approaches that have raised controversial opinions and discussions about their (range of) validity. The earliest and most fundamental approaches

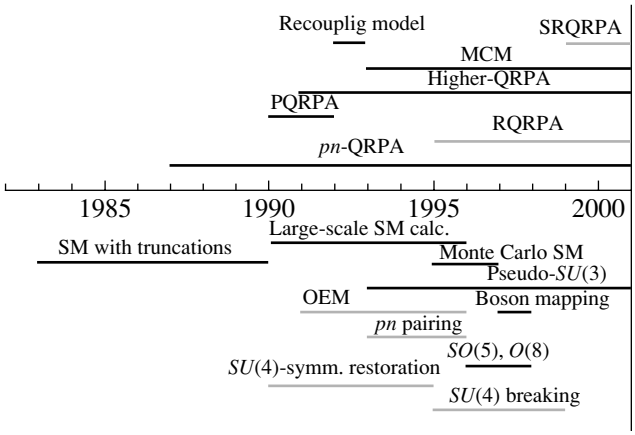

Fig. 1. Time span of the various nuclear models used to calculate nuclear matrix elements involved in double-beta-decay transitions. The gray horizontal histograms denote models that are either under debate or considered to be ruled out.

can be considered to come from the family of the direct shell-model (SM) approaches. As mentioned in the Introduction, the very early SM approaches [1–3] can be considered to be small-scale either heavily truncated or weak-coupling calculations. The years between 1990–1997 contain hectic application of the large-scale SM approach [21–26] and the use of the Monte Carlo SM approach [27, 28]. This sudden push in the SM calculations was based on improved computer hardware and improved computer codes to enable full calculations in realistic single-particle model spaces. Especially, the Monte Carlo SM seemed to open the possibility of going toward heavy nuclei in realistic computations. However, after the initial ecstasy, it was realized that not even the large-scale calculations were able to describe the medium-heavy open-shell (beyond a few exceptions) and heavy open and near-open-shell nuclei in an unambiguously solid way. At the same time, the Monte Carlo SM was facing the troubles connected to the extrapolation of the double-beta observables to the needed zero-temperature limit. Given these obstacles caused the SM efforts to cease and remain waiting for the next push in hardware and software development.

A new era in the calculation of the double-beta-decay observables was opened by the introduction of the proton–neutron particle–particle interaction channel into the framework of the random-phase approximation (RPA). This approach, called the proton–neutron quasiparticle RPA (pn-QRPA), was based on the work of Halbleib and Sorensen [29] and further developed by Vogel and Zirnbauer [30]. Since then, very many applications of this method have taken place (for a comprehensive review, see [5,

31]), and the pn-QRPA method continues to be in active use even at the present. A particle-number-projected version of the pn-QRPA, called PQRPA in Fig. 1, was introduced in [32, 33], but no remarkable advantages of this method over the pn-QRPA could be witnessed [34, 35].

When the interest in the $\beta\beta$ decays to the excited states started to attract interest [36], the theory called multiple-commutator model (MCM) was developed [37] and applied to $2\nu\beta\beta$ decays to 2^+ final states in [16] and to the two-phonon 0^+ states in [17]. This model is closely related to the approach introduced in [38], which is called the recoupling model in Fig. 1. The relation of the MCM with the early higher QRPA approach of [39] was discussed in [40]. A comprehensive review of the available experimental and theoretical results for the involved nuclear matrix elements is given in [31].

A new type of approach, going beyond the pn-QRPA level, was introduced in [41]. In this approach, called the renormalized pn-QRPA (RQRPA), an attempt was made to include the relevant parts of the Pauli principle in the pn-QRPA framework by renormalizing the pn-QRPA matrix equation by the particle-number densities in the correlated ground state. Since its introduction [31, 42–44], a lively discussion about the merits and demerits of the RQRPA has continued up to these days, and that is why it has been marked by the gray histogram in Fig. 1. To the same gray category, I have included the attempts to extend the RQRPA philosophy to the so-called self-consistent formulation (self-consistent RQRPA, SRQRPA), examples of which are given in, e.g., [45]. Another line of approach to the self-consistent QRPA has been developed in the interesting articles [46, 47] based on the previous studies of [48].

Other approaches worth of mentioning in connection of the $\beta\beta$ decays are the pseudo-$SU(3)$ model for axially symmetric deformed nuclei, the boson mapping method, and the various schematic models ($SO(5)$, $O(8)$, generalized Lipkin model) discussed in [5, 49–52] and references therein. Some models have been under serious criticism, like the operator expansion method (OEM), the inclusion of the pn pairing, and the $SU(4)$ symmetry restoration and breaking schemes (see the extensive discussion in [5] and more recently in [53]).

3. NEUTRINOLESS DOUBLE-BETA DECAY TO EXCITED STATES

The present calculations are based on the pn-QRPA, the QRPA for like-nucleon excitations, and the MCM introduced in [37]. An extensive review of these methods and their use in beta decay and $2\nu\beta\beta$ decay has been done in [5], and I refer the reader to the aforementioned articles for further information on these models. Instead, a short review of the use of these models in connection with the $0\nu\beta\beta$-decay mode is given below.

The neutrinoless mode of the double-beta decay is the more interesting one from the point of view of modern particle physics and cosmology since it involves ingredients that go beyond the scope of the Standard Model of electroweak and strong interactions. These extensions of the Standard Model include various grand-unification theories (GUT) and superstring theories with or without supersymmetry. The minimal extension of the Standard Model accommodates right-handed currents and the corresponding couplings between left-handed and right-handed terms, the most trivial theory of this type being the $SU(5)$ GUT [54], which has been ruled out by experiments on proton decay. However, several more complicated GUT scenarios are alive and under enthusiastic study at the present [55]. These schemes contain Majorana mass for the neutrinos generated by the so-called seesaw mechanism, a simple scheme to generate a left-handed electron neutrino mostly consisting of light Majorana-mass eigenstates and a right-handed one mostly consisting of heavy Majorana-mass eigenstates [56]. To achieve this, the mass term of the weak-interaction Lagrangian is supposed to contain very light ($m_L \sim 0$) left-handed masses and very heavy right-handed ones ($m_R \sim M_{\mathrm{GUT}} \sim 10^{14}$ GeV), and the Dirac masses should be on the order of typical fermion (charged lepton or quark) masses. In the GUT, the electron-neutrino Majorana mass is expected to be within the range 10^{-4}–10^{-9} eV.

In the GUT models, one starts from the most general effective weak-interaction Hamiltonian density

$$h_W = (G_{\mathrm{F}}\cos\theta_{\mathrm{C}}/\sqrt{2})\left(j_{L\mu}J_L^{\mu\dagger} + \kappa j_{L\mu}J_R^{\mu\dagger} + \eta j_{R\mu}J_L^{\mu\dagger} + \lambda j_{R\mu}J_R^{\mu\dagger}\right) + \mathrm{h.c.}, \quad (1)$$

where $G_{\mathrm{F}} = 1.16637\times10^{-5}$ GeV^{-2} is the Fermi coupling constant and θ_{C} is the mixing angle of the Cabibbo–Kobayashi–Maskawa mechanism for mixing quark flavors. In the case of the $\beta^-\beta^-$ decay mode, the left- and right-handed leptonic ($j_{L\mu}, j_{R\mu}$) currents are given by the expressions

$$j_{L\mu} = \overline{e}\gamma_\mu(1-\gamma_5)\nu_{e,L}, \quad (2)$$

$$j_{R\mu} = \overline{e}\gamma_\mu(1+\gamma_5)\nu'_{e,R}, \quad (3)$$

where the weak eigenstates of the neutrino, $\nu_{e,L}$ and $\nu'_{e,R}$, are given in terms of the mass eigenstates N_{jL} and N_{jR} as

$$\nu_{e,L} = \sum_{j=1}^{2N_g} U_{ej}N_{jL}, \qquad \nu'_{e,R} = \sum_{j=1}^{2N_g} V_{ej}N_{jR}. \quad (4)$$

Above, N_g is the number of generations, and the notation used is the standard one [56]. The matrices U and V are the mixing matrices of the weak eigenstates (left- and right-handed electron neutrinos, $\nu_{e,L}$ and $\nu_{e,R}$) and the mass eigenstates (N_{jL} and N_{jR}) of the neutrino. At the quark level, the expressions for the hadronic currents are given in terms of the u and d quarks as

$$J_L^{\mu\dagger} = \overline{u}\gamma^\mu(1-\gamma_5)d, \tag{5}$$

$$J_R^{\mu\dagger} = \overline{u}\gamma^\mu(1+\gamma_5)d, \tag{6}$$

and on the nucleon level in a nucleus, assuming the validity of the impulse approximation, the leading-order terms of the effective hadronic weak current (β^- decay) can be written as

$$J_{L/R}^{\mu\dagger} = \bar{\Psi}(x)\tau^- \left(g_V\gamma^\mu - ig_W\sigma^{\mu\nu}q_\nu \mp g_A\gamma^\mu\gamma_5 \pm g_P\gamma_5 q^\mu\right)\Psi(x), \tag{7}$$

where $g_{V,A,W,P}$ denote the vector, axial-vector, weak-magnetism, and induced pseudoscalar form factors, respectively. The quantity $\Psi(x)$ is the nucleon field at the spacetime point x. For the β^+ decay, τ^- is replaced by τ^+.

The current–current couplings are specified by the parameters κ, η, and λ. The actual values of these couplings can only be determined once specific models for the neutrino mixing and masses of the gauge bosons are defined. Using the general Hamiltonian of (1), one can derive the following expression for the decay half-life of a nucleus in a $0\nu\beta\beta$ transition to the final ground state:

$$[t_{1/2}^{(0\nu)}]^{-1} = C_{mm}^{(0)}\left(\frac{\langle m_\nu\rangle}{m_e}\right)^2 + C_{m\lambda}^{(0)}\langle\lambda\rangle\left(\frac{\langle m_\nu\rangle}{m_e}\right) + C_{m\eta}^{(0)}\langle\eta\rangle\left(\frac{\langle m_\nu\rangle}{m_e}\right) + C_{\lambda\lambda}^{(0)}\langle\lambda\rangle^2 + C_{\eta\eta}^{(0)}\langle\eta\rangle^2 + C_{\lambda\eta}^{(0)}\langle\lambda\rangle\langle\eta\rangle, \tag{8}$$

where CP conservation was assumed, and the effective parameters $\langle m_\nu\rangle$ (Majorana-neutrino mass) and $\langle\lambda\rangle$ and $\langle\eta\rangle$ (relative magnitudes of the coupling coefficients of the right-handed weak-interaction currents) are obtained from the corresponding bare quantities through mixing of the light-neutrino eigenstates in the electron-flavor eigenstate appearing in the vertices of the $0\nu\beta\beta$ decay, namely,

$$\langle\lambda\rangle = \lambda\frac{g_V^{'}}{g_V}\sum_j{}' U_{ej}V_{ej}, \quad \langle\eta\rangle = \eta\sum_j{}' U_{ej}V_{ej}\,. \tag{9}$$

The summations are restricted to the light-neutrino-mass eigenstates (this is indicated by the primed sum), and the matrices U and V are given in (4). The number of generations is restricted to N_g generations. The neutrino-mass sector can be written as

$$\langle m_\nu\rangle = \sum_j{}' \lambda^{CP} m_j |\, U_{ej}\,|^2, \tag{10}$$

where λ^{CP} are the CP phases. The $C^{(0)}$ coefficients in (8) are combinations of leptonic phase-space integrals and various nuclear matrix elements as given, e.g., in [5, 56, 57]. The quantity m_e is the electron rest mass.

In a rather good approximation, one can write the $C_x^{(0)}$ coefficients in approach [57], by retaining only the leading contributions, as

$$C_{mm}^{(0)} \simeq \left(M_m^{(s)}\right)^2 G_1, \tag{11}$$

$$C_{m\lambda}^{(0)} \simeq -M_m^{(s)}\left(M_-^{(s)} - \frac{1}{3}M_-^{(p)}\right)G_3 + \frac{1}{3}M_m^{(s)}M_-^{(p)}G_4, \tag{12}$$

$$C_{m\eta}^{(0)} \simeq -M_m^{(s)}\left(M_+^{(s)} - \frac{1}{3}M_+^{(p)}\right)G_3 + \frac{1}{3}M_m^{(s)}M_+^{(p)}G_4 - M_R M_m^{(s)}G_6 + M_m^{(s)}M_P G_5, \tag{13}$$

$$C_{\lambda\lambda}^{(0)} \simeq \left(M_-^{(s)} - \frac{1}{3}M_-^{(p)}\right)^2 G_2 - \frac{2}{3}\left(M_-^{(s)} - \frac{1}{3}M_-^{(p)}\right)M_-^{(p)}G_3 (M_-^{(p)})^2 G_4, \tag{14}$$

$$C_{\eta\eta}^{(0)} \simeq \left(M_+^{(s)} - \frac{1}{3}M_+^{(p)}\right)^2 G_2 - \frac{2}{3}\left(M_+^{(s)} - \frac{1}{3}M_+^{(p)}\right)M_+^{(p)}G_3 + (M_+^{(p)})^2 G_4 + M_R^2 G_9 - M_R M_P G_7 + M_P^2 G_8, \tag{15}$$

$$C_{\lambda\eta}^{(0)} \simeq 2\left(M_-^{(s)} - \frac{1}{3}M_-^{(p)}\right)\left(M_+^{(s)} - \frac{1}{3}M_+^{(p)}\right)G_2 - \frac{2}{3}\left[\left(M_-^{(s)} - \frac{1}{3}M_-^{(p)}\right)M_+^{(p)} + \left(M_+^{(s)} - \frac{1}{3}M_+^{(p)}\right)M_-^{(p)}\right]G_3 + 2M_-^{(p)}M_+^{(p)}G_4, \tag{16}$$

where $M_m^{(s)} \simeq M_{\rm F}^{(s)} - M_{\rm GT}^{(s)}$ and all the involved matrix elements $M^{(s)}$ (s-wave matrix elements) and $M^{(p)}$ (p-wave matrix elements) and the integrals G_i, $i = 1, ..., 9$, are defined in [57]. Similar definitions are given in [14, 56].

The nuclear matrix elements can be decomposed into a transition-operator-dependent part and a product of two one-body transition densities (OBTD) as

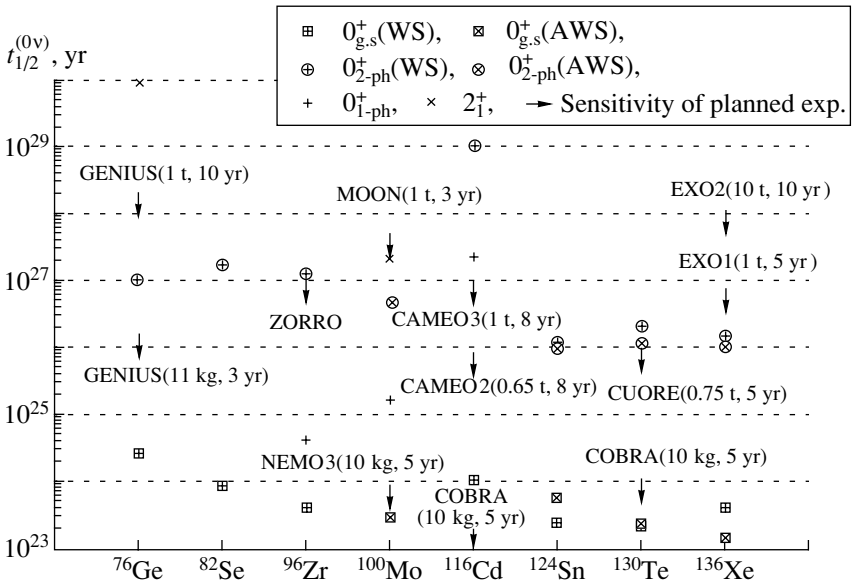

Fig. 2. Predicted half-lives (in units of a year) for several $0\nu\beta\beta$-decay transitions to the ground state and excited 0^+ and 2^+ states in the final nuclei. On the horizontal axis, the initial nucleus is indicated. The WS and the AWS bases (see the text) have been used in the calculations. The weak-interaction parameters of (24) were used. For comparison, a set of expected sensitivities of currently planned large-scale underground experiments has been given along with the masses of the source materials and the measuring times.

described in [14]. The OBTDs contain the information about the initial and final states, as well as the intermediate J^π multipole states. For the initial branch, one has the following OBTD within the pn-QRPA approach [5],

$$(J^\pi_m||[c^\dagger_p\tilde{c}_n]_J||0^+_I) = \hat{J}[u_pv_nX_{pn}(J^\pi_m) + v_pu_nY_{pn}(J^\pi_m)], \quad (17)$$

and for the various final branches, one obtains [5, 18, 19]

$$(0^+_{g.s}||[c^\dagger_{p'}\tilde{c}_{n'}]_J||J^\pi_{m'}) = \hat{J}[\bar{u}_{n'}\bar{v}_{p'}\bar{X}_{p'n'}(J^\pi_{m'}) + \bar{u}_{p'}\bar{v}_{n'}\bar{Y}_{p'n'}(J^\pi_{m'})], \quad (18)$$

$$(0^+_{2-ph}||[c^\dagger_{p'}\tilde{c}_{n'}]_J||J^\pi_{m'}) \quad (19)$$
$$= -4\sqrt{10}\sum_{p_1n_1}(-1)^{J+j_{p'}+j_{n_1}}W(j_{p'}\,j_{p_1}\,j_{n'}\,j_{n_1};2\,J) \times [\bar{u}_{p'}\bar{v}_{n'}\bar{Z}_{p'p_1}(2^+_1)\bar{Z}_{n'n_1}(2^+_1)\bar{X}_{p_1n_1}(J^\pi_{m'}) + \bar{v}_{p'}\bar{u}_{n'}\bar{W}_{p'p_1}(2^+_1)\bar{W}_{n'n_1}(2^+_1)\bar{Y}_{p_1n_1}(J^\pi_{m'})],$$

$$(0^+_{1\text{-ph}}||[c^\dagger_{p'}\tilde{c}_{n'}]_J||J^\pi_{m'}) \quad (20)$$
$$= 2\sum_{p_1}\delta_{j_{p_1}j_{p'}}\hat{j}^{-1}_{p'}[\bar{u}_{p'}\bar{u}_{n'}\bar{Z}_{p'p_1}(0^+_1)\bar{X}_{p_1n'}(J^\pi_{m'}) - \bar{v}_{p'}\bar{v}_{n'}\bar{W}_{p'p_1}(0^+_1)\bar{Y}_{p_1n'}(J^\pi_{m'})]$$
$$- 2\sum_{n_1}\delta_{j_{n_1}j_{n'}}\hat{j}^{-1}_{n'}[\bar{v}_{p'}\bar{v}_{n'}\bar{Z}_{n_1n'}(0^+_1)\bar{X}_{p'n_1}(J^\pi_{m'}) - \bar{u}_{p'}\bar{u}_{n'}\bar{W}_{n_1n'}(0^+_1)\bar{Y}_{p'n_1}(J^\pi_{m'})],$$

where the coefficients $W(\,)$ in (19) are the usual Racah coefficients and the forward-going (X) and backward-going (Y) amplitudes of the charge-changing pn-QRPA phonon are defined as

$$|J^\pi_{m'}M\rangle = \sum_{pn}[\bar{X}_{pn}(J^\pi_{m'})A^\dagger(pn;J^\pi M) - \bar{Y}_{pn}(J^\pi_m)\tilde{A}(pn;J^\pi M)]|\text{QRPA}\rangle. \quad (21)$$

The 2^+ and 0^+ one-phonon states are defined as

$$|J^+_kM\rangle = \sum_{aa'}[\bar{Z}_{aa'}(J^+_k)A^\dagger(aa';J^+M) - \bar{W}_{aa'}(J^+_k)\tilde{A}(aa';J^+M)]|\text{QRPA}\rangle, \quad (22)$$

where Z are the forward-going and W are the backward-going amplitudes in the like-nucleon QRPA approach. Above the quasiparticle-pair operators A are the ones defined in [5], and $|\text{QRPA}\rangle$ is the QRPA vacuum. The barred quantities refer to the BCS (amplitudes u and v) and pn-QRPA calculation for the final nucleus. The lowest 2^+ and 0^+ states, 2^+_1 and 0^+_1, are the ones involved in the two-phonon and monopole-vibrational states in the final nucleus. Namely, the 2^+_1 state forms the two-phonon 0^+ state as $|0^+_{2-\text{ph}}\rangle = \frac{1}{\sqrt{2}}|[2^+_1\otimes 2^+_1]_0\rangle$, and the 0^+_1 state is directly the monopole-vibrational state.

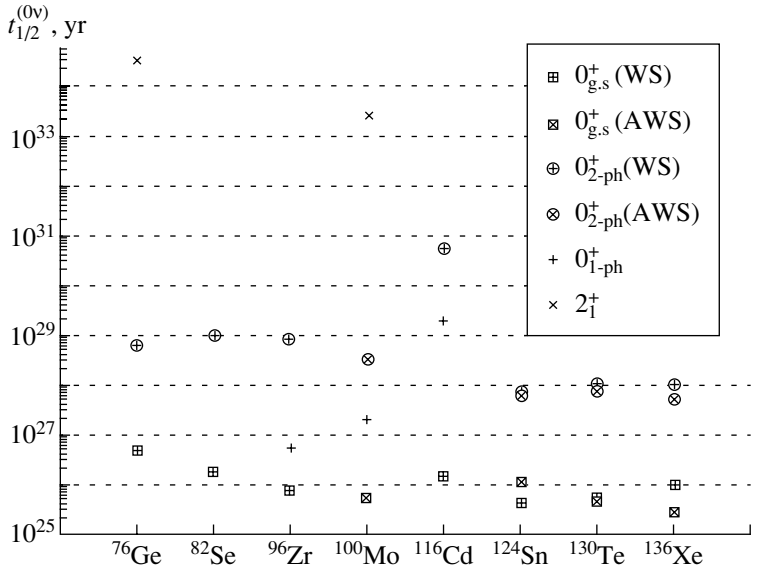

Fig. 3. The same as Fig. 2, but for $\langle m_\nu \rangle = 0.1$ eV without a contribution from the right-handed currents.

Two different pn-QRPA calculations are needed to reach the intermediate J^π states, the corresponding amplitudes being $X(\bar{X})$ and $Y(\bar{Y})$ for the pn-QRPA calculation starting from the initial(final) nucleus. The overlap method [14] has been used to match the two sets of J^π states by inserting

$$\langle J^\pi_m | J^\pi_{m'} \rangle = \sum_{pn} (\bar{X}_{pn}(J^\pi_m) X_{pn}(J^\pi_{m'}) - \bar{Y}_{pn}(J^\pi_m) Y_{pn}(J^\pi_{m'})) \quad (23)$$

into the product of the initial and final OBTDs.

4. RESULTS AND DISCUSSION

In this section, we summarize the results concerning the $0\nu\beta\beta$ decays of ^{76}Ge, ^{82}Se, ^{96}Zr, ^{100}Mo, ^{116}Cd, ^{124}Sn, ^{130}Te, and ^{136}Xe to the excited 0^+ states in the final nuclei ^{76}Se, ^{82}Kr, ^{96}Mo, ^{100}Ru, ^{116}Sn, ^{124}Te, ^{130}Xe, and ^{136}Ba, respectively. The formalism of Section 3 was used with the two-body matrix elements derived from the Bonn one-boson-exchange potential via the G-matrix procedure. At least two complete harmonic-oscillator major shells (with spin–orbit partners included) around the proton and neutron Fermi surfaces were included in the single-particle basis. The single-particle energies were obtained from the Coulomb-corrected Woods–Saxon well (WS), and in some cases, these energies were slightly altered in the very vicinity of the Fermi surfaces (this is called the adjusted WS basis, AWS, from here on) in order to better reproduce the single-quasiparticle type of states in the neighboring proton- and neutron-odd nuclei. For more details concerning the basis states, the reader is referred to the works of [18–20, 58]. The G-matrix interaction was renormalized both in the proton and neutron pairing channels and in the proton–neutron 1^+ and proton–proton and neutron–neutron 0^+ and 2^+ channels in order to take into account the finite active valence single-particle space (see the above references for more details on the renormalization).

The final results, namely, the predicted half-lives, have been collected in Figs. 2–4. In Figs. 2 and 3, the decay half-lives for the above-mentioned $0\nu\beta\beta$ transitions to the ground state, the two-phonon 0^+ state ($0^+_{2\text{-ph}}$), and the monopole-vibrational 0^+ state ($0^+_{1\text{-ph}}$) are given. For comparison, the decay half-lives for the transitions to the first excited 2^+ state (2^+_1) are given for the decays of ^{76}Ge and ^{100}Mo by using the phase-space factors of [14] and the matrix elements of [15]. The half-lives of Fig. 2 have been calculated by using the parameter set

$$\langle m_\nu \rangle \leq 0.723 \text{ eV}; \quad \langle \eta \rangle \leq 7.55 \times 10^{-9}; \quad \langle \lambda \rangle \leq 9.40 \times 10^{-7}, \quad (24)$$

extracted as a conservative upper limit from the best measured lower limit for the $0\nu\beta\beta$-decay half-life ($t^{(0\nu)}_{1/2}(0^+_{g.s}) > 1.2 \times 10^{25}$ yr (90% C.L.) from the Heidelberg–Moscow experiment [59]) of the $^{76}\text{Ge} \rightarrow ^{76}\text{Se}$ ground-state-to-ground-state transition. These parameter values thus produce the best lower limits for the half-lives of the other decay transitions discussed in this section, and, consequently, these limits can be used to discuss the sensitivity of the other present-day or future experiments listed in Fig. 2. In Fig. 3, the same data is given, but excluding

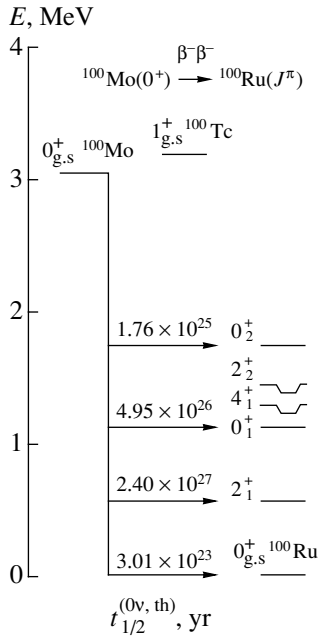

Fig. 4. Predicted half-lives (in units of a year) for the $0\nu\beta\beta$ decays of ^{100}Mo to the ground state and excited 0^+ and 2^+ states in ^{100}Ru.

the right-handed currents ($\langle\eta\rangle = 0$, $\langle\lambda\rangle = 0$) and taking $\langle m_\nu\rangle = 0.1$ eV as a potential value emerging from the near-future Heidelberg–Moscow or other experiments.

The data of Fig. 2 are summarized in Fig. 4 for the case of the ^{100}Mo decay, where one can see a clear hierarchy of half-lives ranging from 3.01×10^{23} yr for the ground-state transition up to 2.40×10^{27} yr for the transition to the 2_1^+ state. Here, 0_1^+ is considered to be a two-phonon state and 0_2^+ a monopole-vibrational state. As seen here and in Figs. 2 and 3, the monopole-vibrational states are always (when/if they exist at low energies) more favorable for detection than the two-phonon states. This is particularly striking in the case of the ^{96}Zr decay to the 0_1^+ state in ^{96}Mo, assumed to be a monopole-vibrational state. Here, the difference in half-life to the ground-state decay is only one order of magnitude, and a massive source of some 100 kg of enriched ^{96}Zr would already yield effective neutrino masses on the scale $\langle m_\nu\rangle \leq 0.08$ eV [19]. This idea of using ^{96}Zr as a massive source has been presented under the code name ZORRO (Zirconium ORiented Rare-event Observatory) in the review of the planned experiments in Fig. 2. On the other hand, the half-lives for the transitions to the two-phonon 0^+ states are at least 10^{26} yr, so that these decay transitions are hardly detectable in the near future. Furthermore, from Fig. 3, one notices that the transitions to the 2_1^+ states are not detectable when no right-handed currents exist. They are easier to detect in the presence of right-handed currents, as seen from Fig. 2. This means that the decays to 2_1^+ states are relatively more sensitive to the right-handed currents than to the neutrino mass.

4. CONCLUSIONS

In conclusion, in the present article, I have briefly reviewed the status of the various popular nuclear-structure theories used to calculate double-beta-decay observables during the last 20 years. In addition, I have discussed $0\nu\beta\beta$ decays to the ground state and excited 0^+ states in the framework of the quasiparticle random-phase approximation with realistic two-body interaction matrix elements obtained from a renormalized Bonn-A G matrix. It was found that most likely all the transitions to the excited states would remain undetected in the near future, the most favorable transition occurring in the decay of ^{96}Zr to the first excited 0^+ state in ^{96}Mo. It seems that an experiment (proposed working name ZORRO) using the γ-coincidence techniques with a massive source (100 kg) of ^{96}Zr would be competitive with the experiments measuring the transitions to the ground state.

ACKNOWLEDGMENTS

The help of M. Aunola and M. Kortelainen in preparing the figures of this article is gratefully acknowledged.

REFERENCES

1. L. D. Skouras and J. D. Vergados, Phys. Rev. C **28**, 2122 (1983).
2. W. C. Haxton and G. J. Stephenson, Jr., Prog. Part. Nucl. Phys. **12**, 409 (1984).
3. T. Tsuboi, K. Muto, and H. Horie, Phys. Lett. B **143B**, 293 (1984).
4. M. Aunola and J. Suhonen, Nucl. Phys. A **602**, 133 (1996).
5. J. Suhonen and O. Civitarese, Phys. Rep. **300**, 123 (1998).
6. A. S. Barabash *et al.*, Phys. Lett. B **345**, 408 (1995).
7. A. S. Barabash *et al.*, Yad. Fiz. **62**, 2211 (1999) [Phys. At. Nucl. **62**, 2039 (1999)].
8. L. De Braeckeleer, M. Hornish, A. S. Barabash, and V. Umatov, Phys. Rev. Lett. **86**, 3510 (2001).
9. A. S. Barabash, in *Proceedings of the MEDEX'01 Workshop, Prague, Czech Republic, 2001.*
10. V. I. Tretyak and Yu. G. Zdesenko, At. Data Nucl. Data Tables **61**, 43 (1995).
11. J. D. Vergados, Phys. Rep. **133**, 1 (1986).
12. H. V. Klapdor-Kleingrothaus, Int. J. Mod. Phys. A **13**, 3953 (1998).

13. A. Faessler and F. Šimkovic, J. Phys. G **24**, 2139 (1998).
14. T. Tomoda, Rep. Prog. Phys. **54**, 53 (1991).
15. T. Tomoda, Phys. Lett. B **474**, 245 (2000).
16. J. Suhonen and O. Civitarese, Phys. Lett. B **308**, 212 (1993).
17. O. Civitarese and J. Suhonen, Nucl. Phys. A **575**, 251 (1994).
18. J. Suhonen, Phys. Lett. B **477**, 99 (2000).
19. J. Suhonen, Phys. Rev. C **62**, 042501(R) (2000).
20. J. Suhonen, Nucl. Phys. A **700**, 649 (2002).
21. L. Zhao, B. A. Brown, and W. A. Richter, Phys. Rev. C **42**, 1120 (1990).
22. K. Ogawa and H. Horie, *Nuclear Weak Process and Nuclear Structure* (World Sci., Singapore, 1989), p. 308.
23. E. Caurier, A. Poves, and A. P. Zuker, Phys. Lett. B **252**, 13 (1990).
24. D. Zheng, L. Zamick, and N. Auerbach, Ann. Phys. (N.Y.) **197**, 343 (1990).
25. E. Caurier, F. Nowacki, A. Poves, and J. Retamosa, Phys. Rev. Lett. **77**, 1954 (1996).
26. J. Suhonen, P. C. Divari, L. D. Skouras, and I. P. Johnstone, Phys. Rev. C **55**, 714 (1997).
27. P. B. Radha *et al.*, Phys. Rev. Lett. **76**, 2642 (1996).
28. S. E. Koonin, D. J. Dean, and K. Langanke, Phys. Rep. **278**, 1 (1997).
29. J. A. Halbleib and R. A. Sorensen, Nucl. Phys. A **98**, 542 (1967).
30. P. Vogel and M. R. Zirnbauer, Phys. Rev. Lett. **57**, 3148 (1986).
31. J. Suhonen, Yad. Fiz. **61**, 1286 (1998) [Phys. At. Nucl. **61**, 1186 (1998)].
32. O. Civitarese, A. Faessler, J. Suhonen, and X. R. Wu, Phys. Lett. B **251**, 333 (1990).
33. O. Civitarese, A. Faessler, J. Suhonen, and X. R. Wu, J. Phys. G **17**, 943 (1991); Nucl. Phys. A **524**, 404 (1991).
34. J. Suhonen, O. Civitarese, and A. Faessler, Nucl. Phys. A **543**, 645 (1992).
35. J. Suhonen, J. Phys. G **19**, 139 (1993).
36. A. S. Barabash, Pis'ma Zh. Éksp. Teor. Fiz. **51**, 181 (1990) [JETP Lett. **51**, 207 (1990)].
37. J. Suhonen, Nucl. Phys. A **563**, 205 (1993).
38. A. Griffiths and P. Vogel, Phys. Rev. C **46**, 181 (1992).
39. A. A. Raduta, A. Faessler, S. Stoica, and W. A. Kaminski, Phys. Lett. B **254**, 7 (1991); A. A. Raduta, A. Faessler, and S. Stoica, Nucl. Phys. A **534**, 149 (1991).
40. A. A. Raduta and J. Suhonen, Phys. Rev. C **53**, 176 (1996); J. Phys. G **22**, 123 (1996).
41. J. Toivanen and J. Suhonen, Phys. Rev. Lett. **75**, 410 (1995).
42. J. Suhonen *et al.*, Z. Phys. A **358**, 297 (1997).
43. J. Toivanen and J. Suhonen, Phys. Rev. C **55**, 2314 (1997).
44. J. Suhonen and J. Toivanen, Czech J. Phys. **48**, 263 (1998).
45. A. Bobyk, W. A. Kaminski, and F. Šimkovic, Phys. Rev. C **63**, 051301(R) (2001).
46. F. Krmpotić *et al.*, Nucl. Phys. A **637**, 295 (1998).
47. D. S. Delion *et al.*, Phys. Rev. C **62**, 044311 (2000).
48. J. Dukelsky and P. Schuck, Nucl. Phys. A **512**, 446 (1990); Phys. Lett. B **387**, 233 (1996); J. Dukelsky, G. Röpke, and P. Schuck, Nucl. Phys. A **628**, 17 (1998).
49. M. Sambataro and J. Suhonen, Phys. Rev. C **56**, 782 (1997); Europhys. Lett. **44**, 173 (1998).
50. S. Stoica, J. Suhonen, and I. Mihut, Nucl. Phys. A **620**, 16 (1997).
51. I. Mihut, S. Stoica, and J. Suhonen, Eur. Phys. J. A **3**, 319 (1998).
52. S. Stoica, I. Mihut, and J. Suhonen, Phys. Rev. C **64**, 017303 (2001).
53. O. Civitarese and J. Suhonen, Phys. Lett. B **482**, 368 (2000).
54. H. Georgi and S. L. Glashow, Phys. Rev. Lett. **32**, 438 (1974).
55. R. N. Mohapatra, Prog. Part. Nucl. Phys. **26**, 1 (1991).
56. M. Doi, T. Kotani, and E. Takasugi, Prog. Theor. Phys. Suppl. **83**, 1 (1985).
57. J. Suhonen, S. B. Khadkikar, and A. Faessler, Phys. Lett. B **237**, 8 (1990); Nucl. Phys. A **529**, 727 (1991); **535**, 509 (1991).
58. M. Aunola and J. Suhonen, to be published.
59. H. V. Klapdor-Kleingrothaus, Yad. Fiz. **61**, 967 (1998) [Phys. At. Nucl. **61**, 875 (1998)].

Physics of Atomic Nuclei, Vol. 65, No. 12, 2002, pp. 2184–2187. From Yadernaya Fizika, Vol. 65, No. 12, 2002, pp. 2247–2250.

DOUBLE BETA DECAY

Analysis of Solar-Neutrino-Induced $\beta\beta$ Processes for Several Nuclei*

S. V. Semenov**, **Yu. V. Gaponov**, **F. Šimkovic**[1)], **and P. Domin**[1)]

Russian Research Centre Kurchatov Institute, pl. Kurchatova 1, Moscow, 123182 Russia

Received April 17, 2002

Abstract—We investigate neutrino-flux-induced $\beta\beta$ transitions in targets built of ^{112,114,116}Cd and ^{18}O isotopes. In addition to the known $\beta^-\beta^-$ channel, we consider new $\beta^-\beta^+$ and $\beta^-\beta^+\gamma$ modes of the neutrino-induced $\beta\beta$ process. A possibility of detection of the solar neutrinos via the induced $\beta\beta$ transitions of interest is discussed. We note that the β^- part of the solar-neutrino-induced $\beta^-\beta^+$ process in ^{18}O was already discussed in connection with possible influence of high-energy electron production of this origin on the Super-Kamiokande results. © *2002 MAIK "Nauka/Interperiodica".*

The exploitation of stable isotopes in neutrino physics establishes an effective experimental basis for investigation of the solar neutrino deficit and different neutrino aspects of various double beta processes ($\beta\beta$ processes) including problems of the nature and the masses of neutrinos, right-handed currents, etc. [1–3]. The theoretical study of the neutrino-induced $\beta\beta$ transitions [4, 5] allows one to extend the group of nuclei for experimental investigation of the $\beta\beta$ processes and to develop new methods for detection of solar, atmospheric, and terrestrial (reactor, accelerator, and artificial source) neutrinos. Until now, attention has been paid only to processes of spontaneous nuclear $\beta\beta$ decay.

Recently, it has been pointed out that ^{100}Mo is a suitable isotope for registration of the low-energy solar neutrino [6] due to its low reaction threshold of 0.168 MeV. An analysis of the associated $\beta\beta$ transitions based on the previous study for this isotope [5] was carried out in [7]. In this contribution, we propose other stable isotopes, in particular, ^{112,114,116}Cd and ^{18}O, for detection of solar neutrinos via the neutrino-induced $\beta\beta$ transitions. In addition, new β^-/EC and $\beta^-\beta^+$ channels [7] of the induced $\beta\beta$ process are examined.

The neutrino-induced $\beta\beta$ transition

$$\nu_e + (A, Z) \to (A, Z+2) + 2e^- + \bar{\nu}_e \qquad (1)$$

is a second-order process in the weak interaction, which is allowed within the Standard Model. The amplitude of this process exhibits resonant behavior and strongly depends on the widths of the intermediate nuclear states.

The total cross section $\sigma(\varepsilon_\nu)$ of the neutrino-induced $\beta\beta$ process can be written as [4, 7]

$$\sigma(\varepsilon_\nu) = \sum_{m=0}^{m^{\mathrm{RS}}} \sigma_\beta^{(m)}(\varepsilon_\nu)\frac{\gamma_{mf}}{\gamma_m}, \qquad (2)$$

where m^{RS} denotes the highest lying real excited state of the intermediate nucleus that is allowed by energy conservation, and $\sigma_\beta^{(m)}(\varepsilon_\nu)$ is the cross section of the neutrino-induced single β process associated with transition from the ground state of the initial nucleus to the mth excited state of the intermediate nucleus. The total and the partial (related to β^+, β^-, and EC decay channels) widths of this state are denoted as γ_m and γ_{mf}, respectively. It is worthwhile to note that, in the case of the excited states of the intermediate nucleus, the ratio γ_{mf}/γ_m is small due to corresponding large electromagnetic widths. It means that the induced $\beta\beta$ process through excited intermediate nuclear states without additional γ-ray emission is strongly suppressed. This fact points out the importance of the $\beta\beta$ process with γ-ray emission associated with electromagnetic transitions from the excited to the ground state of the intermediate nucleus and a subsequent single β transition to the final state. The cross section $\sigma_\beta^{(m)}(\varepsilon_\nu)$ can be expressed

*This article was submitted by the authors in English.

[1)]Department of Nuclear Physics, Comenius University, Bratislava, Slovakia.

**e-mail: semenov@imp.kiae.ru

Table 1. Solar neutrino absorption rates R_ν in ^{112}Cd, ^{114}Cd, and ^{116}Cd and production rates I in 10 t of these isotopes per day for induced $\beta\beta$ transitions ($E_{\nu,\mathrm{thr}}$ and τ denote the solar neutrino threshold energy for induced $\beta\beta$ process for the given isotope and the expected time delay between the emission of two electrons in this process, respectively)

Nucleus	$E_{\nu,\mathrm{thr}}$, MeV	$\log(ft_{\mathrm{EC}})$	τ	R_ν, SNU		I, event/(10 t d)
^{112}Cd	2.578	4.7	14.4 min	^{8}B:	3.49	0.016 { 0.007 $\beta^-\beta^-$; 0.004 $\beta^-\beta^+$; 0.005 β^-/EC
^{114}Cd	1.444	4.9	71.9 s	^{8}B:	3.04	0.014
				^{15}O:	0.46	0.002
^{116}Cd	0.465 ($1^+_{\mathrm{g.s.}}$)	4.39 ($1^+_{\mathrm{g.s.}}$)	14.1 s	^{7}Be(2):	237.11	1.06
	1.465 (1^+_1)	4.98 (1^+_1)		^{8}B:	12.63 ($1^+_{\mathrm{g.s.}}$)	0.057
	2.665 (1^+_2)	4.83 (1^+_2)			2.49 (1^+_1)	0.011
					2.49 (1^+_2)	0.011
				^{13}N:	18.39	0.083
				^{15}O:	37.08	0.166

with the help of the $\log(ft_{\beta^+,\mathrm{EC}})$ value as follows:

$$\sigma_\beta^{(m)}(\varepsilon_\nu) = \frac{2(\ln 2)(2J_m+1)\pi^2}{m_e^3 \times 10^{\log(ft_{\beta^+,\mathrm{EC}})}} \pi_r^{(m)} \varepsilon_r^{(m)} F(Z,\varepsilon_r^{(m)}) \tag{3}$$

$$= \frac{0.2625(2J_m+1)}{10^{\log(ft_{\beta^+,\mathrm{EC}})}} \pi_r^{(m)} \varepsilon_r^{(m)} F(Z,\varepsilon_r^{(m)}) \times 10^{-40}\ \mathrm{cm}^2.$$

Here, J_m is the angular momentum of the mth excited state of the intermediate nucleus; $\log(ft_{\beta^+,\mathrm{EC}})$ is related to the β transition from the mth state of the intermediate nucleus to the initial nucleus; $\pi_r^{(m)}$ and $\varepsilon_r^{(m)}$ are the momentum and the energy of the outgoing electron in units of the electron mass m_e, respectively; $\varepsilon_r^{(m)} = \varepsilon_\nu - \varepsilon_m + \varepsilon_i$, where ε_i and ε_m are the energies of the initial and the intermediate nuclear states; and $F(Z,\varepsilon_r^{(m)})$ is the Coulomb correction function. The neutrino threshold energy for the induced $\beta\beta$ process is given by $\varepsilon_{\nu,\mathrm{thr}} = \varepsilon_m - \varepsilon_i + 1$.

The production rate for solar neutrino events per day in 10 t of ^{100}Mo was calculated in [7]. The expected experimental signal consists of two emitted electrons with the time delay of 15.8 s. The subtraction of the two-neutrino double-beta-decay ($2\nu\beta\beta$ decay) background seems to be a serious problem for this type of detector. However, it could be eliminated by the coincidence measurements as in the $2\nu\beta\beta$ decay, where two electrons are emitted simultaneously.

In this work, we present solar neutrino absorption and production rates for ^{112,114,116}Cd and ^{18}O isotopes. The absorption rate for a given component s of the solar neutrino flux takes the form [8]

$$R_\nu = \int \sigma^{(m)}(\varepsilon_\nu)\rho_s(\varepsilon_\nu)d\varepsilon_\nu. \tag{4}$$

Here, $\rho_s(\varepsilon_\nu)$ is the energy distribution of solar neutrinos of the origin s. In Table 1, we present results for cadmium nuclei. The production rates I were obtained for a detector consisting of 10 t of the given cadmium isotope. We considered only those components of the solar neutrino spectrum which give significant contributions to solar neutrino absorption rates. In the case of ^{112,114}Cd, only transitions through the ground state of the intermediate nucleus were taken into account, as contributions from transitions through excited states are negligible. There is a different situation in the case of ^{116}Cd. For correct evaluation of the ^{8}B solar-neutrino-induced $\beta\beta$ process in this isotope, it is important to consider also transitions through the 1^+_1 and 1^+_2 excited states of ^{116}In, which are accompanied with γ-ray emission. We note that $\log(ft_{\mathrm{EC}})$ values associated with the β transition from the excited states of ^{116}In were calculated from Gamow–Teller strengths of ^{116}In measured by the ^{116}Cd(^{3}He)^{116}In reaction in [9]. From Table 1, we can conclude that ^{116}Cd is a good candidate for detection of a Be(2) solar neutrino flux.

The solar-neutrino-induced $\beta\beta$ transition introduced in (1) is the dominant mode in the case of ^{114}Cd and ^{116}Cd. It is worthwhile to note that there are two additional channels of this process within the Standard Model, namely, the $\beta^-\beta^+$ and β^-/EC

Table 2. Solar neutrino absorption rate R_ν and production rates I in 1000 t of ^{18}O per year associated with the induced $\beta^-\beta^+$ processes in (6) and (7)

Reaction	$E_{\nu,\mathrm{thr}}$, MeV	logft	τ, min	R, SNU	I, event/(1000 t yr)
(6)	1.655	3.57	109.77	20.06	20535
(7)	2.695	3.47	109.77	6.11	6259

modes [7],

$$\nu_e + (A,Z) \to (A,Z) + e^- + e^+ + \nu_e,$$
$$\nu_e + e^- + (A,Z) \to (A,Z) + e^- + \nu_e. \quad (5)$$

The branching ratios for the $\beta^-\beta^+$ and β^-/EC channels of the solar-neutrino-induced $\beta\beta$ process in ^{114}Cd are on the order of 1.9 and 0.004% percent, respectively.

In the case of ^{100}Mo, the contribution from the $\beta^-\beta^+$ channel to the full cross section of the $\beta\beta$ process is strongly suppressed. It is due to the fact that this transition is realized through excited states m of the intermediate nucleus ^{100}Tc for which the ratio $\gamma_{m\beta^+}/\gamma_m$ is negligibly small due to large associated electromagnetic widths γ_m [7]. In the case of ^{112}Cd, there is a different scenario as the ground state of ^{112}In is unstable in respect to the β^-, β^+ decays and electron capture [β^- (44%), β^+ (34%), and EC (22%)]. Thus, the ^{8}B solar-neutrino-induced $\beta^-\beta^+$ transition in ^{112}Cd is allowed. However, the counting rate for emission of positrons is low due to a small neutrino absorption cross section for this isotope.

It is worth mentioning that the solar neutrino registration with the help of the emitted positrons in the induced $\beta^-\beta^+$ process is favored. The annihilation of the positron with the atomic electron leads to a signal of two simultaneously emitted γ rays with a significant time delay in respect to emission of the first electron. This fact allows considerable reduction of background. However, it is desirable that, in the detection of solar neutrinos via induced $\beta^-\beta^+$ transition, a target with large values of the inverse β-decay cross section and the branching ratio for the β^+ decay from the intermediate nucleus is chosen. We find ^{18}O to be a good candidate for this purpose. The open decay channels of the ground state of the neighbor nucleus ^{18}F are β^+ decay and electron capture with the branching ratios on the order of 97 and 3%, respectively. A rather high abundance (0.2%) and effective technology of its production allow this isotope to be produced in a sufficient amount for solar neutrino experiments. The threshold energy for absorption of solar neutrinos in this isotope is $E_{\nu,\mathrm{thr}} = 1.655$ MeV, which is significantly small in comparison with the threshold energy of 6.5 MeV for detection of solar neutrinos in the Super-Kamiokande experiment.

The above arguments together with the large value of the cross section for the neutrino-induced $\beta^-\beta^+$ process and the expected suppressed background mostly due to the absence of $2\nu\beta\beta$-decay events suggest that ^{18}O is a promising tool for investigation of the ^{8}B solar neutrino flux in view of the measured discrepancy between the Standard Solar Model prediction and the Super-Kamiokande measurement [8]. The relevant processes are given by

$$\nu_e + {}^{18}\mathrm{O} \to {}^{18}\mathrm{O} + e^+ + e^- + \nu_e, \quad (6)$$

$$\nu_e + {}^{18}\mathrm{O} \to {}^{18}\mathrm{O} + e^+ + e^- + \nu_e + \gamma \quad (1.04\ \mathrm{MeV}). \quad (7)$$

Here, we assume that, in reaction (7), the emitted γ ray originates from the electromagnetic disintegration of excited state of ^{18}F, i.e., its energy is fixed by the energy difference of the corresponding nuclear levels. This electromagnetic radiation is expected to be a useful signal in detection of solar neutrinos.

The dominant contributions to the cross section of the neutrino-induced $\beta^-\beta^+$ process in ^{18}O comes from the transitions through the $1^+_{\mathrm{g.s}}$ ground state and the 0^+ excited state of ^{18}F. In that contribution, the transition through the 1^+_1 excited state of ^{18}F is not taken into account, since its contribution to the absorption rate is expected to be small. We note that the β^- part of the solar neutrino induced $\beta^-\beta^+$ process in ^{18}O was already discussed in [10, 11] in connection with possible influence of high-energy electron production of this origin on the Super-Kamiokande results.

The calculated production rates for solar neutrino events in 1000 t of ^{18}O per year associated with reactions (6) and (7) are listed in Table 2. From these, we conclude that a neutrino detector that uses the advantage of registration of neutrinos with the help of the neutrino-induced $\beta^-\beta^+$ process in ^{18}O could be employed for investigation of different problems of weak interaction and nuclear physics, in particular, the solar neutrino deficit and determination of the neutrino component of the reactor antineutrino flux. The experimental signal consists of an emitted electron followed by two time-delayed γ quanta due

to positron–electron annihilation and, in the case of reaction (7), a γ ray with an energy of 1.04 MeV coming from the electromagnetic deexcitation of the intermediate nucleus ^{18}F. From Table 2, it follows that the intensity of reaction (7) is about 3 times smaller than that for reaction (6).

In summary, a possibility of the registration of solar neutrinos via different neutrino-induced $\beta\beta$ processes was addressed. The calculations were performed for several nuclear systems of interest. The role of the neutrino-induced $\beta\beta$ processes accompanied with emission of a γ ray was discussed. We found that ^{18}O is a good candidate for the study of the solar neutrino deficit with the help of the neutrino-induced $\beta^-\beta^+$ process.

ACKNOWLEDGMENTS

This work was supported by the Grant Agency of the Czech Republic under contract no. 202/02/0157.

REFERENCES

1. Yu. V. Gaponov, S. V. Semenov, and L. V. Inzhechik, in *Isotopes: Properties, Production, Applications,* Ed. by V. Yu. Baranov (IzdAT, Moscow, 2000).
2. A. Faessler and F. Šimkovic, J. Phys. G **24**, 2139 (1998).
3. V. I. Tretyak and Yu. G. Zdesenko, At. Data Nucl. Data Tables **61**, 43 (1995); **80**, 84 (2002); Yu. G. Zdesenko, Rev. Mod. Phys. **74**, 663 (2002).
4. S. V. Semenov, Yu. V. Gaponov, and R. U. Khafizov, Yad. Fiz. **61**, 1379 (1998) [Phys. At. Nucl. **61**, 1277 (1998)].
5. L. V. Inzhechik, Yu. V. Gaponov, and S. V. Semenov, Yad. Fiz. **61**, 1384 (1998) [Phys. At. Nucl. **61**, 1282 (1998)].
6. H. Ejiri *et al.*, Phys. Rev. Lett. **85**, 2917 (2000); H. Ejiri, Phys. Rep. **338**, 265 (2000).
7. P. Domin, F. Šimkovic, S. V. Semenov, and Yu. V. Gaponov, Czech. J. Phys. **52**, 451 (2002).
8. Y. Suzuki, in *Proceedings of "Neutrino 1998," Takayama, Japan,* http://www.sk.icrr.u-tokyo.ac.jp/nu98/index.html.
9. G. Akimune *et al.*, Phys. Lett. B **394**, 23 (1997).
10. W. C. Haxton, Phys. Rev. D **36**, 2283 (1998).
11. W. C. Haxton and R. G. H. Robertson, Phys. Rev. C **59**, 515 (1999).

Physics of Atomic Nuclei, Vol. 65, No. 12, 2002, pp. 2188–2197. From Yadernaya Fizika, Vol. 65, No. 12, 2002, pp. 2251–2260.

CAMEO/GEM Program and Future of Double-β-Decay Research*

Yu. G. Zdesenko**

Institute for Nuclear Research, National Academy of Sciences of Ukraine, Kiev, Ukraine

Received February 13, 2002

Abstract—The current results and future prospects of the 2β-decay research are reviewed. The requirements for supersensitivity experiments are formulated and a conclusion is derived that, in the developed CAMEO and GEM projects, the restrictions on the neutrino mass would be pushed down to $m_\nu \leq (0.015–0.05)$ eV. Moreover, the GEM I setup with natural HPGe detectors could advance the best current limits on the existence of neutralinos—as dark matter candidates—by three order of magnitudes and, at the same time, would be able to identify unambiguously the dark matter signal by detection of its seasonal modulation. © *2002 MAIK "Nauka/Interperiodica".*

1. INTRODUCTION

Studies on double-beta (2β) decay play a very important role in neutrino physics [1–4], which has undergone a revolution. Indeed, the latest solar neutrino data [5, 6], the measured deficit of the atmospheric muon neutrinos flux [7], and the result of the LSND accelerator experiment [8] all could be explained by means of the neutrino oscillations, requiring nonzero neutrino masses (m_ν) and demonstrating an existence of new physical effects beyond the Standard Model (SM) [9]. However, oscillation experiments are sensitive to neutrino mass difference, while only the measured $0\nu2\beta$-decay rate can indicate the Majorana nature of the neutrino and give the absolute scale of its effective mass [10, 11]. The neutrinoless $(0\nu)2\beta$ decay is forbidden in the SM since it violates lepton-number (L) conservation. However, many extensions of the SM incorporate such interactions and could lead to $0\nu2\beta$ decay, whose nonvanishing rate requires neutrinos to be massive Majorana particles [12].

Therefore, the $0\nu2\beta$ decay is considered now as a powerful test of new physical effects beyond the SM, which allows one to narrow a wide choice of theoretical models and to reach the multi-TeV energy range competitive to accelerator experiments [1–4].

Despite many efforts to detect $0\nu2\beta$ decay, this process still remains unobserved [13]. The highest half-life limits were set in direct experiments: $T^{0\nu}_{1/2} \geq 10^{22}$ yr for ^{82}Se [14], ^{100}Mo [15]; $T^{0\nu}_{1/2} \geq 10^{23}$ yr for ^{116}Cd [16], ^{128}Te, ^{130}Te [17], ^{136}Xe [18]; and $T^{0\nu}_{1/2} \geq 10^{25}$ yr for ^{76}Ge [19, 20]. These results have brought the most stringent restrictions on the Majorana neutrino mass $m_\nu \leq (0.5–5.0)$ eV, right-handed admixture in the weak interaction $\lambda \approx 10^{-5}$, the ν–Majoron coupling constant $g_M \approx 10^{-4}$, and the R-parity[1)]-violating parameter of the minimal SUSY model $\varepsilon \approx 10^{-4}$. It is very desirable to improve this level of sensitivity by one to two orders of magnitude [2, 4]. There are strong reasons that such a goal has to be reached with several nuclei. First, there are large discrepancies between calculated [1, 3] and measured half-lives of the $2\nu2\beta$ decay of ^{48}Ca, ^{76}Ge, ^{82}Se, ^{96}Zr, ^{100}Mo, ^{116}Cd, and ^{150}Nd [13]; therefore, a variety of 2β candidates has to be studied.[2)] Second, the 2β-decay research is on the front edge of modern technology; thus, new development could bring an advantage to particular 2β-decay candidates, and, hence, several of them should be used. Third, if $0\nu2\beta$ decay is observed by one experiment, such a discovery will have to be confirmed with other nuclides and by using another technique that should be properly developed by then. For instance, the ^{76}Ge result $T^{0\nu}_{1/2} \geq 10^{21}$ yr obtained in 1970 [21] was advanced up to $T^{0\nu}_{1/2} \geq 10^{25}$ yr after 30 years of strong efforts [19, 20].

There are two classes of 2β-decay experiments: with a "passive" source and with an "active" source, where the detector containing 2β candidate nuclei

*This article was submitted by the author in English.

** e-mail: zdesenko@kinr.kiev.ua

[1)] R-parity is defined as $R_p = (-1)^{3B+L+2S}$, where B and L are the baryon and lepton numbers, respectively, and S is the spin.

[2)] Let us reinforce it by a citation from [4]: "The nuclear structure uncertainty can be reduced by further development of the corresponding nuclear models. At the same time, by reaching comparable experimental limits in several nuclei, the chances of a severe error in the NME will be substantially reduced."

serves as source and detector simultaneously. If the $0\nu2\beta$ decay occurred, the sharp peak at the $Q_{\beta\beta}$ value would be observed in the electron sum energy spectrum of the detector. The sensitivity of the setup can be expressed in terms of a lower half-life limit as following [22, 23]: $\lim T_{1/2} \sim \eta\delta\sqrt{(mt)/(R \cdot \mathrm{Bg})}$. Here, η is the detection efficiency; δ is the abundance or enrichment of candidate nuclei contained in the detector; t is the measuring time; m is the total mass of the active or passive source; R is the energy resolution (FWHM) of the detector; and Bg is the background rate in the energy region of the 0ν-decay peak. It is clear from this equation that η and δ are the most important characteristics, because all other parameters are under the square root. Obviously, $\approx$ 100% enrichment and detection efficiency are very desirable. The energy resolution of the detector is very essential because events from the high-energy tail of the 2ν distribution run into the energy window of the 0ν peak, generating background that cannot be discriminated from the 0ν signal. Better energy resolution minimizes this irreducible background. Taking into account these considerations and on the basis of the present status of 2β-decay experiments, one can formulate the following requirements for the future projects:

(i) The best 0ν limits were reached with the help of the active source method; thus, most likely, the future projects will belong to the same class because only in this case can the detection efficiency be close to 100%.

(ii) The highest ^{76}Ge results were obtained with $\approx$10 kg of enriched detectors; hence, in the future one has to exploit enriched sources with masses of hundreds of kilograms. Only several candidate nuclei (^{76}Ge, ^{82}Se, ^{116}Cd, ^{130}Te and ^{136}Xe) could be mass-produced by means of centrifugal separation [23].

(iii) Because of the square-root dependence of the sensitivity vs. mass, it is not enough to increase the detector mass alone. The background should also be reduced down practically to zero.

(iv) The energy resolution is a crucial characteristic, and for challenging projects the FWHM value cannot be worse than $\approx$4% at $Q_{\beta\beta}$ energy.

(v) The setups should be as simple as possible to provide reliable operation during long ($\approx$10 yr) future experiments.

Evidently, it is difficult to find a project that would completely satisfy these severe requirements. Let us consider those proposed during the past few years briefly.

A new approach to study 2β decay of ^{136}Xe ($Q_{\beta\beta} = 2468$ keV) makes use of the coincident detection of $^{136}Ba^{2+}$ ions and the $0\nu2\beta$ signal with the energy of 2.5 MeV in a time projection chamber (TPC) filled with liquid or gaseous Xe [24–26]. In the recent EXO project [27], the resonance ionization spectroscopy for the identification of $^{136}Ba^{2+}$ ions would be applied in a 40-m^3 TPC operated at 5–10-atm pressure of 1–2 t of ^{136}Xe. The claimed sensitivity to neutrino mass is 0.01 eV [27]. Another idea is to dissolve 80 kg (1.5 t) of enriched (natural) Xe in the liquid scintillator of the BOREXINO Counting Test Facility (CTF) in order to reach the $T^{0\nu}_{1/2}$ limit in the range of 10^{24}–10^{25} yr [28].

The project MOON aims to make both the study of $0\nu2\beta$ decay of ^{100}Mo ($Q_{\beta\beta} = 3034$ keV) and the real-time studies of low-energy solar ν by inverse β decay [29]. The detector module will be composed of 60 000 plastic scintillators (6 m $\times$ 0.2 m $\times$ 0.25 cm) with 34 t of natural Mo in the form of foil (50 mg/cm^2). The sensitivity of such a module to the neutrino mass could be on the order of 0.05 eV [29].

In the DCBA proposal (KEK, Japan) [30], the drift chamber placed in the magnetic field (0.6 kG) can measure the momentum of each β particle emitted in 2β decay and the position of the decay vertex with the $3D$ reconstruction of the tracking. With 18 kg of an enriched ^{150}Nd ($Q_{\beta\beta} = 3367$ keV) passive source (50 mg/cm^2), the sensitivity to the Majorana neutrino mass is 0.05 eV [30].

The experiment with ^{160}Gd ($Q_{\beta\beta} = 1730$ keV; $\delta =$ 21.9%) by using the GSO multicrystal array with the total mass of 1–2 t (200–400 kg of ^{160}Gd) is suggested with the projected sensitivity to the Majorana neutrino mass of 0.04 eV [31].

The future Yb-loaded liquid scintillation detectors LENS, which is under development for solar neutrino spectroscopy [32], would also be used for studies on $2\beta^-$ decay of ^{176}Yb ($Q_{\beta\beta} = 1087$ keV) and $\varepsilon\beta^+$ decay of ^{168}Yb ($Q_{\beta\beta} = 1422$ keV). With 20 tons of natural Yb (2.5 t of ^{176}Yb), the limit $T^{0\nu}_{1/2} \geq 10^{26}$ yr could be set on $0\nu2\beta$ decay of ^{176}Yb ($m_\nu \leq 0.1$ eV) [33].

There are also two projects, NEMO-3 [34] and CUORICINO [35], under construction now. The sensitivity of the NEMO-3 tracking detector with a passive source of 10 kg of ^{100}Mo would be on the level of 4×10^{24} yr ($m_\nu \leq 0.3$–0.5 eV) [36]. The CUORICINO setup consists of 60 low-temperature bolometers made of TeO_2 crystals (mass of 750 g each) and is designed as a pilot step for a future CUORE project for the 2β decay quest of ^{130}Te with the help of one thousand TeO_2 bolometers (total mass of 750 kg) [35, 37]. With the energy resolution of TeO_2 bolometers of 5–10 keV at 2.5 MeV, the CUORE sensitivity is quoted by authors for a different background rate (0.5–0.05 counts/(yr kg keV)

at 2.5 MeV) and would be as high as $T^{0\nu}_{1/2} \geq (1-5) \times 10^{25}$ yr ($m_\nu \leq 0.05-0.2$ eV) [35, 37].

In addition, there are two projects for the 2β-decay quest of ^{76}Ge (MAJORANA [38] and GENIUS [39]). The idea of the MAJORANA is to use 210 HPGe (enriched in ^{76}Ge to 86%) semiconductor detectors (total mass of 500 kg) contained in a conventional superlow-background cryostat and shielded by HP lead or copper [38]. The segmentation of crystals and pulse-shape analysis of data would reduce background rate to the level of 0.01 counts/(yr kg keV) at an energy of 2 MeV, i.e., 6 times lower than that already reached in the ^{76}Ge experiments [19, 20]. The MAJORANA sensitivity can be expressed with the help of formula

$$\lim T^{0\nu}_{1/2} = (\ln 2)\eta N t / \lim S, \qquad (1)$$

where N is the number of ^{76}Ge nuclei, η is the detection efficiency, t is the measuring time, and $\lim S$ is the maximal number of $0\nu2\beta$ events which can be excluded with a given confidence level. To estimate value of $\lim S$, we can use the so-called "one (two, ...) σ approach," in which $\lim S$ value is determined simply as the square root of the number of background counts in the energy region of interest, multiplied by the parameter 1 (1.6 or 2) for the confidence level of 68% (90 or 95%). After 10 yr of measurements, about 200 background counts will be recorded in the vicinity of 0ν peak (in a 4-keV energy interval), and whereby one can get $\lim S \approx 20$ counts at 90% C.L. On this basis, the half-life limit can be determined by formula (1) as $T^{0\nu}_{1/2} \geq 10^{27}$ yr. Depending on the nuclear matrix element (NME) calculations [1, 3, 19, 40, 41], it leads to the following interval of the neutrino mass limit: $m_\nu \leq 0.05-0.15$ eV.

The GENIUS project intends to operate one ton of "naked" HPGe (enriched in ^{76}Ge to 86%) detectors placed in extremely high purity liquid nitrogen (LN_2), which simultaneously serves as a cooling medium and shield [39]. Owing to that, the background of the GENIUS setup would be reduced by a factor of 300 compared to that of present experiments [19, 20]. The feasibility of operating naked Ge detectors in LN_2 was demonstrated with three HPGe crystals placed inside liquid nitrogen—the energy threshold of 2 keV and the resolution of 1 at 300 keV were obtained [42]. In accordance with the Monte Carlo background simulations [39, 43], the necessary dimensions of the LN_2 shield (to fully suppress the radioactivity from the surroundings) should be about 12 m in diameter and 12 m in height. The required radiopurity of the liquid nitrogen should be as low as 10^{-15} g/g for ^{40}K and ^{238}U, 5×10^{-15} g/g for ^{232}Th, and 0.05 mBq/m^3 for ^{222}Rn [39, 43]. All these requirements (except for radon) are less stringent than those already reached for the liquid scintillators of the BOREXINO CTF (5×10^{-16} g/g for ^{232}Th and ^{238}U) [44]. The final conclusion is derived that the total GENIUS background rate in the energy region of the $0\nu2\beta$-decay peak of ^{76}Ge could be reduced down to 0.2 count/(yr t keV) [39, 43]. On this basis, the $T_{1/2}$ limit can be estimated similarly as for the MAJORANA proposal. For a 10-yr measuring time, the value of $\lim S$ is equal to 5 counts (90% C.L.); thus, with 7×10^{27} nuclei of ^{76}Ge, the bound $T^{0\nu}_{1/2} \geq 10^{28}$ yr could be achieved, which translates to the neutrino mass constraints $m_\nu \leq 0.015-0.05$ eV.

However, all the aforementioned projects require a significant amount of R&D to demonstrate their feasibility; thus, strong efforts and perhaps a long time will be needed before their realization. To this effect, in the present paper, we suggest the CAMEO program of the high-sensitivity 2β-decay experiments, whose accomplishment seems to be realistic.

2. CAMEO EXPERIMENT WITH $^{116}CdWO_4$ SCINTILLATORS

It is proposed [45] to use the already existing BOREXINO CTF [44, 46, 47] for the 2β-decay study of ^{116}Cd by placing 100 kg of enriched $^{116}CdWO_4$ crystal scintillators in the liquid scintillator of the CTF, serving as light guide and veto shield. The CTF (installed in the Gran Sasso Underground Laboratory) consists of an external 1000-t water tank ($\oslash 11 \times 10$ m) serving as shield for 4.8 m^3 of liquid scintillator contained in an inner vessel of $\oslash 2.1$ m. The radiopurity of water is 10^{-14} g/g for U/Th, 10^{-10} g/g for K, and <5 μBq/l for ^{222}Rn [44, 47]. The high-purity (5×10^{-16} g/g for U/Th) liquid scintillator (1.5 g/l of PPO in pseudocumene) has an attenuation length ≥ 5 m above 380 nm and a principal scintillator decay time of 5 ns [48]. The inner transparent vessel made of nylon film, 500 μm thick, allows one to collect the scintillation light with the help of 100 phototubes (PMT) 8 in. in diameter fixed at a diameter of 7 m inside the water tank.

The ^{116}Cd studies performed by the INR (Kiev) in the Solotvina Underground Laboratory with the help of $^{116}CdWO_4$ crystals [16, 49–52] is considered as the pilot step of the CAMEO project. Let us briefly recall their main results. The light output of cadmium tungstate crystal scintillators (enriched in ^{116}Cd to 83%) [49] is 40% of NaI(Tl), and maximal peak emission is at 480 nm with a principal decay time of 14 μs [53]. The refractive index of $CdWO_4$ crystal is 2.3, the density is 7.9 g/cm^3, and the material

is nonhygroscopic and chemically inert. In the latest phase of the experiment, four $^{116}CdWO_4$ crystals (total mass 339 g) have been used. The detectors are viewed by the low background 5 in. EMI tube (with RbCs photocathode) through one light guide $\oslash 10 \times 55$ cm. Enriched detectors are surrounded by an active shield made of 15 natural $CdWO_4$ crystals [54] with a total mass of 20.6 kg. The latter are viewed by a PMT through an active plastic light guide $\oslash 17 \times 49$ cm. The whole $CdWO_4$ array is situated in an additional active shield made of plastic scintillator $40 \times 40 \times 95$ cm^3. The outer passive shield consists of HP copper (3–6 cm), lead (22.5–30 cm), and polyethylene (16 cm). The data acquisition records the amplitude, arrival time, and pulse shape (PS) of each $^{116}CdWO_4$ event. The PS technique is based on an optimal digital filter and ensures clear discrimination between γ rays and α particles and, hence, selection of "illegal" events: double pulses, α events, etc. [53].

The energy resolution of the main detector is 11.5% at 1064 keV and 8.0% at 2615 keV. For the energy spectrum measured for 4629 h with four $^{116}CdWO_4$ crystals [16], the background rate in the energy region of 2.5–3.2 MeV is 0.03 count/(yr kg keV), which is achieved due to PS and time-amplitude analysis of the data. For example, the following sequence of α decays from ^{232}Th family was sought: $^{220}\mathrm{Rn}(Q_\alpha = 6.40\ \mathrm{MeV}, T_{1/2} = 55.6\ \mathrm{s}) \rightarrow {}^{216}\mathrm{Po}(Q_\alpha = 6.91\ \mathrm{MeV}, T_{1/2} = 0.145\ \mathrm{s}) \rightarrow {}^{212}\mathrm{Pb}$. The activity of ^{228}Th in $^{116}CdWO_4$ crystals was determined at 38(3) μBq/kg. The same technique applied to the sequence of α decays from the ^{235}U family yields 5.5(14) μBq/kg for ^{227}Ac impurity in the crystals [16].

The $T_{1/2}$ limits for $0\nu 2\beta$ decay are set at $T^{0\nu}_{1/2} \geq 0.7\ (2.5) \times 10^{23}$ yr at 90% (68%) C.L., while, for 0ν decay with Majoron emission, they are set at $T^{0\nu}_{1/2}(\mathrm{M1}) \geq 3.7\ (5.8) \times 10^{21}$ yr at 90% (68%) C.L. [16]. These translate into constraints on the neutrino mass $m_\nu \leq 2.6\ (1.4)$ eV (using calculations [55]) and on the neutrino-Majoron coupling constant $g_M \leq 12\ (9.5) \times 10^{-5}$ (with [56]), both at 90% (68%) C.L. [16]. However, further advance of the neutrino mass limit into the sub-eV domain could be possible only in case of substantial sensitivity enhancement, which is the main goal of the CAMEO project.

In the preliminary design of the CAMEO experiment, 40 enriched $^{116}CdWO_4$ crystals of large volume (320 cm^3) are placed in the liquid scintillator of the CTF and homogeneously spread on the sphere 0.8 m in diameter. With 2.5 kg of mass for each crystal ($\oslash 7 \times 8$ cm), the total number of ^{116}Cd nuclei is 1.5×10^{26}. It is assumed that 200 PMTs with light concentrators are fixed at a diameter of 5 m, providing an optical coverage of 80%. The $CdWO_4$ scintillator yields 1.5×10^4 emitted photons per 1 MeV of the energy deposited. The GEANT Monte Carlo simulation of the light propagation in this geometry gives 4000 p.e. for 2.8-MeV energy deposit; thus, the $0\nu 2\beta$-decay peak of ^{116}Cd would be measured with an energy resolution FWHM equal to 4%. The principal feasibility of obtaining such an energy resolution with $CdWO_4$ crystal has been demonstrated by the measurements with cylindrical $CdWO_4$ crystal ($\oslash 40 \times 30$ mm) placed in transparent paraffin oil (refractive index 1.5) [45]. A 42% increase of the light collection and improvement of the energy resolution has been obtained: the FWHM values (7.4% at 662 keV, 5.8% at 1064 keV, and 4.3% at 2615 keV) are similar to those for NaI(Tl) crystals and have never been reached before with $CdWO_4$ scintillators [45].

The background simulation for the CAMEO was performed with the help of the GEANT3.21 [57] and DECAY4 [58] codes. The simulated contributions from different background sources and response functions for 2β decay of ^{116}Cd with $T^{2\nu}_{1/2} =$

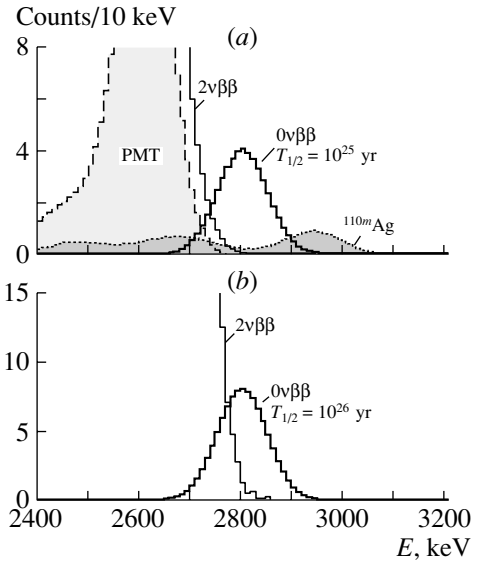

Fig. 1. (*a*) The response functions of the CAMEO [45] with 100 kg of $^{116}CdWO_4$ crystals in the CTF (after 5-yr measuring period) for 2β decay of ^{116}Cd with $T^{2\nu}_{1/2} = 2.7 \times 10^{19}$ yr and $T^{0\nu}_{1/2} = 10^{25}$ yr (solid histogram). The simulated contribution from ^{208}Tl in the PMTs (dashed line) and from cosmogenic ^{110m}Ag (dotted line). (*b*) The response functions of the 1000 kg of $^{116}CdWO_4$ crystals placed into a large liquid neutrino detector (BOREXINO, etc.) for 2β decay of ^{116}Cd with $T^{2\nu}_{1/2} = 2.7 \times 10^{19}$ yr and $T^{0\nu}_{1/2} = 10^{26}$ yr (solid histogram) and for 10-yr measuring time.

2.7×10^{19} yr and $T_{1/2}^{0\nu} = 10^{25}$ yr are depicted in Fig. 1*a*. The sensitivity of the CAMEO experiment is $T_{1/2}^{0\nu} \geq 10^{26}$ yr, which translates to the neutrino mass bound $m_\nu \leq 0.06$ eV [45]. It is also evident from Fig. 1*a* that $0\nu2\beta$ decay of ^{116}Cd with a half-life of 10^{25} yr would be clearly registered. Moreover, with 1 t of $^{116}CdWO_4$ detectors placed in one of the existing or future large underground neutrino detectors as BOREXINO [44], the sensitivity is estimated at $T_{1/2}^{0\nu} \geq 10^{27}$ yr (Fig. 1*b*), which corresponds to the restriction on the neutrino mass of 0.02 eV [45]. The simplicity and reliability are the main advantages of the CAMEO technique with $^{116}CdWO_4$ crystals, but the poor energy resolution of the latter is a factor that limits further sensitivity enhancement. Thus, in the next section, we will consider the GEM project devoted to the 2β-decay study of ^{76}Ge with the help of HPGe semiconductor detectors.

3. THE GEM PROJECT FOR THE 2β-DECAY QUEST OF ^{76}Ge

As it was mentioned, the project GENIUS [39] is aimed at reaching the bound $T_{1/2}^{0\nu} \geq 10^{28}$ yr for the 2β decay of ^{76}Ge ($m_\nu \leq 0.015$–0.05 eV). However, to achieve such a goal, the GENIUS apparatus must satisfy very stringent and contradicting demands. For example, a super-low background rate of detectors requires an ultrahigh purity of liquid nitrogen and large dimensions of the vessel ($\oslash 12 \times 12$ m) with 1000 t of LN_2. The power and maintenance costs of the LN_2 purification system strongly depend on the liquid nitrogen consumption, which, in turn, depends on the dimensions of the LN_2 tank (heat losses through the walls are directly proportional to their square) and the quality of the thermoinsulation. In the GENIUS, a polyethylene foam insulation 1.2 m thick is accepted [39], which would lead to a large LN_2 consumption. Thus, it could be very difficult to maintain the required ultrahigh purity of LN_2 during running of the experiment because evaporation of LN_2 is the method of purification, so pure vapor will leave vessel, while all impurities will stay in the remaining LN_2. These problems would be checked and perhaps solved with the help of the test facility (GENIUS-TF), which is under development now [59]. Anyhow, it is clear that production, purification, operation, and maintenance of more than one kiloton of ultrahigh purity liquid nitrogen in an underground laboratory would require additional efforts and a considerable amount of time.

Aiming to make realization of the high-sensitivity ^{76}Ge experiment simpler, the GEM design is based on the following keystone ideas [60]:

(a) "Naked" HPGe detectors (enriched in ^{76}Ge to 86–90%) operate in the ultrahigh purity liquid nitrogen serving as the cooling medium and the first layer of the shield simultaneously.

(b) LN_2 is contained in the vacuum cryostat made of HP copper. The dimensions of the cryostat are as minimal as necessary to eliminate the contribution of the radioactive contaminations of the Cu cryostat to the detector background.

(c) The shield is composed of two parts: (i) inner shield—ultra-high purity LN_2 (10^{-15} g/g for ^{40}K and ^{238}U, 5×10^{-15} g/g for ^{232}Th, and 0.05 mBq/m^3 for ^{222}Rn); (ii) outer part—HP water, whose volume is large enough to suppress external background to a negligible level.

The optimization of the setup design was performed with the help of the GEANT3.21 package and event generator DECAY4. About 400 HP Ge detectors ($\oslash 8.5 \times 8.5$ cm, weight of 2.5 kg each) are located in the center of a Cu sphere (inner enclosure of the cryostat 4.5 m in diameter and 0.6 cm thick) filled with liquid nitrogen. The detectors, arranged in nine layers, occupied a space of 90 cm in diameter. It is supposed that crystals are fixed with the help of a holder system made of nylon strings. The thin Cu wire $\oslash 0.2$ mm is attached to each detector to provide signal connection. The outer encapsulation of the cryostat 5 m in diameter is also made of HP Cu 0.6 cm thick. Both spheres are connected by two concentric Cu pipes with vacuum pump maintaining 10^{-6}-torr pressure in the space between two walls of the cryostat. The latter allow one to reduce the heat current through the walls of the cryostat to the value of 2.5 W/m^2 [61]; thus, total heat losses (including heat conduction through pipes, support structure, and cables) are near 200 W. This corresponds to a LN_2 consumption less than 100 kg/d. The cryostat is placed into the HP (10^{-14} g/g for ^{40}K, ^{232}Th, and ^{238}U and 10 mBq/m^3 for ^{222}Rn) water shield with a mass of 1000 t contained in the steel tank $\oslash 11 \times 11$ m^2. The dimensions of the CTF water tank are practically the same ($\oslash 11 \times 10$ m); hence, this shield could be also used for the GEM experiment. The design of the GEM setup reduces the LN_2 volume and allows us to solve problems of thermoinsulation, ultrahigh purity conditions, LN_2 consumption, safety requirements, etc.

The described model of the setup was used for background simulations. The total mass of detectors is equal to 1 t, liquid nitrogen mass is about 40 t, Cu cryostat mass is 7 t, mass of the water shield is 1000 t, holder-system mass is 2 kg, and mass of Cu wires is 1 kg. The internal and external origins of the background were investigated carefully. Internal background arises from residual impurities in

the Ge crystals themselves and surroundings (crystal holder system, liquid nitrogen, Cu cryostat, water, steel vessel) and from activation of all aforementioned materials at the Earth's surface. External background is generated by events originating outside the shield, such as photons and neutrons from the Gran Sasso rock, muon interactions, and muon induced activities.

The possible radioactive contaminations of the Ge detectors and materials by ^{40}K and ^{232}Th/^{238}U chains were taken from the real measurements [19, 44, 59, 62, 63]. The radiopurity criteria supposed for the liquid nitrogen (10^{-15} g/g for ^{40}K and ^{238}U, 5×10^{-15} g/g for ^{232}Th) seem to be realistic in light of the purity of the liquid scintillators already achieved by the BOREXINO collaboration [44]. Moreover, recently, the ^{222}Rn contamination of the LN_2 was also reduced down to the level of 1 μBq/m^3 [64]. It was shown by our calculation that requirements for the purity of the GEM water shield can be lowered to the level of about 10^{-13} g/g for U/Th contaminations [60].

Cosmogenic activities in HP ^{76}Ge detectors were estimated with the help of the program COSMO [65]. An activation time of 30 d at sea level[3)] and a deactivation time of 3 yr underground were assumed. It was found that background at 2038 keV is caused mainly by ^{22}Na, ^{60}Co, and ^{68}Ga (a daughter of cosmogenic ^{68}Ge), whose contributions could be lowered to a value less than 3×10^{-2} count/(yr t keV) near 2038 keV [60].

Summarizing all background origins (internal and external), the total background rate of the GEM experiment is less than 0.2 count/(yr t keV) at 2038 keV. The simulated response functions of the GEM setup after a 10-yr measuring time for 2β decay of ^{76}Ge with $T^{2\nu}_{1/2} = 1.8 \times 10^{21}$ yr [62] and $T^{0\nu}_{1/2} = 10^{27}$ yr, as well as the background contribution from the holder system and Cu cryostat, are depicted in Fig. 2. The background at energies below 1950 keV is dominated by $2\nu2\beta$ decay of ^{76}Ge (2.6×10^7 counts), while at 2040 keV the main contributions are from contamination of the holder system and Cu cryostat by U/Th chains. It is evident from Fig. 2 that $0\nu2\beta$ decay of ^{76}Ge with $T^{0\nu}_{1/2} = 10^{27}$ yr would be clearly registered (42 counts in the $0\nu2\beta$-decay peak). For a 10-yr measuring time, the value of $\lim S$ is equal to 5 counts (90% C.L.); thus, taking into account the number of ^{76}Ge nuclei (7×10^{27}) and detection efficiency ($\eta \approx 0.95$), the sensitivity of the GEM (expressed in the same manner as for the GENIUS project) is equal to $T^{0\nu}_{1/2} \geq 10^{28}$ yr ($m_\nu \leq 0.015$–0.05 eV).

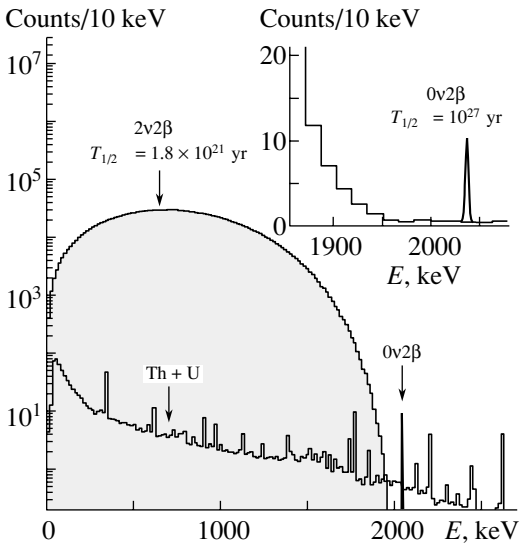

Fig. 2. The response functions of the GEM II setup [60] with 1000 kg of HP ^{76}Ge crystals and after 10 yr of measurements for 2β decay of ^{76}Ge with $T^{2\nu}_{1/2} = 1.8 \times 10^{21}$ yr and $T^{0\nu}_{1/2} = 10^{27}$ yr (solid histogram), as well as the background contribution from contaminations of the holder system and Cu cryostat by ^{232}Th and ^{238}U families. In the inset, the summed spectrum in the vicinity of the $0\nu2\beta$-decay peak of ^{76}Ge is shown on a linear scale.

The realization of the GEM experiment seems to be reasonably simple due to possibility of using the existing BOREXINO CTF as an outer water shield. One of the forthcoming large underground neutrino detectors such as KamLand [66] or BOREXINO [44] could also be appropriate for this purpose. The cost of GEM is estimated at \$150 million, whose main part would be for the production of enriched materials. However, the first phase of the project will be performed with 1 t of natural HPGe detectors (total cost is about \$6 million), which nevertheless would bring outstanding physical results. Indeed, the reachable half-life limit is directly proportional to the enrichment (abundance) of candidate nuclei contained in the detector. For the GEM I, the natural abundance of ^{76}Ge (7.6%) is about 11 times smaller compared to the enrichment assumed for the second stage (86%). Because all other characteristics of the setup (η, m, t, R, Bg) could be the same, the $T_{1/2}$ bound, which would be obtained with natural HPGe detectors, is about one order of magnitude lower: $T^{0\nu}_{1/2} \geq 10^{27}$ yr. This value translates to the neutrino mass constraint $m_\nu \leq 0.05$ eV, which is also of great interest for many theoretical models.

[3)] It was assumed that Ge materials and crystals were shielded against activation during production and transportation.

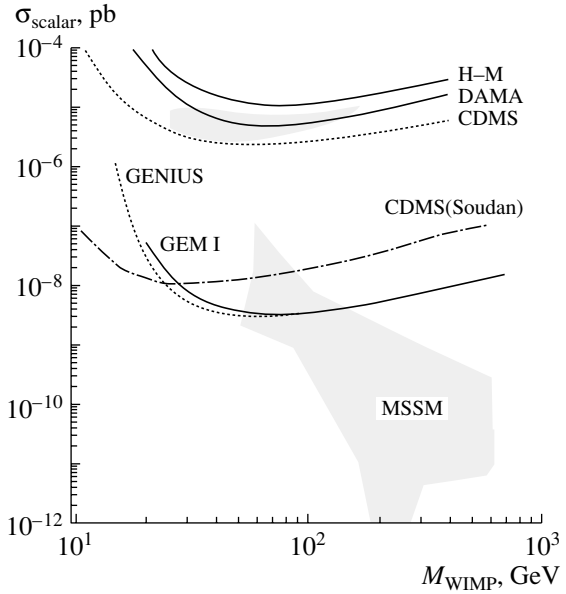

Fig. 3. Exclusion plots of the spin-independent WIMP–nucleon elastic cross section vs. WIMP mass. The regions above the curves are excluded at 90% C.L. Current limits from Heidelberg–Moscow (H–M) [73], DAMA [74], and CDMS [75] experiments are shown in the upper part of figure. The small shaded area: 2σ-evidence region from the DAMA experiment [76]. Projected exclusion plots for the CDMS [77], GENIUS [70], and GEM I [60] experiments are depicted too. The large shaded area represents the theoretical prediction for the allowed spin-independent elastic WIMP–proton scattering cross section calculated in [78].

Furthermore, another important issue of the GEM project is the quest for the dark matter particles (see reviews [67–69]). It has been already shown by Monte Carlo simulations [39, 43] that, for the GENIUS project exploiting 100 kg of natural HPGe detectors, the background rate of 40 counts/(yr t keV) could be obtained in the low-energy region (10–100 keV) relevant for the WIMP dark matter study. The main contributions to this rate are from (a) $2\nu2\beta$ decay of ^{76}Ge (50%); (b) cosmogenic activities in HP Ge crystals (25%); and (c) internal radioactive contamination of the liquid nitrogen, Cu wires, and holder system (25%). It is estimated that even lower background could be reached in the GEM I setup, where only an inner volume with 200 kg of HPGe detectors will be used for the dark matter search, while outer layers with the remaining 800 kg of HPGe crystals would serve as a superhigh-purity passive and active shield for the inner detectors [60]. Thus, the GEM I setup with the energy threshold of 10 keV and background rate of 40 counts/(yr t keV) (below 100 keV)[4] would provide the highest sensitivity for the WIMP dark matter search compared to other projects (see, for example, [71, 72]). It is demonstrated by the exclusion plots of the WIMP–nucleon elastic-scattering cross section, which are calculated for GEM I and depicted in Fig. 3 together with the best current and other projected limits [73–77]. The theoretical prediction for allowed spin-independent elastic WIMP-proton scattering cross section obtained in the framework of the constrained minimal supersymmetric standard model (MSSM) [78] is also shown there.[5] It is obvious from Fig. 3 that GEM I (and GENIUS) would test the MSSM by covering a larger part of the predicted SUSY parameter space. In that sense, both experiments could be competitive even with LHC in the SUSY quest [80]. At the same time, with a fiducial mass of HPGe detectors of 100–200 kg, it would be possible to test and identify unambiguously (within one year of data taking [81]) the seasonal modulation signature of the dark matter signal from the DAMA experiment [76] by using an alternative detector technology.

4. IMPLICATIONS AND CONCLUSIONS

Let us briefly discuss the physical implications of the future 2β-decay experiments. As was mentioned in the Introduction, the modern gauge theories offer many possibilities (besides conventional left-handed neutrino-exchange mechanism) to trigger the $0\nu2\beta$ decay [1–3]. For instance, in left-right symmetric GUT models, $0\nu2\beta$ decay can be mediated by heavy right-handed neutrinos [82]. It was shown [83] that 2β-decay experiments with the sensitivity level of $m_\nu \leq 0.01$ eV would be at the same time sensitive to right-handed W_R boson masses up to $m_{W_R} \geq 8$ TeV (for a heavy right-handed neutrino mass $\langle m_N \rangle = 1$ TeV) or $m_{W_R} \geq 5.3$ TeV (for $\langle m_N \rangle = m_{W_R}$). These limits, which could be established by the GEM II/GENIUS experiments, are nearly the same as expected for LHC [80].

Leptoquarks (LQ), new type of gauge bosons predicted by some GUTs, can induce $0\nu2\beta$ decay via LQ–Higgs couplings; thus, restrictions on their masses and coupling constants can be derived [84]. Direct searches for LQ in deep inelastic ep scattering at HERA give lower limits on their masses $M_{LQ} \geq 225$–275 GeV (depending on the LQ type and coupling) [85]. A detailed study [86] shows that

[4] The main background origin for the dark matter quest with Ge detectors is cosmogenic activity of ^{3}H produced in Ge [39, 43, 70]. For GEM I, the total ^{3}H activity is estimated at 5000 decays/(yr t), which contributes 10 counts/(yr t keV) to the total background rate (10–100 keV) [60] and is in good agreement with the result of [70].

[5] Very similar predictions from theoretical considerations in the MSSM with relaxed unification condition were derived in [79].

a GENIUS-like experiment would reduce the limit on LQ–Higgs couplings down to 10^{-7} for LQ with masses of 200 GeV. If no effect ($0\nu2\beta$ decay) is found, this means that either LQ-Higgs coupling must be smaller than 10^{-7} or there exist no LQ (coupled to electromagnetic strength) with masses below 10 TeV [86].

A hypothetical substructure of quarks and leptons can give rise to a new $0\nu2\beta$-decay mechanism by exchange of composite heavy Majorana neutrinos [87]; thus, compositeness could be checked at low energy. Recent analysis [88] shows that the most sensitive $0\nu2\beta$ results at present with ^{76}Ge [19, 20] yield the bound on the excited Majorana neutrino mass $m_N \geq 272$ GeV, which already exceeds the ability of LEP II to test compositeness, while future ^{76}Ge experiments (GEM II, GENIUS) would shift this limit to $m_N \geq 1$ TeV, competitive with the sensitivity of LHC [88].

There are also possible $0\nu2\beta$-decay mechanisms based on supersymmetric (SUSY) interactions: exchange of squarks, etc., within R-parity-violating [89–92] and exchange of sneutrinos, etc., in R-parity-conserving SUSY models [93]. It allows 2β-decay experiments to enter into the field of supersymmetry, where competitive restrictions on the sneutrino masses, R-parity-violating couplings, and other parameters could be obtained [94, 95].

Now, we are going to consider the role which future 2β experiments can play in the reconstruction of the neutrino mass spectrum. At present, this topic is widely discussed in the literature; thus, interested readers are referred to the latest publications [10, 11, 71, 96–100, 70], while we will summarize the most important results very briefly. There exist several schemes for the neutrino masses and mixing offered by theoretical models on the basis of observed oscillation data for the solar and atmospheric neutrinos [10, 11, 99]. Careful analysis of these schemes performed in [10, 11, 99] leads to the following statements: (a) effective neutrino mass, $\langle m_\nu \rangle$, which is allowed by oscillation data and could be observed in 2β decay, is different for different scenarios; hence, 2β-decay data could substantially narrow or restrict this wide choice of possible models; (b) the whole range of allowed $\langle m_\nu \rangle$ values is 0.001–1 eV, where there are three key scales of $\langle m_\nu \rangle$: 0.1, 0.02, and 0.005 eV [10]. Hence, it is obvious that future 2β-decay experiments, whose sensitivity to the neutrino mass limit would be on the order of 0.05 eV (CAMEO, CUORE, EXO, GEM I, MAJORANA, etc.) and 0.01 eV (GEM II, GENIUS), will bring crucial results for the reconstruction of the neutrino mass spectrum. The following citation [99] emphasizes our statement: "The observation of the $0\nu2\beta$ decay with a rate corresponding to $\langle m_\nu \rangle \approx 0.02$ eV can provide unique information on the neutrino mass spectrum and on the *CP* violation in the lepton sector, and if *CP*-invariance holds, on the relative *CP* parities of the massive Majorana neutrinos."

We can conclude that the challenging scientific goal to reach the (0.01–0.05)-eV neutrino mass domain would indeed be feasible for the CAMEO and GEM experiments, whose realization seems to have practically no technical risk and could be relatively simple due to the attractive possibility of using the already existing BOREXINO CTF. Both experiments will bring outstanding results for the 2β-decay studies as well as for the dark matter searches (GEM I stage), which are of great interest and would provide crucial tests of the key theoretical models of modern astroparticle physics.

REFERENCES

1. A. Faessler and F. Šimkovic, J. Phys. G **24**, 2139 (1998).
2. H. V. Klapdor-Kleingrothaus, Int. J. Mod. Phys. A **13**, 3953 (1998).
3. J. Suhonen and O. Civitarese, Phys. Rep. **300**, 123 (1998).
4. P. Vogel, nucl-th/0005020.
5. Super-Kamiokande Collab. (Y. Suzuki *et al.*), Nucl. Phys. B (Proc. Suppl.) **91**, 29 (2001).
6. SNO Collab. (Q. R. Ahmad *et al.*), Phys. Rev. Lett. **87**, 071301 (2001).
7. Super-Kamiokande Collab. (Y. Fukuda *et al.*), Phys. Rev. Lett. **81**, 1562 (1998); **82**, 1810, 2430 (1999).
8. LSND Collab. (E. D. Church *et al.*), Nucl. Phys. A **663–664**, 799 (2000).
9. J. D. Bjorken, hep-ph/0006180.
10. H. V. Klapdor-Kleingrothaus *et al.*, Phys. Rev. D **63**, 073005 (2001).
11. S. M. Bilenkij *et al.*, Phys. Lett. B **465**, 193 (1999).
12. J. Schechter and J. W. F. Valle, Phys. Rev. D **25**, 2951 (1982).
13. V. I. Tretyak and Yu. G. Zdesenko, At. Data Nucl. Data Tables **61**, 43 (1995); **80**, 84 (2002).
14. S. R. Elliot *et al.*, Phys. Rev. C **46**, 1535 (1992).
15. N. Kudomi *et al.*, Phys. Rev. C **63**, 065501 (2001).
16. F. A. Danevich *et al.*, Phys. Rev. C **62**, 045501 (2000).
17. A. Alessandrello *et al.*, Phys. Lett. B **486**, 13 (2000).
18. R. Luescher *et al.*, Phys. Lett. B **434**, 407 (1998).
19. L. Baudis *et al.*, Phys. Rev. Lett. **83**, 41 (1999).
20. C. E. Aalseth *et al.*, Phys. Rev. C **59**, 2108 (1999); D. Gonzalez *et al.*, Nucl. Phys. B (Proc. Suppl.) **87**, 278 (2000).
21. E. Fiorini *et al.*, Lett. Nuovo Cimento **3**, 149 (1970).
22. M. Moe and P. Vogel, Annu. Rev. Nucl. Part. Sci. **44**, 247 (1994).

23. A. A. Artukhov *et al.*, Yad. Fiz. **61**, 1336 (1998) [Phys. At. Nucl. **61**, 1236 (1998)]; A. Pokidychev and M. Pokidycheva, Nucl. Instrum. Methods Phys. Res. A **438**, 7 (1999).
24. M. K. Moe, Phys. Rev. C **44**, 931 (1991).
25. M. Miyajima *et al.*, KEK Proc. **91** (5), 19 (1991).
26. M. Miyajima *et al.*, AIP Conf. Proc. **338**, 253 (1997).
27. M. Danilov *et al.*, Phys. Lett. B **480**, 12 (2000).
28. B. Caccianiga and M. G. Giammarchi, Astropart. Phys. **14**, 15 (2000).
29. H. Ejiri *et al.*, Phys. Rev. Lett. **85**, 2917 (2000).
30. N. Ishihara *et al.*, Nucl. Instrum. Methods Phys. Res. A **373**, 325 (1996); **443**, 101 (2000).
31. F. A. Danevich *et al.*, Nucl. Phys. A **694**, 375 (2001).
32. LENS Collab. (M. Cribier *et al.*), Nucl. Phys. B (Proc. Suppl.) **87**, 195 (2000).
33. K. Zuber, Phys. Lett. B **485**, 23 (2000).
34. NEMO Collab. (F. Piquemal *et al.*), Nucl. Phys. B (Proc. Suppl.) **77**, 352 (1999).
35. E. Fiorini, Phys. Rep. **307**, 309 (1998).
36. NEMO Collab. (X. Sarazin *et al.*), hep-ex/0006031.
37. CUORE Collab. (G. Gervasio *et al.*), Nucl. Phys. A **663–664**, 873 (2000).
38. MAJORANA Project, http://majorana.pnl.gov.
39. H. V. Klapdor-Kleingrothaus *et al.*, J. Phys. G **24**, 483 (1998).
40. S. Stoica and H. V. Klapdor-Kleingrothaus, Phys. Rev. C **63**, 064304 (2001).
41. A. Bobyk *et al.*, Phys. Rev. C **63**, 051301 (2001).
42. L. Baudis *et al.*, Nucl. Instrum. Methods Phys. Res. A **426**, 425 (1999).
43. O. A. Ponkratenko *et al.*, in *Proceedings of International Conference on Dark Matter in Astro- and Particle Physics, Heidelberg, Germany, 1998,* Ed. by H. V. Klapdor-Kleingrothaus and L. Baudis (Institute of Physics, Bristol, 1999), p. 738.
44. BOREXINO Collab. (G. Bellini *et al.*), Nucl. Phys. B (Proc. Suppl.) **48**, 363 (1996).
45. G. Bellini *et al.*, Phys. Lett. B **493**, 216 (2000); Eur. Phys. J. C **19**, 43 (2001).
46. G. Alimonti *et al.*, Nucl. Instrum. Methods Phys. Res. A **406**, 411 (1998).
47. G. Alimonti *et al.*, Astropart. Phys. **8**, 141 (1998).
48. G. Alimonti *et al.*, Nucl. Instrum. Methods Phys. Res. A **440**, 360 (2000).
49. F. A. Danevich *et al.*, Pis'ma Zh. Éksp. Teor. Fiz. **49**, 417 (1989) [JETP Lett. **49**, 476 (1989)].
50. F. A. Danevich *et al.*, Phys. Lett. B **344**, 72 (1995).
51. F. A. Danevich *et al.*, Nucl. Phys. A **643**, 317 (1998).
52. F. A. Danevich *et al.*, Nucl. Phys. B (Proc. Suppl.) **70**, 246 (1999).
53. T. Fazzini *et al.*, Nucl. Instrum. Methods Phys. Res. A **410**, 213 (1998).
54. A. Sh. Georgadze *et al.*, Instrum. Exp. Tech. **39**, 191 (1996); S. Ph. Burachas *et al.*, Nucl. Instrum. Methods Phys. Res. A **369**, 164 (1996).
55. A. Staudt *et al.*, Europhys. Lett. **13**, 31 (1990).
56. M. Hirsch *et al.*, Phys. Lett. B **372**, 8 (1996).
57. R. Brun *et al.*, CERN Program Library Long Write-up W5013 (CERN, 1994).
58. O. A. Ponkratenko, V. I. Tretyak, and Yu. G. Zdesenko, Yad. Fiz. **63**, 1355 (2000) [Phys. At. Nucl. **63**, 1282 (2000)].
59. L. Baudis *et al.*, hep-ex/0012022.
60. Yu. G. Zdesenko *et al.*, J. Phys. G **27**, 2129 (2001).
61. R. H. Kropschot, Cryogenics **1**, 171 (1961).
62. M. Gunther *et al.*, Phys. Rev. D **55**, 54 (1997).
63. P. Jagam and J. J. Simpson, Nucl. Instrum. Methods Phys. Res. A **324**, 389 (1993).
64. G. Heusser *et al.*, Appl. Radiat. Isot. **52**, 691 (2000).
65. C. J. Martoff and P. D. Lewin, Comput. Phys. Commun. **72**, 96 (1992).
66. A. Suzuki, Nucl. Phys. B (Proc. Suppl.) **77**, 171 (1999).
67. G. Jungmann *et al.*, Phys. Rep. **267**, 195 (1996).
68. Y. Ramachers, astro-ph/9911260.
69. L. Baudis and H. V. Klapdor-Kleingrothaus, astro-ph/0003434.
70. H. V. Klapdor-Kleingrothaus and B. Majorovits, hep-ph/0103079.
71. H. V. Klapdor-Kleingrothaus, hep-ph/0102319.
72. H. V. Klapdor-Kleingrothaus *et al.*, hep-ph/0103082.
73. L. Baudis *et al.*, Phys. Rev. D **59**, 022001 (1999).
74. R. Bernabei *et al.*, Nucl. Phys. B (Proc. Suppl.) **70**, 79 (1998); Phys. Lett. B **389**, 757 (1996).
75. R. Abusaidi *et al.*, Phys. Rev. Lett. **84**, 5699 (2000).
76. R. Bernabei *et al.*, Phys. Lett. B **480**, 23 (2000).
77. R. Abusaidi *et al.*, Nucl. Instum. Methods Phys. Res. A **444**, 345 (2000).
78. J. Ellis *et al.*, Phys. Lett. B **481**, 304 (2000).
79. V. A. Bednyakov and H. V. Klapdor-Kleingrothaus, Phys. Rev. D **63**, 095005 (2001).
80. T. Rizzo, hep-ph/9612440; M. Cvetic and S. Godfrey, hep-ph/9504216; S. Godfrey *et al.*, hep-ph/9704291.
81. S. Cebrian *et al.*, Astropart. Phys. **14**, 339 (2001).
82. M. Doi *et al.*, Prog. Theor. Phys. Suppl. **69**, 602 (1983); Prog. Theor. Phys. **89**, 139 (1993); R. N. Mohapatra, Nucl. Phys. B (Proc. Suppl.) **77**, 376 (1999).
83. H. V. Klapdor-Kleingrothaus and M. Hirsch, Z. Phys. A **359**, 361 (1997).
84. M. Hirsch *et al.*, Phys. Lett. B **378**, 17 (1996); Phys. Rev. D **54**, 4207 (1996).
85. H1 Collab. (S. Aida *et al.*), Phys. Lett. B **369**, 173 (1996).
86. H. V. Klapdor-Kleingrothaus *et al.*, MPI-Report MPI-H-V26-1999 (Heidelberg, 1999).
87. N. Cabibbo *et al.*, Phys. Lett. B **139B**, 459 (1984); O. Panella *et al.*, Phys. Rev. D **56**, 5766 (1997).
88. O. Panella *et al.*, Phys. Rev. D **62**, 015013 (2000).
89. R. Mohapatra, Phys. Rev. D **34**, 3457 (1986).
90. M. Hirsch *et al.*, Phys. Rev. Lett. **75**, 17 (1995); Phys. Rev. D **53**, 1329 (1996); Phys. Lett. B **372**, 181 (1996); **459**, 450 (1999).

91. A. Faessler *et al.*, Phys. Rev. Lett. **78**, 183 (1997); Phys. Rev. D **58**, 055004, 115004 (1998).
92. A. Wodecki *et al.*, Phys. Rev. D **60**, 115007 (1999).
93. M. Hirsch *et al.*, Phys. Lett. B **398**, 311 (1997); **403**, 291 (1997); Phys. Rev. D **57**, 2020 (1998).
94. M. Hirsch *et al.*, Phys. Rev. D **57**, 1947 (1998).
95. G. Bhattacharyya *et al.*, Phys. Lett. B **463**, 77 (1999).
96. F. Vissani, JHEP **9906**, 022 (1999).
97. M. Czakon *et al.*, Acta Phys. Pol. B **30**, 3121 (1999).
98. M. Czakon *et al.*, Acta Phys. Pol. B **31**, 1365 (2000).
99. S. M. Bilenky *et al.*, hep-ph/0102265; hep-ph/0104218.
100. H. V. Klapdor-Kleingrothaus, hep-ph/0102276; hep-ph/0103074.

Physics of Atomic Nuclei, Vol. 65, No. 12, 2002, pp. 2198–2201. From Yadernaya Fizika, Vol. 65, No. 12, 2002, pp. 2261–2264.

An Update on the Start-up of the Double-Beta-Decay Experiment Nemo 3*

C. S. Sutton**
(for the NEMO Collaboration)

Mount Holyoke College, S. Hadley, MA, USA

Received February 13, 2002

Abstract—The NEMO collaboration is in the final stages of completing a detector to search for neutrinoless double-beta decay. The experiment is called NEMO 3 and came on line at the beginning of 2002. Located in the Fréjus Underground Laboratory, the detector holds 10 kg of double-beta-decay isotopes, allowing one to study the effective neutrino mass down to approximately 0.1 eV. Thus, the detector has the potential to confirm physics beyond the Standard Model. Three of the detector's sectors have been operating since June 2000 to perform diagnostic tests on the track recognition, the calorimeter, and the software. The results of these diagnostic tests are presented with a discussion of the detector and source backgrounds. © *2002 MAIK "Nauka/Interperiodica".*

1. INTRODUCTION

The recent experimental findings from the Super-Kamiokande detector [1] and the Sudbury Neutrino Observatory (SNO) [2] point toward massive neutrinos given the solar and atmospheric neutrino data. These findings raise the fundamental question: Are the neutrinos Dirac or Majorana particles? This question is best answered through neutrinoless double-beta decay ($\beta\beta0\nu$).

The objective of the NEMO (Neutrino Ettore Majorana Observatory) collaboration is to measure, via $\beta\beta0\nu$, the effective neutrino mass $\langle m_\nu \rangle$ with a limit approaching 0.1 eV. This corresponds to a half-life on the order of 10^{25} yr. To achieve this goal, two prototypes were constructed. NEMO 2 [3] with a few hundred grams of double-beta-decay isotopes made significant progress in the area of two-neutrino double-beta decay ($\beta\beta2\nu$). Here, NEMO 2 made high-statistics measurements for the $\beta\beta2\nu$ half-lives of ^{100}Mo [4, 5], ^{116}Cd [6], ^{82}Se [7], and ^{96}Zr [8]. Additionally, valuable knowledge of backgrounds and data analysis was gained. A description of the NEMO 3 detector, the current status of the experiment, and estimates of backgrounds are given in this article.

2. NEMO 3 EXPERIMENT

The NEMO 3 experiment uses the same technologies as NEMO 2; however, all of the components have been carefully selected for their radiopurity. The NEMO 3 detector is also capabable of holding 20 times the source material as NEMO 2. The construction of this experiment has been possible through a moderately large international collaboration (approximately 45) involving the following laboratories and institutions: LAL (Orsay), CENBG (Bordeaux), IReS (Strasbourg), CFR (Gif-sur-Yvette, France), CTU FNSPE (Czech Republic), JINR (Dubna, Russian), ITEP (Moscow, Russia), INEEL (Idaho Falls), MHC (South Handley, USA), and Jyväskylä University (Finland). NEMO 3, as was NEMO 2, is located in the Fréjus Underground Laboratory (LSM Modane) in France.

The experiment is based on the direct detection of two electrons from thin foils of double-beta-decay isotopes. Due to its design (see figure), the NEMO 3 device is able to easily operate with several double-beta-decay isotopes and can accomodate up to 10 kg of such sources in the form of thin foils which are $\sim$50 μm thick. Special interest is given to the isotopes with high Q values of $\beta\beta$ decay, specifically ^{100}Mo ($Q_{\beta\beta} = 3034$ keV) and ^{82}Se ($Q_{\beta\beta} = 2995$ keV).

Particle detection and identification involve two measurements. A tracking volume allows reconstruction of the paths of charged particles inside the detector, and a calorimeter is capable of measuring the energy of α, e^+, e^-, and γ particles. The tracking part is composed of 6180 open octogonal drift cells, 270 cm long, which operate in Geiger mode. These provide three-dimensional tracking of charged particles. The wire chambers are filled with a mixture of helium gas and 4% ethyl alcohol to minimize

*This article was submitted by the author in English.

**e-mail: ssutton@mtholyoke.edu

1063-7788/02/6512-2198$22.00

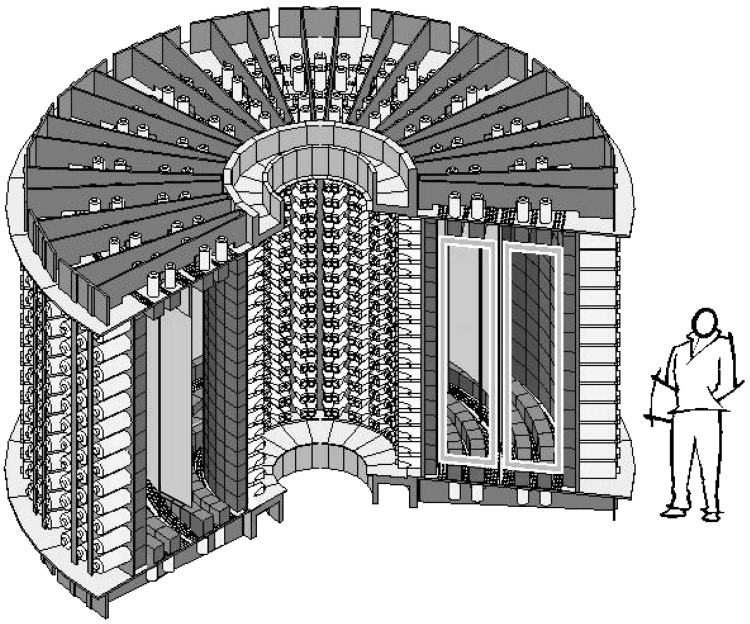

Schematic view of the NEMO 3 detector.

multiple-scattering effects. The tracking volume is surrounded by a calorimeter that is made of 1940 blocks of plastic scintillators coupled to very low-radioactivity Hammamatsu PMTs. The activity of the PMTs are three orders of magnitude below standard PMTs.

A daily survey of the absolute time and energy calibrations with a laser system is planned for the NEMO 3 calorimeter. In this system, a small scintillator converts the laser pulse into a properly shaped and wavelength-shifted (420 nm) signal that simulates a one-electron event in the scintillator. This light is delivered by optical fibers (1940 fibers in all) to the PMTs. An accuracy of 1% for this energy calibration survey is assured by a comparison with six reference PMTs that are continuously exposed to ^{207}Bi sources.

The recognition of pair production (e^+e^-) in the source foils is accomplished with a vertical magnetic field of 30 G, generated with a solenoid that surrounds the detector. An external shield, made of low-radioactivity iron and 20 cm thick, covers the detector in order to reduce γ-ray and thermal-neutron external backgrounds coming from the laboratory walls. To thermalize fast neutrons present in the laboratory, an additional outer shield of water is planned. It will be made of ten water tanks that provide a 35-cm layer of water.

3. CURRENT STATUS OF THE EXPERIMENT

3.1. Status of the Detector Construction

The construction of the 20 sectors has been completed. All the sectors are equipped with source foils, mounted on the detector frame, and merged in the Fréjus Underground Laboratory. By the end of August 2001, the detector had been filled with He gas. The Geiger cells and PMTs are currently being tested and calibrated. After this, the magnetic coil, the iron shielding, and the neutron shield will be added.

Though NEMO 3 was originally designed to run with 10 kg of ^{100}Mo, the detector is currently equipped with 7.2 kg of ^{100}Mo and other different double-beta-decay isotopes. Finally, there are also foils devoted to measurements of external background. A list of foil materials and respective quantities is summarized in Table 1.

Table 1. Sources installed in the NEMO 3 detector and their respective quantities

Isotope	Study	Mass, kg	Number sector
^{100}Mo	$\beta\beta0\nu$, $\beta\beta2\nu$	7.2	12
^{82}Se	$\beta\beta0\nu$, $\beta\beta2\nu$	1	2.3
^{116}Cd	$\beta\beta0\nu$, $\beta\beta2\nu$	0.4	1
^{130}Te	$\beta\beta0\nu$, $\beta\beta2\nu$	0.6	1.8
^{150}Nd	$\beta\beta0\nu$, $\beta\beta2\nu$	0.048	0.14
^{96}Zr	$\beta\beta2\nu$	0.02	0.03
^{48}Ca	$\beta\beta2\nu$	0.07	0.03
Cu	Background	0.6	1
$^{nat}TeO_2$	Background	0.9	1.0

Table 2. Total activity for each of the components of the detector

Component name	Weight, kg	Total activity, Bq			
		^{40}K	^{214}Bi	^{208}Tl	^{60}Co
PMTs	600	830	300	18	
Scintillators	5000	<100	<0.7	<0.3	1.8 ± 0.4
Copper frame	25 000	<125	<25	<10	<6
Iron petals	10 000	<50	<6	<8	17 ± 4
μ metal	2000	<17	<2	2.0 ± 0.7	4.3 ± 0.7
Wires	1.7	$<8 \times 10^{-3}$	$<10^{-3}$	$<6 \times 10^{-4}$	10^{-2}
Iron shielding	180 000	<3000	<300	<300	300 ± 100

3.2. Studies Carried Out with Three Sectors

As a preliminary test, three sectors have been successfully running since June 2000. Tests on the tracking and scintillator detectors were carried out to adjust the PMTs and the Geiger cells for optimal working voltages. Simultaneously, trigger and data acquisition tests were also carried out. Finally, thorough studies of track and vertex reconstruction for the tracking volume were carried out.

For track reconstruction, a neutron source, ^{252}Cf with a flux of 1300 neutrons per second, was placed on the exterior wall of the three sectors. Neutrons were thermalized by a paraffin shield surrounding the ^{252}Cf source. Some neutrons were then captured on the copper inside the frame of the detector, which generated high-energy photons. These photons Compton scattered in the plastic scintillators to give high-energy electrons ($E_e > 3.5$ MeV). Due to the absence of a magnetic field, the electrons leave straight tracks in the tracking chamber and are used to study longitudinal and transverse track reconstruction provided by the Geiger cells. The results of the 11-h run showed that the average transverse resolution of the Geiger cells (in the horizontal plane of the detector) is 0.7 mm and the longitudinal resolution (in the vertical direction, along the drift cell) is 1 cm.

The vertex reconstruction was also studied with ^{207}Bi, a β emitter. These sources have an activity of 2–3 nCi and were placed in special tubes designed for calibration measurements. The tubes were then inserted along the source foils inside the detector. Each sector has one such tube accomodating three calibration sources. It was found that the transverse resolution is 0.2 to 0.3 cm and the longitudinal one is 0.8 to 1.1 cm. This range of values depends on the electron energy. The lower values correspond to electrons with 1 MeV, while the higher ones to electrons with 500 keV. In summary, the track and vertex reconstruction performances are more than sufficient for NEMO 3.

Table 3. Measured activities of the source foils

NEMO 3 foil		Activity, μBq/kg	
isotope	type	^{208}Tl	^{214}Bi
^{100}Mo	Metallic	<104	<300
^{100}Mo	Composite	<140	<90
^{82}Se	Composite	400 ± 100	1200 ± 500
^{116}Cd	Metallic	<500	<1500
^{130}Te	Composite	<510	<680
Cu	Metallic	<33	<117
$^{nat}TeO_2$	Composite	<333	<167

4. EXPECTED BACKGROUND AND SOURCE RADIOPURITY

Backgrounds in the experiment are identified as one of two types. The first one originates in the $\beta\beta$ source foils and is called the internal background. The second, called external background, has its origin outside the detector, in the laboratory hall. The external background is mainly due to photons, neutrons, and radon gas. The cosmic-ray contribution is negligible because the detector is located in the Fréjus Underground Laboratory, providing an efficient shield of 1780 m of rock that corresponds to 4850 mwe.

For NEMO 3, the expected background for the $\beta\beta0\nu$ signal has three origins. The first one is due to the β decays of ^{214}Bi and ^{208}Tl (both having high Q values), which are present as an "internal background" and come from the uranium and thorium decay chains. They can mimic double-beta-decay events by β emission followed by the Möller effect

or by a β–γ cascade followed by a Compton effect. The second origin of the $\beta\beta0\nu$ background comes from the interaction of high-energy γ rays with the source foils (external background). These photons are created by neutron captures inside the detector frame and from radioactivity in the detector components. It seems now that the above-mentioned backgrounds can be reduced to a negligible level. However, another background is the most troublesome one. It is the tail of the $\beta\beta2\nu$ decay, which is always present in the window of interest, 2.8 to 3.2 MeV.

All the detector components have been carefully selected to be ultrafree of ^{214}Bi, ^{208}Tl, and ^{40}K. In Table 2, radioactivity measurements with HPGe detectors of the NEMO 3 components are shown. Note the radioactive contamination in the detector is dominated by the low-radioactivity PMT glass.

The limits on the source foil radiopurity were determined in order to minimize the contribution to the $\beta\beta0\nu$ signal from ^{208}Tl and ^{214}Bi. The objective for the ^{100}Mo source strips was for them to have activities less than 20 μBq/kg in ^{208}Tl and 300 μBq/kg in ^{214}Bi. To reach these strict specifications, purification methods for molybdenum were successfully developed.

The first one, which was developed at ITEP (Moscow, Russia), is based on purification by local melting of a solid molybdenum rod with an electron beam and then drawing an ultrapure ^{100}Mo monocrystal from the liquid portion. After that, the crystal is rolled into a thin metallic foil ready to be used in the detector.

The second method of purification is chemical in nature and was developed at INEEL (Idaho, USA). Purified ^{100}Mo is produced in the form of powder that is then used for fabrication into sandwichlike composite foils with a binding paste and mylar strips. The mylar strips were previously irradiated with an ion beam and then etched with a chemical process to form a good bonding surface.

The radiopurity of the these and other source foils were measured by HPGe detectors in the LSM. Table 3 shows that, with the exception of the ^{82}Se foils, only upper limits in ^{208}Tl and ^{214}Bi activities were established for all the foils installed inside the NEMO 3 detector.

5. CONCLUSION

The sensitivity of the NEMO 3 detector to see the $\beta\beta0\nu$ signal has been calculated for five years of data acquisition. This has been done for the energy window of 2.8–3.2 MeV for the ^{100}Mo and ^{82}Se sources. The $\beta\beta0\nu$ detection efficiency is estimated to be 14%. Under the assumption that $\beta\beta2\nu$ decay is the only background, then there will be six background events for 7 kg of ^{100}Mo and zero background events for 1 kg of ^{82}Se.

Since June 2000, the three sectors have been successfully running in the LSM laboratory. This trial run has provided a thorough test of the functionality of the counters and a study of the track and vertex reconstruction ability of the wire chamber. It was verified that the reconstruction performances of the tracking device fully satisfy the NEMO 3 requirements. At the beginning of 2001, the complete detector started its investigation of neutrinoless double-beta decay.

REFERENCES

1. S. Fukuda *et al.*, Phys. Rev. Lett. **86**, 5651 (2001); T. Toshito *et al.*, hep-ex/0105023.
2. Q. R. Ahmad *et al.*, Phys. Rev. Lett. **87**, 071301 (2001).
3. R. Arnold *et al.*, Nucl. Instrum. Methods Phys. Res. A **354**, 338 (1995).
4. D. Dassié *et al.*, Phys. Rev. D **51**, 2090 (1995).
5. R. Arnold *et al.*, Nucl. Instrum. Methods Phys. Res. A **401**, 144 (1997).
6. R. Arnold *et al.*, Z. Phys. C **72**, 239 (1996).
7. R. Arnold *et al.*, Nucl. Phys. A **636**, 209 (1998).
8. R. Arnold *et al.*, Nucl. Phys. A **658**, 299 (1999).

Physics of Atomic Nuclei, Vol. 65, No. 12, 2002, pp. 2202–2209. From Yadernaya Fizika, Vol. 65, No. 12, 2002, pp. 2265–2272.

NEUTRINO OSCILLATIONS AND MIXINGS, NEUTRINOS FROM THE SUN, REACTORS, AND ACCELERATORS

Neutrino Beams at Accelerators*

A. Guglielmi**

INFN and Department of Physics G. Galilei, Padova, Italy

Received February 13, 2002

Abstract—Prospects for neutrino oscillation experiments with neutrino factories based on muon decay and conventional superbeams are discussed with a special emphasis on the neutrino beam properties.

1. INTRODUCTION

Experimental results on solar and atmospheric neutrinos [1, 2] have opened a new and exciting era. Oscillations between neutrinos of different flavor require a neutrino mass term and a flavor lepton number violation that cannot be accommodated simply within the Standard Model. The neutrino flavor eigenstates $|\nu_\alpha\rangle$ ($\alpha = e, \mu, \tau$) are then expressed in terms of their mass eigenstates $|\nu_i\rangle$ ($i = 1, 2, 3$), $|\nu_\alpha\rangle = U_{\alpha i}|\nu_i\rangle$. The mixing matrix U can be parametrized with six independent parameters: three mixing angles θ_{12}, θ_{13}, θ_{23}; two mass-squared differences Δm^2_{12}, Δm^2_{23} ($\Delta m^2_{ij} = m^2_i - m^2_j$); and a *CP*-violating phase δ. In the current interpretation of the collected data (Fig. 1),

(i) the solar neutrino deficit could be accounted for by $\nu_e \to \nu_\mu$ oscillations with $|\Delta m_{12}|^2 \sim 10^{-5}$ eV^2 and $\sin^2\theta_{12} \sim 5 \times 10^{-3}$ (SMA) or 0.8 (LMA) or $|\Delta m_{12}|^2 \sim 10^{-7}$ eV^2 (LOW) [1];

(ii) the Super-Kamiokande data on atmospheric neutrinos [2], combined with the CHOOZ results [3] which give a limit $\sin^2\theta_{13} \leq 0.05$, exclude $\nu_\mu \to \nu_e$ oscillations, resulting in $\nu_\mu \to \nu_\tau$ with $|\Delta m_{23}|^2 \sim 2.5 \times 10^{-3}$ eV^2 and $\sin^2\theta_{23} \sim 1$;

(iii) all three known neutrinos participate actively in the oscillations; in the limit $|\Delta m^2_{12}| \ll |\Delta m^2_{23}|$, the oscillations driven by $|\Delta m^2_{12}|$ can be neglected and the solar and atmospheric ν oscillations appear to be largely decoupled. The resulting leading-oscillation probabilities for ν of energy E_ν propagating for a distance L in vacuum are described by only Δm^2_{23}, θ_{13}, and θ_{23}:

$$P_{\nu_e\to\nu_\mu} = \sin^2\theta_{23}\sin^2 2\theta_{13}\sin^2\frac{\Delta m^2_{23}L}{4E_\nu}, \quad (1)$$

$$P_{\nu_e\to\nu_\tau} = \cos^2\theta_{23}\sin^2 2\theta_{13}\sin^2\frac{\Delta m^2_{23}L}{4E_\nu}, \quad (2)$$

$$P_{\nu_\mu\to\nu_\tau} = \cos^4\theta_{13}\sin^2 2\theta_{23}\sin^2\frac{\Delta m^2_{23}L}{4E_\nu}. \quad (3)$$

However, accounting for the most favored LMA solar solution, all six parameters of the mixing matrix are involved, i.e.,

$$\begin{aligned} P_{\nu_e\to\nu_\mu} &= \sin^2\theta_{23}\sin^2 2\theta_{13}\sin^2\left(\frac{\Delta m^2_{23}L}{4E_\nu}\right) \quad (4)\\ &+ \cos^2\theta_{23}\sin^2 2\theta_{12}\sin^2\left(\frac{\Delta m^2_{12}L}{4E_\nu}\right)\\ &+ J\cos\left(\delta - \frac{\Delta m^2_{23}L}{4E_\nu}\right)\frac{\Delta m^2_{12}L}{4E_\nu}\sin\left(\frac{\Delta m^2_{23}L}{4E_\nu}\right), \end{aligned}$$

where $J = \cos\theta_{13}\sin 2\theta_{23}\sin 2\theta_{13}$.

This phenomenological description will result in a more complex one if the claim of the LSND experiment on $\bar\nu_\mu \to \bar\nu_e$ [4] is confirmed (large parts of the parameters have been excluded by KARMEN II [5]).

Experiments at accelerators can explore different regions of the $\sin^2 2\theta$–Δm^2 plane according to L/E. In particular, the study of the LSND effect and of the atmospheric ν requires $L/E_\nu \sim 1$ and 100 km/GeV, respectively. Over the next ten years, a new generation of experiments at accelerators with long-baseline ν_μ beams [6], K2K at KEK ($L = 250$ km, $E_\nu \sim 1.5$ GeV), NUMI at FNAL, and CNGS at CERN ($L = 732$ km, $E_\nu \sim 8$, 17.7 GeV), are expected to confirm the $\nu_\mu \to \nu_\tau$ interpretation of the atmospheric ν deficit and to measure $\sin^2 2\theta_{23}$ and $|\Delta m^2_{23}|$ within 20% if $|\Delta m^2_{23}| > 10^{-3}$ eV^2. A direct check of the LSND results will be performed by the MiniBooNE experiment ($L \sim 0.5$ km, $E_\nu \sim 0.8$ GeV) [4]. In addition, further solar ν measurements and new long-baseline reactor experiments are expected to select the solar oscillation solution [7]. However, in the end, some open questions will still remain:

*This article was submitted by the author in English.

** e-mail: alberto.guglielmi@pd.infn.it

(i) the angle θ_{13}, which is the link between the solar and the atmospheric ν;

(ii) the sign of Δm^2_{23}, which determines the mass spectrum of the three-family ν;

(iii) the existence of a leptonic CP-violating phase $\delta \neq 0$.

2. CONVENTIONAL HIGH-ENERGY NEUTRINO BEAMS

High-energy accelerators provide neutrino beams through the decay of π and K produced by high-energy protons on light targets. Positive (negative) mesons are focused (defocused) by magnetic horns in a long evacuated decay tunnel where ν_μ ($\bar{\nu}_\mu$) are generated. The residual hadrons and muons are stopped by a heavy absorber. This conventional scheme, successfully applied in the past (see Fig. 2 [8]) and also in the K2K experiment, will be used in the MiniBooNE and CNGS, and NUMI long-baseline projects. Typically, such a ν_μ beam has a contamination of $\bar{\nu}_\mu$ at the few-percent level and $\sim 1\%$ of ν_e and $\bar{\nu}_e$ coming from $K^\pm$, K^0, and μ^+ decays, which affect the experimental sensitivity in the oscillation searches.

A sound knowledge of π and K production is required in order to predict ν energy spectra and composition. Indeed, the accurate description of the K^+ flux relative to the π^+ flux is essential to calculate the ν_e component in the beam. For these purposes, direct measurements of π and K production in Be by 400-GeV/c protons were performed by the NA20 collaboration [9] and by the SPY collaboration [10] (at 450 GeV/c with a precision better than 3% on the K/π ratio). Monte Carlo generators of hadronic interactions have a poor accuracy for the meson production, which limits the sensitivity to neutrino oscillation searches. The best agreement between predictions and data was found with the FLUKA standalone code [11], which reproduces the measured π and K yields at the level of $\sim 20\%$ (Figs. 3, 4) and the corresponding K^+/π^+ at 10% in the momentum region 30–100 GeV/c, which is expected to contribute most to a ν flux [12].

A neutrino beam at a high-energy proton accelerator is a quite complicated cascade of meson decay and reinteraction processes in the beam-line materials. An accurate description of the primary proton beam spot, the focusing system, and the materials inserted in the beam line from the target to the dump is necessary. Protons missing the target will interact in the downstream materials, producing a large fraction ($\sim 30\%$) of the defocused component $\bar{\nu}_\mu$ and $\bar{\nu}_e$.

These studies have been particularly relevant for the NOMAD experiment [13] searching for the

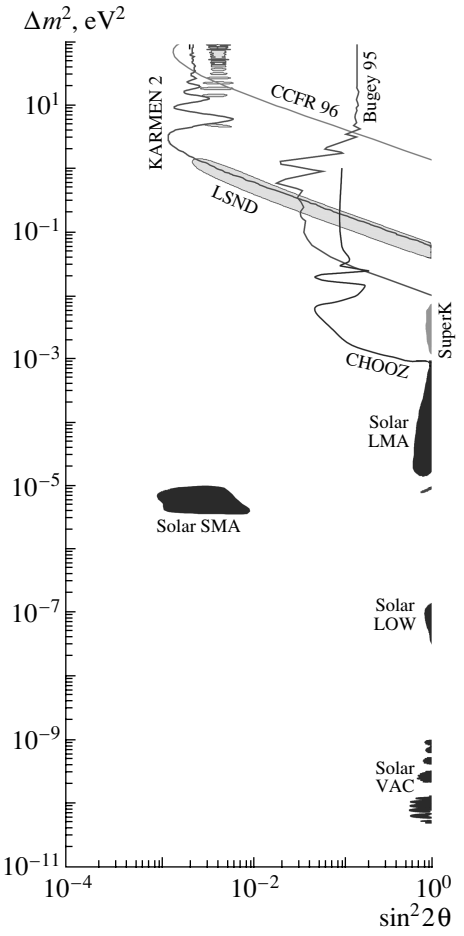

Fig. 1. Atmospheric, solar, and LSND ν oscillation parameter regions and the corresponding CHOOZ, KARMEN II, and Bugey 90%-C.L. exclusion plots.

$\nu_\mu \to \nu_\tau$ and $\nu_\mu \to \nu_e$ oscillations at CERN SPS [8], using such a conventional ν_μ beam ($E_\nu \simeq 24$ GeV) produced by 450-GeV/c protons on a Be target. The $\nu_\mu \to \nu_e$ transitions were searched for as an excess of the ν_e events with respect to that expected from the natural contamination of the beam ($\phi_{\nu_e}/\phi_{\nu_\mu} \sim 1\%$). The high resolution and granularity of the NOMAD detector allowed the study of this conventional neutrino beam with an unprecedented accuracy and statistics resulting in a stringent benchmark for the neutrino beams for the K2K, NUMI, and CNGS projects. A complete analysis of this ν beam was performed by a beam-line simulation from the Be target up to the NOMAD detector including the FLUKA generator with further corrections to the meson production based on the residual differences between the predicted and measured meson yield in Be. The agreement with the measured ν interactions in NOMAD is at the few-percent level with a sys-

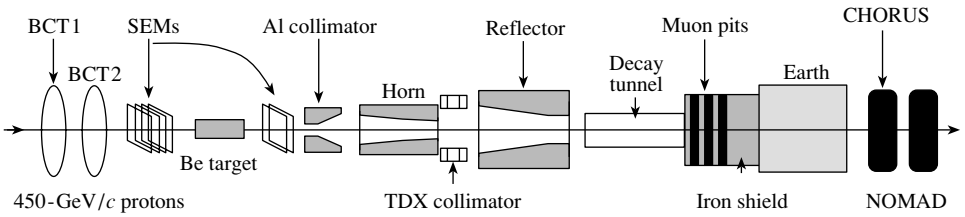

Fig. 2. Beam line of the WANF at CERN SPS (baseline distance 840 m).

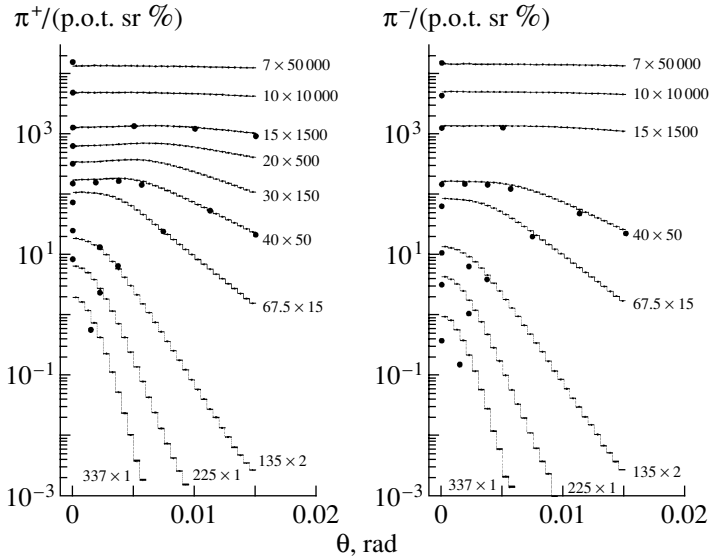

Fig. 3. Pion yields from the 100-mm Be target at different momenta P and production angles θ calculated by FLUKA and compared with the SPY and NA20 data (•, the difference in the primary proton momentum is taken into account). Both data and Monte Carlo are rescaled by a common factor different for each momentum value quoted in the labels, i.e., 67.5×15 means that at $P = 67.5$ GeV/c the data are rescaled by a factor of 15.

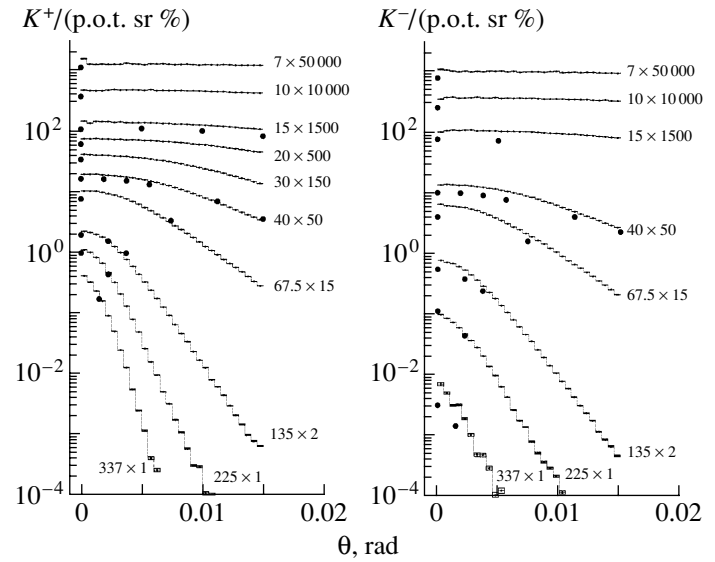

Fig. 4. Kaon yields from the 100-mm Be target at different momenta P and production angles θ calculated by FLUKA and compared with the SPY and NA20 data (see Fig. 3 for the symbols).

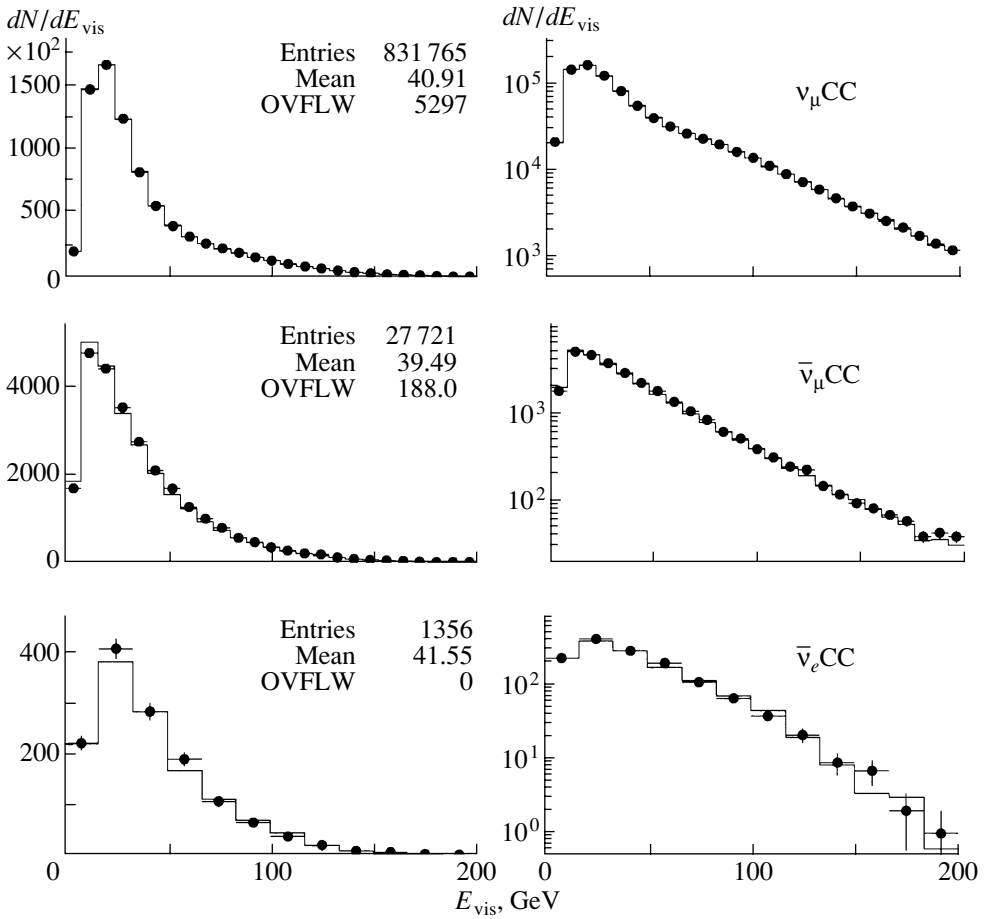

Fig. 5. Comparison of MC (solid line) and data (•) for the reconstructed ν_μ, $\bar{\nu}_\mu$, and $\bar{\nu}_e$ charged current interactions in the NOMAD experiment. The MC ν_μCC are normalized to the data.

tematic error of ~7% on ν_μCC/p.o.t. and of ~5% on ν_e/ν_μ event ratio (Fig. 5).

As a conclusion, conventional ν beams at accelerators are not pure ν_μ (ν_e) beams and knowledge of their composition suffers mainly from the uncertainties on the hadronic processes involved during generation and particle transport. In order to solve the neutrino mass and mixing puzzles, higher intensity, more collimated, and better defined ν beams than the conventional ones are needed in the next-generation experiments.

3. THE NEUTRINO FACTORY

As an alternative approach to overcome the limitations from conventional neutrino beams, the neutrino production by muon decay from a pure muon beam can be considered. This is indeed a perfectly well-known weak process, and the muon beams can be well measured in momentum and intensity. The basic concepts for a muon collider were introduced by Budker and Skrinsky [14]. Detailed calculations for such a neutrino factory (νF) were presented by Koshkarev [15] and then developed in the United States [16] and CERN [17] as the first step of a larger new physics program based on muon colliders.

In the CERN-proposed layout for a νF (Fig. 6), a 4-MW proton beam is accelerated up to 2.2 GeV/c by a superconducting proton linac (SPL) to produce low-energy π in a thin Hg target (10^{23} p.o.t./yr) after some accumulation and bunch compression. A collection system (magnetic horns) is envisaged to capture as many π and μ produced in their decay in few tens of meters as possible. Muons are then cooled and phase-rotated to reduce their phase space before being accelerated through a system of linacs up to 50 GeV/c. Finally, the 50 GeV/c μ of well-defined charge and momentum are injected into the accumulator, where they will circulate until they decay, delivering two intense ν beams along the two main straight sections. Either muon sign can be selected.

From a general point of view, the νF approach relies on a completely different strategy than conventional ν facilities, where only a fraction of the fo-

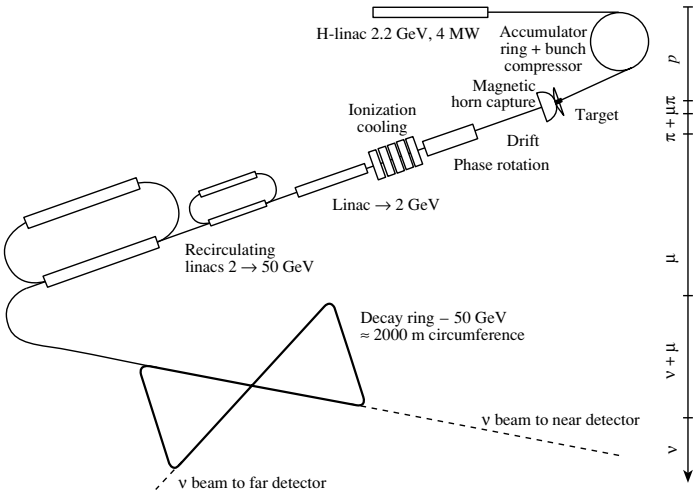

Fig. 6. Possible layout for the neutrino factory.

cused high-energy mesons produced by high-energy protons on a target decay giving neutrinos. In a νF based on μ decay, the primary beam power is used to produce as many π (and μ) per GeV as possible. Hence, the factory has to capture the largest fraction of resulting μ and to manipulate them in order to reduce their phase space in view of the final acceleration stage to produce high-energy ν. The decay tunnel typical of the conventional ν beam is replaced by the storage ring, where each μ circulates until it decays. The major advantages of a νF over a conventional ν source are the following:

(i) The decay $\mu^+ \to e^+\nu_e\bar{\nu}_\mu$ ($\mu^- \to e^-\bar{\nu}_e\nu_\mu$) produces a pure neutrino beam with equal numbers of $\bar{\nu}_\mu$, ν_e (ν_μ, $\bar{\nu}_e$).

(ii) The resulting ν are well collimated: their angular divergence is extended a factor of 5 less than in a conventional ν beams, extending neutrino exploitation to over several thousand kilometers of distance.

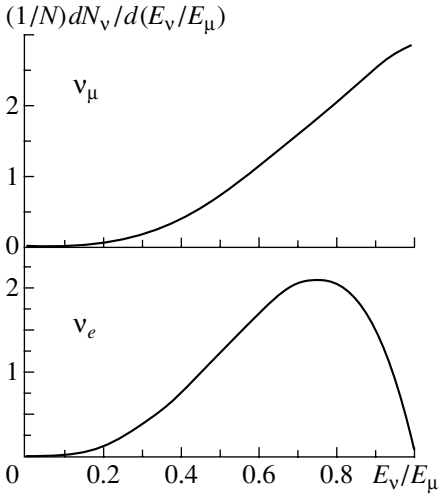

Fig. 7. Neutrino spectra at νF.

(iii) The μ momentum and neutrino energy spectra are well defined (accurate determination of P_μ by spin precession measurement) and tunable to experimental requirements:

$$\frac{d^2N_{\nu_\mu,\bar{\nu}_\mu}}{dy\,ds} = \frac{E_\mu^2}{\pi m_\mu^2 L^2}\,2y^2(3-2y)\Theta(y)\Theta(1-y), \tag{5}$$

$$\frac{d^2N_{\nu_e,\bar{\nu}_e}}{dy\,ds} = \frac{E_\mu^2}{\pi m_\mu^2 L^2}\,12y^2(1-y)\Theta(y)\Theta(1-y), \tag{6}$$

where ds is the detector area at a distance L, $y = E_\nu/E_\mu$, and the Θ functions account for the angular distributions (Fig. 7).

(iv) The neutrino flux $\phi_\nu \simeq E_\nu^2$, while in conventional neutrino beams $\phi_\nu \simeq E_\nu$; the expected number of charged current neutrino events and of the corresponding oscillation events at a distance L will be

$$N_{\rm CC} \simeq \phi_\nu\sigma_\nu \simeq \frac{{E_\nu}^3}{L^2}, \tag{7}$$

$$N_{\rm osc} \simeq \phi_\nu\sigma_\nu P_{\rm osc} \simeq \frac{{E_\nu}^3}{L^2}\sin^2\frac{L}{E_\nu} \simeq E_\nu, \tag{8}$$

where σ_ν is the charged current interaction cross section and $P_{\rm osc}$ is the oscillation probability. The optimal beam energy at the νF will be as large as possible: $E_\mu = 50$ GeV ($E_{\nu_\mu} \sim 34$ GeV).

(v) The ν flux intensity is expected to be more than 100 times the one in conventional beams: with $P_\mu = 50$ GeV/c and 0.3×10^{21} μ decay/yr, the expected ν interaction events at 732 km of distance are

Oscillation channels accessible at νF (μ^+ decay)

Oscillation channel	Experimental signature
$\nu_e \to \nu_\mu$	Appearance mode: detection of wrong-sign muons, μ^-
$\bar{\nu}_\mu \to \bar{\nu}_e$	Appearance mode: detection of wrong-sign electrons, e^+
$\nu_e \to \nu_x$	Disappearance mode: energy spectrum and NC/CC
$\bar{\nu}_\mu \to \bar{\nu}_x$	Disappearance mode: energy spectrum and NC/CC
$\nu_e \to \nu_\tau$	Appearance mode: detection of τ^- events
$\bar{\nu}_\mu \to \bar{\nu}_\tau$	Appearance mode: detection of τ^+ events

0.6×10^6 ν_μCC/(kt yr) (from μ^- decay) and 0.5×10^6 ν_eCC/(kt yr) (from μ^+ decay) to be compared to 2.4×10^3 ν_μCC/(kt yr) and 20 ν_eCC/(kt yr) for the CNGS ν beam.

(vi) The νF will give a pure ν beam: the sensitivity to oscillations will increase linearly with the statistics,

$$P_{\nu_\mu \to \nu_e} \simeq \frac{1}{\phi_{\nu_\mu}}, \tag{9}$$

while in the conventional beams it increases only with the square root of the statistics because of the ν_e contamination of the beam $B = \phi_{\nu_e}/\phi_{\nu_\mu}$:

$$P_{\nu_\mu \to \nu_e} \simeq \frac{\sqrt{\phi_{\nu_e}}}{\phi_{\nu_\mu}} = \frac{\sqrt{B}}{\sqrt{\phi_{\nu_\mu}}}. \tag{10}$$

(vii) The ν intensity can be precisely determined (within 1%) from the measurement of a monochromatic μ current circulating in the storage ring.

The νF lends itself naturally to the exploration of ν oscillations between ν flavors with a high sensitivity to small mixing angles and small mass differences (see table). The detector should be able to perform both appearance and disappearance experiments, providing final lepton identification and charge discrimination, which is a tag of the initial flavor and oscillation.

Among the many possibilities for studying ν oscillations in different channels, the search for $\nu_e \to \nu_\mu$ probing small $\sin^2 2\theta_{13}$ appears to be very attractive at νF. In fact, this transition can be studied in the appearance mode looking for μ^- (appearance of wrong-sign μ—see table) in ν beams where the searched-for ν type is totally absent (μ^+ beam in νF). Detailed studies for a 40-kt magnetic detector were performed [18–20]. Assuming $\Delta m^2_{23} \simeq 3 \times 10^{-3}$ eV^2 and $\sin^2 2\theta_{23} \simeq 1$, it will be possible to measure θ_{13} with a 0.2° precision down to 1° at $L = 3500$ km for 10^{21} μ decays, $E_\mu = 50$ GeV. Similarly, it will be possible to detect $\bar{\nu}_\mu \to \bar{\nu}_\tau$ transitions by both $\bar{\nu}_\mu$ disappearance and τ^+ appearance measuring $\sin^2 2\theta_{23}$ and $|\Delta m^2_{23}|$ within 1%.

If neutrinos are propagated for large distances through the Earth, the oscillation probabilities for transitions involving also ν_e or $\bar{\nu}_e$ will be modified by the MSW effect depending upon the sign of Δm^2_{23} (neglecting the difference Δm^2_{12}):

$$\Delta m^2_{32} \to -\Delta m^2_{32}, \quad \text{if} \quad P_{\nu_e \to \nu_\mu} \to P_{\bar{\nu}_e \to \bar{\nu}_\mu}. \tag{11}$$

At the distance $L \sim 3500$ km, $\sin^2 2\theta_{13} \ll 1$, for $\Delta m^2_{23} > 0$ ($\Delta m^2_{23} < 0$) the probability $P_{\nu_e \to \nu_\mu}$ is enhanced (suppressed) and $P_{\bar{\nu}_e \to \bar{\nu}_\mu}$ is suppressed (enhanced) by matter effects. Thus, comparison of the $\nu_e \to \nu_\mu$CC event rate with the $\bar{\nu}_e \to \bar{\nu}_\mu$CC rate can discriminate the Δm^2_{23} sign at 99% C.L. for $\theta_{13} \sim 1°$–$10°$ and $|\Delta m^2_{23}| \sim (1\text{–}5) \times 10^{-3}$ eV^2, with 10^{21} μ decays for both μ^+ and μ^- beams.

Potentially, a *CP*-violation test in the lepton sector is envisaged in the LMA scenario measuring, with both μ^+ and μ^- beams, the asymmetry

$$A = \frac{P_{\nu_e \to \nu_\mu} - P_{\bar{\nu}_e \to \bar{\nu}_\mu}}{P_{\nu_e} \to \nu_\mu + P_{\bar{\nu}_e \to \bar{\nu}_\mu}} = \frac{\sin 2\theta_{12}}{\sin \theta_{13}} \sin\delta \sin \frac{\Delta m^2_{12} L}{4E_\nu}, \tag{12}$$

by detecting "wrong-sign muons." In this case, δ and $\sin\theta_{13}$ have to be measured simultaneously in both μ^+ and μ^- beams, requiring the use of a "near" ($L = 732$ km) and a "far" ($L = 3500$ km) detector (matter effects will also introduce a fake *CP*-violating term that hides the genuine one). dependence of A on E_ν and L will allow one to disentangle δ and $\sin\theta_{13}$. The case $\delta = 0$ (no *CP* violation) will be recognized from $\delta = 90°$ (maximum *CP* violation) at 99% C.L. at 3500 km of distance if $|\Delta m^2_{12}| \geq 2 \times 10^{-5}$ eV^2.

Finally, a close detector located at the end of the straight section of the νF allows a very rich physics

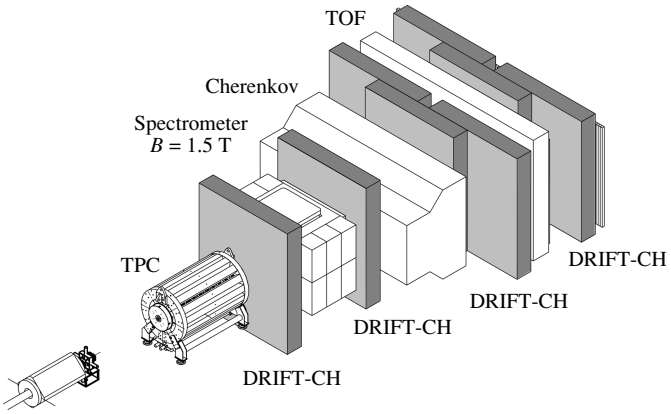

Fig. 8. HARP apparatus.

program. The beam would be very intense and collimated: $\sim 3 \times 10^6$ ν interactions can be observed per (kg yr) of the target detector. Precise measurements of structure functions, valence and sea quark distributions, spin content of quarks, and $\sin^2\theta_{\rm W}$ could be obtained.

4. SUPERBEAMS

As a different option, production of a conventional ν superbeam of very high intensity and low energy has been considered.

In the CERN–Modane project, similar to the Neutrino Factory scheme, a 4-MW 2.2-GeV proton beam from the SPL will generate an intense focused π^+ (π^-) beam that will produce an intense ν_μ ($\bar{\nu}_\mu$) beam with an average energy of 0.25 GeV by π decay: $\pi^+ \to \nu_\mu \mu^+$, $\mu^+ \to \bar{\nu}_\mu \nu_e e^+$. The expected flux at 50 km is $\phi_\nu \sim 1.7 \times 10^{14} \nu_\mu/(10^{23}$ p.o.t. 100 m^2). The ν_e component from K^+ decay will be largely suppressed: the resulting $\phi_{\nu_e}/\phi_{\nu_\mu} \sim 0.4\%$ contamination, essentially from the μ decay, will be known within 2%. The use of a near and a far detector at $L = 130$ km will allow both ν_μ disappearance and ν_e appearance experiments. With a far 40-kt water Cherenkov detector, it will be possible to measure in 5 years (10^{23} p.o.t./yr) $\sin^2(2\theta_{13}) \geq 0.007$ and $\sin^2(2\theta_{23})$ and $|\Delta m^2_{23}|$ within 2% of error in the parameter region of the atmospheric ν [21]. However, a poor sensitivity to *CP* violation is expected; the case $\delta = 0$ can be distinguished from $\delta = 90^\circ$ at 90% C.L. only for a restricted set of parameters.

Similar sensitivities are expected in the JHF project [22], where a 50-GeV/c proton beam of 0.77 MW from the PS (upgraded to 4 MW in the second phase) will produce a very intense ν_μ superbeam with an energy of 1 GeV. For 10^{21} p.o.t./yr, about 5000 ν_μCC/yr are expected in the Super-Kamiokande detector at 295 km of distance. However, due to the high proton energy, this superbeam will be affected by the problems of the conventional neutrino beam: as in the past, the experimental sensitivity will be limited by the K^+/π^+ uncertainty.

5. THE HARP EXPERIMENT

The design of the sophisticated setup of νF requires large R&D on hadron production, muon cooling, and storage facilities. The existing data on π production [23], mainly on Be targets with $\sim 15\%$ precision, cover only a small fraction of the phase space at low momenta, requiring extrapolations by production models. However, current simulations show 30–100% discrepancies with respect to the available data.

The HARP experiment [24], in operation at CERN PS, was designed to measure with a 2% overall precision the secondary hadron production on various nuclear targets by proton and pion beams in the momentum range between 2 and 15 GeV/c:

(i) to acquire adequate knowledge of π yields for an optimal design of a νF: the π yield per incident proton per GeV; the transverse (P_T) and longitudinal (P_L) momenta of the secondaries, which affect the efficiency of the transverse capture and the first phase rotation, respectively;

(ii) to improve substantially the calculation of the atmospheric ν flux needed for refined study of atmospheric ν;

(iii) to measure the low-momentum backward-going π yield for a high-intensity stopped-muon source;

(iv) to increase the reliability of hadron generators in MC simulations.

Dedicated measurements with the target of the K2K and MiniBooNE experiments will be performed at 12- and 8-GeV/c proton momenta, respectively.

The experimental exploitation requires P measurements in the 100 MeV/c–10 GeV/c range, a large acceptance (also in the backward direction), and a good e, μ, π, K, p recognition. Different particle identification techniques are used in HARP (Fig. 8): for low momenta dE/dx in Ar and methane TPC complemented with TOF measurements, $\sigma_{\mathrm{TOF}} \leq$ 200 ps resolution, with RPC counters and a scintillation counter TOF wall (10 m of flight base-line); for high momenta a C_4F_{10} threshold Cerenkov counter complemented with the TPC informations.

The target will be placed inside the TPC in a 0.7-T solenoid that will provide the particle identification at large P_T and total P measurement of the secondaries. The P measurement of the secondaries in the forward direction is performed by a magnetic spectrometer composed of a large-aperture magnet with $B = 1.5$ T embedded in large drift chambers. The π^0 measurement and beam muon identification are performed with an electromagnetic and a hadron calorimeter.

REFERENCES

1. S. Fukuda *et al.*, Phys. Rev. Lett. **86**, 5651 (2001); **86**, 5656 (2001); Q. R. Ahmad *et al.*, Phys. Rev. Lett. **87**, 71301 (2001); J. N. Abdurashitov *et al.*, Phys. Rev. Lett. **83**, 4686 (1999); T. A. Kirsten, Nucl. Phys. B **77**, 26 (1999).
2. Y. Fukuda *et al.*, Phys. Rev. Lett. **81**, 1562 (1998); **85**, 3999 (2000).
3. M. Apollonio *et al.*, Phys. Lett. B **466**, 415 (1999).
4. I. Stancu, in *Proceedings of the 9th International Workshop "Neutrino Telescopes",* Ed. by M. Baldo-Ceolin (Papergraf, Padua, Italy, 2001), p. 143.
5. K. Eitel, in *Proceedings of the 9th International Workshop "Neutrino Telescopes",* Ed. by M. Baldo-Ceolin (Papergraf, Padua, Italy, 2001), p. 156.
6. R. J. Wilkes, in *Proceedings of the 9th International Workshop "Neutrino Telescopes",* Ed. by M. Baldo-Ceolin (Papergraf, Padua, Italy, 2001), p. 179; S. Wojcicki, in *Proceedings of the 9th International Workshop "Neutrino Telescopes",* Ed. by M. Baldo-Ceolin (Papergraf, Padua, Italy, 2001), p. 191.
7. M. Altmann *et al.*, Phys. Lett. B **490**, 16 (2000); M. A. Hallin, Nucl. Phys. A **663**, 787 (2000); A. Ianni *et al.*, Nucl. Phys. A **663**, 791 (2000); A. Suzuki, in *Proceedings of the 8th International Workshop "Neutrino Telescopes"* (Papergraf, Padua, Italy, 1999).
8. L. Casagrande *et al.*, CERN Report 96-06 (1996).
9. H. W. Atherton *et al.*, CERN Report 80-07 (1980).
10. G. Ambrosini *et al.*, Eur. Phys. J. C **10**, 605 (1999).
11. A. Ferrari and P. R. Sala, in *Proceedings of Conference on Nuclear Data for Science and Technology* (ICTP, Trieste, 1998).
12. G. Collazuol *et al.*, Nucl. Instrum. Methods Phys. Res. A **449**, 609 (2000).
13. J. Altegoer *et al.*, Nucl. Instrum. Methods Phys. Res. A **404**, 96 (1997).
14. G. I. Budker, AIP Conf. Proc. **352**, 4 (1996); A. N. Skrinsky, AIP Conf. Proc. **352**, 6 (1996).
15. D. G. Koshkarev, CERN Internal Report CERN/ISR-DI/74-62 (1974).
16. Muon Collider Collab. (C. Ankenbrandt *et al.*), www.cap.bnl.gov/mumu/status_report.html.
17. CERN Report 99-2, EFCA 99-197, Ed. by B. Autin, A. Blondel, and J. Ellis (1999).
18. A. Cervera *et al.*, Nucl. Instrum. Methods Phys. Res. A **451**, 123 (2000).
19. S. Geer, hep-ph/0008155; A. Blondel *et al.*, CERN-EP-2000-053.
20. A. Cervera *et al.*, Nucl. Phys. B **579**, 17 (2000); J. Burguet Castell *et al.*, Nucl. Phys. B **608**, 301 (2001).
21. J. J. Gomez-Cadenas, in *Proceedings of the 9th International Workshop "Neutrino Telescopes",* Ed. by M. Baldo-Ceolin (Papergraf, Padua, Italy, 2001), p. 143.
22. Y. Itow *et al.*, hep-ex/0106019.
23. J. V. Allaby *et al.*, CERN Report 70-12 (1970); T. Eichten *et al.*, Nucl. Phys. B **44**, 333 (1972); T. Abbott *et al.*, Phys. Rev. D **45**, 3906 (1992).
24. M. G. Catanesi *et al.*, CERN-SPSC/99-35, SPSC/P315 (1999).

Physics of Atomic Nuclei, Vol. 65, No. 12, 2002, pp. 2210–2217. From Yadernaya Fizika, Vol. 65, No. 12, 2002, pp. 2273–2280.

NEUTRINO OSCILLATIONS AND MIXINGS, NEUTRINOS FROM THE SUN, REACTORS, AND ACCELERATORS

Neutrino–Astrophysics, Nuclear Physics, and Particle Physics at Intense, Pulsed, Stopped-Pion Sources*

F. T. Avignone III[1] and Yu. V. Efremenko[2]

Physics Division, Oak Ridge National Laboratory, Oak Ridge, TN, USA

Received April 14, 2002

Abstract—Intense pulsed proton beams of ~ 1 GeV impinging on high-Z targets are intense sources of ν_μ from the ($\tau = 26$ ns) decay of π^+, and $\bar{\nu}_\mu$ and ν_e from the stopped μ^+ decays. A pulse structure, narrow in time, allows the separation of reactions due to ν_μ from those from reactions involving $\bar{\nu}_\mu$ and ν_e. The energy spectra are in the energy range of interest to nuclear astrophysics. A number of possible experiments relevant to solar neutrinos, supernovae collapse, weak interactions in nuclei, and intrinsic properties of neutrinos are discussed. © *2002 MAIK "Nauka/Interperiodica".*

1. INTRODUCTION

The announcement at this conference by the Sudbury Neutrino Observatory (SNO) collaboration contained compelling evidence that there is an active nonelectron-flavor neutrino component in the solar neutrino flux [1]. Combining their experimental rate for the reaction $d(\nu_e, e^-)pp$ from solar neutrinos, with the neutral-current rate of solar neutrino–electron elastic scattering data from Super-Kamiokande (SK) [2], they conclude that the total flux of active neutrinos from the ^{8}B branch is in agreement with the predictions of the Standard Solar Model (SSM) of Bahcall and his coworkers [3]. The issue is now convincingly settled; the SSM is now confirmed. The ν_e deficit in the solar neutrinos is due to $\nu_e \to \nu_\mu, \nu_\tau$ oscillations. There are two very recent updates from the SK collaboration on solar neutrino oscillations [4].

The earlier report of the strong azimuthal-angle dependence of the e/μ ratio in the SK detector [1] was strong evidence of $\nu_\mu \to \nu_\tau, \nu_s (\bar{\nu}_\mu \to \bar{\nu}_\gamma, \bar{\nu}_s)$ oscillations (ν_s are hypothetical sterile neutrinos [5]). Reactor neutrino experiments place strong constraints on electron antineutrino oscillations, implying that ν_e and $\bar{\nu}_e$ play a very small role if any in explaining the atmospheric e/μ ratios [6].

The final open question concerns the excess events from the reaction $p(\bar{\nu}_e, e^+)n$ in the LSND detector at Los Alamos [7]. This has been interpreted as direct evidence of $\bar{\nu}_\mu \to \bar{\nu}_e$ oscillations. All attempts to interpret all three types of neutrino oscillation evidence from solar neutrino, atmosphere neutrino, and the LSND neutrino experiments failed to produce a single coherent scenario unless one introduces a fourth generation of neutrinos. They must be "sterile" with respect to "normal" weak interactions [5]. Another common interpretation is that the evidence of excess $\bar{\nu}_e$ observed in the LSND is due to phenomena other than neutrino $\bar{\nu}_\mu \to \bar{\nu}_e$ oscillations. To insist on accepting one or the other of these options at the present time is to accept an unsubstantiated theoretical prejudice. This issue is still very much an open one.

Accordingly, there are three most important questions to be settled experimentally. The LSND results must be tested independently; the parameters δm_{ij} and $\sin^2 2\theta_{ij}$ must be measured accurately; and finally the theoretical cross section [8] of the reaction $d(\nu_e, e^-)pp$ should be confirmed experimentally. This last measurement is necessary even though the charge-current-to-neutral-current interaction ratio is far less dependent on nuclear theory than each individually. The above cross section can be measured at stopped-pion neutrino sources using a detector similar to the SNO detector, but smaller.

Many other neutrino experiments of interest in astrophysics can be done at spallation neutron sources, because the energy of the neutrinos from stopped pions and stopped muons is similar to that from supernovae collapse, for example. A sample of such measurements will be discussed in this article.

*This article was submitted by the authors in English.

[1]Department of Physics and Astronomy, University of South Carolina, Columbia, SC 29208, USA; e-mail: waters@sc.edu

[2]Department of Physics and Astronomy, University of Tennessee, Knoxville, TN 37996, USA

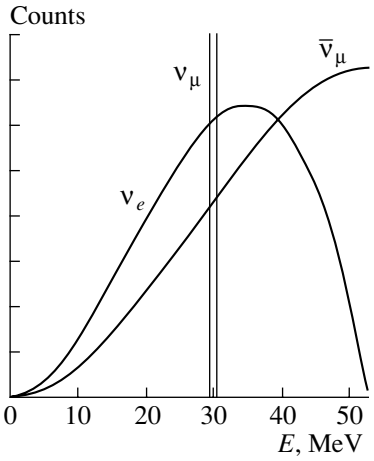

Fig. 1. Neutrino spectra from pions decaying at rest.

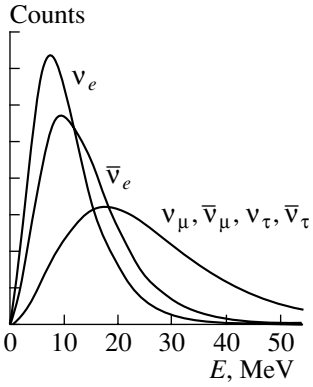

Fig. 2. Typical neutrino spectra predicted from supernova during collapse assuming a Fermi–Dirac distribution with characteristic neutrino temperatures: $T(\nu_\mu\nu_\tau) \sim 8$ MeV; $T(\bar{\nu}_e) \sim 4.5$ MeV; $T(\nu_e) \sim 3.5$ MeV.

2. NEUTRINO PRODUCTION AT THE SPALLATION NEUTRON SOURCE

The Spallation Neutron Source (SNS) linear accelerator will produce a 2-mA beam of 1-GeV protons on a mercury target which will be an intense pulsed (FWHM = 400 ns) source of neutrons, pions resulting in an isotropic source of intermediate-energy neutrinos [9]. This will produce $\sim 10^{15}$ neutrinos/s, corresponding to $\sim 3 \times 10^6$ $\nu/(\mathrm{cm}^2\ \mathrm{s})$ of each flavor, ν_μ, $\bar{\nu}_\mu$, and ν_e, with a suppression of $\bar{\nu}_e$ by a factor of 2.4×10^{-4} relative to the other flavors. The spectra are well known and can be calculated with the following analytical expressions:

$$N(\nu_e) = (12/W^4)\, E_\nu^2\, (W - E_\nu), \qquad (1)$$

$$N(\bar{\nu}_\mu) = (6/W^4)\, E_\nu^2\, (W - 2/3\, E_\nu), \qquad (2)$$

where $W = 52.83$ MeV. Figures 1 and 2 show these spectra and the predicted spectra from supernova collapse models [10].

This similarity in energy spectra yields an opportunity to investigate neutrino nucleus cross sections to study fundamental weak interactions in nuclei and cross sections important in supernovae, as well as the important cross sections utilized by the SNO experiment to yield the important results reported in this conference by J. Farine and in [1].

To perform this and many other measurements, including neutrino oscillation searches at intermediate energies, will require a $\sim$ 200-t detector. One such detector has been investigated at ORNL and is described briefly below. As an example, we consider the neutrino laboratory ORLaND proposed at the Oak Ridge National Laboratory.

The Oak Ridge Laboratory for Neutrino Detectors (ORLaND) is a proposed national and international user facility to be located near the target station of the Spallation Neutron Source (SNS) under construction at the Oak Ridge National Laboratory. The neutrino laboratory would be an underground detector hall capable of housing one large ($\sim$2000 t) multipurpose Cherenkov/scintillating Cherenkov detector and between six and eight smaller detectors (100–200 t). The hall would be located approximately 7 m underground, with 3 m of steel and 3 m of concrete overhead and between 6 and 9 m from the target building. The steel and concrete overburden will absorb the hadronic component cosmic rays completely and attenuate the muon flux by a factor of 4. The materials between the target and the laboratory would be equivalent to 12 m of steel in shielding against neutrons from the SNS. The proton beam will be pulsed, which will severely reduce the background from cosmic rays.

The bunker or hall design is a cylinder approximately 33.5 m deep and 25 m in diameter. It is designed to have three levels to support the smaller detectors; the large detector would penetrate the upper floors. The tank to contain the large detector is designed as a triple-walled steel tank with an outside diameter of 14 m and 14 m deep. A one-meter-thick liquid scintillator veto detector will surround the inner wall of the tank and will cover the top and bottom.

The central volume of the detector will be lined with approximately 5000 33-cm-diameter photomultiplier tubes to provide a 50% photocathode area coverage. The central volume could be filled with H_2O, pure mineral oil, mineral oil with dilute scintillator, or a variety of aqueous solutions. One possible configuration under consideration has an acrylic container of D_2O located in the center of the detector, surrounded with either pure H_2O or mineral oil. The large detector is being designed to be as versatile as possible. Some of the experiments

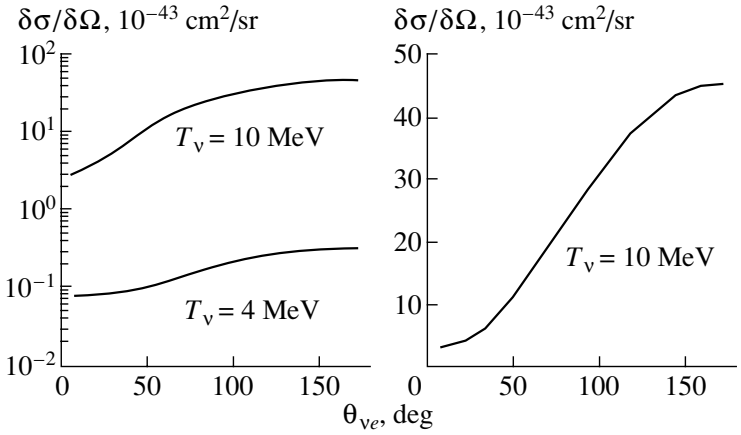

Fig. 3. Differential cross sections for the reaction $^{16}\mathrm{O}(\nu_e, e^-)^{16}\mathrm{F}$, calculated by Haxton [12].

possible with this detector involve the following reactions: $^{16}\mathrm{O}(\nu_e, e^-)^{16}\mathrm{F}$, $d(\nu_e e^-)p$, $^{16}\mathrm{O}(\nu_x, n\gamma)^{15}\mathrm{O}$, $^{16}\mathrm{O}(\nu_x, \nu'_x p\gamma)^{15}\mathrm{N}$, $\nu e^- \to \nu' e^{-\prime}$, $\bar{\nu}_\mu \to \bar{\nu}_e$ (oscillation), $\nu_\mu \to \nu_e$ (oscillation), $^{12}\mathrm{C}(\nu_e, e^-)^{12}\mathrm{N}$, $^{12}\mathrm{C}(\nu_x, \nu'_x)^{12}\mathrm{C}^*$, and, with such a large detector and intense flux, possibly $^{13}\mathrm{C}(\nu_e, e^-)^{13}\mathrm{N}$ [11].

3. THE DISINTEGRATION OF THE DEUTERON BY NEUTRINOS

One of the most important experiments ongoing to understand the Sun and its production of neutrinos is that at the SNO. The two reactions to be exploited are

$$\nu_e + d \to p + p + e^-, \tag{3}$$

$$\nu_x + d \to n + p + \nu'_x. \tag{4}$$

Reaction (4) obviously is completely blind to neutrino flavor. An accurate measurement of the neutral current rate would be enough to completely determine the total production rate of ν_e, independently of neutrino oscillations, but only as precisely as we know the cross section. The measurement of the ratio of the rates $R(\nu_e e^-)/R(\nu_x, \nu'_x)$ was of great help in settling the solar neutrino problem, but again only if we know the cross sections. The only measured cross section is that of $d(\nu_e, e^-)pp$, and it is known with an accuracy of 37% at a 68% C.L. [9]. The neutral current rate has only been measured with reactor neutrinos and also with insufficient accuracy for use in the interpretation of SNO data [1].

A computational feasibility study has been made for a precision measurement of the cross section $\sigma[d(\nu_e, e^-)pp]$ at ORLaND. The detector configuration used in the study was an acrylic sphere containing D_2O, suspended near the center of the large detector containing either H_2O or pure mineral oil. A sphere of $\sim$ 5.5-m diameter would contain $\sim$100 t of D_2O. The theoretical total cross section is 5.4×10^{-41} cm^2 [8], which would yield $\sim$9000 events/yr. The measurement of the excitation function would then be possible [11].

Let us assume that the rest of the 2000-t volume was filled with H_2O. The theoretical cross section for $^{16}\mathrm{O}(\nu_e, e^-)^{16}\mathrm{F}$ is 6.1 times smaller, so that there should appear a sudden difference in event rate between the D_2O and H_2O volumes clearly defining the mean radius of the D_2O volume and hence the fiducial volume. While a statistical accuracy of $<1\%$ is straight forward, the systematic errors due to the uncertainty in the neutrino flux and fiducial volume must also be very well controlled.

To achieve this, the neutrino–electron elastic scattering rate would have to be monitored throughout all of the experiments. This cross section, $\nu_x e^-$, is accurately predicted by the standard model, and its rate can be measured to $<1\%$, but only with a 2000-t detector. With this combination, one can hope to approach the measurement of $\sigma[d(\nu_e, e^-)pp]$ with an uncertainty between 2 and 3%.

One exciting possibility is to use this cross section to make an isospin rotation to independently determine the cross section [8] for the reaction

$$p + p \to d + e^+ + \nu_e, \tag{5}$$

which is at the top of the chain of reactions that generates 99.75% of the neutrinos from the Sun. One can also use the results of the effective field theory calculations [8] which reproduce this cross section, as well as that of the neutral current disintegration of the deutron, given in (4), within an unknown parameter called a counter term. This counter term can be deduced from measuring the cross section of reaction (3) as a function of electron energy. This is an indirect calibration of the solar fusion rate. It is of crucial importance in the solar model and holds one

of the important keys to our understanding of energy production in the Sun [3].

4. $d^2\sigma/dE_e d\Omega$ OF THE REACTION $^{16}\mathrm{O}(\nu_e, e^-)^{16}\mathrm{F}$

There are several motivations for this measurement. It is a rigorous test of theoretical treatments of weak interactions in nuclei [14]; it is an important reaction in the formulation of nucleosynthesis in stellar collapse models [10], and it is intimately connected to the core temperature of supernova through the forbidden contributions [12].

The calculation by Haxton [12] shows a very strong angular distribution of electrons from the reaction with a very strong energy dependence, as shown in Fig. 3. Aside from a direct test of the weak interaction nuclear physics, this measurement would provide valuable information for the interpretation of supernova data recorded with large water Cerenkov detectors. Let us assume that there would not be neutrino oscillations of the type $\nu_\mu, \nu_\tau \to \nu_\mu$ from the collapse process. Then considering Fig. 3, we expect the emitted e^- to be almost isotropic and probably lost in the isotropic distribution of e^+ from $\bar{\nu}_e + p \to e^+ + n$. If, however, the ν_τ and ν_e escaping from the core at higher temperature were converted to ν_e by oscillations, then they could be energetic enough to enjoy forbidden transitions to higher excited states of ^{16}F with a very strong back angle emission of e^-. This could be a unique signal for $\nu_\tau \to \nu_e$ oscillations.

The cross section calculated by Haxton, $\langle\sigma\rangle = 8.84 \times 10^{-42}$ cm^2 [12], would result in a total event rate of 12 300 events/yr, including the reduction due to the 30% detector efficiency. A precision measurement of $d^2\sigma/dEd\Omega$ would require about two years of data.

Two related reactions are those mediated by the weak neutral current, namely, $^{16}\mathrm{O}(\nu_x, \nu'_x n\gamma)^{15}\mathrm{O}$ and $^{16}\mathrm{O}(\nu_x, \nu'_x p\gamma)^{15}\mathrm{N}$. These reactions have been investigated theoretically in [13, 14]. Using their cross sections, the reaction resulting in ^{15}O would produce $\sim 4 \times 10^3$ events/yr, while that resulting in ^{15}N would result in $\sim 2.1 \times 10^4$ events/yr. This reaction could be isolated from others by using the 600-ns pulse of ν_μ and identified by the resulting gamma rays. These reactions have also been suggested as mechanisms to explore the temperature of supernovae [13].

To make any cross-section measurements with accuracies from 2 to 3%, the neutrino flux must be measured with a known fundamental cross section. The only option is to continuously measure neutrino–electron elastic scattering both to monitor the flux and to more accurately measure the interference term between the charge and neutral currents. Diagrams representing these currents are shown in Fig. 4.

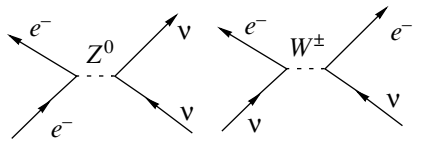

Fig. 4. Feynman diagrams describing electron–neutrino elastic scattering.

5. NEUTRINO–ELECTRON ELASTIC SCATTERING

The differential cross sections are given by [15]

$$\frac{d\sigma(\nu_i)}{dT} = \frac{2G_\mathrm{F}^2 m_e}{\pi} \times \left[g_{iL}^2 + g_R^2 \left(1 - \frac{T}{E_\nu}\right)^2 - g_{iL} g_R \frac{m_e T}{E_\nu^2} \right], \tag{6}$$

where i substitutes for e or μ, and

$$\frac{d\sigma(\bar{\nu}_i)}{dT} = \frac{2G_\mathrm{F}^2 m_e}{\pi} \times \left[g_R^2 + g_{iL}^2 \left(1 - \frac{T}{E_\nu}\right)^2 - g_{iL} g_R \frac{m_e T}{E_\nu^2} \right]. \tag{7}$$

In the above, $g_R = \sin^2\theta_\mathrm{W}$, $g_{eL} = 1/2 + \sin^2\theta_\mathrm{W}$, and $g_{\mu L} = -1/2 + \sin^2\theta_\mathrm{W}$. We define the ratio R as

$$R \equiv \frac{\sigma(\nu_\mu e)}{\sigma(\nu_e e) + \sigma(\bar{\nu}_\mu e)}, \tag{8}$$

keeping in mind that ν_μ events can be cleanly separated from ν_e and $\bar{\nu}_\mu$ events using the pulse structure. Integrating over the electron's final kinetic energy, R can be expressed in terms of $\sin\theta_\mathrm{W}$ as follows:

$$R = \frac{3/4 - 3\sin^2\theta_\mathrm{W} + 4(\sin^2\theta_\mathrm{W})^2}{1 + 2\sin^2\theta_\mathrm{W} + 8(\sin^2\theta_\mathrm{W})^2}. \tag{9}$$

The accurate determination of the ratio of the counting rates in (8) would be the first accurate measurement of the interference between the two diagrams shown in Fig. 4, although the LSND group has made a recent measurement [16]. The ratio R can be taken directly from the event rates,

$$\frac{N(\nu_\mu)(\tau = 26\,\mathrm{ns})}{N(\nu_e) + N(\bar{\nu}_\mu)(\tau = 2.2\,\mu\mathrm{s})}, \tag{10}$$

in which the flux cancels to an excellent approximation. The small correction due to early decays of

muons can be made using known decay times of π^+ and μ^+.

These results can also be used to measure $\sin^2\theta_W$ at a very low momentum exchange ($Q \simeq 0.002$ GeV). Previous atomic-parity-violating experiments at low Q disagree with one popular method of determining the running of this fundamental parameter [17].

6. NEUTRINO–NUCLEUS INTERACTION CROSS SECTIONS

Charge-current and neutral-current neutrino–nucleus cross sections are important inputs to numerical models of supernova [10]. The only reactions that have been measured at energies of interest in astrophysical processes are $d(\nu_e, e^-)pp \pm 34\%$, $^{56}\mathrm{Fe}(\nu_e, e^-)^{56}\mathrm{Co}$ $\pm 36\%$, and $^{12}\mathrm{C}(\nu_e, e^-)^{12}\mathrm{N}$ $\pm 10\%$. Only the ^{12}C measurement is useful; however, it could be measured to a few percent or less at ORLaND for use as a neutrino flux monitor in future scintillator experiments.

Here, we give a very brief description of a highly granular detector that can be used to make an accurate cross section measurement of the reaction $^{56}\mathrm{Fe}(\nu_e, e^-)^{56}\mathrm{Co}$ and many other targets as discussed below. More detailed descriptions have been given earlier [18]. Iron is very important in supernova collapse models, and this cross section is not measured with the required accuracy.

The detector is similar in concept to the Soudan-II detector; it consists of 10^5 iron tubes, 10 mm in outside diameter, with 0.5-mm-thick walls. This is equivalent to 3400 tube/t for a tube length of 3.5 m. Each tube contains a gas detector that need only detect a hit by an energetic electron and be capable of modest timing to determine position. The detector is designed to be placed 50 m from the SNS target station and has 10^5 tubes stacked in a $3.5 \times 3.5 \times 3.5$ m cube. The fiducial volume is a cube $2.5 \times 2.5 \times 2.5$ m and has a fiducial mass of 13.5 t. The theoretical cross section of Kolbe, Langanke, and Martinez-Pinedo [19] ($\langle\sigma\rangle = 2.73 \times 10^{-40}$ cm^2) was used to determine that, with a predicted 30% efficiency, the event rate would be 75 event/(t yr) live time.

Detailed Monte Carlo computations were made to determine that electrons traversing the detector can be distinguished from all other particles, except for positrons. The backgrounds are predicted to be extremely low. Cross sections of any element that can be made into rigid tubes, with the mechanical strength to allow stacking, can be measured with an accuracy of $\sim 5\%$.

A list of some interesting targets and their natural isotopic abundance follows: ^{9}Be (100%), ^{11}B (80%), ^{27}Al (100%), ^{51}V (99.8%), ^{52}Cr (84%), ^{55}Mn (100%), ^{56}Fe (92%), ^{59}Co (100%), ^{209}Bi (100%), ^{181}Ta (100%), and natural Pb.

Other techniques, liquid Cerenkov detectors, and fine-grained hanging file detectors of alternating planes of target and scintillator, can also be used to measure cross sections of neutrino interactions on ^{7}Li (92%), ^{12}C (98.9%), ^{14}N (99.6%), ^{16}O (99.8%), ^{19}F (100%), ^{23}Na (100%), ^{28}Si (92%), ^{31}P (100%), ^{32}S (95%), ^{39}K (93%), ^{40}Ca (97%), ^{45}Sc (100%), ^{89}Y (100%), ^{115}In (96%), ^{127}I (100%), ^{133}Cs (100%), ^{139}La (100%), ^{159}Tb (100%), and ^{169}Tm (100%).

Using a variety of techniques involving liquid scintillator, reactions involving ^{12}C can be measured increasing the present accuracy. This is particularly true if the large detector contains scintillator.

The ^{12}C isotope forms one of the "onion skin" shells of a large star just prior to collapse, because stellar evolution creates ^{12}C in the 3α burning cycle. Naturally, it will constitute much of the ejects that later will interact with the neutrinos to possibly reheat the shock front. Also, ^{12}C forms an isospin triplet with ^{12}B, ^{12}C, and $^{12}\mathrm{N}(J^\pi, T = 1^+, 1)$ in its 15.11-MeV excited state and can be excited from its $(J^\pi, T = 0^+, 0)$ ground state by the weak neutral current. This reaction allows investigation of the details of the isovector and axial vector part of the weak hadronic current. The reaction is well understood theoretically; however, this is a reaction that can be used to tune small nuclear details.

The reaction $^{12}\mathrm{C}(\nu_e, e^-)^{12}\mathrm{N}^*$ excites ^{12}N to five excited states that decay by proton emission. Several states in ^{11}C decay by gamma emission, but the single-pronged proton and gamma events will suffer more background; however, it may be feasible.

The reaction $^{12}\mathrm{C}(\nu_x, \nu'_x)^{12}\mathrm{C}$ (15.1 MeV) can be done at short time intervals following the proton pulse, thereby being dominated by (ν_μ, ν'_μ) reactions.

The neutral-current-to-charge-current cross-section ratio, averaged over the stopped-pion neutrino spectrum, was measured only by the KARMEN group. Their result was $1.17 \pm 0.11 \pm 0.012$ [20]. The three calculated values are 1.08 [21], 1.13 [22], and 1.27 [23].

7. NEUTRINO OSCILLATIONS

The 2000-t detector has been studied with extensive Monte Carlo simulations, but only with a photocathode coverage of 25%. The combination of the detector fiducial volume (18 times that of the LSND), the $\bar{\nu}_\mu$ flux, and the pulse structure was used to determine that the statistical accuracy in the same live time would be 100 times that of LSND. The technique

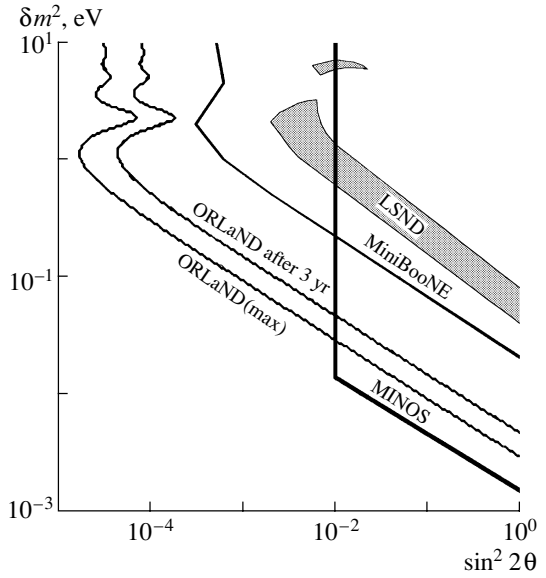

Fig. 5. Projected sensitivities of the ORLaND large detector to $\bar{\nu}_\mu \to \bar{\nu}_e$ oscillations compared to MiniBooNe, MINOS, and the positive result reported by LSND.

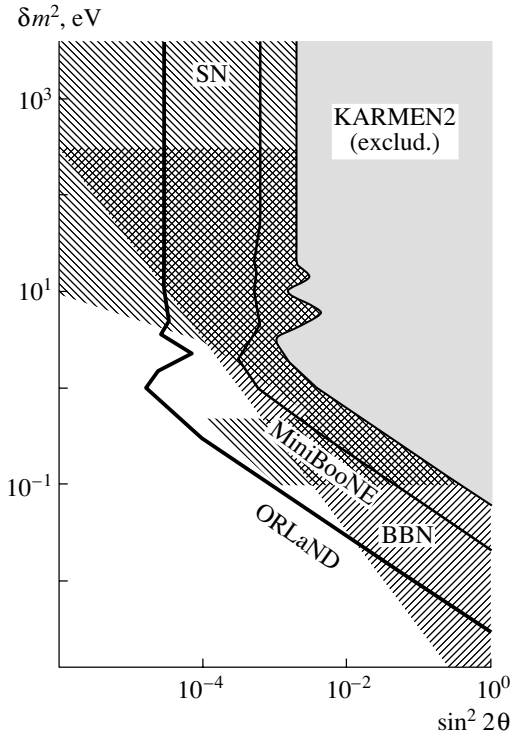

Fig. 6. Projected sensitivity of the ORLaND large detector, MiniBooNE, and the region excluded by KARMEN. The lined areas denote regions of interest to supernovae (SN) and big bang nucleosynthesis (BBN) models.

involves searching for the appearance of $\bar{\nu}_e$ in a dilute-scintillator-filled detector. First, the Cerenkov cone from the positron from the reaction $\bar{\nu}_e + p \to e^+ + n$ is recorded. The neutron is moderated and is captured in a mean time of 186 μs, resulting in a 2.2-MeV γ ray via the neutron capture reaction $n + p \to d +$ 2.2 MeV γ.

Figure 5 shows the projected sensitivity compared to the LSND result and the predicted sensitivity of the MiniBooNE experiment at Fermilab. One unique feature of ORLaND is that the few $\bar{\nu}_e$ that come from μ^- decay ($\bar{\nu}_e/\bar{\nu}_\mu \simeq 3 \times 10^{-4}$) come dominantly in the first ~ 1 μs due to the capture rates. Therefore, it should be possible to experimentally explore this contamination for the first time. There are four other reactions that are sensitive to neutrino oscillations that can be utilized at ORLaND; however, we choose to discuss only the most sensitive one here.

One very interesting possibility offered by the sensitivity discussed above is the ability to probe regions of δm^2 and $\sin^2 2\theta$ that have impact on models of big bang nucleosynthesis and nucleosynthesis in collapsing stars shown in Fig. 6 [24].

The construction of the Spallation Neutron Source at the Oak Ridge National Laboratory presents exciting potential opportunities to the field of neutrino astrophysics, of which neutrino telescopes play a central role. The proposed user facility called the ORLaND is being designed to accommodate a broad selection of neutrino experiments of importance in our field. The cost of the laboratory itself, including the base triple-walled tank of the large liquid detector, was estimated by two engineering companies to cost about 2.5% of the SNS project. Other articles describing various aspects have appeared in other literature [25, 26]. Much of the contents herein can be applied to any intense pulsed spallation neutron source.

ACKNOWLEDGMENTS

Research at the Oak Ridge National Laboratory is supported by the US Department of Energy under contract DE-AC05-00OR22725 with UT-Battelle, LLC. Research at the University of Tennessee is supported by USDOE grant no. DEFG0591ER40627, and at the University of South Carolina by USDOE grant no. DEFG0295ER40910. L.C. is supported by NSF grant no. PHY-0074759.

The large detector is now called CoNDOR, the Comprehensive Neutrino Detector at Oak Ridge. The following are members of the ORLaND Large Detector Collaboration and others participating in the development of ORLaND science: F.T. Avignone III[1)], T.C. Awes[2)], C. Baktash[2)], J. Ball[2)], D. Bardayan[2)],

[1)] The University of South Carolina, Columbia, SC 29208, USA
[2)] Oak Ridge National Laboratory, Oak Ridge, TN 37831, USA.

J. Beene[2], S.C. Berridge[3], F. Bertrand[2], W. Bilpuch[4, 5], J. Blackmon[2], R. Boyd[6], C.L. Britton[2], W. Bugg[3], R.L. Burman[7], J. Busenitz[8], C. Cardall[3], H.K. Carter[9], L. Chatterjee[10], V. Cianciolo[2], H.O. Cohn[3], M. Danilov[11], D.J. Dean[2], L. DeBraeckeleer[4, 5], P. Degtiarenko[12], G. Dodson[2], Yu. Efremenko[2, 3], M.A. Elaasar[13], A.R. Fazely[14], T.A. Gabriel[2], A. Galindo-Uriberri[2], C. Gould[15, 5], Z.D. Greenwood[16], V. Gudkov[1], R. Gunasingha[14], T. Handler[3], C. Hargrove[17], E. Hart[3], R.L. Imlay[18], Yu. Kamushkov[3], H.J. Karwowski[19], D. Koetke[20], K. Kubodera[1], K. Lande[21], C. Lane[22], R.W. Mainweiler[20], W.J. Metcalf[18], A. Mezzacappa[2], G. Mills[7], L.W. Mo[23], A. Murphy[6], T. Numamaker[23], S. Nussinov[24], A. Piepke[8], F. Plasil[2], J.J. Reidy[25], C. Rosenfeld[1], D. Rupnik[14], D. Smith[26], I. Stancu[8], S. Stanislaus[20], R.I. Steinberg[22], M. Strayer[2], R. Svoboda[18], R. Tashakkori[27], W. Tornow[4, 5], G.J. VanDalen[28], J. Watson[29], P. Wildenhain[21], A. Wintenberg[2], J. Wolf[8], G. Young[2], O. Zeldovich[11], and W.-M. Zhang[29].

[3] University of Tennesse, Knoxville, TN 37996, USA.
[4] Duke University, Durham, NC 27708, USA.
[5] Triangle Universities Nuclear Laboratory, Durham, NC 27708, USA.
[6] Ohio State University, Columbus, OH 43210, USA.
[7] Los Alamos National Laboratory, Los Alamos, NM 87545, USA.
[8] University of Alabama, Tuscaloosa, AL 35487, USA.
[9] Oak Ridge Associated Universities, Oak Ridge, TN 37831, USA.
[10] Cumberland University, Lebanon, TN 37087, USA
[11] Institute for Theoretical and Experimental Physics, Moscow, Russia.
[12] Jefferson Laboratory, Newport News, VA 23606, USA.
[13] Southern University, New Orleans, LA 70126, USA.
[14] Southern University, Baton Rouge, LA 70813, USA.
[15] North Carolina State Universtiy, Raleigh, NC 27695, USA.
[16] Louisiana Technical University, Ruston, LA, USA
[17] Carleton University, Ottawa, Canada.
[18] Louisiana State University, Baton Rouge, LA 70803, USA.
[19] University of North Carolina, Chapel Hill, NC 27599, USA.
[20] Valparaiso University, IN 46383, USA.
[21] University of Pennsylvania, Philadelphia, PA 19104, USA.
[22] Drexel University, Philadelphia, PA 19104, USA.
[23] Virginia Tech., Blacksburg, VA 24061, USA.
[24] Tel Aviv University, Tel Aviv, Israel.
[25] University of Mississippi, Oxford, MS 38677, USA.
[26] Embry-Riddle University, Prescott, AZ 86301, USA.
[27] Appalachian State University, Boone, NC 28608, USA
[28] University of California, Riverside, CA 92521, USA.
[29] Kent State Universtiy, Kent, OH, USA.

REFERENCES

1. SNO Collab. (Q. R. Ahmad *et al.*), submitted to Phys. Rev. Lett.; J. Farine, Yad. Fiz. **65**, 2210 (2002) [Phys. At. Nucl. **65**, 2147 (2002)].
2. Super-Kamiokande Collab. (H. Sobel *et al.*), Nucl. Phys. B (Proc. Suppl.) **91**, 127 (2001); Y. Fakuda *et al.*, Phys. Rev. Lett. **81**, 1562 (1998); **82**, 1810 (1999).
3. J. N. Bahcall and M. H. Pinsonneault, Rev. Mod. Phys. **67**, 781 (1995); for an update on uncertainties in the models see J. N. Bahcall, S. Basu, and M. H. Pinsonneault, Phys. Lett. B **433**, 1 (1998); J. N. Bahcall, Nucl. Phys. B (Proc. Suppl.) **91**, 9 (2001).
4. S. Fakuda *et al.*, Phys. Rev. Lett. **86**, 5651, 5656 (2001).
5. J. Ellis, Nucl. Phys. B (Proc. Suppl.) **91**, 503 (2001).
6. M. Apollonio *et al.*, Phys. Lett. B **420**, 397 (1998); **466**, 415 (1990); F. Boehm *et al.*, Nucl. Phys. B (Proc. Suppl.) **91**, 91 (2001).
7. G. B. Mills, Nucl. Phys. B (Proc. Suppl.) **91**, 198 (2001).
8. S. Nakamura, T. Sato, V. Gudkov, and K. Kubodera, Phys. Rev. C **63**, 034617 (2001); J. N. Bahcall, K. Kubodera, and S. Nozawa, Phys. Rev. D **38**, 1030 (1988); M. N. Butler and J.-W. Chen, Nucl. Phys. A **675**, 575 (2000); M. Butler, J.-W. Chen, and X. Kong, nucl-th/0008032; D. B. Kaplan, M. J. Savage, and M. B. Wise, Phys. Lett. B **424**, 390 (1988); Nucl. Phys. B **534**, 329 (1998); Phys. Rev. C **59**, 617 (1999).
9. F. T. Avignone III and Yu. V. Efremenko, Nucl. Phys. B (Proc. Suppl.) **87**, 304 (2000).
10. A. Mezzacappa, Nucl. Phys. B (Proc. Suppl.) **91**, 338 (2001).
11. *Scientific Opportunities at the Oak Ridge Laboratory for Neutrino Detectors (ORLaND), A Report on the Workshop on Neutrino–Nucleus Physics Using a Stopped Pion Facility, 2000, Oak Ridge, Tennessee.*
12. W. C. Haxton, Phys. Rev. D **36**, 2283 (1987).
13. K. Langanke, P. Vogel, and E. Kolb, Phys. Rev. Lett. **76**, 2629 (1996).
14. E. Kolbe, K. Langanke, and F.-K. Thielmann, Eur. Phys. J. A **3**, 389 (1998).
15. L. B. Okun, *Leptons and Quarks* (Nauka, Moscow, 1982; North-Holland, Amsterdam, 1984).
16. LSND Collab. (L. B. Auerbach *et al.*), hep-ex/0101039.
17. A. Czarnecki and W. J. Marciano, Int. J. Mod. Phys. A **13**, 2235 (1998); **15**, 2365 (2000).
18. Yu. Efremenko, F. T. Avignone III, and A. Mezzacappa, in *Proceedings of Carolina Conference on Neutrino Physics, Columbia, 2000,* Ed. by J. N. Bahcall, W. C. Haxton, K. Kubodera, and C. P. Poole (World Sci., Singapore, 2001), p. 248.
19. E. Kolbe, K. Langanke, and G. Martinez-Pinedo, Phys. Rev. C **60**, 52801 (1999).

20. R. Maschew *et al.*, Prog. Part. Nucl. Phys. **40**, 183 (1998).
21. M. Fugita *et al.*, Phys. Lett. B **212**, 139 (1988).
22. E. Kolbe *et al.*, Phys. Rev. C **49**, 1122 (1994).
23. T. W. Donnelly, Program NUEE, private communication to the KARMEN Collab.
24. G. M. Fuller, Phys. Rep. **227**, 149 (1993).
25. F. T. Avignone III and Yu. Efremenko, in *Proceedings Carolina Symposium on Neutrino Physics, Columbia, 2000,* Ed. by J. N. Bahcall, W. C. Haxton, K. Kubodera, and C. P. Poole (World Sci., Singapore, 2000), p. 214; F. T. Avignone III, L. Chtterjee, Yu. Efremenko, *et al.*, Nucl. Phys. B (Proc. Suppl.) **91**, 113 (2001).
26. F. T. Avignone III *et al.*, Yad. Fiz. **63**, 1082 (2000) [Phys. At. Nucl. **63**, 1007 (2000)].

Physics of Atomic Nuclei, Vol. 65, No. 12, 2002, pp. 2218–2224. From Yadernaya Fizika, Vol. 65, No. 12, 2002, pp. 2281–2286.

COSMOLOGY AND ASTROPHYSICS. DARK MATTER

Dark Matter in Susy Models*

R. Arnowitt, B. Dutta, and Y. Santoso**

Center For Theoretical Physics, Department of Physics, Texas A&M University, College Station, TX 77843, USA

Received February 13, 2002

Abstract—Direct detection experiments for neutralino dark matter in the Milky Way are examined within the framework of SUGRA models with R-parity invariance and grand unification at the GUT scale, M_G. Models of this type apply to a large number of phenomena, and all existing bounds on the SUSY parameter space due to current experimental constraints are included. For models with universal soft breaking at M_G (mSUGRA), the Higgs mass and $b \to s\gamma$ constraints imply that the gaugino mass, $m_{1/2}$, obeys $m_{1/2} > 300$–400 GeV, putting most of the parameter space in the coannihilation domain, where there is a relatively narrow band in the m_0–$m_{1/2}$ plane. For $\mu > 0$, we find that the neutralino–proton cross section is $\gtrsim 10^{-10}$ pb for $m_{1/2} < 1$ TeV, making almost all of this parameter space accessible to future planned detectors. For $\mu < 0$, however, there will be large regions of parameter space with cross sections $< 10^{-12}$ pb and, hence, unaccessible experimentally. If, however, the muon magnetic moment anomaly is confirmed, then $\mu > 0$ and $m_{1/2} \lesssim 800$ GeV. Models with nonuniversal soft breaking in the third generation and Higgs sector can allow for new effects arising from additional early Universe annihilation through the Z-channel pole. Here, cross sections that will be accessible in the near future to the next generation of detectors can arise, and can even rise to the large values implied by the DAMA data. Thus, dark matter detectors have the possibility of studying the post-GUT physics that control the patterns of soft breaking.

1. INTRODUCTION

The recent BOOMERanG, Maxima, and DASI data have allowed a relatively precise determination of the mean amount of dark matter in the Universe, and these results are consistent with other astronomical observations. Within the Milky Way itself, the amount of dark matter is estimated to be

$$\rho_{\rm DM} \cong 0.3\text{–}0.5\ {\rm GeV/cm}^3. \qquad (1)$$

Supersymmetry with R-parity invariance possesses a natural candidate for cold dark matter (CDM), the lightest neutralino, $\tilde{\chi}_1^0$, and SUGRA models predict a relic density consistent with the astronomical observations of dark matter. Several methods for detecting the Milky Way neutralinos exist:

(i) Annihilation of $\tilde{\chi}_1^0$ in the halo of the Galaxy leading to antiproton or positron signals. There have been several interesting analyses of these possibilities [1, 2], but there are still uncertainties as to astronomical backgrounds.

(ii) Annihilation of the $\tilde{\chi}_1^0$ in the center of the Sun or Earth leading to neutrinos and detection of the energetic ν_μ by neutrino telescopes (AMANDA, Ice Cube, ANTARES). Recent analyses [3, 4] indicate that these detectors can be sensitive to such signals, but for the Minimal Supersymmetric Standard Model (MSSM) one requires $m_{\tilde{\chi}_1^0} > 200$ GeV (i.e., $m_{1/2} > 500$ GeV) and $\tan\beta > 10$, and for SUGRA models one is restricted to $\tan\beta > 35$ [3].

(iii) Direct detection by scattering of incident $\tilde{\chi}_1^0$ on nuclear targets of terrestrial detectors. Current detectors are sensitive to such events for $\tilde{\chi}_1^0$–p cross sections in the range

$$\sigma_{\tilde{\chi}_1^0 - p} \gtrsim 1 \times 10^{-6}\ {\rm pb} \qquad (2)$$

with a possible improvement by a factor of 10–100 in the near future. Future detectors (GENIUS, Cryoarray, ZEPLIN IV) may be sensitive down to 10^{-9}–10^{-10} pb, and we will see that this would be sufficient to cover the parameter space of most SUGRA models.

In the following, we will consider SUGRA models with R-parity invariance based on grand unification at the GUT scale $M_G \cong 2 \times 10^{16}$ GeV. In particular, we will consider two classes of models: minimal supergravity models (mSUGRA [5, 6]) with universal soft breaking masses at M_G and nonuniversal models with nonuniversal soft breaking at M_G for the Higgs bosons and the third generation of squarks and

*This article was submitted by the authors in English.

**e-mail: arnowitt@physics.tamu.edu

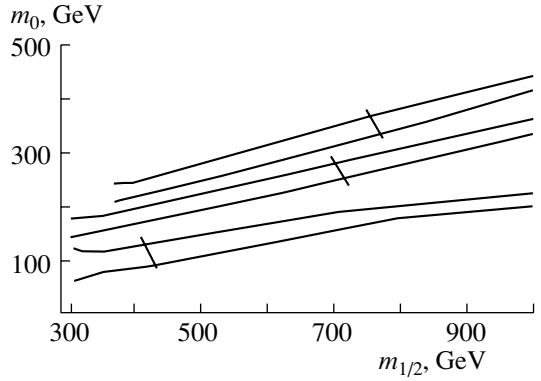

Fig. 1. Corridors in the m_0–$m_{1/2}$ plane allowed by the relic density constraints for $A_0 = 0$, $\mu > 0$, and (bottom to top) $\tan\beta = 10$, 30, 40. The lower bound on $m_{1/2}$ is due to the m_h lower bound for $\tan\beta = 10$ and due to the $b \to s\gamma$ bound for $\tan\beta = 40$, while both these contribute equally for $\tan\beta = 30$. The short lines cutting the channels represent upper bound from the g_μ-2 experiment [13].

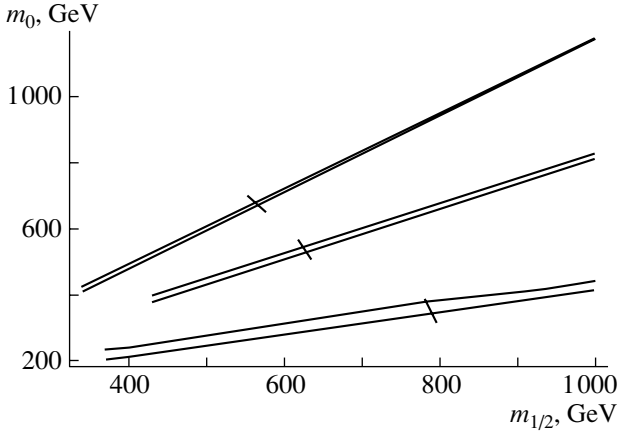

Fig. 2. Corridors in the m_0–$m_{1/2}$ plane allowed by the relic density constraint for $\tan\beta = 40$, $\mu > 0$, and (bottom to top) $A_0 = 0$, $-2m_{1/2}$, $4m_{1/2}$. The curves terminate at the lower end due to the $b \to s\gamma$ constraint, except for $A_0 = 4m_{1/2}$, which terminates due to the m_h constraint. The short lines cutting the corridors represent the upper bound on $m_{1/2}$ due to the g_μ-2 experiment [13].

sleptons. Here, the gaugino masses ($m_{1/2}$) and the cubic soft-breaking masses (A_0) at M_G are assumed universal.

SUGRA models apply to a wide range of phenomena, and data from different experiments interact with each other to sharpen the predictions greatly. We list here the important experimental constraints:

(i) Higgs mass: $m_h > 114$ GeV [7]. The theoretical calculation of m_h still has an error of ~ 3 GeV, and so we will (conservatively) interpret this bound to mean $m_h(\text{theory}) > 111$ GeV.

(ii) $b \to s\gamma$ branching ratio. We take a 2σ range around the central CLEO value [8]:

$$1.8 \times 10^{-4} \leq \text{BR}(B \to X_s\gamma) \leq 4.5 \times 10^{-4}. \quad (3)$$

(iii) $\tilde{\chi}_1^0$ relic density: We assume here

$$0.02 \leq \Omega_{\text{DM}} h^2 \leq 0.25. \quad (4)$$

The lower bound takes into account of the possibility that there is more than one species of DM. However, results are insensitive to raising it to 0.05 or 0.10.

(iv) Muon $a_\mu = (g_\mu - 2)/2$ anomaly. The Brookhaven E821 experiment [9] reported a 2.6σ deviation from the Standard Model value in their measurement of the muon magnetic moment. Recently, a sign error in the theoretical calculation [10, 11] has reduced this to a 1.6σ anomaly, though recent measurements [12] used to calculate the hadronic contribution may have raised the deviation. Since there is a great deal more data currently being analyzed (with results due this spring) that will reduce the errors by a factor of ~ 2.5, we will assume here that there is a deviation in a_μ due to SUGRA of amount

$$11 \times 10^{-10} \leq a_\mu^{\text{SUGRA}} \leq 75 \times 10^{-10}. \quad (5)$$

We will, however, state our results with and without including this anomaly.

To illustrate how the different experimental constraints affect the SUSY parameter space, we consider the mSUGRA example:

(i) The m_h and $b \to s\gamma$ constraints put a lower bound on $m_{1/2}$:

$$m_{1/2} \gtrsim 300\text{–}400 \text{ GeV}, \quad (6)$$

which means $m_{\tilde{\chi}_1^0} \gtrsim 120\text{–}160$ GeV (since $m_{\tilde{\chi}_1^0} \cong 0.4 m_{1/2}$).

(ii) Equation (6) now means that most of the parameter space is in the $\tilde{\tau}_1$–$\tilde{\chi}_1^0$ coannihilation domain in the relic density calculation. Then, m_0 (the squark and slepton soft-breaking mass) is approximately determined by $m_{1/2}$, as can be seen in Figs. 1 and 2.

(iii) If we include the a_μ anomaly, since a_μ^{SUGRA} is a decreasing function of $m_{1/2}$ and m_0, the lower bound of (5) produces an upper bound on $m_{1/2}$ and the positive sign of a_μ implies that the μ parameter is positive. In addition, one gets a lower bound on $\tan\beta$ of $\tan\beta > 5$. Thus, the parameter space has begun to be strongly constrained, allowing for more precise predictions. In order to carry out detailed calculations, however, it is necessary to include a number of analyses to obtain accurate results. We list some of these here.

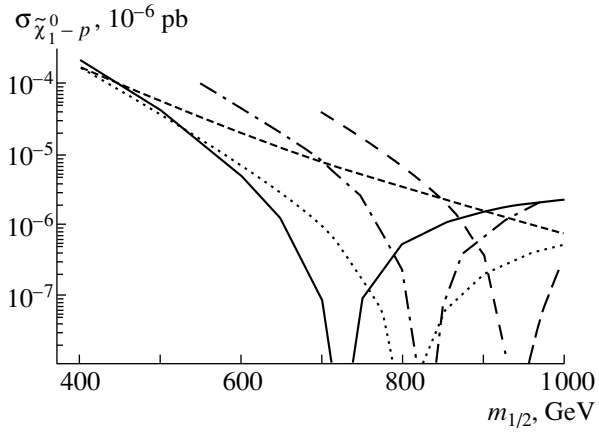

Fig. 3. $\sigma_{\tilde{\chi}_1^0 - p}$ for mSUGRA for $\mu < 0$, $A_0 = 1500$ GeV, for $\tan\beta = 6$ (short dash), 8 (dotted), 10 (solid curve), 20 (dash-dotted), and $\tan\beta = 25$ (long dashed). Note that the $\tan\beta = 6$ curve terminates at low $m_{1/2}$ due to the Higgs mass constraint, and the other curves terminate at low $m_{1/2}$ due to the $b \to s\gamma$ constraint [18].

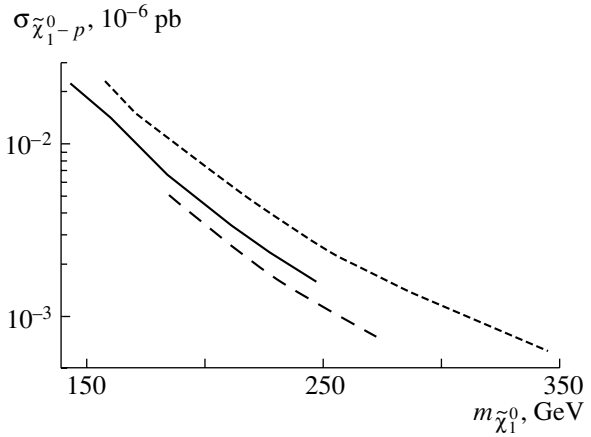

Fig. 4. $\sigma_{\tilde{\chi}_1^0 - p}$ as a function of the neutralino mass $m_{\tilde{\chi}_1^0}$ for $\tan\beta = 40$, $\mu > 0$ for $A_0 = -2m_{1/2}$, $4m_{1/2}$, 0 from bottom to top. The curves terminate at small $m_{\tilde{\chi}_1^0}$ due to the $b \to s\gamma$ constraint for $A_0 = 0$ and $-2m_{1/2}$ and due to the Higgs mass bound ($m_h > 114$ GeV) for $A_0 = 4m_{1/2}$. The curves terminate at large $m_{\tilde{\chi}_1^0}$ due to the lower bound on a_μ of (5) [13].

Two-loop gauge and one-loop Yukawa renormalization group equations (RGE) are used in going from M_G to the electroweak weak scale $M_{\rm EW}$, and QCD RGE are used below $M_{\rm EW}$ for the light quark contributions. Two-loop and pole-mass corrections are included in the calculation of m_h. One-loop corrections to m_b and m_τ [14, 15] are included, which are important at large $\tan\beta$. Large $\tan\beta$ NLO SUSY corrections to $b \to s\gamma$ [16, 17] are included. In calculating the relic density, all stau–neutralino coannihilation channels are included, and this calculation is done in a fashion valid for both small and large $\tan\beta$.

We do not include Yukawa unification or proton decay constraints, since these depend sensitively on post-GUT physics, about which little is known.

2. mSUGRA MODEL

The mSUGRA model is the simplest and hence most predictive of the supergravity models in that it depends on only four new parameters and one sign (in addition to the usual SM parameters). We take these new parameters to be m_0 and $m_{1/2}$ (the universal soft-breaking scalar and gaugino masses at M_G), A_0 (the universal cubic soft-breaking mass at M_G), $\tan\beta = \langle H_2\rangle/\langle H_1\rangle$ at the electroweak scale (where $\langle H_2\rangle$ gives rise to up-quark masses and $\langle H_1\rangle$ to down-quark masses), and the sign of μ (the Higgs mixing parameter which appears in the superpotential as $\mu H_1 H_2$). We examine these parameters over the range $m_0, m_{1/2} \le 1$ TeV, $2 < \tan\beta < 50$, $|A_0| \le 4m_{1/2}$. The bound on $m_{1/2}$ corresponds to the gluino mass bound of $m_{\tilde{g}} < 2.5$ GeV, which is also the reach of the LHC.

The relic density analysis involves calculating the annihilation cross section for neutralinos in the early Universe. This characteristically proceeds through Z and Higgs s-channel poles (Z, h, H, A, where H and A are heavy CP-even and CP-odd Higgs bosons) and through t-channel sfermion poles. However, if there is a second particle that becomes nearly degenerate with the neutralino, one must include it in the early Universe annihilation processes, which then leads to the coannihilation phenomena. In mSUGRA models, this accidental near degeneracy occurs naturally for the light stau, $\tilde{\tau}_1$. One can understand this semiquantitatively by considering the low and intermediate $\tan\beta$ region, where the RGE give for the right selectron, $\tilde{e}_R$, and the neutralino the following masses at the electroweak scale:

$$m^2_{\tilde{e}_R} = m_0^2 + 0.15 m_{1/2}^2 - \sin^2\theta_{\rm W} M_W^2 \cos 2\beta, \quad (7)$$

$$m^2_{\tilde{\chi}_1^0} = 0.16 m_{1/2}^2, \quad (8)$$

the numerics coming from the RGE analysis. The last term in (7) is $\simeq (40\ {\rm GeV})^2$. Thus, for $m_0 = 0$, the $\tilde{e}_R$ will become degenerate with the $\tilde{\chi}_1^0$ at $m_{1/2} \cong 400$ GeV, and coannihilation thus begins at $m_{1/2} \cong 350$–400 GeV. As $m_{1/2}$ increases, m_0 must be raised in lock step (to keep $m_{\tilde{e}_R} > m_{\tilde{\chi}_1^0}$). More precisely, it is the light stau, which is the lightest slepton, that dominates the coannihilation phenomena. However, one ends up with corridors in the m_0–$m_{1/2}$ plane for allowed relic density with m_0 closely correlated with $m_{1/2}$, increasing as $m_{1/2}$ does, as seen in Figs. 1 and 2.

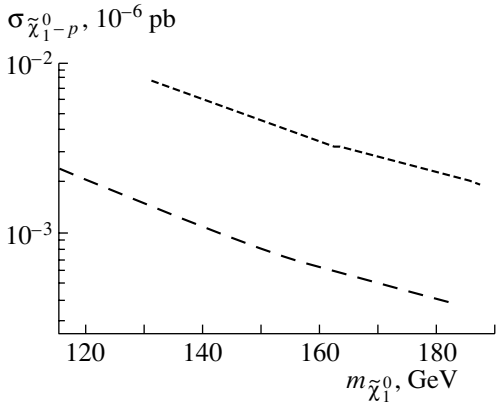

Fig. 5. $\sigma_{\tilde{\chi}_1^0-p}$ as a function of $m_{\tilde{\chi}_1^0}$ for $\tan\beta = 10$, $\mu > 0$, $m_h > 114$ GeV for $A_0 = 0$ (upper curve), $A_0 = -4m_{1/2}$ (lower curve). The termination at low $m_{\tilde{\chi}_1^0}$ is due to the m_h bound for $A_0 = 0$, and the $b \to s\gamma$ bound for $A_0 = -4m_{1/2}$. The termination at high $m_{\tilde{\chi}_1^0}$ is due to the lower bound on a_μ of (5) [13].

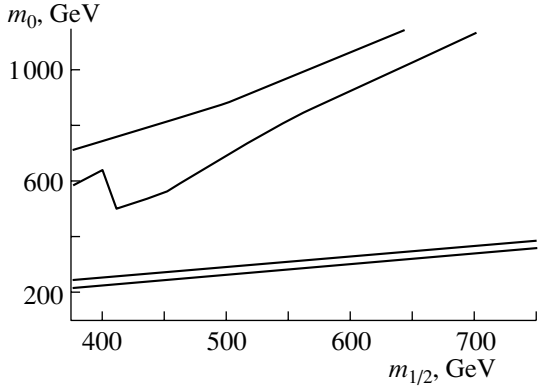

Fig. 6. Effect of a nonuniversal Higgs soft breaking mass enhancing the Z^0 s-channel pole contribution in the early Universe annihilation for the case of $\delta_2 = 1$, $\tan\beta = 40$, $A_0 = m_{1/2}$, $\mu > 0$. The lower band is the usual $\tilde{\tau}_1$ coannihilation region. The upper band is an additional region satisfying the relic density constraint arising from increased annihilation via the Z^0 pole due to the decrease in μ^2 increasing the higgsino content of the neutralino [18].

For dark matter detectors with heavy nuclei targets, the spin-independent neutralino–nucleus cross section dominates, which allows one to extract the $\tilde{\chi}_1^0$–proton cross section, $\sigma_{\tilde{\chi}_1^0-p}$. The basic quark diagrams for this scattering go through s-channel squark poles and t-channel Higgs (h, H) poles. The general features of $\sigma_{\tilde{\chi}_1^0-p}$ that explain its properties are the following:

$$\sigma_{\tilde{\chi}_1^0-p} \quad \text{increases with increasing} \quad \tan\beta, \tag{9}$$

$$\sigma_{\tilde{\chi}_1^0-p} \quad \text{decreases with increasing} \quad m_{1/2} \quad \text{and increasing} \quad m_0. \tag{10}$$

Since coannihilation generally correlates m_0 and $m_{1/2}$, if $m_{1/2}$ increases so does m_0 (at fixed $\tan\beta$ and A_0).

The smallest cross sections occur for the case $\mu < 0$. This is because a special cancellation can occur over a fairly wide range of $\tan\beta$ and $m_{1/2}$ [18, 19] driving the cross section below 10^{-13} pb (Fig. 3). In these regions, there would be no hope for currently planned dark matter detectors to be able to detect Milky Way neutralinos. However, if the a_μ anomaly is confirmed by the new BNL E821 data (currently being analyzed), then $\mu < 0$ is forbidden, and the special cancellations do not occur for $\mu > 0$. Large cross sections can then occur for large $\tan\beta$. This is seen in Fig. 4 for $\tan\beta = 40$, with $m_h > 114$ GeV. If the Higgs mass bound were to rise, the lower bounds on $m_{1/2}$ would increase. Thus, for $m_h > 120$ GeV, one has $m_{\tilde{\chi}_1^0} > (200, 215, 246)$ GeV for $A_0 = (-2, 0, 4)m_{1/2}$.

The lowest cross sections for $\mu > 0$ are expected to occur for small $\tan\beta$ and large $m_{1/2}$. This is seen in Fig. 5 for $\tan\beta = 10$, where one also sees that decreasing A_0 gives smaller cross sections. In general, one finds

$$\sigma_{\tilde{\chi}_1^0-p} \gtrsim 10^{-10} \text{ pb} \quad \text{for} \quad \mu > 0, \quad m_{1/2} < 1 \text{ TeV}. \tag{11}$$

Such cross sections are within the reach of future planned detectors.

3. NONUNIVERSAL MODELS

New results can occur if we relax the universality of the squark, slepton, and soft-breaking Higgs masses at M_G. To maintain the flavor-changing neutral current bounds, we do this only in the third generation and for the Higgs bosons. One may parametrize the soft-breaking masses at M_G as follows:

$$\begin{aligned} m_{H_1}^2 &= m_0^2(1+\delta_1); \quad m_{H_2}^2 = m_0^2(1+\delta_2); \\ m_{q_L}^2 &= m_0^2(1+\delta_3); \quad m_{t_R}^2 = m_0^2(1+\delta_4); \\ m_{\tau_R}^2 &= m_0^2(1+\delta_5); \quad m_{b_R}^2 = m_0^2(1+\delta_6); \\ m_{l_L}^2 &= m_0^2(1+\delta_7) \end{aligned} \tag{12}$$

with $-1 \le \delta_i \le +1$. While the nonuniversal models introduce a number of new parameters, it is possible to understand qualitatively what effects they produce on dark matter detection rates, since the parameter μ^2 governs much of the physics. Thus, as μ^2 decreases (increases), the higgsino content of the neutralino increases (decreases), and then $\sigma_{\tilde{\chi}_1^0-p}$ increases (decreases). One can further see semiquanitatively the

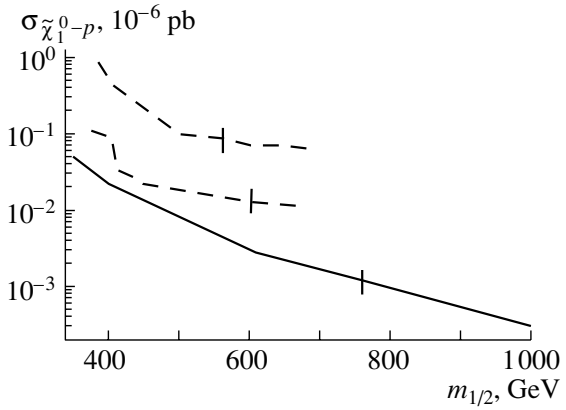

Fig. 7. $\sigma_{\tilde{\chi}_1^0-p}$ as a function of $m_{1/2}$ ($m_{\tilde{\chi}_1^0} \cong 0.4 m_{1/2}$) for $\tan\beta = 40$, $\mu > 0$, $m_h > 114$ GeV, $A_0 = m_{1/2}$ for $\delta_2 = 1$. The lower curve is for the $\tilde{\tau}_1 - \tilde{\chi}_1^0$ coannihilation channel, and the dashed band is for the Z s-channel annihilation allowed by nonuniversal soft breaking. The curves terminate at low $m_{1/2}$ due to the $b \to s\gamma$ constraint. The vertical lines show the termination at high $m_{1/2}$ due to the lower bound on a_μ of (5) [21].

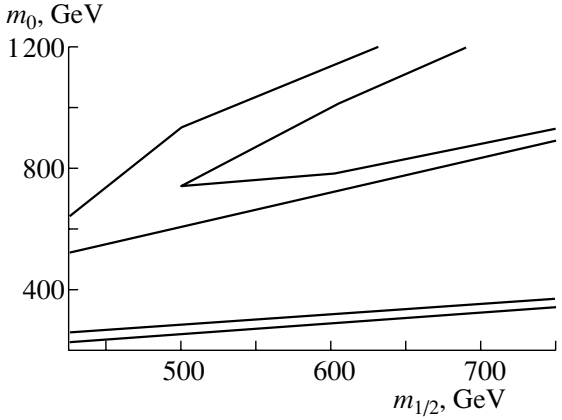

Fig. 8. Allowed regions in the m_0–$m_{1/2}$ plane for the case $\tan\beta = 40$, $A_0 = m_{1/2}$, $\mu > 0$. The bottom curve is the mSUGRA $\tilde{\tau}_1$ coannihilation band of Fig. 1 (shown for reference). The middle band is the actual $\tilde{\tau}_1$ coannihilation band when $\delta_{10} = -0.7$. The top band is an additional allowed region due to the enhancement of the Z^0 s-channel annihilation arising from the nonuniversality lowering the value of μ^2 and hence raising the higgsino content of the neutralino. For $m_{1/2} \lesssim 500$ GeV, the two bands overlap [18].

dependence of μ^2 on the nonuniversal parameters for low and intermediate $\tan\beta$, where the RGE may be solved analytically [20]:

$$\mu^2 = \frac{t^2}{t^2-1}\left[\left(\frac{1-3D_0}{2} + \frac{1}{t^2}\right) + \frac{1-D_0}{2}(\delta_3+\delta_4) - \frac{1+D_0}{2}\delta_2 + \frac{\delta_1}{t^2}\right] m_0^2 + \text{universal parts} + \text{loop corrections}, \quad (13)$$

where $t = \tan\beta$ and $D_0 \simeq 1 - (m_t/200\sin\beta)^2$. In general, D_0 is small ($D_0 \approx 0.25$) and one sees that the universal part of the m_0^2 contribution is quite small, and it does not take a great deal of nonuniversal contribution to produce additional effects.

Most interesting things happen when μ^2 is decreased, since the increased Higgsino content of the neutralino increases the $\tilde{\chi}_1^0$–$\tilde{\chi}_1^0$–Z coupling, and this coupling opens a new annihilation channel through the Z pole in the relic density calculations. As a simple example, we consider the case, where only the H_2 soft-breaking mass is affected, i.e., $\delta_2 = 1$ and all other $\delta_i = 0$. Figure 6 shows the new allowed region in the m_0–$m_{1/2}$ plane for $\tan\beta = 40$, $A_0 = m_{1/2}$, $\mu > 0$, and Fig. 7 shows the corresponding effect on the neutralino–proton cross section. One sees that the coannihilation corridor is significantly raised and widened due to the new Z-channel annihilation, and the cross section is significantly increased. The next round of upgraded dark matter detectors should be able to reach parts of this parameter space if such a nonuniversality were to occur.

As a second example, we consider a soft-breaking pattern conistent with an $SU(5)$ invariant model with $\delta_{10}(= \delta_3 = \delta_4 = \delta_5) = -0.7$ and all other $\delta_i = 0$. Here, the $\tilde{\tau}_R$ soft-breaking mass is reduced, i.e., $m_{\tilde{\tau}_R}^2 = m_0^2(1+\delta_5) < m_0^2$. Thus, the $\tilde{\tau}_1 - \tilde{\chi}_1^0$ coannihilation occurs at a larger value of m_0 than in mSUGRA. In addition again a new Z-channel neutralino annihilation channel occurs since μ^2 is

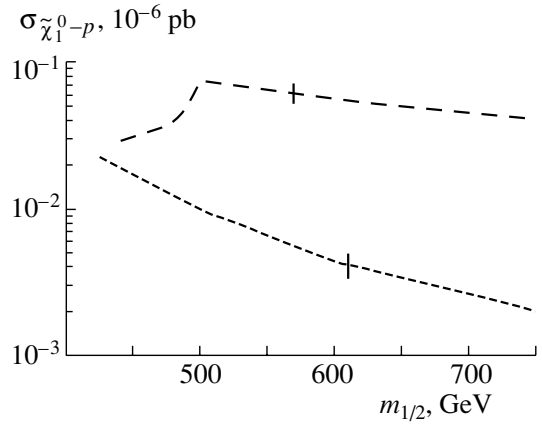

Fig. 9. $\sigma_{\tilde{\chi}_1^0-p}$ as a function of $m_{1/2}$ for $\tan\beta = 40$, $\mu > 0$, $A_0 = m_{1/2}$, and $m_h > 114$ GeV. The lower curve is for the bottom of the $\tilde{\tau}_1$–$\tilde{\chi}_1^0$ co-annihilation corridor, and the upper curve is for the top of the Z-channel band. The termination at low $m_{1/2}$ is due to the $b \to s\gamma$ constraint, and the vertical lines are the upper bound on $m_{1/2}$ due to the lower bound of a_μ of (5) [21].

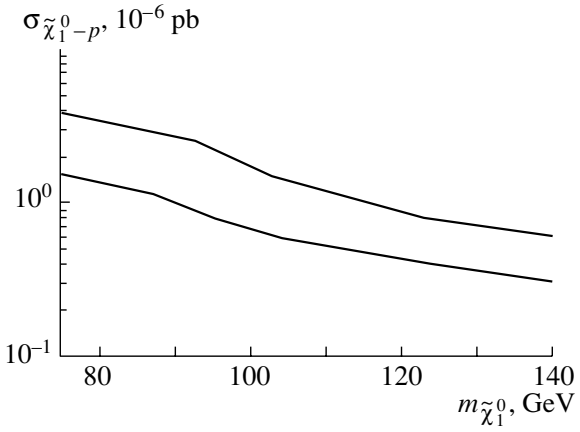

Fig. 10. Maximum value of $\sigma_{\tilde{\chi}_1^0-p}$ as a function of $m_{\tilde{\chi}_1^0}$ for the nonuniversal model with $\mu > 0$, δ_1, δ_3, $\delta_4 < 0$, $\delta_2 > 0$. The lower curve is for $\tan\beta = 7$, and the upper curve is for $\tan\beta = 12$.

reduced. The effects are shown in Figs. 8 and 9 for $\tan\beta = 40$, $A_0 = m_{1/2}$, $\mu > 0$. Again, the cross sections are larger and should be accessible to CDMS when it moves to the Soudan mine and to GENIUS.

The maximum value of $\sigma_{\tilde{\chi}_1^0-p}$ for fixed $\tan\beta$ and A_0 occurs when we chose the nonuniversalities to minimize μ^2. This occurs when $\delta_{1,3,4} < 0$ and $\delta_2 > 0$. This is shown in Fig. 10, where the maximum cross section is plotted for $A_0 = 0$, $\tan\beta = 12$ (upper curve), $\tan\beta = 7$ (lower curve). The bound that $m_h > 114$ GeV eliminates the region with $m_{\tilde{\chi}_1^0} < 100$ GeV. However, one sees for this case that it is possible to have detection cross sections in the region of the DAMA data.

4. CONCLUSIONS

We have discussed here direct detection of Milky Way neutralinos for SUGRA type models with R-parity invariance and grand unification at the GUT scale. By combining data from a variety of sources, e.g., Higgs mass bound, $b \to s\gamma$ branching ratio, relic density constraints, and the possible new muon magnetic moment anomaly of the BNL E821 experiment, one can greatly sharpen predictions.

For the mSUGRA model, the m_h and $b \to s\gamma$ bounds create a lower bound on $m_{1/2}$ of $m_{1/2} \gtrsim (300\text{–}400)$ GeV (i.e., $m_{\tilde{\chi}_1^0} \gtrsim (120\text{–}140)$ GeV). This puts the parameter space mostly in the $\tilde{\tau}_1$–$\tilde{\chi}_1^0$ coannihilation domain, which strongly correlates m_0 with $m_{1/2}$. For $\mu > 0$ and $m_{1/2} < 1$ TeV, one finds $\sigma_{\tilde{\chi}_1^0-p} \lesssim 10^{-10}$ pb, which is within the upper reach of future planned dark matter detectors, while for $\mu < 0$ there will be large regions unaccessible to such detectors. If the a_μ anomaly is confirmed, then $\mu > 0$ and $m_{1/2} < 800$ GeV.

Nonuniversal soft-breaking models allow one to raise $\sigma_{\tilde{\chi}_1^0-p}$ by a factor as large as 10–100, which could account for the large cross sections of the DAMA data. They can also open new allowed regions of the m_0–$m_{1/2}$ plane from the Z-channel annihilation in the relic density calculation. The new Z-channel regions have larger cross sections, though still below the DAMA region, but they should be accessible when CDMS moves to the Soudan mine and to the GENIUS-TF detector. Thus, dark matter detectors should be able to investigate the nature of SUSY soft breaking, i.e., the nature of the post-GUT physics that determine the soft-breaking pattern.

ACKNOWLEDGMENTS

This work was supported in part by the National Science Foundation, grant nos. PHY-0070964 and PHY-0101015.

REFERENCES

1. G. L. Kane, L.-T. Wang, and J. D. Wells, hep-ph/0108138.
2. E. A. Baltz, J. Edsjo, K. Freese, and P. Gondolo, astro-ph/0109318.
3. V. Barger, F. Halzen, D. Hooper, and C. Kao, hep-ph/0105182.
4. A. Bottino, N. Fornengo, S. Scopel, and F. Donato, hep-ph/0105233.
5. A. H. Chamseddine, R. Arnowitt, and P. Nath, Phys. Rev. Lett. **49**, 970 (1982).
6. R. Barbieri, S. Ferrara, and C. A. Savoy, Phys. Lett. B **119B**, 343 (1982); L. Hall, J. Lykken, and S. Weinberg, Phys. Rev. D **27**, 2359 (1983); P. Nath, R. Arnowitt, and A. H. Chamseddine, Nucl. Phys. B **227**, 121 (1983).
7. P. Igo-Kemenes, *LEPC Meeting, Nov. 3, 2000* (http://lephiggs.web.cern.ch/LEPHIGGS/talks/index.html).
8. CLEO Collab. (S. Chen *et al.*), Phys. Rev. Lett. **87**, 251807 (2001).
9. Muon (g-2) Collab. (H. N. Brown *et al.*), Phys. Rev. Lett. **86**, 2227 (2001).
10. M. Knecht and A. Nyffeler, hep-ph/0111058; M. Knecht, A. Nyffeler, and E. De Raphael, hep-ph/0111059.
11. M. Hayakawa and T. Kinoshita, hep-ph/0112102; I. Blokland, A. Czernecki, and K. Melnikov, hep-ph/0112117.
12. R. R. Akhmetshin *et al.*, hep-ex/0112031.
13. R. Arnowitt, B. Dutta, and Y. Santoso, Phys. Rev. D **64**, 113010 (2001).

14. R. Rattazi and U. Sarid, Phys. Rev. D **53**, 1553 (1996).
15. M. Carena, M. Olechowski, S. Pokorski, and C. Wagner, Nucl. Phys. B **426**, 269 (1994).
16. G. Degrassi, P. Gambino, and G. Giudice, JHEP **0012**, 009 (2000).
17. M. Carena, D. Garcia, U. Nierste, and C. Wagner, Phys. Lett. B **499**, 141 (2001).
18. R. Arnowitt, B. Dutta, and Y. Santoso, Nucl. Phys. B **606**, 59 (2001).
19. J. Ellis, A. Ferstl, and K. A. Olive, Phys. Lett. B **481**, 304 (2001); Phys. Rev. D **63**, 065016 (2001).
20. R. Arnowitt and P. Nath, Phys. Rev. D **56**, 2820 (1997).
21. R. Arnowitt, B. Dutta, B. Hu, and Y. Santoso, Phys. Lett. B **505**, 177 (2001).

Physics of Atomic Nuclei, Vol. 65, No. 12, 2002, pp. 2225–2228. From Yadernaya Fizika, Vol. 65, No. 12, 2002, pp. 2287–2290.

COSMOLOGY AND ASTROPHYSICS. DARK MATTER

Supersymmetric Candidates for Nonbaryonic Dark Matter*

N. Fornengo**

Dipartimento di Fisica Teorica, Università di Torino, and INFN, Italy

Received February 13, 2002

Abstract—We analyze how detectability of relic neutralinos by direct means is related to their local and cosmological densities. We show to what extent the present experiments of direct searches for weakly interacting massive particles, when interpreted in terms of relic neutralinos, probe interesting regions of the supersymmetric parameter space. Our analysis is performed in a number of different supersymmetric schemes. © *2002 MAIK "Nauka/Interperiodica"*.

1. INTRODUCTION

Evidence for existence of dark matter and dark energy in the Universe is provided by a host of observational data: properties of galactic halos and clusters of galaxies, large scale structures, cosmic microwave background, and high-redshift supernovae SNe Ia. As far as dark matter is concerned, a favorite range for $\Omega_m h^2$ (Ω_m being the matter density divided by the critical density and h the present-day value of the Hubble constant in units of $\mathrm{km\,s^{-1}\,Mpc^{-1}}$) may be set as $0.05 \lesssim \Omega_m h^2 \lesssim 0.3$.

2. SENSITIVITY RANGE FOR CURRENT WIMP DIRECT SEARCHES

In this paper, we focus our analysis on the weakly interacting massive particle (WIMP) mass range, which, in the light of experimental data, appears particularly appealing:

$$40 \leq m_{\mathrm{WIMP}} \leq 200\ \mathrm{GeV}. \qquad (1)$$

Notice that the mass range of (1) is quite appropriate for neutralinos. Actually, the lower extreme is indicative of the LEP lower bound on the neutralino mass m_χ. As for the upper extreme, we notice that, though a generic range for m_χ might extend up to about 1 TeV, requirements of no excessive fine tuning [1] would actually favor an upper bound on the order of 200 GeV, in accordance with (1).

In what follows, we will discuss the discovery potential of WIMP direct searches for WIMPs in the mass range of (1). Particular attention will be paid to capabilities of the present experiments. In case of WIMPs whose coherent interactions with ordinary matter are dominant over the spin-dependent ones, the current sensitivity may be stated, in terms of the quantity $\xi\sigma_{\mathrm{scalar}}^{(\mathrm{nucleon})}$, as

$$4 \times 10^{-10} \leq\ \xi\sigma_{\mathrm{scalar}}^{(\mathrm{nucleon})} \leq 2 \times 10^{-8}\ \mathrm{nb}. \qquad (2)$$

3. SUPERSYMMETRIC DARK MATTER

We turn now to calculations performed in specific supersymmetric schemes, assuming that R parity is conserved and thus that the LSP is stable. The nature of the LSP depends on the SUSY breaking mechanism and on the specific regions of the SUSY parameter space. We consider here gravity-mediated schemes and domains of the parameter space where the LSP is the neutralino. Extensive calculations on relic neutralino phenomenology in gravity-mediated models have been performed in the literature (see, for instance, references in [2]).

In Figs. 1 and 2, we give the scatter plots for $\sigma_{\mathrm{scalar}}^{(\mathrm{nucleon})}$ vs. $\Omega_\chi h^2$ for two different schemes: universal SUGRA and a low-energy realization of SUSY models (effMSSM) [4]. For the SUGRA scheme, we only display the results corresponding to positive values of μ, since, for negative values, the constraint on $b \to s + \gamma$ implies a large suppression of $\sigma_{\mathrm{scalar}}^{(\mathrm{nucleon})}$. The calculations of $\sigma_{\mathrm{scalar}}^{(\mathrm{nucleon})}$ have been performed with the formulas reported in [3]; set 1 for the quantities $m_q\langle\bar{q}q\rangle$ has been used (see [3] for definitions); the evaluation of $\Omega_\chi h^2$ follows the procedure given in [5]. The two horizontal lines bracket the sensitivity region defined by (2), when ξ is set equal to one. The two vertical lines denote the favorite range for $\Omega_m h^2$, $0.05 \leq \Omega_m h^2 \leq 0.3$.

Figures 1 and 2 show that the present experimental sensitivity in WIMP direct searches allows the exploration of SUSY configurations compatible with

*This article was submitted by the author in English.

**e-mail: fornengo@to.infn.it

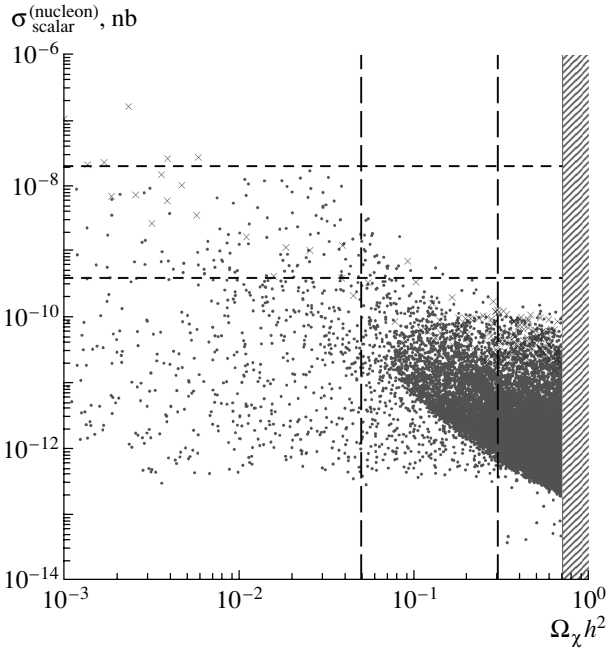

Fig. 1. Scatter plot of $\sigma^{(\mathrm{nucleon})}_{\mathrm{scalar}}$ vs. $\Omega_\chi h^2$ for universal SUGRA. Set 1 for the quantities $m_q\langle\bar{q}q\rangle$ is employed [3]. Only configurations with positive μ are shown, and m_χ is taken in the range of (1). The two horizontal lines bracket the sensitivity region defined by (2), for $\xi = 1$. The two vertical lines denote the range $0.05 \leq \Omega_m h^2 \leq 0.3$. The region above $\Omega_\chi h^2 = 0.7$ is excluded by current limits on the age of the Universe. Dots (crosses) denote gaugino (mixed) configurations.

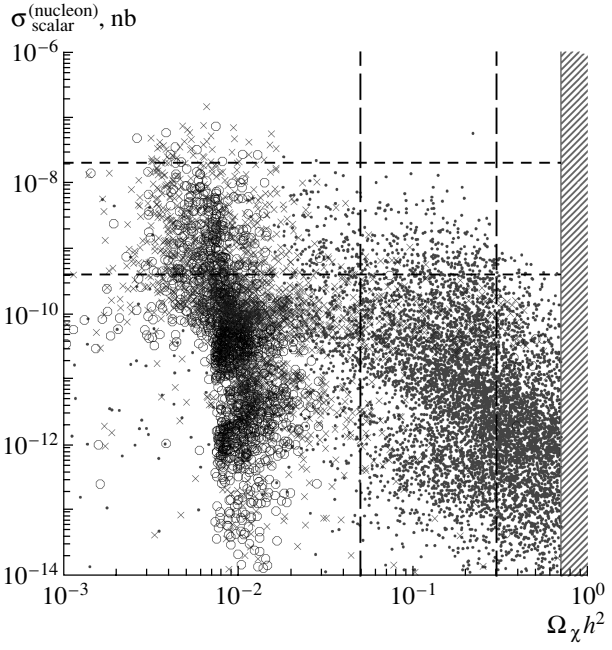

Fig. 2. Scatter plot of $\sigma^{(\mathrm{nucleon})}_{\mathrm{scalar}}$ vs. $\Omega_\chi h^2$ for effMSSM. Notation as in Fig. 1. Both signs of μ are shown. Dots, circles, and crosses represent gauginos, higgsinos, and mixed configurations, respectively.

current accelerator bounds. A number of configurations stay inside the region of cosmological interest, also in the constrained SUGRA scheme. The region of experimental sensitivity and cosmological interest is covered with an increasingly larger variety of SUSY configurations as one moves from SUGRA to effMSSM; this latter fact is expected from the intrinsic features of the various schemes.

Once a measurement of the quantity $\rho_\chi\sigma^{(\mathrm{nucleon})}_{\mathrm{scalar}}$ is performed, values for the local density ρ_χ vs. the relic abundance $\Omega_\chi h^2$ may be deduced by proceeding in the following way [3]: (i) ρ_χ is evaluated as $[\rho_\chi\sigma^{(\mathrm{nucleon})}_{\mathrm{scalar}}]_{\mathrm{exp}}/\sigma^{(\mathrm{nucleon})}_{\mathrm{scalar}}$, where $[\rho_\chi \times \sigma^{(\mathrm{nucleon})}_{\mathrm{scalar}}]_{\mathrm{exp}}$ denotes the experimental value and $\sigma^{(\mathrm{nucleon})}_{\mathrm{scalar}}$ is calculated as indicated above; (ii) to each value of ρ_χ, one associates the corresponding calculated value of $\Omega_\chi h^2$. The scatter plot in Fig. 3 is derived from the lowest value of the annual-modulation region of [6], $[(\rho_\chi/(0.3\ \mathrm{GeV\ cm^{-3}}))\sigma^{(\mathrm{nucleon})}_{\mathrm{scalar}}]_{\mathrm{exp}} = 1 \times 10^{-9}$ nb, and by taking m_χ in the range of (1). This plot, obtained in case of effMSSM, shows that the most interesting region, i.e., the one with $0.2 \leq \rho_\chi \leq 0.7$ GeV cm^{-3} and $0.05 \leq \Omega_m h^2 \leq 0.3$ (cross-hatched region in the figure), is covered by SUSY configurations probed by the WIMP direct detection.

Let us examine the various sectors of Fig. 3. Configurations above the upper horizontal line are incompatible with the upper limit on the local density of dark matter in our Galaxy and must be disregarded. Configurations above the upper slanted dash-dotted line and below the upper horizontal line would imply a stronger clustering of neutralinos in our halo as compared to their average distribution in the Universe. This situation may be considered unlikely, since in this case neutralinos could fulfill the experimental range for ρ_χ, but they would contribute only a small fraction to the cosmological cold dark matter content. For configurations that fall inside the band delimited by the slanted dash-dotted lines and simply hatched in the figure, the neutralino would provide only a fraction of the cold dark matter at the level of local density and of the average relic abundance, a situation that would be possible, for instance, if the neutralino is not the unique cold dark matter particle component. To neutralinos belonging to these configurations, one should assign a rescaled local density [4].

We remind the reader that the scatter plot in Fig. 3 refers to a representative value of $[\rho_\chi\sigma^{(\mathrm{nucleon})}_{\mathrm{scalar}}]$ inside the current experimental sensitivity region; thus, the plot in Fig. 3 shows that current experiments of WIMP direct detection are probing relic neutralinos

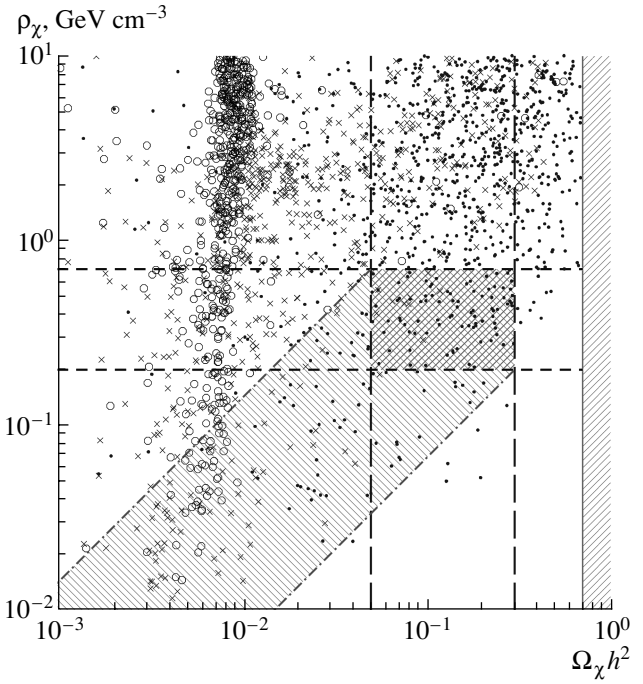

Fig. 3. Scatter plot of ρ_χ vs. $\Omega_\chi h^2$ for the effMSSM. This plot is derived from the experimental value $[(\rho_\chi/(0.3\ \text{GeV cm}^{-3}))\sigma_{\text{scalar}}^{(\text{nucleon})}]_{\text{exp}} = 1 \times 10^{-9}$ nb and by taking m_χ in the range of (1), according to the procedure outlined in the text. Set 1 for the quantities $m_q\langle\bar{q}q\rangle$ is employed [3]. The two horizontal lines delimit the range 0.2 GeV cm$^{-3} \leq \rho_\chi \leq 0.7$ GeV cm^{-3}; the two vertical lines delimit the range $0.05 \leq \Omega_m h^2 \leq 0.3$. The region above $\Omega_\chi h^2 = 0.7$ is excluded by current limits on the age of the Universe. The band delimited by the two slanted dash-dotted lines and simply hatched is the region where rescaling of ρ_l applies. Dots denote gauginos, circles denote higgsinos, and crosses denote mixed configurations.

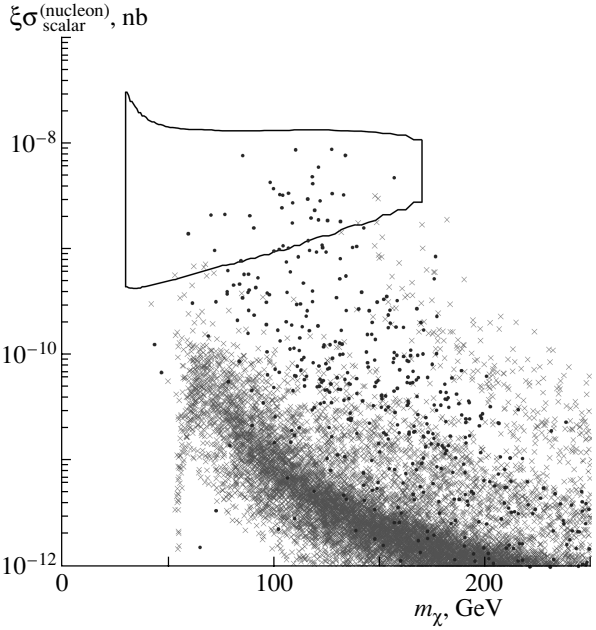

Fig. 4. Scatter plot of $\xi\sigma_{\text{scalar}}^{(\text{nucleon})}$ vs. m_χ in the case of universal SUGRA. Set 1 for the quantities $m_q\langle\bar{q}q\rangle$ is employed [3]. Crosses (dots) denote configurations with $\Omega_\chi h^2 > 0.05$ ($\Omega_\chi h^2 < 0.05$). The solid contour denotes the 3σ annual-modulation region of [6] (with the specifications given in the text).

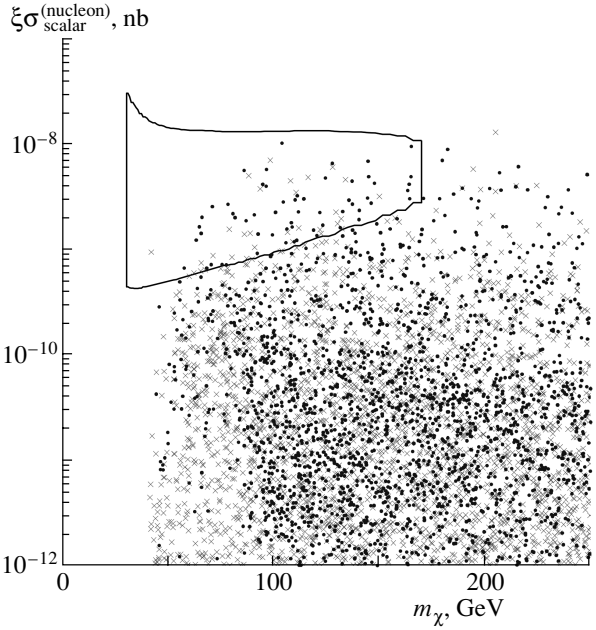

Fig. 5. Same as in Fig. 4 in the case of effMSSM.

which may reach values of cosmological interest, but also neutralinos whose local and cosmological densities may provide only a very small fraction of these densities.

For sake of comparison with specific experimental results, we provide in Figs. 4 and 5 the scatter plots for the quantity $\xi\sigma_{\text{scalar}}^{(\text{nucleon})}$ vs. m_χ in the two SUSY schemes. In these figures, the solid line denotes the frontier of the 3σ annual-modulation region of [6], when only the uncertainties in ρ_l and in the dispersion velocity of a Maxwell–Boltzmann distribution, but not the ones in other astrophysical quantities, are taken into account. Our results in Figs. 4 and 5 show that the SUSY scatter plots reach up the annual-modulation region of [6], even with the current stringent bounds from accelerators (obviously, more easily in effMSSM than in SUGRA).

4. CONCLUSION

We have shown that the current direct experiments for WIMPs, when interpreted in terms of relic neutralinos, are indeed probing regions of the SUSY

parameter space compatible with all present bounds from accelerators. We have quantified the extent of the exploration attainable by WIMP direct experiments in terms of different SUSY schemes, from a SUGRA scheme with unification assumptions at the grand unification scale to an effective model, effMSSM, at the electroweak scale. It has been stressed that, due the large uncertainties in the unification assumptions in SUGRA schemes, the effMSSM framework turns out to be the most convenient model for neutralino phenomenology.

We have proved that part of the configurations probed by current WIMP experiments entail relic neutralinos of cosmological interest, and, a fortiori, also neutralinos which might contribute only partially to the required amount of dark matter in the Universe. The cosmological properties have been displayed in terms of a plot of the local density vs. the average relic abundance, i.e., in a representation which proves particularly useful to summarize the properties of relic neutralinos (Fig. 3).

The question: Are relic neutralinos of very low (local and cosmological) densities detectable by current experiments of WIMP direct detection? finds a straightforward and affirmative answer in the ρ_χ vs. $\Omega_\chi h^2$ plot. Direct detectability is possible even for neutralino densities quite minuscule as compared to the ones of cosmological interest.

In the present note, our discussions were mainly focused on implications of direct detection results. However, also WIMP indirect searches are quite important. Measurements of up-going muon fluxes from the center of the Earth and from the Sun can potentially either find a signal or, at least, place significant constraints (though some uncertainties about a possible solar-bound population still have to be resolved) [4]. Also, measurements of low-energy antiprotons [7] or antideuterons [8] in space may provide interesting constraints on the SUSY model parameters [4].

We notice that the detectability of relic neutralinos by measurements of up-going muon fluxes from the center of the Earth and from the Sun at neutrino telescopes is more favorable in the case of low local and average densities. We have shown that the annual-modulation effect measured by the DAMA collaboration may be interpreted as due to relic neutralinos, which are compatible with all current constraints from accelerator measurements and WIMP indirect searches. In our evaluations, we have taken into account that the determination of the actual sensitivity region in terms of the WIMP–nucleon cross section and of the WIMP mass from the experimental data depends quite sizeably on uncertainties of various origins, mainly: (i) possible effects due to a halo bulk rotation and/or to asymmetries in the distribution of WIMP velocities and (ii) significant uncertainties in the determination of Higgs quark–quark and neutralino–quark–squark couplings. We stress that all these effects have to be taken properly into account when conclusions about comparison of theory with experiments are drawn. Finally, we wish to point out that a SUSY Higgs boson at a mass of about 115 GeV, as possibly hinted by the Higgs LEP experiments, would fit remarkably well in the scenario depicted above [9].

ACKNOWLEDGMENTS

This study was performed in collaboration with A. Bottino, S. Scopel, and F. Donato.

This work was supported in part by research grants from the Italian Ministero dell'Universitá e della Riserca Scientifica e Tecnologica (MURRST) within the Astroparticle Physics Project.

REFERENCES

1. V. Berezinsky, A. Bottino, J. Ellis, *et al.*, Astropart. Phys. **5**, 1, 333 (1996).
2. A. Bottino, F. Donato, N. Fornengo, and S. Scopel, in *Proceedings of "Les Rencontres de Physique de la Vallee d'Aoste," La Thuile, 2001*.
3. A. Bottino, F. Donato, N. Fornengo, and S. Scopel, Astropart. Phys. **13**, 215 (2000).
4. A. Bottino, F. Donato, N. Fornengo, and S. Scopel, Phys. Rev. D **62**, 056006 (2000).
5. A. Bottino, V. de Alfaro, N. Fornengo, *et al.*, Astropart. Phys. **2**, 67 (1994).
6. DAMA Collab. (R. Bernabei *et al.*), Phys. Lett. B **480**, 23 (2000); Eur. Phys. J. C **18**, 283 (2000).
7. A. Bottino, F. Donato, N. Fornengo, and P. Salati, Phys. Rev. D **58**, 123503 (1998).
8. F. Donato, N. Fornengo, and P. Salati, Phys. Rev. D **62**, 043003 (2000).
9. A. Bottino, N. Fornengo, and S. Scopel, Nucl. Phys. B **608**, 461 (2001).

Physics of Atomic Nuclei, Vol. 65, No. 12, 2002, pp. 2229–2231. From Yadernaya Fizika, Vol. 65, No. 12, 2002, pp. 2291–2293.

COSMOLOGY AND ASTROPHYSICS. DARK MATTER

Familon Emissivity of Dense e^-e^+ Plasma in an External Magnetic Field*

N. V. Mikheev and E. N. Narynskaya**

Yaroslavl State University, Sovetskaya ul. 14, Yaroslavl, 150000 Russia

Received April 17, 2002

Abstract—Emission of a familon due to the processes $e^- \to e^- + \phi$ and $e^- \to \mu^- + \phi$ by dense magnetized plasma is analyzed as a possible mechanism of energy and momentum losses by astrophysical objects. The field-induced effective familon–photon coupling in the familon-emission process is taken into account. The contribution of these processes to the familon emissivity of a magnetized plasma in a supernova explosion is calculated. It is shown that there is asymmetry of familon emission in the process $e^- \to \mu^- + \phi$. © *2002 MAIK "Nauka/Interperiodica".*

1. INTRODUCTION

The familon, the Nambu–Goldstone boson, associated with spontaneous breakdown of a global family symmetry, is of interest not only in the theoretical aspect of elementary particle physics, but also in some astrophysical and cosmological applications [1]. In particular, through coupling to the electron and photons, the familon could give a contribution to the energy and momentum losses by a stellar object.

In this paper, we study familon-cyclotron-emission processes $e^- \to e^- + \phi$ and the transition $e^- \to \mu^- + \phi$ forbidden in vacuum and their contributions to the energy losses by the magnetized plasma. We consider the physical situation when the typical energy of the plasma electrons, E, is the largest physical parameter,[1)]

$$E^2 \gg eB \gg m_e^2. \tag{1}$$

Condition (1) corresponds to relatively weak magnetic field, when plasma electrons occupy the highest Landau levels. At the same time, the magnetic field is still strong enough in comparison with the Schwinger value $B \gg B_e$, $B_e = m_e^2/e \simeq 4.41 \times 10^{13}$ G. Such extreme conditions as high density of matter $\sim 10^{14}$ g/cm^3, a large electron chemical potential $\mu \sim 500 m_e$, and a strong magnetic field up to $B \sim 10^{17}$ G could exist, for example, in the core of an exploding supernova.

It is known that the problem of studying of the quantum processes under conditions (1) reduces to calculation in the constant crossed field [2]. It is because, in the rest frame of a high-energy electron, a relatively weak and smooth external electromagnetic field looks very similar to the constant crossed field ($\mathbf{B} \perp \mathbf{E}, |\mathbf{B}| = |\mathbf{E}|$), where $(FF) = (\tilde{F}F) = 0$ and $F^{\mu\nu}$ and $\tilde{F}^{\mu\nu}$ are the tensor and the dual tensor of the external field. Thus, the result actually depends only on the dimensionless dynamic parameter χ,

$$\chi^2 = \frac{e^2(pFFp)}{m^6}, \tag{2}$$

where p_μ is the particle 4-momentum and m is the particle mass. Inside the parentheses, the tensor indices are cancelled systematically, for example, $(pFFp) = p_\alpha F_{\alpha\beta} F_{\beta\nu} p_\nu$.

2. FAMILON CYCLOTRON EMISSION

The familon cyclotron emission by the plasma electron has two possible channels shown in Fig. 1. The process $e^- \to e^- + \phi$ due to direct familon–electron coupling (Fig. 1*a*) can be described by the effective Lagrangian in the following form:

$$L_{\phi e} = \frac{g_{\phi e}}{2m_e} [\overline{\Psi}_e \gamma_\alpha \gamma_5 \Psi_e] \partial_\alpha \Phi, \tag{3}$$

where Φ and Ψ_e are the familon and electron fields, respectively; $g_{\phi e} = 2m_e/F$; and F is the family symmetry-breaking scale. The astrophysical constraint gives $g_{\phi e} < 1.4 \times 10^{-13}$ ($F > 7 \times 10^9$ GeV) [3].

It is important that the magnetic field induces a new effective interaction between the familon and the photon of the type

$$L_{\phi\gamma} = g_{\phi\gamma} (\partial_\beta A_\alpha) \tilde{F}^{\alpha\beta} \Phi, \tag{4}$$

*This article was submitted by the authors in English.

**e-mail: elenan@uniyar.ac.ru

1)We use natural units in which $c = \hbar = 1$, $e > 0$ is the elementary charge.

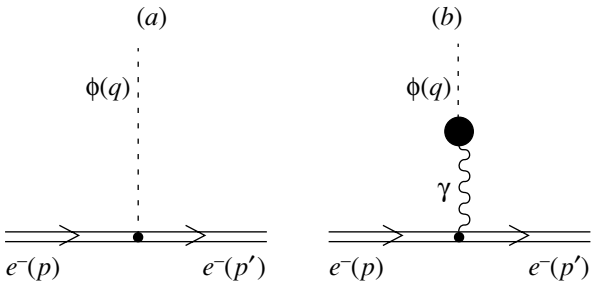

Fig. 1. The Feinman diagrams for the familon cyclotron emission by plasma electron in the presence of a magnetic field.

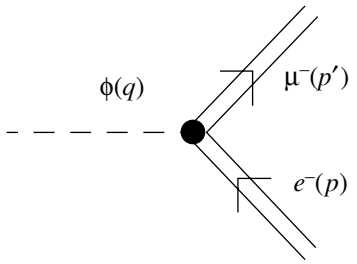

Fig. 2. The Feinman diagram for transition $e^- \to \mu^- + \phi$ in the presence of magnetized plasma.

where A_μ is the 4-potential of the quantized electromagnetic field and $g_{\phi\gamma}$ is the effective familon–photon coupling constant in the presence of the external field. This constant $g_{\phi\gamma}$ could be extracted from the paper [4], where the effective field-induced interaction of a pseudoscalar particle with photons was investigated. Note that, if the magnetic field is not so strong ($B \ll B_\mu = m_\mu^2/e \simeq 1.8 \times 10^{18}$ G, m_μ being the mass of the muon), only the virtual electron gives a contribution to $g_{\phi\gamma}$, so for $g_{\phi\gamma}$ one can obtain the following result:

$$g_{\phi\gamma} = \frac{\alpha}{\pi}\frac{g_{\phi e}}{m_e}.$$

The S-matrix element of the process $e^- \to e^- + \phi$ is

$$S = \frac{1}{F\sqrt{2\omega V}}\left[\frac{2\alpha e}{\pi}(q\tilde{F}G^L I^{(\mathrm{em})}) - (qI^{(5)})\right],$$

where $I_\mu^{(\mathrm{em})} = \int d^4x\overline{\psi}_e(p',x)\gamma_\mu\psi_e(p,x)e^{iqx}$, $I_\mu^{(5)} = \int d^4x\overline{\psi}_e(p',x)\gamma_\mu\gamma_5\psi_e(p,x)e^{iqx}$, ψ_e is the solution of the Dirac equation in the constant crossed field [5], $q^\alpha = (\omega, \mathbf{q})$ is the familon 4-momentum, $p^\alpha = (E, \mathbf{p})$ and $p'^\alpha = (E', \mathbf{p}')$ are the 4-momenta of the initial and final electrons, and $G^L_{\alpha\beta}$ is the longitudinal plasmon propagator. The longitudinal plasmon propagator $G^L_{\alpha\beta}$ in the limit of weak magnetic field (1) can be written as

$$G^L_{\alpha\beta} \simeq \frac{l_\alpha l_\beta}{q^2 - \Pi^L},$$

$$l_\alpha = \sqrt{\frac{q^2}{(uq)^2 - q^2}}\left(u_\alpha - \frac{(uq)}{q^2}q_\alpha\right).$$

Here, l_α and Π^L are the eigenvector and eigenvalue of the polarization operator corresponding to the longitudinal plasmon, respectively, and u_α is the 4-vector of the velocity of the medium.

3. TRANSITION $e^- \to \mu^- + \phi$

The phenomenon of fermion mixing gives rise to flavor-nondiagonal familon–fermion interaction. As a result, the processes with lepton-number violation of the type $e^- \to \mu^- + \phi$, $\mu^- \to e^- + \phi$ become possible. We investigate the transition $e^- \to \mu^- + \phi$ as an additional channel of the familon emission by the plasma electron (Fig. 2).

This process was studied earlier [6] in the strong magnetic field limit under the condition of smallness of the difference $\mu - m_\mu$, when $\mu^2 - m_\mu^2 \ll eB$, so the final muons are produced only in the lowest Landau level. In contrast to [6], we consider, as an example, the conditions in a supernova core with a relatively weak magnetic field, when $\mu^2 - m_\mu^2 \gg eB$, and therefore muons can occupy a great number of excited Landau levels.

The interaction of the familon with the electron and the muon is described by the effective Lagrangian in the form

$$L = \frac{1}{F}[\overline{\Psi}_\mu\gamma_\alpha(a + b\gamma_5)\Psi_e + \overline{\Psi}_e\gamma_\alpha(a + b\gamma_5)\Psi_\mu]\partial_\alpha\Phi, \tag{5}$$

where Ψ_μ is the muon field and $a^2 + b^2 = 1$.

The S-matrix element of the process $e^- \to \mu^- + \phi$ can be obtained immediately from Lagrangian (5) by substitution of solutions to the Dirac equation in the crossed field:

$$S = \frac{-1}{\sqrt{2\omega V}F}\int d^4x\overline{\psi}_\mu(p',x)\hat{q}(a + b\gamma_5)\psi_e(p,x)e^{iqx},$$

where $p'^\alpha = (E', \mathbf{p}')$, $p^\alpha = (E, \mathbf{p})$ are the muon and electron 4-momenta, respectively.

4. FAMILON EMISSIVITY

To illustrate possible astrophysical applications of the result obtained, we estimate the energy losses of plasma via the familon emission:

$$\dot{\varepsilon} = \frac{1}{(2\pi)^3}\int\frac{dW}{d\omega}\omega d\omega\frac{d^3p}{e^{(E-\mu)/T} + 1}, \tag{6}$$

where $\dot{\varepsilon}$ is the volume density of the plasma energy losses per unit time, ω is the energy of the emitted

familon, and $dW/d\omega$ is the differential probability of the process considered.

The volume density of the plasma energy losses caused by the familon emission can be represented as the sum of two contributions

$$\dot{\varepsilon}_\phi = \dot{\varepsilon}_{e^-\to e^-\phi} + \dot{\varepsilon}_{e^-\to\mu^-\phi}.$$

We estimate the familon emissivity under the conditions that could be realized in a supernova explosion. As an example, we take $\mu = 250$ MeV, $T = 35$ MeV, and $B = 10^{17}$ G:

$$\dot{\varepsilon}_\phi \simeq 10^{27}\left[0.56_{(e\to e\phi)} + 0.81_{(e\to e\phi)^{(\gamma)}} + 0.82_{(e\to\mu\phi)}\right]\left(\frac{7\times10^9\ \mathrm{GeV}}{F}\right)^2\left[\frac{\mathrm{erg}}{\mathrm{cm}^3\ \mathrm{s}}\right]. \quad (7)$$

It is seen from (7) that the contributions from the process $e^- \to \mu^- + \phi$ and the familon cyclotron emission $e^- \to e^- + \phi$ are of the same order for the parameters considered, while the familon luminosity $L_\phi \sim 10^{46}$erg/s is much less than the neutrino luminosity $L_\nu \sim 10^{52}$erg/s from the supernova core during the first few seconds after the collapse.

It should be pointed out that, at the cooling stage, when the temperature becomes on the order of MeV, the process $e^- \to \mu^- + \phi$ begins to dominate over the cyclotron emission $e^- \to e^- + \phi$,

$$\dot{\varepsilon}_\phi \simeq \dot{\varepsilon}_{e^-\to\mu^-\phi} \simeq 0.92\times10^{25}\left(\frac{7\times10^9\ \mathrm{GeV}}{F}\right)^2\left[\frac{\mathrm{erg}}{\mathrm{cm}^3\mathrm{s}}\right],$$

and could provide competition with the neutrino energy losses at this stage, $\dot{\varepsilon}_\nu \sim 10^{26}$ erg/(cm^3 s) [1].

Another interesting feature of the processes considered is the asymmetry of familon emission:

$$A = \frac{1}{\dot{\varepsilon}}\int \frac{q_3 d^3p/(2\pi)^3}{e^{(E-\mu)/T}+1}dW,$$

where q_3 is the component (parallel to the field) of the familon momentum.

Our calculations show that only the transition $e^- \to \mu^- + \phi$ gives a contribution to this asymmetry, which has a very simple form:

$$A \simeq \frac{ab}{3}\frac{eB}{m_\mu^2}. \quad (8)$$

As one can see, the dependence of the asymmetry A on plasma parameters—the electron chemical potential μ and temperature T—is totaly canceled. Recall, however, that the result (8) was obtained under the assumption that μ is the largest physical parameter of the problem. The asymmetry of familon emission leads to the familon force action on the magnetized plasma along the magnetic field, which, in turn, leads to the kick velocity of the supernova remnant. Our estimates indicate that, on the scale of the magnetic field up to 10^{17} G, the kick velocity does not exceed 100 km/s. Thus, the familon emission asymmetry cannot solve the problem of the proper velocity of the pulsars.

In conclusion, we have studied familon emission by plasma electrons via the processes $e^- \to \mu^- + \phi$, $e^- \to e^- + \phi$. Due to very weak interaction of the familon with matter, the above processes could be important in astrophysics and cosmology. As a specific application of the results obtained, we have calculated the plasma energy–momentum losses via familon emission in a supernova explosion.

ACKNOWLEDGMENTS

This work was supported in part by the Russian Foundation for Basic Research, project no. 01-02-17334, and the Ministry of Education of the Russian Federation, grant no. E00-11.0-5.

REFERENCES

1. G. G. Raffelt, *Stars as Laboratories for Fundamental Physics* (University of Chicago Press, Chicago, 1996).
2. G. K. Artimov and V. I. Ritus, Zh. Éksp. Teor. Fiz. **90**, 816 (1986) [Sov. Phys. JETP **63**, 476 (1986)].
3. Particle Data Group (C. Groom *et al.*), Eur. Phys. J. C **15**, 309 (2000).
4. N. V. Mikheev, A. Ya. Parkhomenko, and L. A. Vassilevskaya, Phys. Rev. D **60**, 035001 (1999).
5. V. B. Berestetskiĭ, E. M. Lifshitz, and L. P. Pitaevskiĭ, *Quantum Electrodynamics* (Nauka, Moscow, 1989; Pergamon, Oxford, 1982).
6. A. V. Averin, A. V. Borisov, and A. I. Studenikin, Phys. Lett. B **231**, 280 (1989).

Physics of Atomic Nuclei, Vol. 65, No. 12, 2002, pp. 2232–2237. From Yadernaya Fizika, Vol. 65, No. 12, 2002, pp. 2294–2299.

TEST OF NEW PHYSICS IN RARE PROCESSES AND COSMIC RAYS

Test of Exotic Scalar and Tensor Interactions in K_{e3} Decay Using Stopped Positive Kaons*

A. S. Levchenko[**], **A. N. Khotjantsev**, **A. P. Ivashkin**, **M. Abe**[1)], **M. A. Aliev**, **V. V. Anisimovsky**, **M. Aoki**[2)], **I. Arai**[1)], **Y. Asano**[1)], **T. Baker**[2),3)], **M. Blecher**[4)], **P. Depommier**[5)], **M. Hasinoff**[6)], **K. Horie**[7)], **H. C. Huang**[8)], **Y. Igarashi**[2)], **T. Ikeda**[9)], **J. Imazato**[2)], **M. M. Khabibullin**, **Yu. G. Kudenko**, **Y. Kuno**[2),7)], **L. S. Lee**[10)], **G. Y. Lim**[2),10)], **J. A. Macdonald**[11)], **D. R. Marlow**[12)], **C. R. Mindas**[12)], **O. V. Mineev**, **C. Rangacharyulu**[3)], **S. Shimizu**[7)], **Y.-M. Shin**[3)], **A. Suzuki**[1)], **A. Watanabe**[1)], **N. V. Yershov**, and **T. Yokoi**[2)]
The E246 KEK–PS Collaboration

Institute for Nuclear Research, Russian Academy of Sciences, pr. Shestidesyatiletiya Oktyabrya 7a, Moscow, 117312 Russia

Received April 17, 2002

Abstract—The form factors of the decay $K^+ \to \pi^0 e^+ \nu_e$ (K_{e3}) have been determined from the comparison of the experimental and Monte Carlo Dalitz distributions containing about 10^5 K_{e3} events. The following values of the parameters were obtained: $\lambda_+ = 0.0278 \pm 0.0017\,(\text{stat.}) \pm 0.0015\,(\text{syst.})$, $|f_S/f_+(0)| = 0.0040 \pm 0.0160\,(\text{stat.}) \pm 0.0067\,(\text{syst.})$, and $|f_T/f_+(0)| = 0.019 \pm 0.080\,(\text{stat.}) \pm 0.038\,(\text{syst.})$. Both scalar f_S and tensor f_T form factors are consistent with the Standard Model predictions of zero values.

1. INTRODUCTION

The most general Lorentz-invariant form of the matrix element of K_{e3} decay can be written as [1, 2]

$$M \propto f_+(q^2)(P_K + P_\pi)^\lambda \bar{u}_e \gamma_\lambda (1-\gamma_5) u_\nu \quad (1)$$
$$+ f_-(q^2) m_e \bar{u}_e (1-\gamma_5) u_\nu + 2 m_K f_S \bar{u}_e (1-\gamma_5) u_\nu$$
$$+ (2 f_T / m_K)(P_K)^\lambda (P_\pi)^\mu \bar{u}_e \sigma_{\lambda\mu} (1-\gamma_5) u_\nu,$$

where $f_\pm(q^2)$, f_S, and f_T are the vector, scalar, and tensor form factors, and P_K and P_π are 4-momenta of the K^+ and π^0. The vector form factors $f_\pm(q^2)$ are assumed to be linearly dependent on the momentum transfer squared $q^2 = (P_K - P_\pi)^2$, and they can be represented by the equation $f_\pm(q^2) = f_\pm(0)(1 \pm \lambda_\pm(q^2/m_{\pi^0}^2))$. Because of the small mass of the positron, the part of the matrix element that depends on $f_-(q^2)$ is negligible and there are just three free parameters of the theory: λ_+, f_S, and f_T. Within the Standard Model (SM), due to W-boson exchange, no terms other than those of a pure vector nature are expected. A possible contribution to f_S and f_T from electroweak radiative corrections is negligibly small, and, therefore, nonzero values of f_S and f_T would signal new physics beyond the SM. Actually, such deviations from zero for these form factors were measured in [1, 3], but were not confirmed in a recent experiment [4], where f_S and f_T were measured with sensitivity similar to [1, 3].

In this paper, we present the results of the reanalysis of the K_{e3} data taken with the E246 detector at the KEK 12-GeV proton synchrotron. The first result obtained using this data set was published in [4].

2. EXPERIMENT

The experiment was performed with the setup constructed to search for T violation in $K^+ \to \pi^0 \mu^+ \nu_\mu$ decay. The experimental arrangement is

*This article was submitted by the authors in English.

[1)]University of Tsukuba, Japan.
[2)]KEK, Japan.
[3)]University of Saskatchewan, Canada.
[4)]Virginia Polytechnic Institute and State University, Blacksburg, VA 24061, USA.
[5)]University of Montreal, Canada.
[6)]University of British Columbia, Vancouver, Canada.
[7)]Osaka University, Japan.
[8)]National Taiwan University, Taipei, Taiwan.
[9)]Institute of Physical and Chemical Research, Hirosawa, Japan.
[10)]Korea University, Seoul, Korea.
[11)]TRIUMF, Canada.
[12)]Princeton University, Princeton, NJ 08540, USA.
[**]e-mail: levch_a@wocup.inr.troitsk.ru

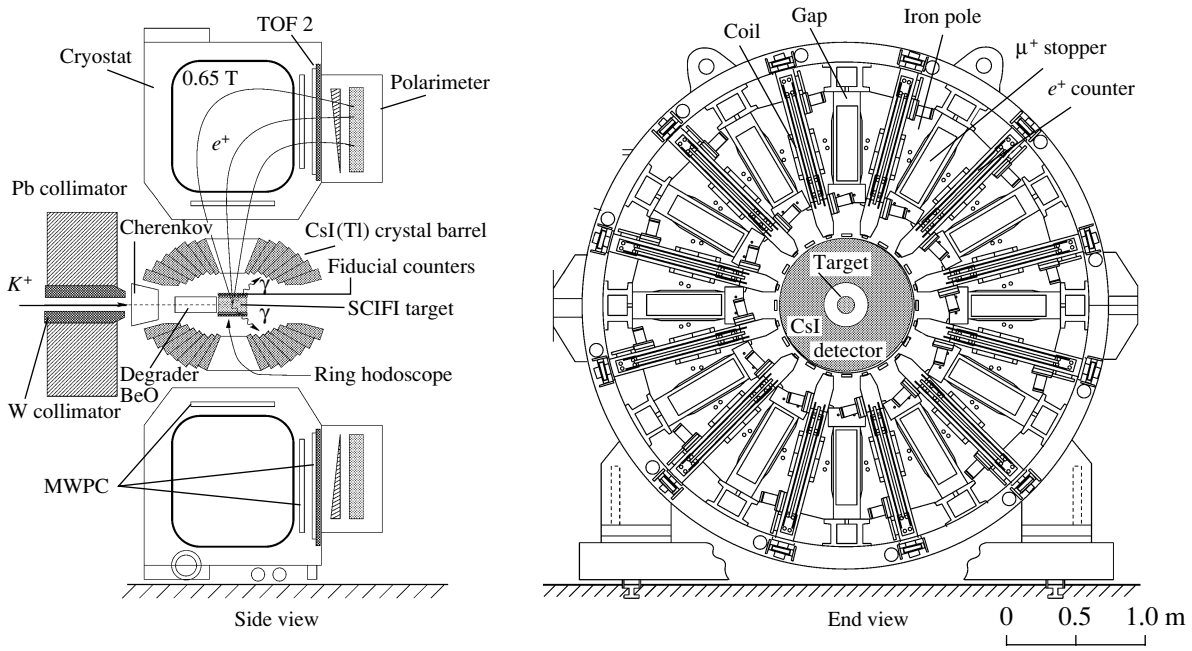

Fig. 1. The layout of the E246 setup.

shown in Fig. 1 and is described in detail elsewhere [5–8]. Kaons with $P_{K^+} = 660$ MeV/c are identified by a Cerenkov counter, slowed in a BeO degrader and then stopped in a target array of 256 scintillating fibers located at the center of a 12-sector superconducting toroidal spectrometer. Charged particles from kaon decays in the target were tracked by means of multiwire proportional chambers at the entrance and exit of each magnet sector, along with the target and a scintillation ring hodoscope around the target. The momentum resolution of $\sigma_P = 2.6$ MeV/c at $P = 205$ MeV/c was obtained using monoenergetic products from the two-body decay $K^+ \to \pi^+\pi^0$.

The energies and angles of the photons from π^0 decays are measured by a CsI(Tl) photon detector consisting of 768 modules [6]. The photon detector covers a solid angle of 3π sr, with openings for the beam entry and exit and 12 holes for charged particles to pass into the magnet gaps. The photon energy was obtained by summing the cluster energy distributed among several crystals surrounding the central crystal. The position of the photon cluster is determined using the energy-weighted "center-of-gravity" method. To suppress accidental background from the beam, timing information from each crystal was used. A time resolution of 3.8 ns (σ) for the wide photon energy range of 10–220 MeV was achieved. The energy resolution was found to be $\sigma_{E_\gamma}/E_\gamma \simeq 3.0\%$ at $E_\gamma = 150$ MeV. The invariant mass resolution of $\sigma_{\gamma\gamma} = 7.5$ MeV/c^2 at $M_{\gamma\gamma} = 133.1$ MeV/c^2 and angular resolution of $\sigma_\theta = 2.4°$ were obtained in the experiment [6, 9].

The study of the K_{e3} decay required a trigger condition different from that of the main experiment. The following trigger was used to accumulate K_{e3} events:

$$C_K \times \mathrm{Fid}_i \times \mathrm{TOF2}_i \times 2\gamma \times \mathrm{GapVeto}. \qquad (2)$$

The Cherenkov condition C_K ensures that the beam particle is a K^+. The coincidence between C_K, delayed by 2 ns, and the fiducial counters (Fid_i) for the charged particles eliminates the triggers due to decays in flight. The time-of-flight signal from the corresponding gap ($\mathrm{TOF2}_i$) completes the charged particle trigger condition. The trigger also required two hits in the CsI (2γ). The requirement GapVeto eliminates events where the charged particle may have lost energy in the CsI crystals around the ith hole. The K_{e3} data were collected for two spectrometer field settings, $B = 0.65$ and 0.9 T.

3. ANALYSIS

K_{e3} events were selected using the following requirements. A clean hit pattern in the target and a delayed decay at least 2 ns after the K^+ arrival time measured by the Cherenkov counter suppressed the K^+ decays in flight. Cuts on the charged-particle momentum, $P < 190$ MeV/c, and the opening angle between π^0 and e^+, $\theta_{\pi^0 e^+} < 170°$, effectively removed the $K_{\pi 2}$ events. π^+ decays in flight were rejected by a cut on the track reconstruction $\chi^2 < 14$. The

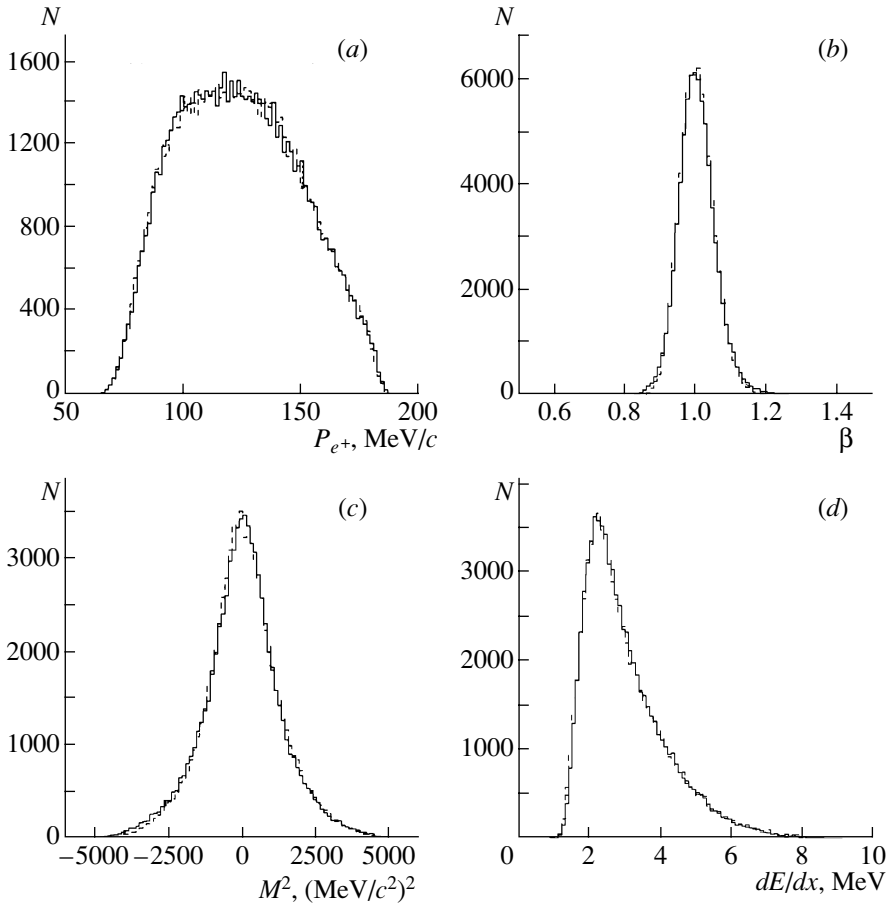

Fig. 2. (*a*) Momentum spectrum of e^+ from the K_{e3} decay; (*b*) β spectra of e^+ ($\beta = L/(\tau c)$); (*c*) reconstructed TOF mass squared of e^+; (*d*) energy deposit of e^+ in the TOF2 counter. The solid line corresponds to experimental and the dashed line to GEANT-simulated events.

photon conversion events were suppressed by requiring single hits in the ring and fiducial counters and a single track in the target. Events with more than two hits in the electromagnetic calorimeter were rejected. The cut on the invariant mass was $75 < M_{\gamma\gamma} < 140$ MeV/c^2. The main criterion separating K_{e3} positrons from $K_{\mu 3}$ muons was derived from the time-of-flight (TOF) measurement between the fiducial counters and scintillating counters (TOF2) located at the exit of each spectrometer gap (Fig. 1). The mass squared of the charged particle was determined as

$$M^2 = P^2\left[\left(\frac{L}{\tau c}\right)^2 - 1\right], \qquad (3)$$

where L and τ are the length and time of flight of the charged particle between fiducial and TOF2 counters, and c is the speed of light in vacuum. The TOF resolution is $\sigma_{\mathrm{TOF}} = 300$ ps, and the mass squared spectrum is shown in Fig. 2. To separate positrons from muons, a cut on the mass squared $-4500 < M^2_{\mathrm{TOF}} < 4500\,(\mathrm{MeV}/c^2)^2$ was chosen.

Compared to the analysis of [4], improvements in reconstruction of the charged-particle track were made. In the new analysis, information about the kaon stopping position from the target (x, y) and ring counter (z) was included in the momentum reconstruction routine. The reconstruction of the π^0 kinematics was also improved by using tighter time windows in CsI and improved calibration. The Monte Carlo routines properly included the correct kaon stopping distribution in the target and the electromagnetic shower leakage effects in CsI. This allowed us to use all CsI crystals for reconstruction of the π^0, while in [4] events where either photon hit a crystal adjacent to the 12 charged-particle holes were rejected. Overall optimization resulted in approximately a factor of 4 increase in acceptance. For a 0.65-T magnetic field we extracted 102K good K_{e3} events with background contamination of 0.21% from $K_{\mu 3}$ and 0.34% from $K_{\pi 2}$ decays. The distributions of the

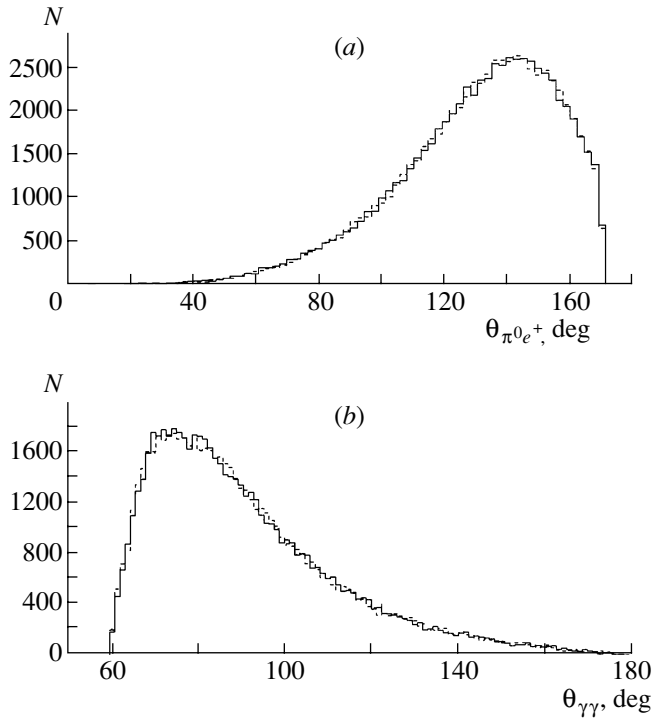

Fig. 3. K_{e3} decays: (a) angle between e^+ and π^0; (b) angle between photons $\theta_{\gamma\gamma}$. The solid line is the experiment, and the dashed line is the Monte Carlo simulation.

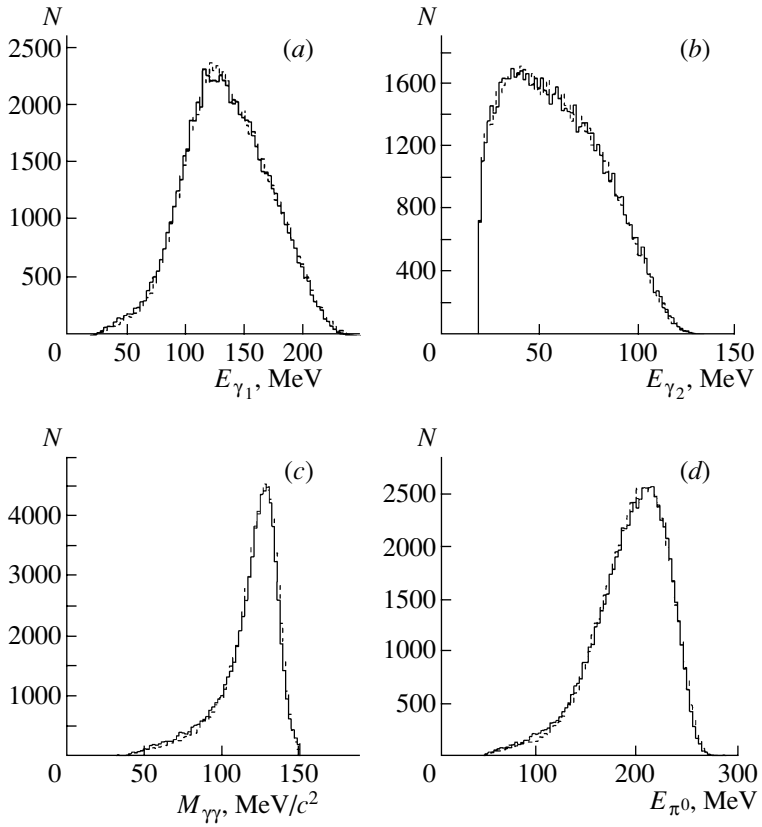

Fig. 4. K_{e3} decays: (a) energy of γ_1 ($E_{\gamma_1} > E_{\gamma_2}$); ($b$) energy of γ_2; (c) invariant mass $M_{\gamma\gamma}$; (d) energy of π^0 ($E_{\pi^0} = E_{\gamma_1} + E_{\gamma_2}$). The solid line is the experiment, and the dashed line is the Monte Carlo simulation.

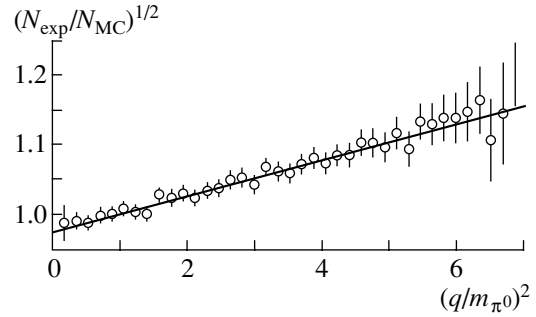

Fig. 5. The q^2 dependence of the ratio N_{exp}/N_{MC}. The straight line shows a linear fit with $\lambda_+ = 0.0278$.

π^0–e^+ opening angle and the opening angle between photons from $\pi^0 \to \gamma\gamma$ for K_{e3} decay is shown in Fig. 3. Energy spectra of the K_{e3} decay are shown in Fig. 4.

The extraction method for the parameters is based on comparison of the experimental and Monte Carlo Dalitz distributions. If one allows for existence of exotic interactions, the Dalitz plot density is given by [10]

$$\rho(E_e, E_\pi) = f_+^2(q^2)(A + B\xi(q^2) + C\xi^2(q^2)), \quad (4)$$

where

$$A = m_K(2E_eE_\nu - m_KE_\pi^{'}) + m_e^2(E_\pi^{'}/4 - E_\nu),$$
$$B = m_e^2(E_\nu - E_\pi^{'}/2), \quad C = m_e^2E_\pi^{'}/4,$$
$$E_\pi^{'} = (m_K^2 + m_\pi^2 - m_e^2)/(2m_K) - E_\pi,$$
$$\xi(q^2) = \frac{(2m_K/m_e)R_S + (m_e/m_K + 2(E_\nu - E_e)/m_e)R_T}{1 + (m_e/m_K)R_T},$$

Systematic errors

Source	λ_+	f_S	f_T
MWPC misalignment	0.0006	0.0010	0.0022
MWPC spatial resolution	0.0002	0.0010	0.0010
e^+ identification	0.0007	0.0022	0.0004
Bremsstrahlung	0.0010	0.0015	0.0280
χ^2 cut point	0.0001	0.0010	0.0018
CsI barrel misalignment	0.0005	0.0042	0.0240
E_γ and $M_{\gamma\gamma}$ cut point	0.0003	0.0020	0.0027
$\gamma \to e^+e^-$ conversion	0.0001	0.0018	0.0100
Pileup in CsI	0.0004	0.0013	0.0015
Total	0.0015	0.0067	0.0380

$$R_S = \frac{f_S}{f_+}, \quad R_T = \frac{f_T}{f_+}.$$

The parameters of the decay can be extracted by selecting the minimum of the χ^2 variable defined as

$$\chi^2 = 2\sum_{i=1}^{n}\left((N_i^{MC} - N_i^{exp}) + N_i^{exp}\log\frac{N_i^{exp}}{N_i^{MC}}\right), \quad (5)$$

where n is the number of bins over the Dalitz plot, N_i^{MC} is the number of Monte Carlo events in each bin, and N_i^{exp} is the number of experimental events in each bin.

Within the Standard Model, the only parameter to be obtained is λ_+. It can be extracted in a model-independent way from the q^2 dependence of f_+. Using (4), we have $\sqrt{\rho(E_e, E_\pi)} \propto f_+ = f_+(0)(1 + \lambda_+q^2/m_{\pi^0}^2)$, and, therefore, λ_+ can be extracted from the ratio

$$(N_{exp}/N_{MC}(\lambda_+ = 0))^{1/2} = 1 + \lambda_+q^2/m_{\pi^0}^2. \quad (6)$$

The q^2 dependence of this ratio shown in Fig. 5 allows us to determine the value $\lambda_+ = 0.0278 \pm 0.0016$ (stat.).

For extraction of all three parameters λ_+, f_S, and f_T, the Dalitz distribution fit was performed using the P_{e^+}, $\theta_{\pi^0e^+}$ variables. The angle between the pion and the positron, $\theta_{\pi^0e^+}$, was preferred instead of the pion energy E_{π^0} in order to reduce the systematic error related to the energy leakage in the electromagnetic calorimeter. The chosen bin sizes were $\Delta P_{e^+} = 3.125$ MeV/c and $\Delta\theta_{\pi^0e^+} = 4.2°$. Radiative corrections to the Dalitz plot were taken into account according to Ginsberg [11]. The χ^2 between the experimental and Monte Carlo Dalitz distributions was minimized by a program based on MINUIT [12]. The values obtained for λ_+ and the scalar and tensor form factors are

$$\lambda_+ = 0.0278 \pm 0.0017 \text{ (stat.)}, \quad (7)$$
$$|f_S/f_+(0)| = 0.004 \pm 0.016 \text{ (stat.)},$$
$$|f_T/f_+(0)| = 0.019 \pm 0.080 \text{ (stat.)}.$$

Since our analysis relies on the proper detector responses used by the Monte Carlo simulation, comparisons and checks were made wherever possible. For example, to check the values obtained and to see possible unknown systematic effects, a similar analysis of the scatter plot $\theta_{\gamma\gamma}$ vs. P_{e^+} was also performed. From this approach, it was found that $\lambda_+ = 0.0281 \pm 0.0017$ (stat.), $|f_S/f_+(0)| = 0.001 \pm 0.018$ (stat.), and $|f_T/f_+(0)| = 0.007 \pm 0.100$ (stat.). No significant variations of the λ_+ value were seen, and values of the form factors were consistent with

zero within a 1σ uncertainty. The main sources of systematic errors were related to detector inefficiencies, misalignments of the detector elements, background contamination, and uncertainties connected to the Monte Carlo simulation. All these sources were studied, and the estimations of the systematic errors are presented in the table.

4. RESULT

The result presented here is based on about 10^5 good K_{e3} events. We have obtained

$$\lambda_+ = 0.0278 \pm 0.0017\,(\text{stat.}) \pm 0.0015\,(\text{syst.}), \quad (8)$$
$$|f_S/f_+(0)| = 0.0040$$
$$\pm 0.0160\,(\text{stat.}) \pm 0.0067\,(\text{syst.}),$$
$$|f_T/f_+(0)| = 0.019 \pm 0.080\,(\text{stat.}) \pm 0.038\,(\text{syst.}).$$

Using only one data set at $B = 0.65$ T, we have improved statistical errors by a factor of 1.5 and systematic errors for λ_+, f_S, and f_T were reduced by the factors 2.0, 2.1, and 2.4, respectively, compared to our previous result [4]. This result is in agreement with the Standard Model prediction, and there is no evidence for a deviation from zero for the values of the scalar and tensor form factors. We expect to further improve our accuracy after completing the analysis of the K_{e3} data accumulated at $B = 0.9$ T.

REFERENCES

1. H. J. Steiner *et al.*, Phys. Lett. B **36B**, 521 (1971).
2. Particle Data Group (D. E. Groom *et al.*), Eur. Phys. J. C **15**, 1 (2000).
3. S. A. Akimenko *et al.*, Phys. Lett. B **259**, 225 (1991).
4. S. Shimizu *et al.*, Phys. Lett. B **495**, 33 (2000).
5. M. Abe *et al.*, Phys. Rev. Lett. **83**, 4253 (1999).
6. D. V. Dementyev *et al.*, Nucl. Instrum. Methods Phys. Res. A **440**, 151 (2000).
7. A. P. Ivashkin *et al.*, Nucl. Instrum. Methods Phys. Res. A **394**, 321 (1997).
8. M. P. Grigor'ev *et al.*, Instrum. Exp. Tech. **41**, 803 (1998).
9. M. M. Khabibullin *et al.*, Instrum. Exp. Tech. **43**, 589 (2000).
10. H. Braun *et al.*, Nucl. Phys. B **89**, 210 (1975).
11. E. S. Ginsberg, Phys. Rev. **162**, 1570 (1967).
12. F. James, *MINUIT Reference Manual* (CERN, Geneva, 1994).

Physics of Atomic Nuclei, Vol. 65, No. 12, 2002, pp. 2238–2242. From Yadernaya Fizika, Vol. 65, No. 12, 2002, pp. 2300–2304.

TEST OF NEW PHYSICS IN RARE PROCESSES AND COSMIC RAYS

New Measurement of the $\eta \to \pi^0\gamma\gamma$ Branching Ratio and the Slope Parameter for $\eta \to 3\pi^0$ Decay with the Crystal Ball*

S. Prakhov**
(for the Crystal Ball Collaboration)[1)]
University of California, Los Angeles, CA 90024, USA
Received February 13, 2002

Abstract—We have measured the quadratic slope parameter α for $\eta \to 3\pi^0$ decay. Our final result is $\alpha = -0.031(4)$. We have also obtained the branching ratio (BR) for the double radiative decay $\eta \to \pi^0\gamma\gamma$. Our preliminary result is $\mathrm{BR}(\eta \to \pi^0\gamma\gamma) = 3.2(9) \times 10^{-4}$. These new measurements were performed using the recent (1998) high-statistics sample of 1.9×10^7 η produced at the AGS at BNL in $\pi^- p \to n\eta$ close to threshold. The η decay into neutrals was detected with the Crystal Ball multiphoton spectrometer. Both measurements provide important tests of chiral perturbation theory (χPTh). Our result for α is four times more precise than the present world data and disagrees with current χPTh calculations by about four standard deviations. Our branching ratio for $\eta \to \pi^0\gamma\gamma$ is about half the current value and is in agreement with the χPTh predictions. © *2002 MAIK "Nauka/Interperiodica".*

The decay $\eta \to 3\pi$ violates G parity and, except for a small electromagnetic contribution, occurs because of the u–d quark mass difference. Any low-energy theory must predict both the rate and the spectrum of the pions correctly. This decay provides an important testing ground for χPTh, a practical, low-energy effective theory for QCD based on the chiral symmetry of the massless QCD Lagrangian that is broken when the quark masses are included. In the χPTh momentum expansion, the leading $\mathcal{O}(p^2)$ term of the decay amplitude explicitly exhibits $A(\eta \to 3\pi) \sim m_d - m_u$. However, this term yields a decay width $\Gamma^{(0)}_{\mathrm{th}}(\eta \to \pi^+\pi^-\pi^0) = 66(8)$ eV that is smaller than the measured value of $\Gamma_{\mathrm{exp}}(\eta \to \pi^+\pi^-\pi^0) = 281(28)$ eV by a factor of 4; when the second-order $\mathcal{O}(p^4)$ counterterms are included, the predicted rate increases to 167(50) eV [1]. Dispersive methods, which include pion rescattering to all orders, raise the predicted rate to 209(56) eV [2]. This improves the agreement, but the χPTh prediction is still somewhat below the experimental value. Besides the decay rate, one must also consider the pion spectrum in the final state. Since the Q value is small, the $\eta \to 3\pi^0$ decay amplitude and width may be parameterized as $A(\eta \to 3\pi^0) \sim (m_d - m_u)(1 + \alpha z)$ and $\Gamma(\eta \to 3\pi^0) \sim (m_d - m_u)^2(1 + 2\alpha z)$. The variable z is defined as $z = 6\sum_{i=1}^{3}(E_i - m_\eta/3)^2/(m_\eta - 3m_{\pi^0})^2 = \rho^2/\rho^2_{\max}$, where E_i is the energy of the ith pion in the η rest frame and ρ is the distance from the center of the Dalitz plot. The variable z varies from 0, when all three π^0 have the same energy of $m_\eta/3$, to 1, when one π^0 is at rest. The quadratic energy dependence indicated by the α term arises at $\mathcal{O}(p^6)$; it is, strictly speaking, outside the one loop $\mathcal{O}(p^4)$ calculation of [1]. However, a nonzero value is expected in a dispersive calculation where rescattering effects are treated to all orders. The predicted values for α in [2] are in the range $-(0.014–0.007)$ depending on the value of a parameter in their calculation.

There are two main previous experimental determinations of α: $\alpha = -0.022(23)$ based on 50K events [3] and $\alpha = -0.052(20)$ [4] from a sample of 9.8×10^4

*This article was submitted by the author in English.

**e-mail: prakhov@bmkn5.physics.ucla.edu

[1)]The Crystal Ball Collaboration: E. Berger, M. Clajus, A. Marušić, S. McDonald, B.M.K. Nefkens, N. Phaisangittisakul, S. Prakhov, J.W. Price, M. Pulver, A. Starostin, W.B. Tippens (*University of California Los Angeles*); D. Isenhower, M. Sadler (*Abilene Christian University*); C. Allgower, H. Spinka (*Argonne National Laboratory*); J. Comfort, K. Craig, T. Ramirez (*Arizona State University*); T. Kycia (*Brookhaven National Laboratory*); J. Peterson (*University of Colorado*); W. Briscoe, A. Shafi (*The George Washington University*); H.M. Staudenmaier (*Universität Karlsruhe*); D.M. Manley, J. Olmsted (*Kent State University*); D. Peaslee (*University of Maryland*); V. Bekrenev, A. Koulbardis, N. Kozlenko, S. Kruglov, I. Lopatin (*Petersburg Nuclear Physics Institute*); G.M. Huber, N. Knecht, G.J. Lolos, Z. Papandreou (*University of Regina*); I. Slaus, I. Supek (*Rudjer Bošković Institute*); D.Grosnick, D. Koetke, R. Manweiler, S. Stanislaus (*Valparaiso University*).

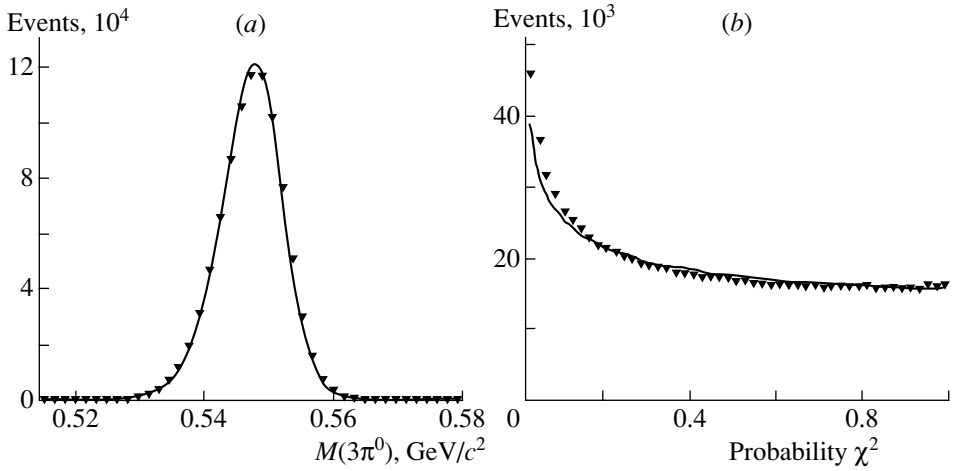

Fig. 1. Comparison of the data (▼) and MC distribution (curves): (*a*) the reconstructed $3\pi^0$ invariant mass, (*b*) the χ^2 probability.

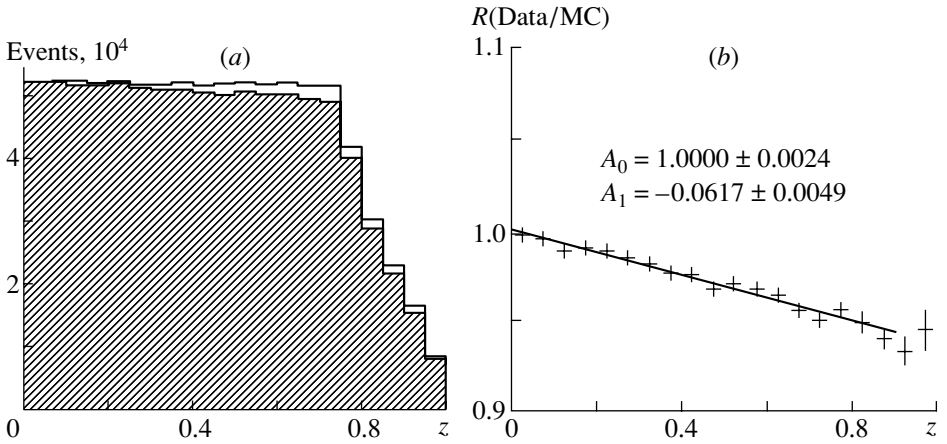

Fig. 2. (*a*) Comparison of the $\eta \to 3\pi^0$ z distributions obtained from the data (shaded histogram) and MC (upper histogram). (*b*) Linear fit to the ratio $R = A_0 + A_1 z$ for $z < 0.9$; $\alpha = A_1/2$.

$\bar{p}p \to \eta\pi^0\pi^0 \to 5\pi^0$ events. The resulting world average is $-0.039(15)$ [5], but the nearly 40% uncertainty does not provide a strong constraint on theoretical calculations.

We have made a new high-statistics measurement of α based on 1.9×10^7 η mesons produced in a two week run in 1998 with the Crystal Ball (CB) multiphoton spectrometer installed in the C6 beam line of the Alternating Gradient Synchrotron (AGS) at Brookhaven National Laboratory (BNL). The CB consists of 672 optically isolated NaI crystals arranged in two hemispheres that cover 93% of 4π sr [6]. A momentum-analyzed 720-MeV/c pion beam incident on a 10-cm-long liquid hydrogen (LH_2) target produced the η mesons near the threshold of the reaction $\pi^- p \to n\eta$. The process $\pi^- p \to n\eta \to n3\pi^0 \to n6\gamma$ was identified by analyzing the neutral, six-cluster events detected in the CB. A "cluster" is a group of neighboring crystals in which energy is deposited from a one-photon electromagnetic (em) shower. The neutral clusters required a 17.5-MeV threshold in software; they were analyzed as photons. In principle, the neutron could produce an additional, seventh, cluster in the CB, but near the threshold of $\pi^- p \to n\eta$, about 99% of these neutrons passed undetected through the downstream aperture of the CB detector. Finally, the six-cluster only events were subjected to a kinematic fit testing the $\pi^- p \to n\eta \to n3\pi^0 \to n6\gamma$ hypothesis. All fifteen possible pairings of six photons to form three π^0 mesons were considered; the best pairing combination was chosen as the one with the lowest χ^2 value. Events were required to satisfy the kinematic hypothesis with a probability greater than 2%, i.e., a 2% confidence level (C.L.). A sample of 1.6×10^7 $\pi^- p \to n\eta \to n3\pi^0 \to n6\gamma$ events was generated for the Monte Carlo (MC)

Theoretical calculations for the $\eta \to \pi^0\gamma\gamma$ decay rate (ENJL—Extended Nambu–Jona-Lasinio model; VMD—vector meson dominance model)

Theory	$\Gamma(\eta \to \pi^0\gamma\gamma)$, eV	Reference
χPTh, $\mathcal{O}(p^2)$	0	L. Amettler *et al.*, Phys. Lett. B **276**, 185 (1992)
χPTh, $\cdots + \mathcal{O}(p^4)$	0.004	L. Amettler *et al.*, Phys. Lett. B **276**, 185 (1992)
χPTh, $\cdots + \mathcal{O}(p^6)$	0.42 ± 0.20	L. Amettler *et al.*, Phys. Lett. B **276**, 185 (1992)
χPTh, $\cdots + \mathcal{O}(p^6)$	0.47	P. Ko, Phys. Lett. B **349**, 555 (1995)
χPTh, ENJL, $\cdots + \mathcal{O}(p^6)$	0.58 ± 0.30	S. Bellucci and C. Bruno, Nucl. Phys. B **452**, 626 (1995)
χPTh, ENJL, $\cdots + \mathcal{O}(p^6)$	$0.27^{+0.18}_{-0.07}$	J. Bijnens *et al.*, Phys. Lett. B **379**, 209 (1996)
VMD	0.30 ± 0.15	J. N. Ng and D. J. Peters, Phys. Rev. D **46**, 5034 (1992)
Q box	0.70	J. N. Ng and D. J. Peters, Phys. Rev. D **47**, 4939 (1993)
VMD	0.4	W. Alles *et al.*, Nuovo Cimento A **45**, 272 (1966)

determination of the CB acceptance and analysis efficiency based on a full GEANT (version 3.21) simulation of the detector. For the simulation, α was set to zero. Much attention was given to reproducing the experimental efficiencies, resolutions, and the production features of the $\pi^- p \to n\eta$ reaction [7].

A sample of 0.95×10^6 experimental events survived the analysis. The combined effect of the finite geometrical acceptance, photon conversions in the target and vetoing system, the hardware trigger conditions, photon-cluster reconstruction efficiency, and the kinematic-hypothesis test yields a final acceptance of 17.5%. The level of background contamination of the selected events was estimated to be much less than 1%. The $3\pi^0$ invariant mass distribution (formed by omitting the η mass constraint in the hypothesis) has a centroid of 547.3 MeV with $\sigma_m = 5$ MeV, and the MC distribution agrees with these values within 0.2 MeV for both the centroid and the width (Fig. 1*a*).

Figure 1*b* demonstrates the agreement between the data and MC for the probability distributions of the kinematic fit for our hypothesis. Figure 2*a* compares the distributions of the variable z obtained from our data and MC ($\alpha = 0$). The bin width (0.05) was chosen to be $\approx 1.4\sigma_z$. The MC z distribution is normalized to obtain a ratio of unity at $z = 0$. The shape of the MC distribution shows that our acceptance for the $\eta \to 3\pi^0$ Dalitz plot is nearly flat. Note that, near the edge $z = 1$, the density distributions have poorer statistics and are more sensitive to effects of finite resolution since they correspond to the edges of the Dalitz distribution. Thus, the fits to the data to determine α were made for the full z distribution and also for $z \leq 0.9$.

In order to estimate the systematic error for α, we have investigated in detail a number of different parameters of the analysis [7]. We have studied the effect of varying the minimum confidence level used for event selection, the effect of the combinatoric background, the effect of the software changing the CB acceptance, cluster reconstruction parameters, bin size for z distribution, and many others. In Fig. 2*b*, we show a straight-line fit ($z < 0.9$) to the ratio of the data and normalized MC z distributions for events selected at the 5% C.L. The value $\chi^2/\mathrm{ndf} = 5.2/16$ indicates good agreement with the linear-fit hypothesis. The goodness of fit precludes fitting to higher order terms. The investigation of our systematic uncertainties did not reveal any significant change in the α values depending on variations in the parameters. Their fluctuations were consistent with the allowed statistical variation of α due to changing the sample size. Since these variations represent the combined effect of both statistical and systematic uncertainties, we took as our combined systematic and statistical error the largest variation in α. Our final result is $\alpha = -0.031(4)$ [8]. This value for α is within errors in agreement with previous measurements. However, the error in our measurement is several times smaller. Compared to the present χPTh dispersive calculations, our result for α agrees with them in sign but is too large in magnitude. A possible conclusion of our result is that there are dynamical effects which are contributing to the $\eta \to 3\pi^0$ decay. One example of a dynamical term is an $\mathcal{O}(p^6)$ contribution such as the effective chiral Lagrangian $\mathcal{L}^6 \sim F_\pi^2 \mathrm{tr}((\chi U^\dagger + U\chi^\dagger) D^\mu U D_\mu U^\dagger D^\nu U D_\nu U^\dagger)$. The coefficients of such terms are not constrained by the strictures of chiral invariance and are experimentally undetermined at present. Clearly, an improved measurement of the charged decay $\eta \to \pi^+\pi^-\pi^0$, together with our result,

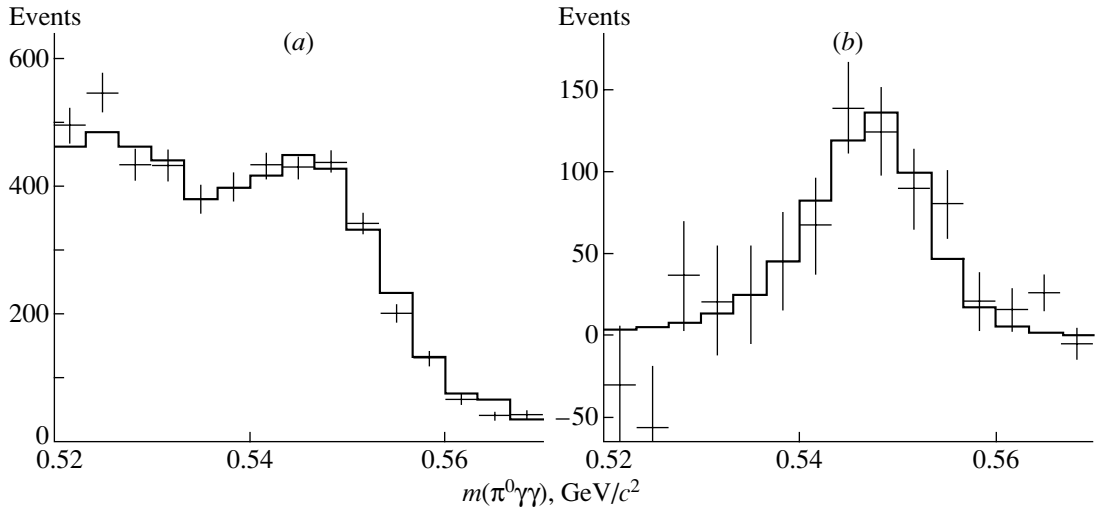

Fig. 3. The $m(\pi^0\gamma\gamma)$ distributions for events selected with the 20% C.L. and $|Z_{\rm vrtx}| < 5$ cm: (a) the fit of the MC (crosses) to the data (histogram); (b) MC of $\pi^- p \to n\eta \to n\pi^0\gamma\gamma$ normalized according to the fit result (histogram), and the experimental distribution after the background subtraction (crosses).

would provide tighter constraints on the χPTh calculations.

The double radiative decay $\eta \to \pi^0\gamma\gamma$ has drawn much attention over the years. Its decay rate is suppressed due to chiral symmetry. In the χPTh momentum expansion, since the leading $\mathcal{O}(p^2)$ term is absent and $\mathcal{O}(p^4)$ is very small because there is no direct photon coupling to π^0 and η, the main contribution comes from $\mathcal{O}(p^6)$. Therefore, the experimental value for $\mathrm{BR}(\eta \to \pi^0\gamma\gamma)$ provides a unique test of the third-order term of the χPTh expansion of the decay amplitude. The results of the existing theoretical estimates for $\Gamma(\eta \to \pi^0\gamma\gamma)$ are summarized in the table.

As every model predicts its own matrix element for the decay amplitude, the experimental measurement of the $\eta \to \pi^0\gamma\gamma$ Dalitz plot also provides an important test of the χPTh calculations. However, the experimental situation for measuring $\eta \to \pi^0\gamma\gamma$ decay is rather poor. There is only one extensive measurement of $\mathrm{BR}(\eta \to \pi^0\gamma\gamma)$ so far: the GAMS-2000 group [3] quotes $\mathrm{BR}(\eta \to \pi^0\gamma\gamma) = (7.1 \pm 1.7) \times 10^{-4}$ (or $\Gamma(\eta \to \pi^0\gamma\gamma) = 8.4 \pm 1.9$ eV) based on a signal of ~ 40 events. This result is greater than every prediction based on χPTh. No experimental decay distributions have been presented for η. Certainly, a new measurement of the $\eta \to \pi^0\gamma\gamma$ decay is needed.

To search for the $\eta \to \pi^0\gamma\gamma$ decays, the same CB data set with 1.9×10^7 η mesons has been analyzed. In this article, we give a brief description of the analysis and our preliminary result for $\mathrm{BR}(\eta \to \pi^0\gamma\gamma)$; more details may be found in [9]. Events with four clusters detected in the CB were considered in order to identify the process $\pi^- p \to n\eta \to n\pi^0\gamma\gamma \to n4\gamma$. The selection criteria were optimized for suppressing background processes to the level where the number of expected events from $\eta \to \pi^0\gamma\gamma$ would be comparable to the number of background events in the η-mass region. The first source of the background is the same reaction $\pi^- p \to n\eta$ but with η decaying into $3\pi^0$, $\mathrm{BR}(\eta \to 3\pi^0) = 0.322$. This background contributes to the four-cluster events because of photons escaping the CB, or because of strongly overlapping em showers. The case of overlapping showers results in a "fake" peak at the η-mass region. The investigation of the $\eta \to 3\pi^0$ background was made with 1.6×10^7 $\pi^- p \to n\eta \to n3\pi^0$ events simulated for measuring the parameter α. The second source of background is the process $\pi^- p \to n\pi^0\pi^0$, which at our beam momenta has a cross section of $\sim$1.8 mb; that is comparable to the $\sim$2 mb for $n\eta$. The $\pi^0\pi^0$ background does not produce a peak at the η-mass region, but for proper simulation of this process, one has to reproduce its complicated dynamics. Finally, 2×10^7 $\pi^- p \to n\pi^0\pi^0$ events were simulated according to the $\pi^0\pi^0 n$ Dalitz plot measured with the CB [10]. For the process $\pi^- p \to n\eta \to n\pi^0\gamma\gamma$, we simulated 2×10^5 events where η mesons decay in accordance with phase space.

To suppress the $\pi^0\pi^0$ background, we discarded from the analysis all events where at least one combination of the four clusters satisfied the $\pi^- p \to n\pi^0\pi^0 \to n4\gamma$ kinematic-fit hypothesis with probability $>0.01\%$. Next, we selected only events that satisfied the $\pi^- p \to n\pi^0\gamma\gamma \to n4\gamma$ hypothesis at the 10% C.L. A study of the MC events for background

reactions showed that their Z vertices reconstructed as part of the kinematic fit were distributed very differently from the spectrum expected for the signal. So we applied a selection cut on the Z vertex to increase the signal/background ratio. A further suppression of the $\eta \to 3\pi^0$ background from strongly overlapping photon showers was achieved by applying a cut on the so-called effective radius of a cluster. It was observed that, for the clusters produced due to overlapping showers, the effective radius was systematically larger compared to the normal one-photon clusters. As a result of applying all the above selection criteria, we suppressed the $\eta \to 3\pi^0$ background in the η-mass region to a level that is similar to the one expected from $\eta \to \pi^0\gamma\gamma$ decays, if $\mathrm{BR}(\eta \to \pi^0\gamma\gamma) = 0.00071$. At the same time the detection efficiency for $\eta \to \pi^0\gamma\gamma$ events turned out to be about 16.5%.

The $\eta \to \pi^0\gamma\gamma$ events can be separated from the background contributions even better if we consider a two-dimensional distribution like $m(\pi^0\gamma\gamma)$ vs. $m_{\max}(\pi^0\gamma)$ where all invariant masses are calculated from the results of the kinematic fit to the hypothesis $\pi^- p \to n\pi^0\gamma\gamma \to n4\gamma$. The three plots for the MC events, one for the $\eta \to \pi^0\gamma\gamma$ events and two for background processes, were found to have their own characteristic features. In order to fit our plots with a binned maximum likelihood technique, we used the HMCMLL routine (HBOOK program library) modified to work with two-dimensional histograms. To investigate our systematic uncertainties in the determination of the $\eta \to \pi^0\gamma\gamma$ fraction, we performed a number of fits where we varied the limits of the plots and the criteria for event selection: the kinematic fit confidence level, Z vertex, effective radius of cluster, and others. As an example, we show in Fig. 3 the fit results for the $m(\pi^0\gamma\gamma)$ distribution obtained as a projection of the experimental and MC plots corresponding to events selected with the 20% C.L. and $|Z_{\mathrm{vrtx}}| < 5$ cm. Note that the experimental distribution $m(\pi^0\gamma\gamma)$ remaining after background subtraction despite the large statistical errors shows a clean signal of ~ 500 events with a shape similar to the peak from the MC of $\eta \to \pi^0\gamma\gamma$.

The average of all tests that were made gave $\mathrm{BR}(\eta \to \pi^0\gamma\gamma) = (3.2 \pm 0.8) \times 10^{-4}$, where the error includes the combined effect of statistics and systematics. There is also another source of systematics that, in our opinion, should be incorporated in the final error. This is an uncertainty due to the possible difference of the real decay amplitude for $\eta \to \pi^0\gamma\gamma$ from the phase space used in the MC. In the case of a significant difference between them, changing the selection criteria and limits on the plot variables may lead to a different fraction of $\eta \to \pi^0\gamma\gamma$ events accepted in the data and in the MC. Although the statistical errors in the experimental distribution remaining after background subtraction were rather large, we did not see any significant difference of the experimental $\eta \to \pi^0\gamma\gamma$ Dalitz plot from the MC one. The comprehensive study of this source of systematics showed that the corresponding uncertainty does not exceed 10%. Including this uncertainty in the total error yields a branching ratio $\mathrm{BR}(\eta \to \pi^0\gamma\gamma) = 3.2(9) \times 10^{-4}$, which is about one-half the existing value [3]. Our result disagrees with the old measurement by about three standard deviations. Note that our value for $\mathrm{BR}(\eta \to \pi^0\gamma\gamma)$ is in much better agreement with the χPTh predictions.

ACKNOWLEDGMENTS

This work was supported in part by US DOE, NSF, NSERC, RMS, and VS.

REFERENCES

1. J. Gasser and H. Leutwyler, Nucl. Phys. B **250**, 539 (1985).
2. J. Kambor *et al.*, Nucl. Phys. B **465**, 215 (1996); A. Anisovich and H. Leutwyler, Phys. Lett. B **375**, 335 (1996).
3. GAMS-2000 Collab. (D. Alde *et al.*), Z. Phys. C **25**, 225 (1984).
4. Crystal Barrel Collab. (A. Abele *et al.*), Phys. Lett. B **417**, 193 (1998).
5. Review of Particle Physics, Eur. Phys. J. C **15**, 27 (2000).
6. Crystal Ball Collab. (S. Prakhov *et al.*), Phys. Rev. Lett. **84**, 4802 (2000); Crystal Ball Collab. (A. Starostin *et al.*), Phys. Rev. C **64**, 055205 (2001).
7. V. Bekrenev, CB Report CB-99-012; S. Prakhov, CB Reports CB-99-003, CB-00-005, CB-00-011. (http://bmkn8.physics.ucla.edu/Crystalball/Docs/documentation.html).
8. Crystal Ball Collab. (W. B. Tippens *et al.*), Phys. Rev. Lett. **87**, 192001 (2001).
9. S. Prakhov, CB Reports CB-01-008, CB-01-009.
10. K. K. Craig, PhD Thesis (http://bmkn8.physics.ucla.edu/Crystalball/Docs/Theses/craig.ps).